INVESTIGATION OF HIGH-ENTROPY ALLOYS FOR USE IN ADVANCED NUCLEAR APPLICATIONS

A thesis submitted in partial fulfilment for the degree of doctor of philosophy at University of Technology Sydney

Daniel J. M. King

Certificate of Authorship / Originality

I certify that the work in this thesis has not previously been submitted for a degree nor has it been submitted as part of the requirements for a degree except as fully acknowledged within the text.

I also certify that the thesis has been written by me. Any help that I have received in my research work and the preparation of the thesis itself has been acknowledged. In addition, I certify that all information sources and literature used are indicated in the thesis

Signed:

Acknowledgements

The occurrence and fruition of this project was one born from serendipity, ultimately beginning with my dear wife, Shirin-Rose King. Her role in the completion of this PhD, through both emotional and practical support, has been constant over the past three years and I am very thankful. It was through her that I was able to attend a week-long visit to ANSTO where I met Dr. Simon Middleburgh who proposed the current project. I may never meet another person such as Simon. There are very few people who can consistently induce confidence in oneself and abilities. A natural leader, his passion, curiosity and work ethic is incredibly inspiring and I attribute a lot of the success of this PhD to his unwavering guidance, support and boundless knowledge. I remember the first day I started my PhD, two students from Imperial College London (now Dr. Hassan Tahini and Dr. Patrick Burr) were visiting ANSTO. We all huddled around Simon's desk in excitement over a new finding like children who had found a strange insect. It was then that I knew that that research was the right path for me.

Of course, none of this would have been possible without Prof. Michael Cortie who supported this project after overhearing me lamenting over the fact I could not find an academic that was willing. Although lecturing is not his favourite past time, he was my favourite teacher during undergraduate studies due to his casual yet concise teaching style. Over the past three years it seems he would consign an infinite amount of time to assist in any problem I had, despite having such a busy schedule. Patient, wise and empathetic, one could not ask for a better mentor.

There are many others that have been of great help to the completion of this project. Namely: Dr. Amelia Liu, a collaborator who treated me like family when I visited Monash University while writing my very first, first name publication, Dr. Daniel Riley who provided insightful technical and practical knowledge as well as a shoulder to lean on, Dr. Timothy Lucey. Dr. Gordon, Dr. Greg Lumpkin, Dr. Edward Obbard, Dr. Patrick Burr, Dr. Massey De Los Reyes, Technicians: Ken Short, Tim Palmer, Kim Lu, Angus Gentle and Geoff McCredie whose contributions were invaluable. Last but not least, I must thank my second cousin, Andrew McGregor, who selflessly dedicated a large amount of his spare time to build the ASAP software and web-integration, tying together a large portion of my work.

Abstract

A preliminary assessment of the suitability of high-entropy alloys (HEAs) for use within a nuclear reactor environment is conducted by combining both experimental and computational techniques. The investigation begins on the V-Zr system where three thin films with stoichiometries (2V:1Zr, 1V:1Zr and 1V:2Zr) were deposited. A metastable amorphous phase was observed and subsequently modelled, for the first time, using static density functional theory (DFT). This methodology is then further developed and the thermodynamics of the binary system were assessed.

Similar computational techniques were then used to investigate CoCrFeNi. Isolated vacancy formation calculations were performed and it was found that vacancies of Co, Fe and Ni are positive, and Cr is negative in energy. This drive for spontaneous segregation of Cr from the FCC matrix is predicted to occur in a vacancy mediated process. It is possible that this mechanism will allow for the formation of a corrosion resistant oxide layer. The addition of Al to form the Al_xCoCrFeNi system, where x is varied from 0 – 2.4 atomic ratio, was then explored. Only when partial ordering was imposed, with Al and Ni restricted to separate sub-lattices, to form an ordering analogous to the B2 NiAl intermetallic, was the BCC packing stable. Decomposition of the ordered BCC single phase into a dual phase (Al-Ni rich and Fe-Cr rich) was also considered.

An algorithm to rapidly screen elemental mixtures to form single phase high-entropy alloys (SPHEAs) was developed. Approximately 186,000,000 compositions of equimolar 4, 5 and 6 element alloys were screened and ~1900 new SPHEAs were predicted using this method.

NbTiV, $Mo_{0.5}$NbTiV, MoNbTiV, NbTiV$Zr_{0.5}$, NbTiVZr and NbTiVZr_2 were experimentally produced via arc melting. As predicted by the screening method, all alloys were found to form a single phase BCC structure with non-equilibrium dendritic microstructures. Au^{5+} and He^{+} ions were used to irradiate TEM samples and a bulk NbTiVZr_2 sample. No changes were observed after ~20-25 dpa in the TEM samples and minimal swelling of the BCC matrix was observed in the bulk sample.

The project has revealed that HEA alloys are potentially candidate materials for structural applications in nuclear reactor environments.

Contents

List of Figures

List of Tables

1

LITERATURE REVIEW

1.1 Introduction

The exploration into metallic systems has been one that humankind has embarked on since the beginning of early civilisation [1]. It is the use of these materials as tools, and the quest to discover and manufacture superior tools, that drives this exploration. Naturally, we began our investigation into metallic systems that feature a single element and progressively continued our search with the addition of a second e.g. gold or copper, then bronze, brass, iron-carbon, pewter etc. In the late 1800's, due to the work of J. Gibbs, M. Planck, L. Boltzmann and many other scientists, a mathematical description of the thermodynamic equilibrium for metallic systems was obtained [2]. This allowed the creation of phase diagrams which are now the most widely used method for the phase prediction of metallic mixtures. Complete descriptions of singular, binary and ternary alloys can be made at equilibrium, but as we attempt to continue beyond ternary systems, we encounter problems. This is because the number of possible permutations increases dramatically and we can no longer easily represent complete systems on a two dimensional platform. More importantly, there was an underlying assumption that when increasing the concentration of elements within such systems, beyond that of minor alloying, intermetallic or amorphous structures would form; the latter being a precursor to high-entropy alloys (HEAs).

It was following the masters theses of K. H. Huang [3] and T. J. Chen [4] in 1996, in the wake of bulk metallic glass research, that Yeh *et al.* first coined the term "high-entropy alloy" in 2004 [5]. In this publication they noted that highly alloyed mixtures composing of five or more elements could produce a body-centred cubic (BCC) or face-centred cubic (FCC) crystal structure and proposed a theory, based on the configurational entropy explaining why this occurs. Furthermore, they speculated how the "high-entropy alloys" might challenge conventional steels in areas such as thermal stability, strength, ductility and hardness.

In parallel, a similar study was conducted by Cantor *et al.* [6] and was published two months after Yeh *et al.* Again, it was demonstrated that highly alloyed mixtures of five or more elements could form solid solutions of BCC and/or FCC structure. Some evidence of prior studies adopting this concept are seen through two examples: A patent of Mo-Nb-Ti-V-Zr for dental applications [7] and the studies of a precipitate in UO_2 nuclear fuel Mo-Pd-Rh-Ru-Tc [8]. In the years since Yeh *et al* and Cantor *et al.*'s description, the number of publications on the topic of "high-entropy alloys" has been steadily increasing, see Figure 1.1.

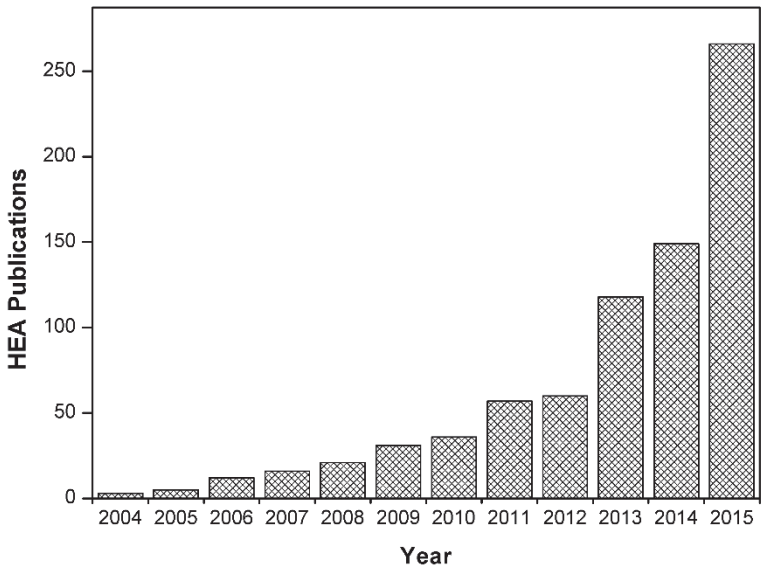

Figure 1.1. Number of publications on the topic "high-entropy alloys" as searched in Web of Science.

Following the original descriptions, there has been much debate as to what exactly constitutes a HEA (which continues today). Yeh *et al.*'s definition describes HEAs "…as those composed of five or more principal elements in equimolar ratios… …[containing] principal elements with the concentration of each element being between 35 and 5 at. %". The ambiguity of this definition has led to two differing opinions: (i) A HEA refers to a mixture of five or more elements in equimolar concentrations, independent of resulting structure. Reports of brittle HEAs with multiple phased microstructures, even amorphous HEAs, are made under this regime, or (ii) a HEA refers to alloys that both contain five or more elements in equimolar concentrations that can produce a single phase solid solution. The latter definition is narrower and makes a lot more sense from the standpoint of technological significance. Regardless of which viewpoint one takes, it seems that the quaternary systems have been neglected. We now have a situation in which binary and ternary systems are relatively well described through phase diagrams, quaternary systems are not, yet do not classify as a HEA (therefore do not warrant investigation).

These issues are addressed through a refined definition and the introduction of a new label "single phase high-entropy alloys" SPHEA [9]. Within this thesis, both a HEA and SPHEA are defined as alloys with four or more alloying elements, at least three of which have a molar ratio between 0.33 – 1 to that of the highest contributing element. SPHEAs must be able to display a single phase of simple, random, close-packed structure below the solidus. The basis for inclusion of quaternaries into the definition of both HEAs and SPHEAs will be made obvious within this dissertation.

Within this critical literature review there are two areas that will be addressed: (1) The evolution of the theoretical understanding of HEAs. (2) Why HEAs are important and how they apply to the nuclear industry.

1.2 The nuclear industry

The nuclear industry is currently at a stage in which a great deal of knowledge has been gained through operation of reactors in generations I to III, with water moderated/cooled reactors dominating the reactor

designs today [10]. Nuclear-grade materials used for both in-core and out-of-core components have been well studied and are well suited for safe operation in current reactor environments. These materials typically include Fe, Mg, Ti, Zr alloys, ZrO_2, SiC-based ceramics [11-14] and low alloy ferritic-steels [15]. Naturally, the next generation of water-cooled nuclear reactors have been designed to optimise performance of the superseded generations. Targeted for wide implementation in the next ten to twenty years; aspects such as safety, lifetime, power output and efficiency have been considered and are intrinsically linked to their design from the onset.

It is widely recognised, however, that even better performance could be obtained in future reactor designs by using other coolant/fuel combinations [16]. For example, a high temperature, gas-cooled reactor, or a molten salt thorium reactor, which present different and harsher environments in comparison to preceding designs and which require new nuclear-grade materials. The composition of available materials must be revised and expanded while their performance in these environments must be understood in a mechanistic and therefore predictable manner.

The types of 'next generation' reactor being considered include the gas-cooled fast reactor (GFR), lead-cooled fast reactor (LFR), molten salt reactor (MSR), sodium-cooled fast reactor (SFR), and supercritical-water-cooled reactor (SCWR) and smaller, modular reactor designs such as the pebble bed reactor (PBR). The outlet temperatures for these reactors range from 550 – 850 °C and new corrosion challenges are present in both the MSR and SCWRs, particularly [17]. The leading design has, so far, not emerged as each has their advantages and drawbacks. It is likely that materials challenges will affect the commercialisation and influence the design chosen by the majority of nuclear power generating utilities.

A typical light water reactor (LWR) in operation today has an outlet temperature of 350 °C and a thermal neutron spectrum. Materials used in the next generation of fission reactors will be subjected to higher temperatures, temperature gradients, neutron fluences, and, possibly, more corrosive environments than the current generation. Although the technology for fusion reactors is comparably less developed, the property requirements for confinement materials are similar. The properties that the next generation of nuclear materials must possess include enhanced dimensional stability under irradiation, resistance to irradiation creep, relaxation, swelling, growth, and corrosion or oxidation. Economic considerations are also required, which take into account the cost of fabrication and operation lifetime of components in each reactor design [18].

Current candidate materials include graphite, stainless or high alloy steels (austenitic, martensitic or ferritic), Ni-based alloys, ceramics, and composites thereof. Information on their prospects in the nuclear industry may be found elsewhere [19]. It is the purpose of this dissertation to evaluate whether HEAs should be included on this list and draw attention to their potential for use in generation III+ and IV power systems.

1.3 Previous and current nuclear materials

1.3.1 Zirconium alloys

Zirconium has a high melting temperature, corrosion resistance, good mechanical properties, relatively high abundance, and very low thermal neutron absorption cross-section [20] (a concept later explained in the methodology chapter). This makes it ideal for use as an in-core structural material. For nuclear applications minor alloying additions of Sn, Fe, Cr and Ni are mixed with Zr to create a solid solution, increase the corrosion resistance and provide a slight increase in strength. Zircaloy -2 and -4 are commercial examples of this which have now been superseded by ZIRLO and M5.

One problem encountered by Zircaloys is oxidation [21] and some susceptibility to the formation of hydrides leading to mechanical degradation [22]. In an oxidising environment, a layer of zirconia (ZrO_2) forms on the surface the material according to the reaction:

$$Zr_{(s)} + 2H_2O_{(l)} \rightarrow ZrO_{2(s)} + 4H_{(g)}$$

This zirconia layer is of a tetragonal structure (stabilised by the large stresses of the metal/oxide interface and other microstructural effects). As this layer grows the inner-most layers adopt a monoclinic structure which is relatively porous allowing for further oxidation.

During the oxidation reaction excess hydrogen is produced which can diffuse into the Zircaloy matrix. This leads to the formation of hydrides on the surface and ultimately hydrogen embrittlement and surface fracture [23]. This process is accelerated at higher temperatures and, in extreme disaster environments, can cause hydrogen explosions [24]. In order to reduce these effects, Zircaloy-4 was produced with almost no Ni (a hydrogen getter) and proved to reduce the hydrogen pickup by a factor of three [25]. Since Ni is insoluble in Zr this has negligible mechanical effects.

1.3.2 Iron alloys

Stainless steels are iron-based alloys, and are very well-studied/understood. They are highly favoured for structural applications as they have very good mechanical properties and corrosion resistance that extend to high temperatures. However, their larger thermal neutron cross-section limits some of their in-core applications.

From an engineering perspective, the workability, low cost, mechanistic understanding and wealth of empirical data for stainless steels allows for the specific tailoring of elemental concentrations for specific uses. Chromium is the main alloying element which provides the excellent corrosion resistance. Other elements such as B, Mo, Nb, Ti and S can be added for special purposes. The 300 series of the American Iron and Steel Institute (AISI) are typically used for nuclear applications. Type 304 contains 0.08% C, 1% Si, 2% Mn, 18-20% Cr, and 8-12% Ni.

Problems associated with stainless steels for nuclear applications include: hydrogen and helium embrittlement and stress corrosion cracking. Despite being highly corrosion resistant, strong reducing environments from nuclear fission products, e.g. chlorides, can cause stress corrosion cracking in steels [26]. In a reactor environment, exposure to corrosive environments, and tensile stress can ultimately lead

to mechanical failure. This occurs by irradiation-induced segregation of elements whereby precipitates such as $Cr_{23}C_6$ form at the grain boundary. This Cr depleted region cannot readily form a passivating layer leading to dissolution at the grain boundaries. Applied stress induces plasticity at any crack tips which further hinders passivation and accelerates crack growth [27].

1.3.3 Nickel-based alloys

Ni alloys (e.g. Hastelloy, Inconel) are most noted for their corrosion resistance and high temperature mechanical properties. They are sometimes preferred over steels for use in high temperature structural applications as they display better creep-rupture strength > 900 °C [20]. Ni alloys do not have phase transitions; the solid solution in phase γ is characterised by a high recrystallization temperature. Formation of dispersed intermetallics such as Ni_3(Ti, Al) is sought to increase strength [23]. The Ni-based alloys are currently the standard for use in very-high-temperature reactors as turbine blades [19]. A trade-off between creep properties and corrosion resistance is reflected by the developments of Inconel and the Hastelloys respectively. Haynes 230 is another good candidate material as it has potential to exhibit both to a satisfactory level [19].

Unfortunately, the relatively large thermal neutron cross-section limits the applications of these alloys. Also, the problem associated with Ni's hydrogen affinity further restrict its use as a cladding material.

1.4 High-entropy alloys

HEAs are not confined to a specific type of element and a theoretical description of HEAs can be achieved through the equation for Gibb's free energy:

$$\Delta G = \Delta H - T\Delta S \tag{1.1}$$

Here, ΔG is the change in free energy, ΔH is the change in enthalpy, ΔS is the change in entropy and T is the temperature upon the mixing of elements. The phase or configuration that yields the lowest ΔG is that which is the most stable at temperature T.

The principle behind HEAs is to maximise the ΔS term of a potential crystalline solid solution phase in order to minimise ΔG. This can be done because the inherent disorder of a solid solution when compared to competing ordered intermetallic phases can lead to a relative minimisation in the Gibbs' free energy.

When considering the contributions to ΔS we find it is influenced by a number of phenomena, viz., configuration, electronic, magnetic and vibration effects [28]. The relative contribution by each of these to the total entropy is disproportionate and in many cases dominated by the configurational contribution [29, 30].

It is thought that the configurational entropy is somewhat unique to a disordered system and, according to ideal solution theory, is increased by the alloying of more components and maximised when they are in equi-molar ratios. We now explore this relationship referred to as configurational entropy, ΔS_{conf} (often referred to as the entropy of mixing). ΔS_{conf} can be calculated as a purely statistical term which is derived from Boltzmann's equation for entropy, S_B [31]:

$$S_B = k_B \ln \omega \tag{1.2}$$

where, k_B is Boltzmann's constant and ω is the number of microstates (number of unique arrangements) corresponding to a given macrostate (the system as a whole). Analogous to ΔS_{conf} of an ideal gas, this equation can be applied to a disordered alloy whereby the total number of atoms $N = N_1 + N_2$, whereby, N_1 and N_2 are the number of atoms of element 1 and 2, respectively, in a binary solid solution where,

$$\omega = \frac{N!}{N_1! N_2!}, \tag{1.3}$$

It is possible to derive the equation for the Gibbs entropy through the following steps:

Using Stirling's approximation [32] for the $\ln N! \approx N \ln N - N$ when $N >> 1$,

$$S_{conf} = k_B \left[N \ln N - N - \left(N_A \ln N_A - N_A + N_B \ln N_B - N_B \right) \right] \tag{1.4}$$

simplifying,

$$S_{conf} = -N k_B \left(-\ln N + 1 + x_A \ln x_A N - x_A + x_B \ln x_B N - x_B \right) \tag{1.1}$$

Where x_A and x_B are the concentration of element A and B, respectively, and $x_A N = N_A$.

Since $x_A + x_B = 1$,

$$S_{conf} = -N k_B \left[-\ln N + x_A \left(\ln x_A + \ln N \right) + x_B \left(\ln x_B + \ln N \right) \right] \tag{1.2}$$

$$S_{conf} = -N k_B \left[-\ln N + x_A \ln x_A + x_B \ln x_B + \left(x_A + x_B \right) \ln N \right] \tag{1.3}$$

$$S_{conf} = -N k_B \left(x_A \ln x_A + x_B \ln x_B \right) \tag{1.4}$$

since $N = n N_A$ and $R = N_A k_B$,

$$S_{conf} = -nR \left(x_A \ln x_A + x_B \ln x_B \right) \tag{1.5}$$

This equation can be extended into a summation for element *i* in a *j* element system:

$$S_{conf} = -nR \sum_{i=0}^{j} x_i \ln x_i \tag{1.6}$$

When the system is in equi-molar concentrations, ie. $x_i = x_{i+1} = \cdots = x_j$,

$$S_{conf} = nR \ln j \tag{1.7}$$

The physical basis for this contribution to the Gibbs free energy is somewhat hard to transfer from an ideal gas to that of a solid solution. However, there is an assumption that each lattice site is indistinguishable from the other and that each atom has an identical chance to be found on each lattice site and there are no chemical interactions. In reality, the mixing of any unlike atoms will inherently introduce a chemical selectivity that will weigh the probability of finding each given species on each given lattice site. This effect is somewhat accounted for in the regular [33] and sub-regular solution [34] models, however, is only introduced through the enthalpy term. That is to say, the term for enthalpy dictates the nature of the atoms' confinement and the entropy is calculated according to those conditions. Only recently has this effect been explored in HEAs as partial ordering [35-37]. Recently, a correction term in the entropy that accounts for the mismatch in atomic radii has been suggested [38].

The mechanism by which S_{conf} can influence the Gibbs free energy in an exclusively non-positive manner can be understood through the theory of quantum mechanics. Put simply, S_{conf} is a count of the microstates within the bulk system. Upon the mixing of an ideal system, there is an intrinsic drive for complete homogenous mixing. Therefore enabling a larger number of microstates is the most energetically favourable outcome leading to a minimisation in free energy. There are many parallels of this behaviour in cosmology, geoscience, computer science and it has recently been thought to be an underlying basis for universal intelligence [39].

Originally it was proposed that only configurational entropy was necessary to stabilise the formation of a SPHEA. Yeh *et al*. [5] used a hypothetical example in which the enthalpy of formation was zero.

Therefore,

$$\Delta G = -T\Delta S \tag{1.8}$$

In an attempt to assess the magnitude of ΔS required to supress a strong intermetallic compound, experimental literature values [31] were substituted for ΔG for NiAl and TiAl and their melting temperatures were substituted for T. Yeh *et al*. argued that by calculating ΔS in this manner it is a good estimation of the configurational entropy for these *ordered* structures; therefore the entropy of a HEA would only need to be of higher magnitude to stabilise the solid solution. This equated to a system with five or more elements. However this logic is flawed for three reasons. Firstly, one cannot discount the enthalpy of formation of a system as it can sometimes dominate the contribution to the Gibbs free energy. Secondly, an ordered compound such as NiAl and TiAl will have a configurational entropy equating to zero as the number of ways of arranging the atoms is 1 (discounting vacancies and anti-sites). Finally, one cannot use two intermetallics to generalise across all solid solutions as many systems will not contain these elements. The failure of this model is outlined in many following publications in which multi-element mixtures were produced yielding multi-phased brittle microstructure [40-42] rather than the desired SPHEA. I will offer a more inclusive theory of HEA formation later in this dissertation.

As previously mentioned, the enthalpy of formation, ΔH, has a large effect on the Gibbs free energy. This term corresponds to the amount of heat released (exothermic) or consumed (endothermic) upon the mixing of the elements. It is calculated as a relative term i.e. $\Delta H = H_{\text{products}} - H_{\text{reactants}}$ and the

value of H alone is arbitrary. Classically H is mathematically represented as $H = U + PV$ where U is the potential energy, P is pressure and V is volume. In this dissertation H is calculated using density functional theory for a system in its ground state. This concept will be elaborated within the methodology. In the context of HEAs, the chemical similarity/difference between the mixed species has a considerable effect on the formability of a SPHEA (especially at low temperatures).

In 2012 Yang *et al*. [43] proposed a new parameter by which solid solution formation could be predicted in HEAs. This parameter was a simple ratio between the two contributions to the Gibbs free energy:

$$\Omega = \frac{T\Delta S_{conf}}{|\Delta H|} \tag{1.9}$$

This parameter was coupled with another of geometric nature:

$$\delta = \sqrt{\sum_{i=1}^{n} c_i \left(1 - r_i / \bar{r}\right)^2} \times 100 \tag{1.10}$$

where c is the concentration of element i, in atomic fraction, in an n element system, r is the Goldschmidt radius and $\bar{r}$ is the average radius of the system. This method was largely successful in separating solid solutions from intermetallic compounds and bulk metallic glasses (BMGs), see Figure 1.2. However, it was unsuccessful in predicting HEAs that display a single phase solid solution from those of dual phase solid solution + intermetallic.

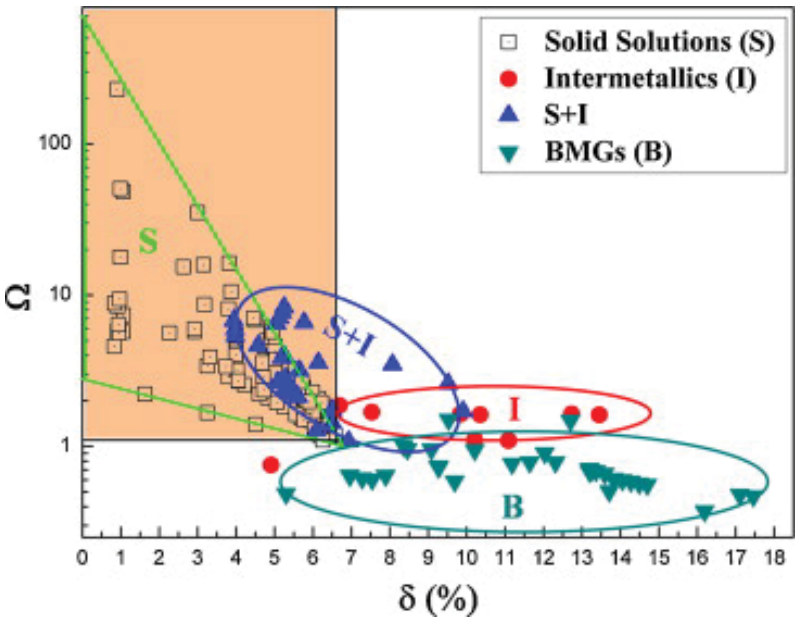

Figure 1.2. Taken from Yang *et al*. 2012 [43], where Ω and δ are plotted for an experimentally characterised system that has been determined to form a single phase solid solution (black squares), dual phase solid solution + intermetallic (blue triangles), intermetallics (red circles) and BMGs (cyan triangles).

The physical basis of the methodology employed by Yang *et al*. to calculate the Ω parameter is not obvious. The argument in favour of this method is that intermetallic compounds often yield a largely

negative ΔH value. If the alloy possesses $T\Delta S_{conf}$ (where T is the melting temperature of the alloy) of a magnitude large enough to surpass that of ΔH then a solid solution will be favoured i.e. the numerator is larger than the denominator in Eq. 1.14. However, similar to Yeh *et al*., the ΔH value is not fully accounted for. When assessing two competing phases (ordered and disordered), the Gibbs free energy of both must be compared. This requires ΔH and $T\Delta S$ of both phases to be considered. Here it is correctly identified that $\Delta S_{conf} = 0$ for an ordered compound therefore only requiring the calculation of $T\Delta S$ for the disordered system. When considering ΔH, however, it remains that both ordered and disordered values must be used in the evaluation of stability. Yang *et al*., instead, used the value for the formation enthalpy of a *liquid* binary alloy, ΔH^{am}. This value is calculated using Miedema's model [44], a semi-empirical macroscopic atom model which is later described in the Methodology chapter. To calculate ΔH of the solid solution Yang *et al*. employed a method developed by Takeuchi and Inoue [45] for BMG systems. In essence it is a weighted sum of the binary ΔH^{am} terms with a correction factor of 4 for equi-molar systems i.e. $c = 0.5$:

$$\Delta H = \sum_{\substack{i=1 \\ i \neq j}}^{n} 4 \Delta H_{ij}^{am} c_i c_j \tag{1.11}$$

where ΔH_{ij}^{am} is the formation enthalpy of a liquid binary alloy between element i and j. A largely overlooked result of this method is the fact that it must follow the regular solution model at which the highest magnitude in formation enthalpy is always when $c = 0.5$. Correction factors that allow for the representation of the sub-regular solution model should be used to avoid this [46]. Despite these shortcomings, this method is the most widely used method for predicting HEA formation within the literature to-date.

A handful of other methods have been developed since, but have not gained traction [38, 47, 48] due to their lack of applicability and reproducibility of results.

1.4.1 Morphology and microstructure

As mentioned, HEAs often display multiphase microstructures. These can be in the form of solid solutions and/or intermetallic phases. The latter can adopt the form of nano- to micro-scale precipitates [49] which are often desired for mechanical purposes due to the effect of precipitate hardening. However, it is also possible to form complex brittle microstructures which are dominated by ordered compounds and generally undesired.

Due to the entropy term, the stability of the solid solution phase will always be lower at lower temperatures and, in general, precipitation of intermetallics is likely to be thermodynamically favourable during annealing at lower temperatures [50]. However due to rapid quenching and "sluggish" diffusion kinetics [51] it is possible to suppress intermetallic formation and maintain a SPHEA at room temperature. In-fact, reports of furnace cooling [52] and annealing at low-temperatures for up to two weeks [53] have reported little-to-no change in microstructure in some cases where intermetallic precipitation might have been expected. It is thought that, due to the intrinsic strain within the solid

solutions' lattice, migration pathways are hindered [54]. This notion of sluggish diffusion has recently been disputed by Jones *et al*. [55], highlighting the need for more work in this area.

Although it is hard to generalise a whole class of alloys, one of the most studied HEAs to-date is the $Al_xCoCrCuFeNi$ system. It was this system that was used as the model for Yeh at al.'s theory of HEA formation where splat quenched as-cast bulk samples were experimentally characterised. One interesting feature of this system is that it undergoes a transition from FCC → BCC+FCC → BCC packing with the increase of Al concentration x, see Figure 1.3.

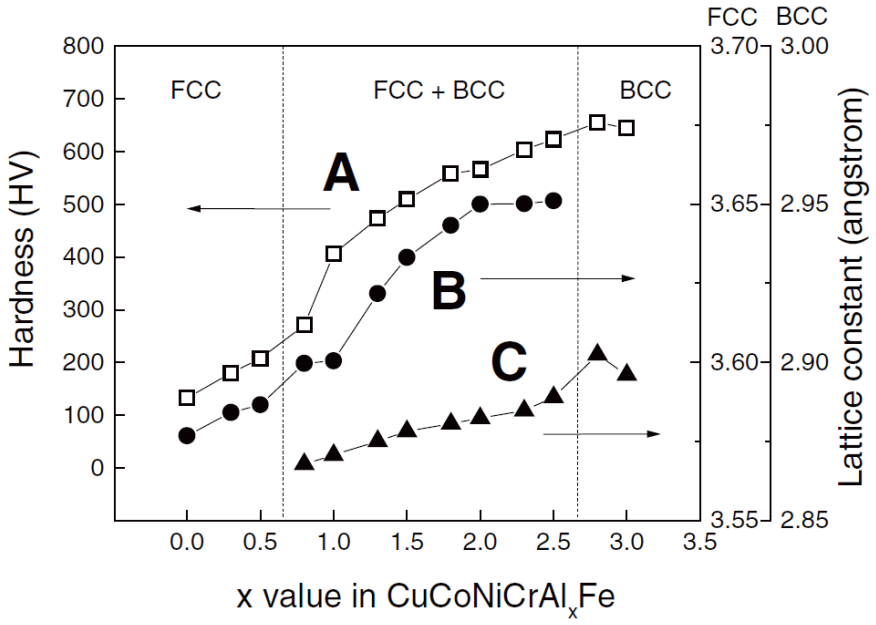

Figure 1.3. Taken from Yeh *et al*. 2004 [5], shows: A. Hardness, B. FCC and C. BCC lattice constants of the AlxCoCrCuFeNi HEA when x (in atomic ratio) is increased from 0 → 3.

The packing shift from single phase FCC to dual phase FCC and BCC to single phase BCC is observed using X-ray diffraction (XRD). When *x* exceeds 0.8 atomic ratio, to that of the other elements, a BCC pattern in observed (in addition to FCC) with a reflection at ~30° 2θ corresponding to a B2 ordering structure designation. Scanning electron microscopy determined the B2 phase to be in the form of nanoprecipitates ranging in size from 7 – 50 nm in diameter.

Follow-up studies on this system reveal a greater level of detail. It was found that the XRD patterns displaying FCC cubic reflections actually contain two FCC phases superimposed. One of these is a disordered solid solution, the other a segregated Cu-rich phase. The Cu segregates from the solid solution due to its positive formation enthalpy with each of the other elements in the mixture. This is a prime example of entropy (in the form of an additional element) not being sufficient to overcome an enthalpy driven reaction.

When Cu is removed, to make the $Al_xCoCrFeNi$ system, only a single FCC phase is observed. Systematic studies on this system were done by Chou *et al*. [56] and Wang *et al*. [57]. It was found that a single

phase FCC forms when $0 \leq x < 0.5$, a dual phase FCC + BCC when $0.5 \leq x < 0.9$ and single phase BCC when $0.9 \leq x \leq 1.0$. Above $x = 1.0$ a dual phase A2 + B2 microstructure is observed. Accompanied by these microstructural changes are changes in the morphology, see Figure 1.4.

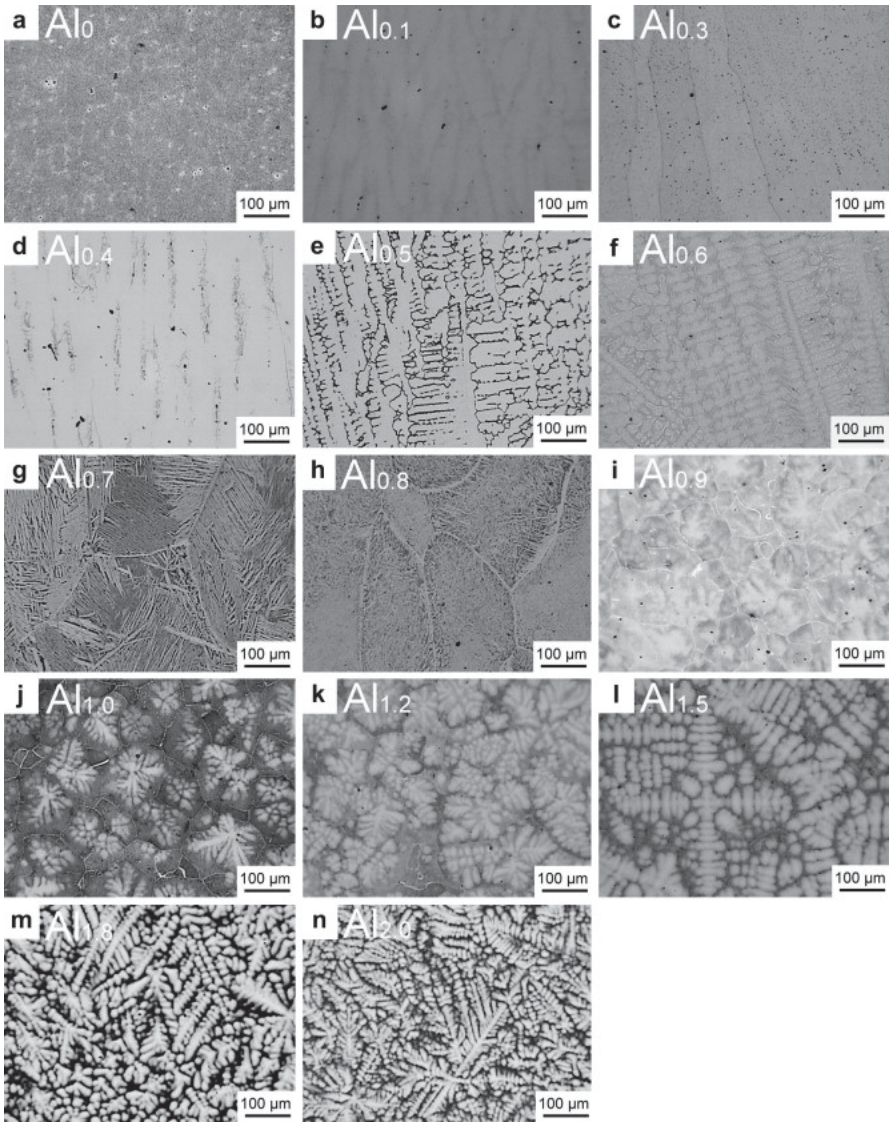

Figure 1.4. Taken from Wang *et al*. 2012 [57] showing optical micrographs of the as-cast samples displaying a columnar cellular structure (a – c), columnar dendrite (d – f), equiaxed nondendritic grain (g – h), equiaxed dendritic grain (i – l), and a non-equiaxed dendritic grain structure (m – n).

The drive for the packing shifts are attributed to a geometric cause [58, 59], whereby Al, which has a larger metallic radius of 1.43 Å compared with the other constituent elements (1.25 Å, 1.36 Å, 1.26 Å, and 1.24 Å [60] for Co, Cr, Fe, and Ni, respectively), will impose a strain on the FCC lattice that will increase upon the further alloying of Al. To alleviate this strain the packing shifts from FCC to a more openly packed BCC structure. This theory is supported by the increase in lattice parameter of the FCC phase as Al is added (Fig. 2). However, this reasoning does not explain why we observe a NiAl B2 phase. Later in this dissertation I will return to this problem and provide a more rigorous explanation through the investigation of the thermodynamic drive for a BCC packing [37].

The long-standing concept of valence electron concentration (VEC) has also been applied to HEAs as a predictor for phase structure [61]. Here it is assumed that each alloying element contributes a number of valence electrons equal to the total number of electrons in its valence band (including d-electrons) according to their parent metals. The resulting alloy then contains a weighted average of the VEC contributions of each element, commonly expressed as an electron:atom ratio. This should not be confused with an alternative method of determining electron concentration (the so-called Hume-Rothery method) whereby only the number of itinerant electrons are considered and denoted as the "e/a" of an alloy. The relationship between VEC and structure is not a new concept [62]. When applied to HEAs, this relationship has been used to varying success and has a few exceptions [63]. Specific bounds were first empirically developed by Guo et al. [61] for HEAs containing Al-Co-Cr-Cu-Fe-Mn-Ni and thus hold well for those systems. However, due to influence of Al within these alloys and the trivial method the VEC is assigned to each element it is easy to understand the inaccuracies when extending to a wider range of HEAs. In a physical system, electrons that are considered "valence electrons" differ depending on the local environment of the atom [64]. Nevertheless, it is predicted that BCC $(\mathrm{VEC} < 6.87)$, BCC + FCC ($6.87 \leq \mathrm{VEC} < 8.00)$ and FCC ($\mathrm{VEC} \leq 8.00)$ morphologies will form as a result of the corresponding VECs. Further work and a more in-depth analysis of this concept can be found in the work by Poletti and Battezzati [63].

When Al is removed from this system, the four element SPHEA CoCrFeNi is formed [53, 65, 66]. This system, along with CoCrFeMnNi [6, 67-70] are considered model FCC SPHEAs. The former adopts a relatively homogeneous structure, see Figure 1.5a, and the latter, a dendritic structure (Figure 1.5b) in the as-cast condition. Dendritic microstructures are typical of a SPHEA and are attributed to the difference in melting temperatures between the constituent elements. The interdendritic material is usually observed as a solid solution phase rich in the element with the lowest melting temperature and arises due to the rapid solidification of the melt [71].

It is important to distinguish between a HEA that consists of a single inhomogeneous solid solution phase in a dendrite/interdendrite morphology from one that forms two distinct solid solution phases, as the former can be homogenised through annealing and will exhibit very different behaviour and mechanical properties. The grain size of the homogenised type of SPHEA has found to follow the Hall-Petch relationship (coarsening with higher and longer annealing) [72].

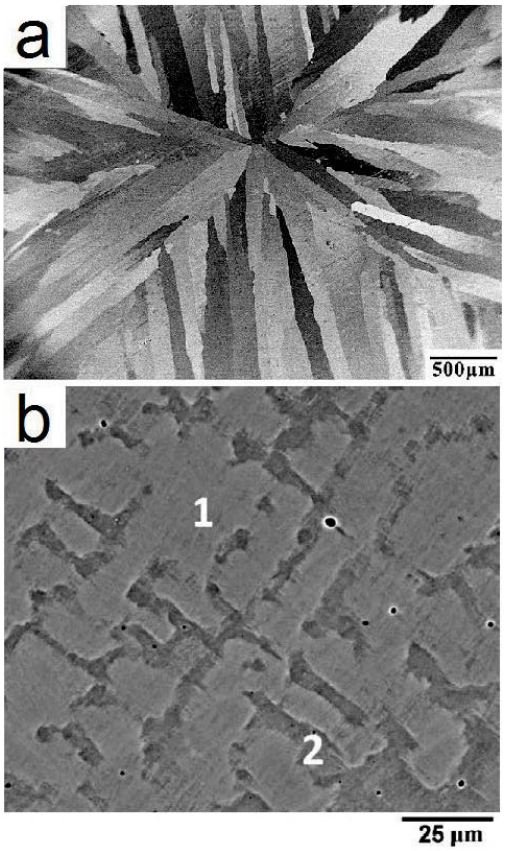

Figure 1.5. BSE image of (a) drop-cast CoCrFeNi and (b) crucible quenched CoCrFeMnNi taken from Wu *et al*. 2014 [66] and Salishchev *et al*. 2014 [73], respectively.

Currently, there is an attraction to design SPHEAs using *refractory* elements because of their chemical similarity and high melting temperatures allowing for high stabilities to be achieved. Some example systems include: **Mo-Nb-Ta-W**, **Mo-Nb-Ta-W-V [74]**, Nb-Cr-Mo-Ta-Ti-Zr [75], **Nb-Ti-V-Zr**, Cr-Nb-Ti-Zr, Cr-Nb-Ti-V-Zr [76], **Hf-Nb-Ta-Ti-Zr**, Al-Mo-Nb-Ta-Ti-Zr, **Al-Hf-Nb-Ta-Ti-Zr** [77], (those that formed a SPHEA in bold). While it is no surprise the addition of Cr will destabilise a refractory SPHEA (due to its comparatively small atomic radius); it is indeed a remarkable result that the addition of Al in the mixture of **Al-Hf-Nb-Ta-Ti-Zr** will remain stable, see Figure 1.6. This surprise is not because of the atomic radius (as Al is considered to have a similar metallic radius to the other elements), but due to its strong tendency to form intermetallics such as AlZr and AlTi.

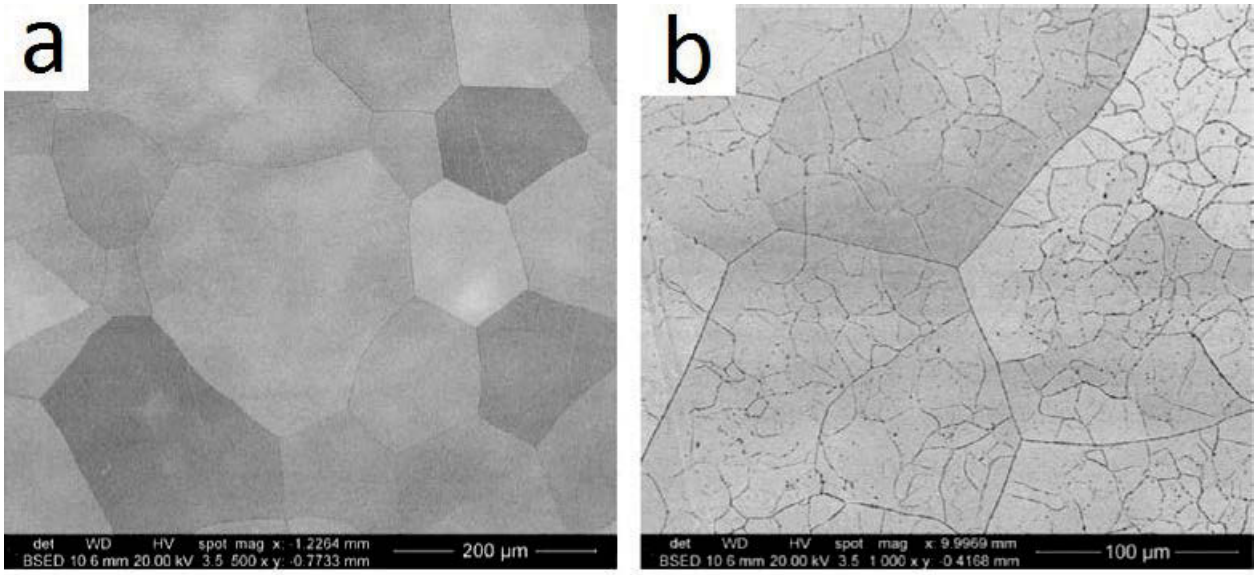

Figure 1.6. SEM micrographs from Senkov *et al* 2014 [78] of (a) equiaxed grain structure and (b) sub-grain structure of Al0.4Hf0.6NbTaTiZr after annealing at 1473 K for 24 hrs.

Nevertheless, Senkov *et al* [77] have reported the $Al_{0.4}Hf_{0.6}NbTaTiZr$ to produce a SPHEA after annealing. Care must be taken in this analysis as there is evidence of nano-sized precipitates (not visible using SEM or XRD) in similar alloys studied by Singh *et al* [79] and Shun *et al* [80].

1.4.2 Mechanical Properties

One of the major driving forces and motivation for research on HEAs is the search for systems with mechanically superior properties to the existing alloys. The assessment of "superior" pertains to an increase in a key physical attribute by ≥10% [81] without a major compromise in other attributes. Perhaps the most obvious of these is strength vs ductility. It seems quite an easy task to produce a stronger alloy, comparing to current alloys, however, to maintain a desirable ductility is a challenge. Where the importance of ductility lies with damage tolerance and safety in structural materials.

One aspect of HEAs that may lead to mechanical superiority are the properties obtained through solid solution strengthening. This phenomenon is inherent to a mixture of unlike atoms in a solid solution and occurs as a result of the hindrance to dislocation propagation by the solute atom within the solution of the host matrix [82]. As the concentration of the solute element increases, the solute-solvent relationship disappears and both elements can be considered solute atoms. This strengthening effect in HEAs has been reported to be as pronounced one whole order of magnitude larger compared to binary alloys [83].

When considering conventional alloys, the most common strengthening method is that of precipitate strengthening [84]. For example, Al alloys rely on Al-Mg-(Cu,Zn) or Al-Cu compounds, steels on pearlite and cementite, and superalloys on Ni_3Al-based compounds. This method requires microstructure control as there is an inverse relationship between particle spacing and alloy strength. In principle, the solid solution strengthening of HEAs coupled with precipitate strengthening, in addition to the inherent ductility of a close-packed system (which provide multiple slip systems for dislocation movement [85]),

could lead to a mechanically superior product. Table 2.1 provides a list of mechanical properties that current alloys are able to achieve and therefore the benchmark HEAs must be able to overcome.

Table 1.1. Mechanical property ranges, at room temperature, for conventional alloys where ρ, E, σ_y, σ_{uts} and K_{Ic} corresponds to density, Young's modulus, yield strength, ultimate tensile strength and fracture toughness, respectively. "Best" values for each property are in bold.

System	ρ (g·cm^{-3})	E (GPa)	σ_y (MPa)	σ_{uts} (MPa)	Elongation (%)	K_{Ic} (MPa-m$^{-1/2}$)
Al alloys [81]	**2.6**–2.9	~70	250–550	300–600	≥10	≥30
Ti alloys [81]	4.4–4.6	100–120	800–1400	900–1600	3–15	20–110
Ni alloys [81]	8–9	210–220	400–1300	1000–1600	15–30	80–120
Zircaloy-2 [25]		~97	~268	~472	~30	-
CoCrFeMnNi [70]	-	202	~410	~763	**~50**	**217**
Nb-Ti-V-Zr [76]	6.34–6.52	80–120	918–1105	~2000	-	-
$AlMo_{0.5}NbTa_{0.5}TiZr$ [77]	7.40	179	**2368**	2000	-	-
$Al_{0.4}Hf_{0.6}NbTaTiZr$ [77]	9.05	78	2269	1841	-	-
$AlCoCrFeNiTi_x$ [86]	-	**66**–188	1070–2070	1670–**4680**	-	-

While only relevant to select applications such as dental tools and blast resistant armour, CoCrFeMnNi is an iconic example of an extremely ductile FCC SPHEA is seen in work by Gludovatz *et al*. [70]. Here the mechanical properties of the CoCrFeMnNi SPHEA was studied in depth and a superior fracture toughness was realised, see Table 1.1. Furthermore, it was shown that an increase in ductility is achieved with decreasing temperature (converse to conventional behaviour) and no ductile to brittle transition temperature is identified [87]. Among the BCC HEAs very high strengths can be achieved. By varying the Ti concentration the precipitate strengthening in the BCC Al-Co-Cr-Fe-Ni-Ti systems can lead to strengths double that of conventional alloys, however, with a compromise to room temperature ductility [86]. This trade-off is also seen in refractory BCC SPHEAs. Nevertheless, results to-date suggest further investigation for structural applications is warranted.

1.4.3 Oxidation and Corrosion

Although important, the oxidation and corrosion resistance of a structural alloy is often only considered during the second screening of advanced materials. For this reason a comparatively small number of studies on this topic have been conducted for HEAs. Again, in order to assess the oxidation and corrosion resistance to HEAs, we must compare to conventional alloys. The processes of oxidation and corrosion of a metallic system can be quite complex. This fact is highlighted by an article, published in 2002, identifying the mechanism of corrosion in stainless steels [88]. In this context, the term oxidation refers to the interaction of gaseous oxygen with the surface and bulk metal matrix. In ideal circumstances an oxide layer (scale) forms on the surface of the material prohibiting further oxidation. Elements that do this best are Al, Cr, Si which also act to reduce oxygen solubility and diffusivity in the matrix [89]. An alloy that exhibits poor oxidation resistance will experience "runaway oxidation" whereby the metal oxide layer is porous or does not provide a diffusion barrier allowing the bulk to continuously form a metal oxide. If the

oxide is soluble in the matrix then it will embrittle the material too. Refractory alloys such as Ti and V are notorious for doing this.

During the oxidation process the material will display a change in mass with time which is one of the measures of oxidation susceptibility. It is thought that, because of the strongly reduced diffusivity in HEAs, some improvement in oxidation resistance of HEAs should be expected [90].

Table 1.2 Weight gain per area when exposed to oxygen flow at 800 °C for 24 hrs.

Sample	**Weight gain per area (mg/cm^2)**
Type 304 stainless steel **[91]**	0.3
SUJ2 (AISI 52100) bearing steel **[92]**	33
SKH51 (AISI M2) high-speed steel **[92]**	22
Ti-6Al-4V **[93]**	11
Fe-16%Al [94]	2
Fe-18%Al [94]	1.25
Fe-19.5%Al/Fe-22%Al [94]	0
$Al_xCrFeMnNi_{0.5}$ **[95]**	1
$Al_xCo1.5CrFeNiTi_y$ **[92]**	0.75
AlCrSiTiV **[93]**	3
$NbCrMo_{0.5}Ta_{0.5}TiV$ @ 1000 °C **[90]**	40

Table 1.2 reports the weight gain per area, for conventional alloys and HEAs, when exposed to oxygen flow at 800 °C for 24 hrs. It is clear that the Al containing HEAs exhibit vastly superior corrosion properties to conventional alloys yet perform worse when compared to type 304 stainless steel which is tailored for oxidation and corrosion resistance. Further work into the diffusion kinetics, behaviour during thermal cycling and long term stability is required in this area.

Corrosion refers to the process of dissolution of the matrix and can occur when the alloy is exposed to a liquid environment (usually acidic). A corrosion-resistant alloy experiences little corrosion. For example, a steel with Cr content of ≥16 at. % is corrosion resistant due to the formation of an impermeable layer of chromium oxide on its surface. In some cases, due to MnS inclusions on the surface of the alloy (from the casting process), the Cr content drops below this threshold and pitting corrosion occurs [88]. Pitting corrosion is a localised phenomenon and very problematic for the structural integrity of alloys [96].

Only a handful of corrosion studies have been conducted on HEAs, with mixed results. Early studies on the $AlCoCrCu_{0.5}NiSi$ HEA revealed a superior corrosion resistance to that of type 304 stainless steel in 1N H_2SO_4 but a susceptibility to pitting corrosion in NaCl environments [97]. A subsequent study found that the Cu segregation into the interdendritic material may be the source of the pitting corrosion [98, 99]. It was also found that the same type of behaviour occurs in the $Al_xCrFe_{1.5}MnNi_{0.5}$ HEA, however, it is the Al that increases the pitting susceptibility in NaCl [100]. This may be due to the AlNi B2 inclusions which have been found to corrode at a higher rate [101, 102]. In H_2SO_4 the corrosion resistance of

$Al_xCrFe_{1.5}MnNi_{0.5}$ was reported to be markedly less than 304 stainless steel [103]. An example of removing these susceptibilities; CoCrFeNi exhibits superior corrosion resistance compared to 304 stainless steel, in both NaCl and H_2SO_4 environments [98, 104].

1.4.4 Simulation of HEAs

Of all the publications on HEAs to-date ~7% of them are theoretical in nature. Among these, a popular method for simulation is through the use of *Computer Coupling of Phase Diagrams and Thermochemistry* which has been built into various commercial algorithms; the most popular being *Calculation of Phase Diagrams* (CALPHAD). This method works on the principles of classical thermodynamics and solves simple linear equations for the Gibbs free energy (Eq. 1.1) using empirical or theoretical values for ΔH and ΔS. This technique requires databases for the elements within the specific system that is to be simulated; where data does not exist, it is extrapolated from lower order systems (binary and ternary). The Gibbs free energy is evaluated at each temperature and composition, and the lowest energy phase is labelled and separated by lines when there is a change in phase preference. It is generally accepted that CALPHAD will provide a good approximation to the lowest energy phase at thermal equilibrium. An example of the output of this method can been seen for the AlCoCrFeNi system [105] in Figure 1.7.

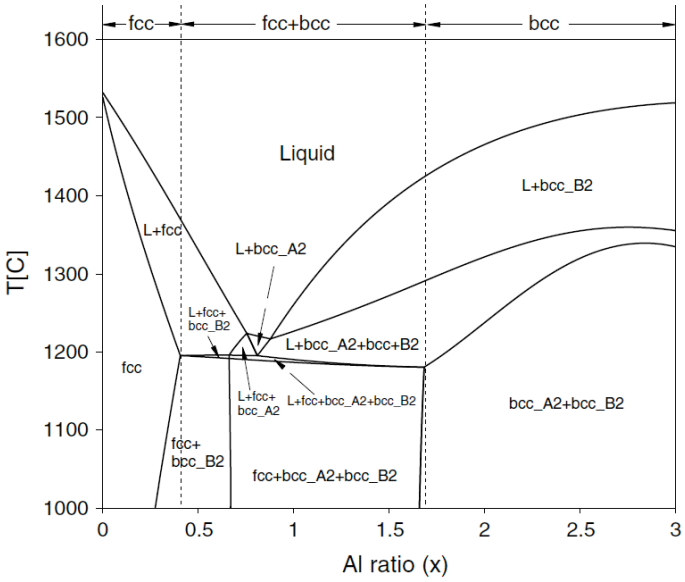

Figure 1.7. Taken from Zhang *et al*. 2012 [105] CALPHAD generated pseudo-binary phase diagram through the Al_xCoCrFeNi system with varying Al atomic ratio *x*.

The extrapolation from lower order data for predictions of HEAs will introduce some discrepancies between the CALPHAD method and experiment [106]. In this specific example it was observed by Kao *et al*. [107] that, when homogenised at 1100 °C, the Al_xCoCrFeNi system will transition from FCC → FCC + BCC and FCC + BCC → BCC when *x* is 0.30 and 1.12 atomic ratio, respectively. Although the effect is properly replicated in the CALPHAD model, the transition contents are shifted to higher Al ratios. Density functional theory has been used to study the Al_xCoCrFeNi system with similar results. A phase change from FCC → BCC + FCC when $x = 0.5$ [108] which corresponds well with the as-cast specimen but not the homogenized. It is possible that the affinity between Al and Ni to form an ordered B2 structure creates a partially ordered microstructure within the BCC solid solution. Preliminary

investigations into the possibility of second-order phase changes from partially ordered to fully disordered FCC structures has been done using DFT [35, 109]. These subtle atomic phenomena cannot be modelled using the CALPHAD method. Nevertheless, CALPHAD's phase prediction calculations are a lot less computationally intensive and have been implemented as a high-throughput screening method by Senkov *et al*. 2015 [110]. This effort requires additional coding for input wrappers to interface with the code (Pandat [111] in this case); 130,000 unique equimolar alloys were screened using this technique. Since CALPHAD is limited by the available thermochemical database which is still incomplete, not all possible combinations (which exceed the millions) can be explored.

DFT techniques can be applied to this problem and represent a very robust and widespread method for simulating physical systems such as HEAs. These methods employ a quantum mechanical approach to model materials on an atomic scale. However, the modelling of disordered systems presents a challenge in small atomic representations. This is due to the periodic boundary conditions that are used to allow the bulk properties to be obtained from a small unit cell. To solve this issue the supercell method must be employed which is a simple scaling of the unit cell (2 atoms of BCC) to a sufficiently large size in which the total free energy converges. Following this, two methods are typically employed to simulate the randomness of a solid solution:

1) Brute force method: Psuedo-randomisations of the atom type across the lattice sites are performed and individual calculations are performed for each randomisation. These results are then averaged to obtain a representation of a bulk solid solution [112].
2) Special quasi-random structures (SQS) [113, 114]: Typically used to model binary and ternary systems, this method attempts to produce the most disordered supercell by minimising the distance between the SQS correlation and the disordered state correlations for a pre-specified set of correlations. Recently, van de Walle *et al*. [115] has improved on this method and implemented it for widespread use within the ATAT package. Niu *et al*. [35] have successfully implemented this method for the simulation of HEAs.

A comparison of these two methods will be made within this dissertation. One of the major benefits of atomic and atomistic calculations is their ability to obtain physical properties such as density, lattice and elastic constants. These outputs can be used to estimate the ideal tensile strength and ductility of materials [116]. This type of work has been carried out on the $Al_xMoNbTiV$ [117], $MoNbTiV_xZr$ [118] and NbTiVZrHf [119] systems with much success.

Recently, DFT calculations were applied to the problem of high-throughput screening of HEAs by Troparevsky *et al*. [120], however, like Yeh, Yang and many others before, there is neglect of the ΔH of the solid solution as "*[HEAs] typically present rather small (and similar) enthalpies of formations*" which is simply not true (as evidenced within this dissertation). Here, Troparevsky uses the ΔH for binary compounds and approximates the Gibbs free energy of the solid solution to equal $-T\Delta S$, see Eq. 1.13. There is much need for a rigorous comparison of the Gibbs free energy between all competing phases within a HEA system. However, doing this using DFT will require a lot of computational resource. I will show in this thesis that there is a more efficient way to work through ΔG using Miedema's model as the

theoretical framework. This seems not to have been done, so far, prior to the present project. Which is surprising as Miedema's model has a database for nearly every element in the periodic table and provides a computationally straightforward method for calculating the ΔH values for concentrated multicomponent alloys.

2

METHODOLOGY

From the outset, the vision for this project has been to balance experimental and theoretical methods of investigation. It is the belief that in doing so, a more thorough and comprehensive analysis will be achieved as one should be able to complement the other. The combination should provide further insights that may not have been previously available. Furthermore, it is important to benchmark theoretical results to that of experiment as many approximations exist, within scientific theoretical framework, to allow for feasible calculations. This section will begin by giving an in-depth description of the theoretical techniques used within this dissertation outlining approximations as-well-as demonstrating the convergence of results. The remainder of the chapter will outline the experimental techniques used within the dissertation, in a less rigorous fashion, to reflect the nature of the work involved.

2.1 Density functional theory

Density functional theory (DFT) is often referred to using a Latin expression "*ab initio*" meaning "from first principles". This is due to its underlying quantum mechanical architecture which is used to calculate the ground state energy of a system. In order to understand how this is achieved, what approximations have been used and the limitations, we must follow its historical evolution which begins with the simple form of the time-independent Schrödinger's equation:

$$H\psi = E\psi \tag{2.1}$$

Where, E is the total energy of the system, ψ are the eigenstates of the Hamiltonian, H. This equation is solvable for systems that have a simple Hamiltonian expression such as a particle in a box or harmonic oscillator. In this case, we require the calculation of a more complex system in which the H can be expanded as:

$$\left[-\frac{1}{2}\sum_{i=1}^{N}\nabla_i^2-\frac{1}{2}\sum_{i=1}^{M}\frac{1}{M_i}\nabla_i^2+\sum_{i=1}^{N}\sum_{j>i}^{N}\frac{1}{|r_i-r_j|}-\sum_{i=1}^{N}\sum_{j=1}^{M}\frac{Z_j}{|r_i-R_j|}+\sum_{i=1}^{M}\sum_{j>i}^{M}\frac{Z_iZ_j}{|r_i-R_j|}\right]\Psi = E\Psi \tag{2.2}$$

Where $\hbar$, m_e and e (Planck's constant, electron's mass and electron charge, respectively) equate to 1 in atomic units, N is the number of electrons, M is the number of nuclei, r is the electron position, R is the nucleus position and Z is the charge of the nucleus. The first two terms of the Hamiltonian equate to the kinetic energy of each electron and each nucleus, and the last three terms; the potential energy between each electron, electron and nuclei, and nuclei. In this case, Ψ is the electronic wave function, which is a function of $4N$ variables i.e. three spatial and one spin. It is easy to see that if we increase the number of nuclei (and electrons) within the system we seek to solve for, the task of calculation quickly becomes quite overwhelming. Furthermore, each individual electron wave function cannot be found without simultaneously considering the individual electron wave functions of all other electrons. In short, it is a many-body problem. It is for these reasons we must make approximations that reduce the complexity. The following concepts are applied and implemented within various computational frameworks. In this dissertation the Vienna Ab initio Simulation Package (VASP) [121] was used.

For some systems that do not express a magnetic behaviour it is possible to omit the spin term, thus simplifying the problem. When dealing with the transition metals it is pertinent to always consider spin polarisation as the unpaired d electrons give rise to paramagnetic behaviour.

2.1.1 Born-Oppenheimer approximation

First described in 1927 by Max Born and J. Robert Oppenheimer [122] this approximation is perhaps the most fundamental used by DFT and takes the form of a two-step process.

(1) It is reasonable to consider the movement of all nuclei to be negligible compared to that of electrons in the same timescale. Due to the mass difference between a nucleus and electron a "clamped nuclei" approximation is used which means that we can calculate the nuclear and electronic components separately. In the electronic part of the calculation we remove the kinetic energy of the nuclei and the potential energy of the nuclei with each other. The electron-nuclei term is parameterised by the externally imposed positions of the nuclei and is often expressed as V_{ext},

(2) This allows us to then solve for either the electronic or nuclear total energy which can be fed into the other. When calculating the electronic part of Schrödinger's equation we define the shape of the electronic orbitals (including the bonding between the atoms) which allows for the evaluation of the forces acting on each atom from the electronic distribution. The positions of each atom are changed, according to the classical laws of inertia [123], until the forces are minimised or the difference in total energy between the last two calculations are below a defined threshold.

2.1.2 Electron density functional

It was not until 1964, in a landmark publication by Hohenberg and Kohn [124], that an alternative to solving the electron wave function was identified. It was found that the ground-state energy is a unique functional of the electron density. To understand this concept we must realise that the wave function for any particular set of coordinates is best represented as the probability that the N electrons are at those coordinates. This probability equates to $\Psi^*(r_1,\cdots,r_N)\Psi(r_1,\cdots,r_N)$ where Ψ^* is the complex conjugate of the electron wave function. A closely related quantity is the density of electrons at a particular position in space, n(r) and can be written in terms of the individual electron wave function as:

$$n(r) = 2\sum_i \Psi_i^*(r)\Psi(r) \tag{2.3}$$

where the factor of 2 arises to account for the spin state of the electrons. This expression is a function of only three variables as opposed to $4N$ variables, drastically decreasing the number of dimensions.

Hohnberg and Kohn identified that the ground-state energy E can be expressed as a functional (function of a function) $E[n(r)]$. Furthermore, the electron density that minimises the energy of the overall functional is the true electron density corresponding to the full solution of the Schrödinger's equation. i.e. a trial density will lead to an energy higher than that of the true ground state energy known. This concept is analogous to a previous method developed by Hartree-Fock [125, 126] and is known as the variational

principle. It should be noted that this approach does not yield the true electron density; however, the ground state still provides the best *n(r)* that we can obtain.

2.1.3 Exchange-correlation

Through rigorous derivation by Kohn and Sham [124, 127] we arrive at a similar yet much simpler equation to Eq. 2.2:

$$\left[-\frac{\hbar}{2m}\nabla^2 + V_{ext}(r) + V_H(r) + V_{XC}(r)\right]\Psi_i(r) = \varepsilon_i\Psi_i(r) \tag{2.4}$$

where the first term is the kinetic energy, the second term is the potential energy (see Eq. 2.2), the third term is the Hartree potential where,

$$V_H(r) = \int \frac{n(r')}{|r-r'|} d^3r' . \tag{2.5}$$

This potential is the electron-electron repulsion term and is written as the classical Coulomb repulsion between two smeared out charge distributions. This also contains a so-called self-interaction contribution which arises because each individual electron described in the Kohn-Sham equation is also part of the total electron density. This leads on to the fourth term, the exchange-correlation potential:

$$V_{\mathrm{XC}}(r) = \frac{\delta E_{\mathrm{XC}}(r)}{\delta n(r)} . \tag{2.6}$$

This term is a functional derivative of the exchange-correlation functional defined to include all quantum mechanical effects i.e. non-classical electron-electron interactions and also any difference in kinetic energy between interacting electrons and non-interacting electrons. It also compensates for the self-interaction contribution caused by the Hartree potential.

This poses a problem – how exactly do we write the exchange-correlation functional? Hohenberg and Kohn's theorem guarantees its existence yet its exact form is simply not known. The first reasonable approximation was derived from the uniform electron gas model. At each point in space we assume the exchange-correlation potential to be that of a uniform electron gas at each specific position. This approximation is known as the local density approximation (LDA) and achieves reasonable results [127]. However, in many materials sharp gradients in electron densities are observed due to effects such as directional or covalent bonding. To account for this a more accurate approach known as the generalised gradient approximation (GGA) has been developed. Like LDA it has a dependency on the density at each point in space but also includes the gradient of this density. Currently the most popular mathematical description of the GGA method was developed by Perdew *et al* in 1996 [128]; which is used for all calculations within this dissertation. This exchange-correlation functional is most widely used as it achieves a good trade-off between compute time and accuracy [129, 130]. In some systems with strong on-site Coulomb interaction of localised electrons a +U Hubbard correction term is required [131].

At this point the reader may recognise that there is a circular dependence to solving the Kohn-Sham equation (Eq. 2.4): To define the Hartree potential we must know the electron density but to find the electron density we must know the single-electron wave functions and to obtain these we must solve the Kohn-Sham equation. A technique that can be used to solve this problem is as follows:

1. Define an initial, trial electron density.
2. Solve the Kohn-Sham equation to obtain the single-particle wave functions.
3. Calculate the electron density using Equation 2.3
4. Compare resulting electron density with that in step 1. If the difference is above a certain threshold, repeat the process in some systematic manner.

This process is referred to as the self-consistent cycle used within DFT.

2.1.4 Periodic boundary conditions

In order to apply this analysis to a real system e.g. a bulk crystalline metal, one must effectively simulate an infinite number of atoms. To do this, the primitive unit cell is first defined e.g. for a BCC crystal one atom at $a(0,0,0)$ and another at $a(0.5,0.5,0.5)$, where a is the lattice constant. This unit cell is then replicated in the X, Y and Z direction infinitely. To solve Schrödinger's equation for this periodic system, the solution must satisfy a fundamental property known as Bloch's theorem:

$$\Phi_k(r) = \exp(ik \cdot r) u_k(r), \tag{2.7}$$

where $u_k(r)$ is a periodic function in space with the same periodicity as the unit cell, k is a vector representing the position in reciprocal space meaning $\exp(ik \cdot r)$ is an arbitrary phase factor that scales the periodic function in the surrounding unit cells. Although any function may be used to expand the Kohn-Sham functions, e.g. some DFT codes use Gaussian functions [132-135], plane-waves are generally used when simulating solid state crystals [121, 136, 137]:

$$u_k(r) = \sum_g \exp(ig \cdot r) c_{g,k} \tag{2.8}$$

where $c_{g,k}$ are Fourier coefficients and g are wave vectors that satisfy the periodicity. The concept of reciprocal space is used for mathematical convenience which introduces another concept known as the Brillouin zone (the reciprocal space encapsulated by the Wigner-Seitz unit cell [138]). A great deal of integrations are performed within the Brillouin zone which is quite a computationally daunting task. For this reason this function is only integrated over the possible values of k allowing us to discretise the problem. Monkhorst and Pack [139] developed a method to employ this concept and it is used within most DFT codes. This then leads to the question – how many k-points are required for a precise solution to be achieved? In general, the more k-points the more precise the calculation, however, like adding trapezoids to calculate the area under a curve; at a certain threshold the increase in k-points will yield little difference in result. It is at this point that the results are said to have converged and are satisfactory for precise analysis.

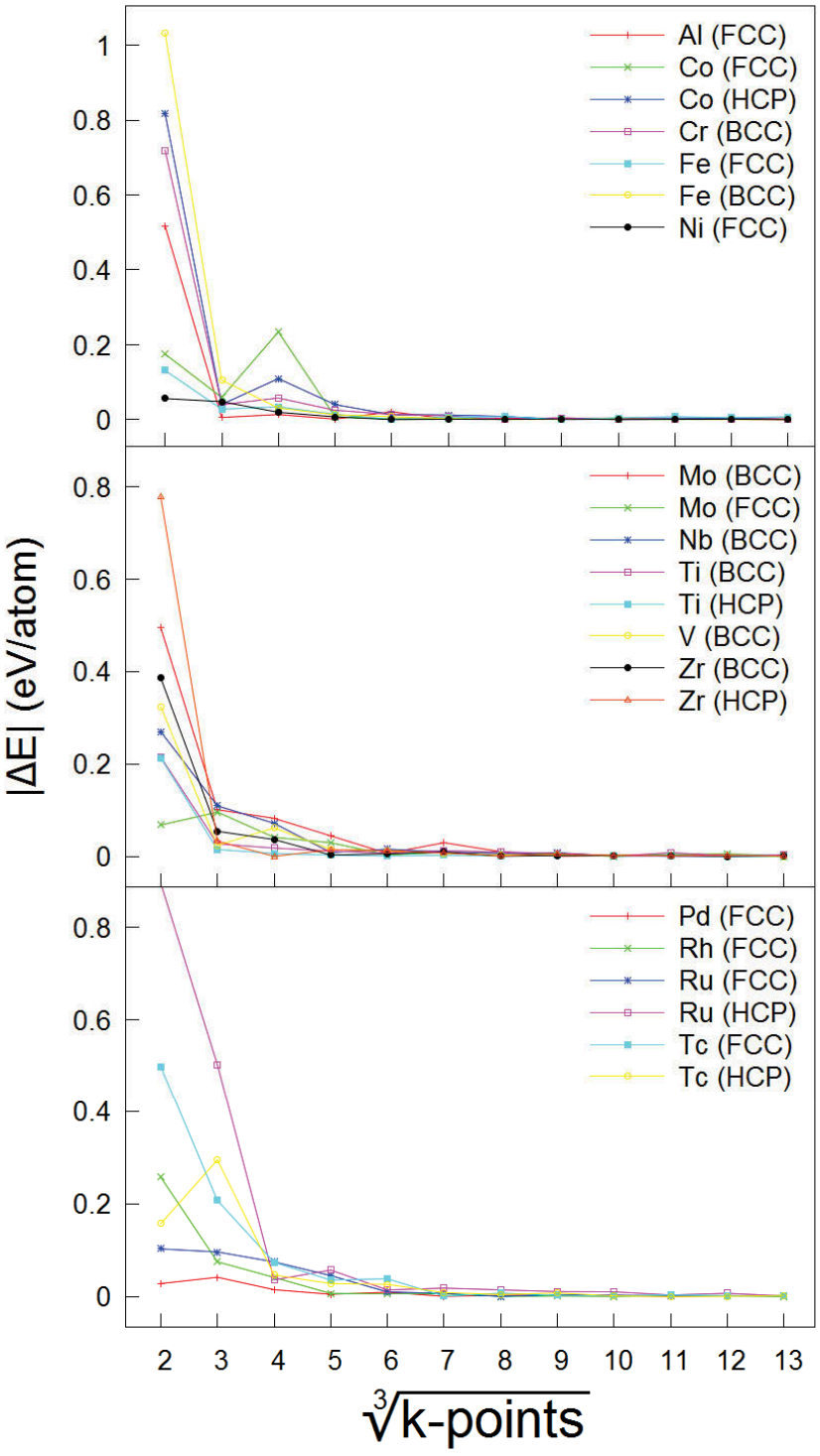

Figure 2.1. Demonstration of convergence of k-points for elements (grouped by HEA system), studied within this dissertation.

This concept is visually represented in Figure 2.1 by plotting the absolute difference in internal energy (normalised per atom) between the primitive unit cell using a *k*-point grid of 20×20×20 (a highly accurate value) to the same unit cells using 2 – 13 *k*-points$^{1/3}$. A suitable convergence is achieved by ~6 – 8 *k*-points$^{1/3}$ but due to the difference in volume of the primitive unit cells identical *k*-point grids will

correspond to varying real space densities. For example, BCC Zr with an 8×8×8 *k*-point grid will have an actual spacing of 0.035×0.035×0.035 $Å^{-1}$ whereas BCC V with the same grid will have an actual spacing of 0.042×0.042×0.042 $Å^{-1}$. To account for this, it is the densities that are kept consistent at a converged value, of the elemental species and alloyed form, for all subsequent calculations within this dissertation. The importance of maintaining a consistent sampling is to avoid errors which may compound if different *k*-point densities are used. By comparing calculations with similar sampling these errors will be partially or completely cancelled out. Another subtlety regarding volume difference is the change in volume before and after geometry optimisation. If this volume change is large enough, numerical errors may be introduced due to the Pulay stress [140]. These errors were corrected for by re-running calculations with updated volumes.

Another important consideration when using the periodic boundary formalism arises when combining Equations 2.7 and 2.8:

$$\Phi_k(r) = \sum_g c_{k+g} \exp[i(k+g)r]. \tag{2.9}$$

In this expression, the solution at even a single point in *k* space involves the summation over an infinite number of possible values of *g*. Fortunately, the functions appearing in Eq. 2.9 have a simple interpretation as solutions of the Schrödinger's equation: they are solutions with kinetic energy i.e.

$$E = \frac{\hbar^2}{2m} | k+g |^2 . \tag{2.10}$$

Here we can approximate the solution to,

$$E_{\text{cut}} = \frac{\hbar^2}{2m} g_{\text{cut}}{}^2, \tag{2.11}$$

as solutions with lower energies are more physically important than solutions with very high energies; a cutoff energy, $E_{cut,}$ is defined to truncate the infinite sum.

The E_{cut} parameter was defined within this dissertation according to the system in question, see Figure 2.2.

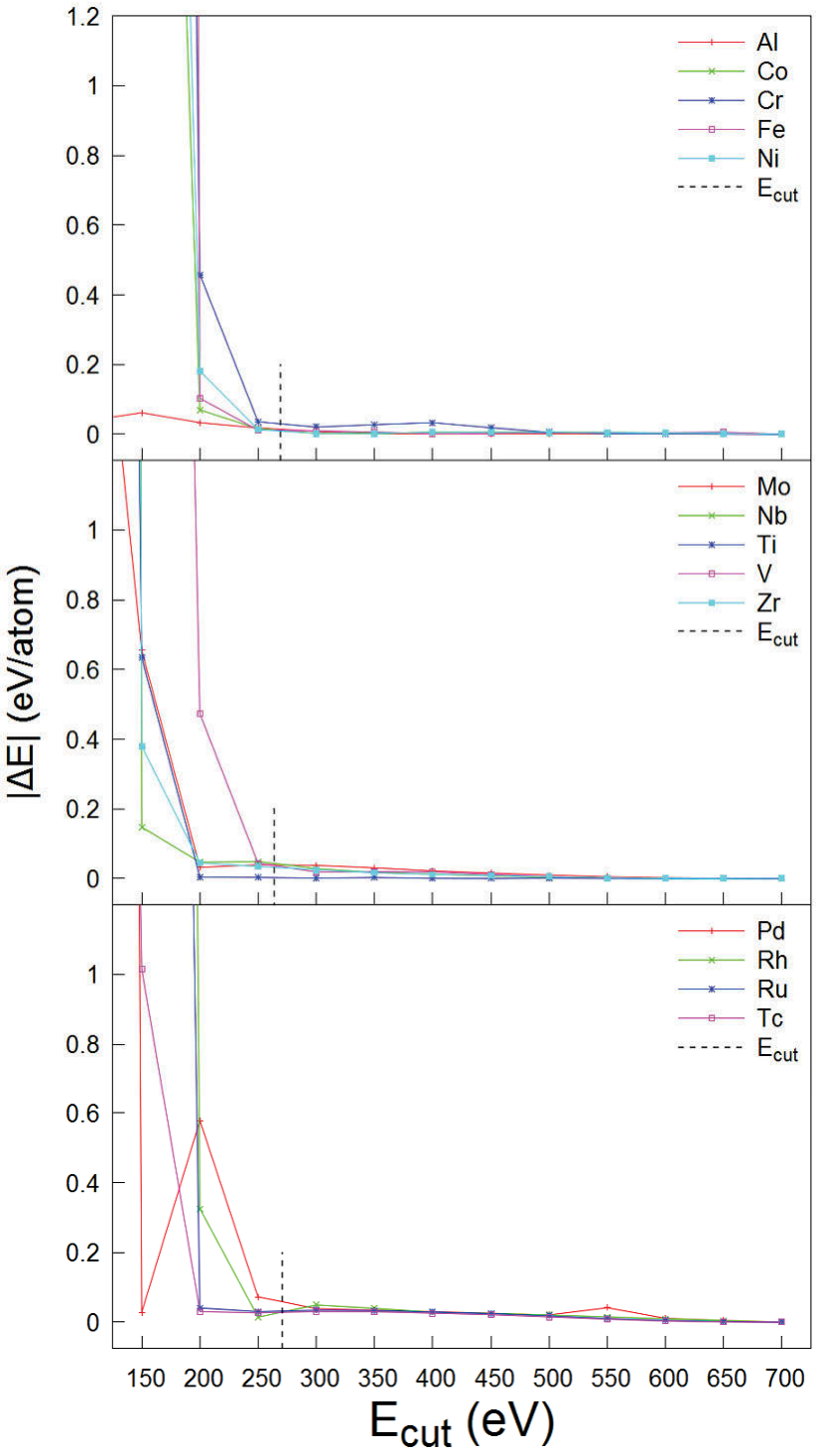

Figure 2.2. Convergence of the plane-wave cutoff energy (Ecut). The black dashed line represents the E_{cut} values used when performing calculations on the elements plotted.

Again, a converged value was obtained by plotting the absolute difference between the internal energy of each pure elemental system in their lowest energy configurations using E_{cut} = 700 eV and E_{cut} values from 100 – 650 eV and normalised for number of atoms within the system. The E_{cut} value used for all subsequent calculations were determined by the "PREC = Accurate" regime and therefore chosen by the

pseudopotentials "ENMAX" value provided within the VASP package (and denoted by the dashed black line).

2.1.5 Pseudopotentials

Pseudopotentials are a long-standing concept used to reduce the number of electrons and mathematical rigor of the DFT calculation. Even using the Kohn-Sham theorem, calculating for an all electron representation is quite costly. When considering the electronic distribution around an atom one can delineate the valence electrons which play a dominating role in chemical bonding and other physical characteristics of the material, from the core electrons which are more tightly bound and have a more subtle influence. For this reason we can define the core electrons as a fixed or "frozen". This allows us to represent them as a smoothened density constructed from the elements in their pure form. It follows that careful consideration must be taken when choosing a pseudopotential as it must replicate the potential of the all-electron potential after a certain radius; below the defined E_{cut} in Equation 2.11. The former requirement is met through rigorous development of pseudopotential databases which are included within VASP. Here a projector augmented-wave (PAW) method [141-143] is employed which combines the pseudopotential approach with a so called "linear augmented-plane-wave method". This technique reintroduces the near-core oscillations of the valence electron wave functions and gives a more reliable representation of materials with strong magnetic moments or that have atoms that have large differences in electronegativity [142].

2.2 Modelling disordered systems

As mentioned previously, the modelling of disordered systems presents a challenge in atom simulation. When considering the periodic nature of the calculations it is clear that any atomic arrangement specified within the unit cell will be replicated infinitely. In this respect, a truly disordered system cannot be described. However, a "supercell" can be defined by combining a number of primitive cells; a threshold size can be achieved in which the energy of the disordered system will converge. This is due to the "screening" effect of neighbouring atoms. This method is used to study surfaces and defects in atomic simulation.

The supercell size that achieved sufficient convergence has been identified to be as low as 24 atoms for an FCC CoCrFeNi system by Niu *et al* [35]. Figure 2.3 shows the effect of scaling on the free energy per atom for the BCC NbTiVZr with a comparison of compute time per ionic step (LOOP+ in VASP's OUTCAR file).

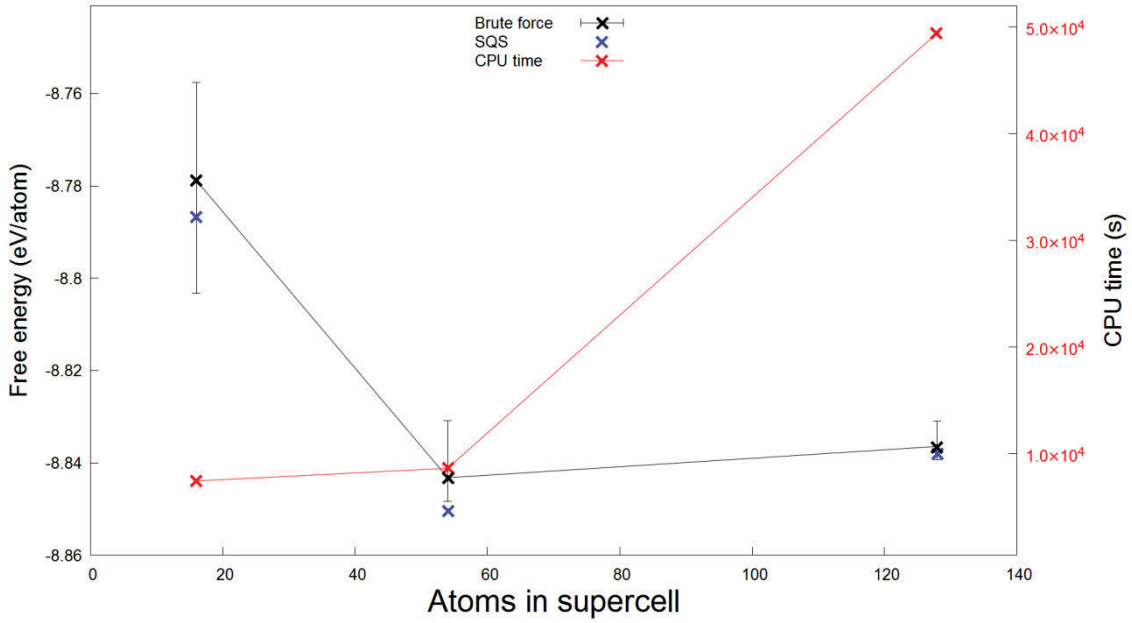

Figure 2.3. The effect of incremental increase in BCC supercell size from 2×2×2 (16 atoms), 3×3×3 (54 atoms) and 4×4×4 (128 atoms) on free energy using the brute force method with the average energies (black crosses) plotted within the spread of energies (error bars). Compared to the SQS method (blue crosses) and the average CPU times on the secondary y-axis (red crosses).

It is clear that the 54 atom supercell is within error of the 128 atom supercell and with a much more feasible compute time. A relatively large spread of energies was found for the smaller supercell which is also observed in Niu *et al*'s work. There is a soft restriction in these three supercell sizes as a cubic supercell should be maintained to allow for consistent *k*-point sampling and minimisation of errors. Any cubic supercells below 16 atoms will not allow for the representation of 4 elements and any over 128 atoms are not feasible within this level of theory.

Another matter of importance is the accurate representation of a "disordered" system. Also previously mentioned in section 1.4.4, there are two methods that have been used to arrange the atoms in a disordered configuration: SQS and the brute force method. It seems that there is no rigorous comparison of these techniques in the literature. It is my opinion that in a truly random arrangement of atoms there will be a statistical degree of probability in which regions of clustering of like atoms will occur. The brute force method has the ability to *quickly* simulate this phenomenon however SQS does not. Here, it is the scatter in properties (denoted by error bars) and an average of a statistically significant dataset that represents the physical system. However, the appeal of the SQS method is the reduction in computational resources required, as only one calculation for each stoichiometry is performed. Counter-intuitively, this leads to an increase in real-time required to obtain a result; as the SQS process can be lengthy and problems of minimising correlations can occur. A simple Python script was employed to randomise the elemental positions and a check was performed to make sure no arrangements were identical. Figure 2.3 shows a comparison in free energy between SQS and the brute force method which shows a more stable (lower energy) structure which is even outside the bounds of the spread in energies for 54 atoms (using a

20 supercell dataset). It is expected that with sufficient sample size the spread in energies would extend to include the SQS cell.

2.3 Defect energies

Similar to the method of modelling a disordered system, the supercell method (Section 2.1) is applied to study isolated defects. In a supercell consisting of 54 atoms, a single atom is removed to simulate a Schottky defect [144]. To simulate an interstitial atom, a single atom is placed at the octahedral site, *a*(0.5, 0.5, 0), in one of the BCC unit cells that have been used to construct the supercell. The defect formation energies are then calculated as follows:

$$\Delta H_D = U_D^{DFT} - U_P^{DFT} \pm \mu^{DFT} \tag{2.12}$$

where U_D^{DFT} and U_P^{DFT} are the total energies calculated by DFT for the defected and pristine supercells, respectively, and μ^{DFT} is the chemical potential of the species either added or removed from the perfect supercell to form the defect. For metallic systems this can be determined through the calculation of the total energy/atom of the elements in their ground state.

2.4 Miedema's model

Miedema's model was developed in the 1950s by a group of researchers in the Netherlands. It is described as a *semi-empirical macroscopic atom model* as it employs empirical results for parameterisation in macroscopic picture of alloying. A full account of the development of this model and its capabilities can be found by de Boer [44] and a practical summary by H. Bakker [145]. In the following description a brief physical basis of the model will be provided, all empirical parameters will be addressed and the mathematical tools used within this dissertation will be recounted.

There are three fundamental quantities involved in Miedema's model:

1. Φ* – The experimentally determined work function (in volts), defined as the energy required to remove a valence electron from its orbital to an infinite distance away from the nucleus. The star following Φ denotes that the values have been adjusted (within the bounds of experimental error) for better data fitting.
2. n_{ws} – The electron density at the boundary to the Wigner-Seitz cell (in empirical density units). This concept is based on the assumption that for non-transition metals the total electronic charge distribution in the metal crystal can be described as the superposition of the charge distributions of free atoms placed at individual lattice points. Thus, n_{ws} is the summation of electron charge densities. The observation of a linear relationship between n_{ws} and the ratio of the bulk modulus, *K*, to molar volume, *V* [146] allows n_{ws} values to be generated for transition metals.
3. $V^{2/3}$ – The molar surface area (in cm^2).

In the context of a macroscopic model, the representation of the pure elements is that of a block of one mole of atoms their bulk state. Energy considerations are made in terms of contact interactions that take place at the interface between dissimilar blocks. For this reason, a lot of attention is focused on the interaction between interfaces and volume changes upon mixing. One of these interactions relates to the

discontinuity between the electron density, n_{ws}, of unlike elements which must be eliminated (requiring energy). When plotting $|\Delta\varphi|$ vs $\Delta n_{WS}^{1/3}$ for solid binary mixtures of transition metals (where the index of 1/3 arises for compatibility with $\Delta\Phi^*$ [147]), a linear separation is observed, see Figure 2.4.

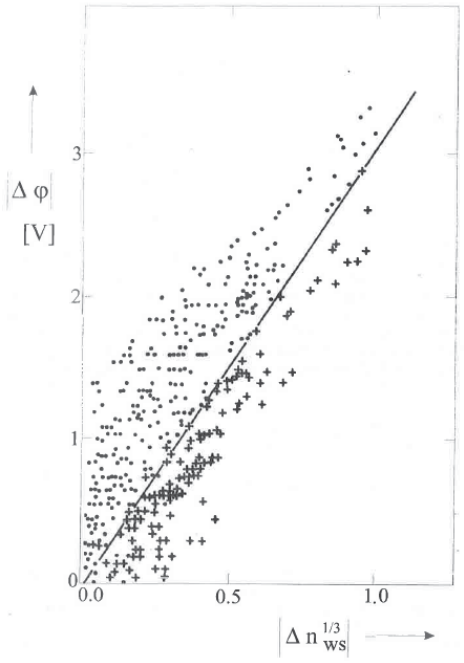

Figure 2.4.Taken from Bakker [145], $|\Delta\varphi|$ vs $|\Delta n_{WS}^{1/3}|$ for solid binary alloys of transitional metals where a solid circle represents compound formation and a cross represents either no intermetallic or both solid solubilities are smaller than 10 at. %. Noticeable discrepancies above the line are Cr-Fe, Cr-U, Cu-Rh and Hf-U; below the line – Au-Cr, Ca-Pr, Cr-Mn, Cr-Mo and Cu-Mn.

This separation is identical for noble metals, alkaline-earth metals and polyvalent non-transition metals. From this slope the ratio of Q:P (proportionality constants) is taken as 9.4 V^2/(density units)$^{2/3}$. The P value has been experimentally estimated to be 14.2 for alloys with valence larger than two and 10.7 for alloys of two monovalent or divalent metals. An intermediate value of P = 12.35 is used.

It is from this relation that the expression for interfacial enthalpy was proposed:

$$\Delta H^{\text{inter}} \propto \left[-P(\Delta\varphi^*)^2 + Q(\Delta n_{WS}^{1/3})^2 \right]. \tag{2.13}$$

By combining this expression from Eq. 2.13 with the concept of surface contact area, $V^{2/3}$, we arrive at the full equation for interfacial enthalpy:

$$\Delta H^{\text{inter}}(\text{A in B}) = \frac{V_A^{2/3}}{\frac{1}{2}\left(\frac{1}{n_{ws}^{A\,1/3} + n_{ws}^{B\,1/3}}\right)} \left\{ -P(\Delta\varphi)^2 + Q(\Delta n_{ws}^{1/3})^2 - R \right\} \tag{2.14}$$

A third term R is introduced as the trend seen in Figure 2.4 deviates when plotting alloys of transition and non-transition metals i.e. the separation takes on more of a hyperbolic curve. De Boer *et al*. explain this to

be connected to the hybridization of *d* and *p*-type wave functions when transition metals and non-transition metals become nearest neighbours, however also confess "*a clear insight into the exact formulation of this term is lacking*". Nevertheless, a *R*:*P* ratio is empirically derived for the generation of the ΔH^{inter} values which are listed in de Boer's publication [44]. A computer program has since been developed by Zhang, R. in 2009 which allows for the calculation of the interfacial enthalpies [148].

These ΔH^{inter} values are used in the calculation of the formation enthalpy for various phases and mixtures of elements. There are subtleties involved between calculating formation enthalpy of the different phases e.g. intermetallic, solid solution, amorphous but they all include a ΔH^{inter} term.

2.4.1 Intermetallic compounds

The main attribute given to intermetallic compounds is the higher degree of surface contact between unlike atoms, f_B^A, compared to a disordered phase, see Figure 2.5.

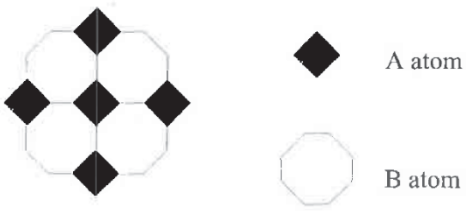

Figure 2.5. Taken from Bakker [145], a two dimensional representation of the surface contact between unlike atoms in an ordered system using the macroscopic atom model.

This term is empirically derived by comparing experimental to theoretical values and calculating the factor by which they differed leading to the equation:

$$f_B^A = c_B^s \left\{1 + 8 \cdot \left(c_A^s c_B^s\right)^2\right\} \tag{2.15}$$

where, *c* is the concentration of element A or B in a binary system. c_A^s is the weighted average of the effective surface concentration of element A or B, calculated by:

$$c_A^s = \frac{c_A V_A^{2/3}}{c_A V_A^{2/3} + c_B V_B^{2/3}}, \tag{2.16}$$

with a similar equation for c_B^s, $V_A = V_A^{atom} - \Delta V_A$ and $V_B = V_B^{atom} - \Delta V_B$, where $\Delta V_A = f_B^A \alpha \frac{(\varphi_A - \varphi_B)}{n_{ws}^A}$, $\Delta V_B = \frac{n_{ws}^A}{n_{ws}^B} \Delta V_A$ to correct for the change in atomic volume upon alloying, where V^{atom} is taken from a list of empirically measured values [44] and $\alpha = 1.5 \frac{V_A^{2/3}}{n_{ws}^{A\ -1/3} + n_{ws}^{B\ -1/3}}$. The terms for c^s and f are calculated iteratively with the updated atomic volumes.

Following this, the total formation enthalpy of an intermetallic compound is calculated as:

$$\Delta H^{form}(\text{A in B}) = c_A^s f_B^A \Delta H^{\text{inter}}(\text{A in B}). \tag{2.17}$$

This equation is referred to the chemical contribution to the formation enthalpy and is assumed to be the only contribution in an intermetallic compound.

Example calculation:

For a NiZr intermetallic,

$$\alpha = 1.5\frac{6.6^{2/3}}{5.36^{-1/3}+2.8^{-1/3}} = 4.12 \quad , \quad \Delta V_{Ni} = 4.12\frac{(5.2-3.45)}{5.36} = 1.35 \ ,$$

$$c_{Ni}^s = \frac{0.5\times 6.6^{2/3}}{0.5\times 6.6^{2/3}+0.5\times 14^{2/3}} = 0.38 \quad , \quad c_{Zr}^s = 0.62$$

$$f_{Zr}^{Ni} = 0.62\left\{1+8\cdot(0.38\times 0.62)^2\right\} = 0.90 ,$$

$$V_{Ni} = 6.6 + 0.9\times 1.35 = 7.81\,\text{cm}^3 ,$$

$$f_{Ni}^{Zr} = 0.38\left\{1+8\cdot(0.38\times 0.62)^2\right\} = 0.54 ,$$

$$V_{Zr} = 14 - 0.54\times\frac{5.36}{2.8} = 12.60\,\text{cm}^3 ,$$

$$c_{Ni}^s = \frac{0.5\times 7.81^{2/3}}{0.5\times 7.81^{2/3}+0.5\times 12.6^{2/3}} = 0.42 , \quad c_{Zr}^s = 0.58$$

$$f_{Zr}^{Ni} = 0.58\left\{1+8\cdot(0.42\times 0.58)^2\right\} = 0.85$$

$$\Delta H^{form} = -70.48\,\text{kJ/mol}$$

2.4.2 Concentrated solid solutions

There are a total of three terms that are included when calculating the formation enthalpy of a solid solution:

$$\Delta H^{form}(ss) = \Delta H^{chem}(ss) + \Delta H^{elastic}(ss) + \Delta H^{struct}(ss). \tag{2.18}$$

The chemical contribution is calculated in a different manner to that in Eq. 2.17 and is instead a weighted sum of the interfacial enthalpy of element A in B and B in A:

$$\Delta H^{chem}(ss) = c_A c_B\left(c_B^s \Delta H^{\text{inter}}(\text{A in B}) + c_A^s \Delta H^{\text{inter}}(\text{B in A})\right). \tag{2.19}$$

where c is the atomic fraction of element A and B. The elastic contribution, $\Delta H^{elastic}(ss)$, follows the elastic theory of Eshelby [149] to calculate the mismatch enthalpy between element A and B. Here, each element is considered to exist as a plastic sphere within the plastic medium for the other element. The effective atomic volume, V^*, is calculated in an identical manner to V with the omission of f. The bulk modulus, K, of the solute atom and the shear modulus, G, of the solute and matrix are used to calculate the equilibrium volume change. After derivation, this term is simplified to:

$$\Delta H^{elastic}(ss) = c_A c_B \left(c_B \Delta H^{elastic}(\text{A in B}) + c_A \Delta H^{elastic}(\text{B in A}) \right), \tag{2.20}$$

where

$$\Delta H^{elastic}(\text{A in B}) = \frac{2K_A G_B (V_A^* - V_B^*)^2}{4G_B V_A^* + 3K_A V_B^*}. \tag{2.21}$$

The final term, $\Delta H^{struct}(ss)$, relates to the rearrangement of electronic charge upon alloying of elements with different valence electron concentrations:

$$\Delta H^{struct}(ss) = \left(\Delta H^{struct}(< z >) - \Delta H^{ref}(< z >) \right). \tag{2.22}$$

Where $< z >$ is the average valence electron concentration per atom of the binary system. Reference data is reported in a study by Niessen *et al*. [150].

Example calculation:

For a solid solution of NiZr,

$$\Delta H^{chem}(ss) = 0.25 \times (0.62 \times -165 + 0.38 \times -237) = -48 \text{ kJ}$$

$$\Delta H^{elastic}(ss) = 0.25 \times (0.5 \times 92 + 0.5 \times 89) = 23 \text{ kJ}$$

$\Delta H^{struct}(ss) = -3 \text{ kJ}$ (as interpreted by Reference [150] for Ni (Z=10) and Zr (Z=4))

$$\Delta H^{form}(ss) = -48 + 23 - 3 = -28 \text{ kJ}$$

2.4.3 Amorphous alloys

Due to the metastable state of amorphous alloys it is safe to approximate that $\Delta H^{form}(\text{amorphous}) > \Delta H^{form}(\text{chem})$ as the amorphous configuration should be less favourable than a crystalline structure of the same composition. For this reason there is a second term which is a positive contribution, labelled the topological enthalpy, $\Delta H^{\text{topological}}(\text{amorphous})$. The magnitude of this difference between crystalline and amorphous is estimated to be equal to RT_m where R is the gas constant 8.3 J/(mol.K) and T_m is the average melting temperature of the mixture. However, there will be some degree

of relaxation to the crystalline structure or contributions from local ordering meaning the scaling factor will be $< R$. An experimental derivation has determined this constant to equate to 3.5 J/(mol.K) leading to the equation:

$$\Delta H^{form}(amorphous) = \Delta H^{chem}(ss) + 3.5(c_A T_{m,A} + c_B T_{m,B}). \quad (2.23)$$

The calculated formation enthalpies for all binary transition metals are tabulated in a 2005 publication by Takeuchi and Inoue [151]. It is this enthalpy that is quoted throughout the HEA literature which is, as I will show, an incorrect representation of intermetallics and solid solutions (according to Miedema's model).

Example calculation:

For amorphous NiZr,

$$\Delta H^{form}(amorphous) = -48 + 3.5(0.5 \times 1.726 + 0.5 \times 2.128) = -41.26 \text{ kJ/mol}$$

2.4.4 Application to HEAs

To extend this model to calculate the formation enthalpy of the whole solid solution, $\Delta H^{form}(ss)$, the weighted contribution of ΔH^{form} between each of the binaries were summed for every element in the solid solution:

$$\Delta H^{form}(ss) = \sum_{i=0}^{j} c_i \sum_{\substack{k=0 \\ k \neq i}}^{j} c_k^f \, \Delta H_{i,k}^{form}(ss). \quad (2.24)$$

where $c_k^f = \frac{c_k}{\sum_{\substack{l=0 \\ l \neq i}}^{j} c_l}$ for a j element alloy where c is the concentration in atomic fraction. This is designed to maintain stoichiometry of 1 mole of solution while accurately weighting the contribution each element to the overall ΔH^{form}.

An explicit explanation as to exactly how Miedema's model is applied to HEAs is given in Chapter 5.

2.5 Magnetron sputtering

Physical vapour deposition techniques, such has magnetron sputtering, are very useful for creating alloys of elements with high melting points, layered or metastable structures. Magnetron sputtering, specifically, is different from other deposition techniques (such as reactive sputtering, gas flow sputtering or evaporation deposition [152]) as it utilises a magnetic field to keep the plasma in front of the target (see Figure 2.6) allowing for increased sputtering rates. The sputter rates, specifically, are unique to the experimental conditions and must be calibrated prior to running the experiment.

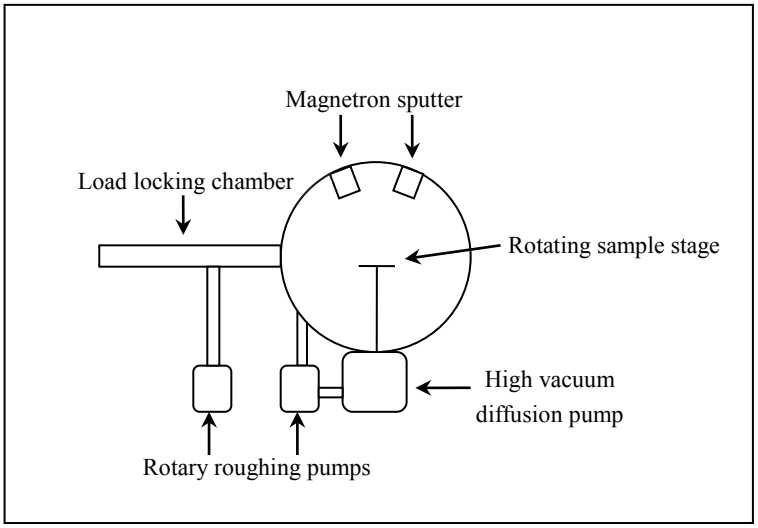

Figure 2.6. Diagram of magnetron sputtering chamber setup with vacuum pumps and sample load locking mechanism.

A series of gun voltages were stepped through and held for 30 seconds at each voltage for both V and Zr targets, separately. The thickness of the deposited layer at each voltage was measured using a quartz crystal microbalance and sputter rates were calculated. Using this information a series of three thin film samples were made by co-deposition in a ratio of 2V:1Zr, 1V:1Zr and 1V:2Zr, all ~200 nm in thickness (deposited on clean crystalline Si wafers). Subsequent XRD and chemical analysis revealed it is extremely important to pump the chamber down to its maximum vacuum pressure (3×10^{-7} Torr) before backfilling with Ar (2×10^{-3} Torr) as otherwise oxides are likely to form.

2.6 Vacuum arc melting

Arc melting is a relatively common method of manufacturing alloys from components with high melting temperatures. It can be used in small laboratory environments or large scale industrial settings. The method of heating relies on thermionic emission between a cathode held above the raw material (the anode). A potential difference is applied between the two electrodes and electrons or ions are emitted by the cathode which ionise the medium between the electrodes (Ar in this case) and a plasma is maintained. This arc allows for a localisation of high temperature focused on the sample which can reach ~3000 ^{o}C. Furthermore, the crucible that holds the melt can be water cooled allowing for rapid quenching.

An Edmund Buhler Arc Melter was used to produce a set of six alloys in the present project. The nominal compositions were:

1. NbTiV
2. $NbTiVZr_{0.5}$
3. NbTiVZr
4. $NbTVZr_2$
5. $Mo_{0.5}NbTiV$
6. MoNbTiV

The metals (99.9% purity) were placed in a water-cooled copper crucible which is the anode in this system and the cathode was a tungsten rod with a sharp tip. The whole system is contained within a hermetically sealed steel cylinder. The chamber was pumped down to 10^{-3} mTorr and then filled with Ar to a pressure of 800 mTorr. After a potential difference is applied between the tungsten cathode and the material in the crucible, an arc is initiated between the electrodes and the material will melt in the crucible. A maximum current of 250 amps was applied to the sample and was melted for 5 minutes. After the sample solidified, the resulting button of material was flipped and the procedure repeated. The button was flipped a total of 4 times resulting in a total melting time of 25 minutes. Samples in the Nb-Ti-V-Zr system contained undissolved Nb and the Mo-Nb-Ti-V system, both Mo and Nb. This was due to the raw pieces of Nb and Mo being too large (2 mm×2 mm×2 mm). To avoid this, shavings should be used in any future work.

2.7 Metallurgical surface preparation

As-cast buttons (described in 2.6) were sectioned twice (Fig. 2.7), using an Accustom-50 saw machine using a diamond tipped blade (Al_2O_3 blades underwent catastrophic failure). These sections were mounted on copper stubs using crystal bond and the cut faces were ground using an Abramin grinding machine with a SiC pad to flatten the surface.

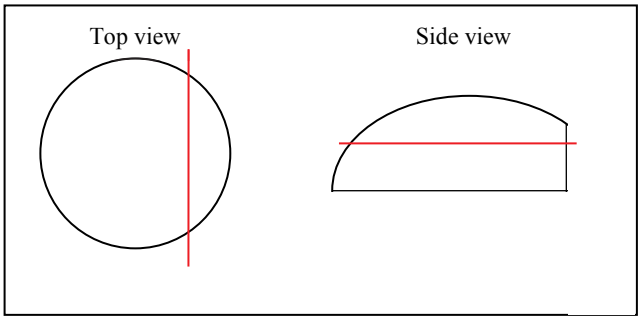

Figure 2.7. Top view and side view of arc melted button with sections in red.

To polish, a Tegramin-25 was used with the following parameters:

Using notation: (Pad type/diamond size/force/time)

1. Largo/9 µm/25 N/until sample was flat.
2. Pan/15 µm/20 N/5 min
3. Pan/15 µm/10 N/5 min
4. Dac/3 µm/20 N/5 min
5. Dac/3 µm/10 N/5 min
6. Nap/1 µm/20 N/5 min
7. Nap/1 µm/10 N/5 min
8. Chem/colloidal silica + oxidising agent/10 N/5 min

These samples were then removed from their mounting and analysed with X-ray diffraction and scanning electron microscopy.

For transmission electron microscopy analysis, a further set of samples were prepared by sectioning multiple 120 μm thick slices with the Accutom-50 saw. Both sides of these slices were polished using the method above and once the thickness was measured as <100 μm, disks of 3 mm diameter were removed with a mechanical punch. Regions of undissolved Nb were excluded in these disks. These disks were jet polished using a range of parameters, however, all underwent cracking. Best results were achieved using the following parameters:

Temperature: -23 ^{o}C
Voltage: 15 V
Flow: 21
Infrared (set 80): 268
Current: 66 mA
Runtime: 62 s

Samples were then etched using a precision ion polishing system with an operating angle of 3 – 4 ^{o} and voltage of 2.5 – 4.5 KeV. Etch times varied widely from hours to days and were conducted in an iterative process. Sharp angles and high voltages (within the specified bounds) were used initially and the effects on the surface were observed. Shallower angles and smaller voltages were used as the disks became thinner. Thin samples were then checked using a transmission electron microscope to determine if they had become electron transparent, at which point, they were analysed.

For the V-Zr thin films, fragments were scratched off the Si substrate using a diamond scribe and ground under ethanol in a mortar and pestle. The dispersion was ultrasonicated and allowed to settle for five minutes. Three drops of the top fraction were dropped onto holey carbon grids for transmission electron microscopy observation.

2.8 X-ray diffraction

X-ray diffraction (XRD) is a standard structure analysis technique that utilises a collimated monochromatic source of X-rays to infer geometrical properties of a material. This is achieved when the X-rays interact with the valence electrons within the material in the low-energy limit and Thomson scattering occurs. The scattered X-rays that satisfy the Bragg condition:

$$n\lambda = 2d\sin\theta\,, \tag{2.25}$$

where n is the order, λ is the wavelength of the incident radiation, d is the interplanar spacing and θ is the reflected angle, interfere constructively and appear as reflections that are detected. In a periodic array of atoms the instances of similar “d-spacings” will contribute to a higher intensity reflection and thus an XRD pattern is recorded. There are many ways that this can be achieved, in this dissertation a standard Bragg-Brentano setup and grazing incidence configuration were employed to control X-ray penetration depth, see Figure 2.8. This was done using a Panalytical Bruker A25 D8 advance diffractometer with Cu-kα X-ray source (wavelength 1.5406 Å). Specific experimental details will be provided for each study.

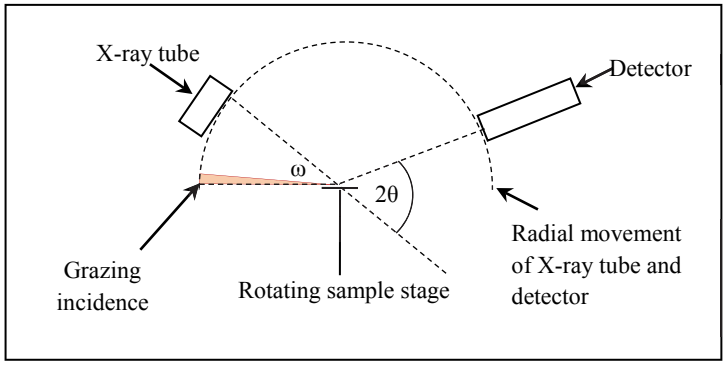

Figure 2.8. Standard Bragg-Brentano experimental XRD setup with GIXRD tube angle of incidence ω denoted by the red arc.

Analyses of the diffraction patterns were done using a peak fitting method known as Rietveld refinement (RR) [153, 154] within the Topas software package [155]. Topas was run in launch mode using jEdit [156] to program the inputs. Asymmetric broadening and peak shift due to GIXRD were corrected for using fundamental parameters. X-ray penetration depth was calculated using Beer-Lambert's law:

$$I_x / I_0 = e^{-(\mu/\rho)\times L} \tag{2.26}$$

Where I_x is the fraction of X-rays reflected I_0 is the initial intensity, and μ is the mass attenuation coefficient and ρ is the density of the material. Equation 2.26 is used to find L, the mean free path. Once this has been determined, the penetration depth (to receive 99% of the maximum intensity) is calculated as:

$$x = 0.5L \times \sin(\omega) \tag{2.27}$$

Where ω is the angle of incidence of the X-ray tube, see Figure 2.8.

2.9 Simulated XRD patterns

The Reflex module within Materials Studio 6 was used to simulate the XRD patterns of the modelled atomic structures. The results that would be obtained through an experimental powder diffraction method are approximated through the calculation of the intensity through the equation:

$$I(\theta) = \sum_{hkl} p_{hkl}(2\theta - 2\theta_{hkl}) I_{hkl} \tag{2.28}$$

where $p_{hkl}(2\theta - 2\theta_{\mathrm{hkl}})$ is the profile function (pseudo-voigt) and I_{hkl} is the integrated Bragg intensity:

$$I_{hkl} = M_{hkl} L_{hkl} \left| F_{hkl} \right|^2 \tag{2.29}$$

where M_{hkl} is the multiplicity of reflection hkl, L_{hkl} is the Lorentz polarisation correction which accounts for the portion of X-rays polarised by the monochromator and subsequently altering the scattering intensities observed according to:

$$L_{hkl} = \frac{p + (1-p)\cdot \cos^2 2\theta}{\sin\theta \sin 2\theta}, \tag{2.30}$$

where p is the polarisation fraction, and the structure factor, F_{hkl} is related to the atomic positions and scattering factors through the equation:

$$F_{hkl} = \sum_{1}^{N} f_n \exp\left(2\pi i[hu_n + kv_n + lw_n]\right) \tag{2.31}$$

and f_n is the atomic scattering factor of the atoms for the radiation used, *h, k, l* are the Miller indices and *u, v, w* are the fractional coordinates.

A single simulated XRD pattern was obtained for each system by averaging the intensities within the patterns of each individual supercell.

2.10 Scanning electron microscopy

Scanning electron microscopy (SEM) is another standard laboratory analysis technique that utilises electrons to probe the microstructure, surface morphology and chemical distribution of a material. When the electrons interact with the sample they produce a number of different signals from the backscattered electrons (BSE), X-rays, and secondary electrons (SEs). SEM is generally carried out by using an electron gun fitted with a tungsten filament or LaB_6 cathode which sends the electron beam through a series of magnetic lenses which deflect and focus the beam in the *x* and *y* axes allowing for a raster scan over a rectangular area of the sample (the sample itself must generally be made of or coated with, a conductive material as to mitigate charging effects). Detectors are placed at various locations around the sample in the vacuum chamber and electronic amplifiers of various types are used to amplify the signals received. These signals are interpreted by a computer and are displayed as a brightness intensity corresponding to the position of the beam on the specimen. When using BSEs, contrast between elements of differing atomic number is seen due to the heavier elements scattering more strongly than the lighter ones. SEs allow for a topological depiction of the sample as the signal generated is highly dependent on the angle the beam enters the specimen. X-rays are monitored in a process known as energy-dispersive X-ray spectroscopy (EDS). This is possible due to the electrons from higher energy orbitals dropping to the lower energies (as a result of inelastic scattering from the electron beam) producing an X-ray that has a characteristic energy and wavelength to the element and electron shell. These X-rays can be quantified and mapped, to the locations they were collected, for elemental analysis.

For the V-Zr thin films and bulk HEA samples a JEOL JSM6300 scanning electron microscope (SEM, JEOL Ltd., Tokyo, Japan) operating at 15 kV and equipped with a Noran Voyager Series IV energy-dispersive spectroscopy system (EDS, Thermo Electron Corporation) was used for microstructural and phase-composition analysis [157]. Ten random spectra were obtained from each sample and the compositions were then averaged. The arc melted samples were analysed using a Zeiss Ultra Plus with an attached Oxford instrument (X-Max 80 mm2 SDD X-ray microanalysis system) and operated at 15 kV accelerating voltage. Three spectra from each dendrite and interdendrite region were acquired and

averaged to obtain each composition and the full six spectra were averaged to obtain the whole chemical composition.

2.11 Transmission electron microscopy

Transmission electron microscopy relies on electrons in a transmission mode rather than backscattering from the sample. For this reason samples must be electron transparent which equates to a < 80 nm thickness. Producing suitable samples can be very difficult and time consuming, however analysis using this technique is very powerful as high resolution (sub 1-nm) structural and morphological information can be obtained. This is achieved by a columnar setup in which an emitted source of electrons (100−400 keV) travels through a condenser aperture, the sample, objective and intermediate apertures and then a range of lenses. The resulting beam is then recorded on a fluorescent screen or CCD detector. This setup is typically under a vacuum of ~10^{-9} Torr. By adjusting the electromagnetic lenses the back focal or image plane can be coincident with the detector resulting in a diffraction pattern or bright field image, respectively. The former case is referred to as selected area electron diffraction (SAED) and produces a diffraction pattern in a similar process to XRD. For crystalline materials the diffraction pattern is seen as a series of bright dots which is a reciprocal space representation of columns of atoms. This is because the spaces between the atoms act as a diffraction grating to the incoming electrons and the atoms that satisfy the Bragg condition (see Section 2.8) will constructively interfere. One major advantage of this setup is the ability to tilt the sample stage and observe different crystal orientations and their corresponding diffraction patterns. By combining Equation 2.25 with the geometric relationship in reciprocal space:

$$\tan 2\theta = D/L, \tag{2.32}$$

where D is the distance between the spots and L is the camera length, we obtain [158]:

$$d = D/\lambda L. \tag{2.33}$$

This allows for the calculation of the d-spacing between the lattice planes and characterisation of the structure. Another useful aspect of TEM is the ability to differentiate amorphous structures from polycrystalline with the former displaying a diffuse ring pattern instead of discrete spots in the diffraction pattern.

Bright field mode allows for TEM micrographs of real space images to be viewed. The contrast within the image arises from the number of electrons transmitted through the specimen. Thicker, denser or areas of high atomic number will produce darker areas due to the number of scattered electrons [158].

Within this dissertation SAED patterns were obtained using a JEOL 2010F operated at 200 kV. The grains were monitored via bright-field images and selected-area electron diffraction patterns. The grains were also monitored at elevated temperature using a Gatan Model 652 double-tilt heating stage to conduct controlled temperature experiments between 300 and 773 K. High-resolution bright-field scanning

transmission electron microscopy (BF-STEM) was performed in a double-corrected FEI Titan^3 80–300 FEGTEM operated at 300 keV with a convergence angle of 21 mrad and a camera length of 91 mm.

2.12 Ion irradiation

Bombardment with heavy ions is often used to simulate the effects of displacive radiation damage by neutrons within an in-core reactor setting. This is achieved through the use of a particle accelerator which is a device that utilises electromagnetic fields to propel charged particles at high speeds. The scale of these devices ranges from a small cathode ray tube to the Large Hadron Collider and in general the larger the device the higher the energies that can be achieved. Within this study a tandem electrostatic nuclear accelerator was used; the "tandem" aspect referring to the dual use of the same high voltage to accelerate the ions. This allows for higher ion speeds as the polarity of the ion is changed mid-flight, typically, a cation beam from a sputtering ion source is injected from a low voltage platform to the high voltage terminal which is positively charged by the incoming cations. The ions are then passed through a foil of carbon or beryllium stripping the ions of their electrons thus changing their charge turning them into cations. One drawback, however, is that it is not possible to make every element into a cation and it is difficult to use noble gases heavier than He [159].

To calculate the damage accrued by a structural material within a reactor lifetime, a measure of displacements per atom (dpa) is used. One dpa of damage refers to a material in which every single atom has been knocked from its lattice site once. Within a standard LWR lifetime, a cladding material is estimated to undergo 100 dpa [160]. In order to calculate the dpa within a material the following equation is used:

$$\mathrm{dpa} = \frac{H_e \times N_d}{\rho}. \tag{2.34}$$

where H_e is the total fluence (ions/cm^2), N_d is the total number of vacancies/cm and ρ is the density of the sample (atoms/cm^3).

The Australian National Tandem Research Accelerator (ANTARES) was used to produce a Au beam from a Cs-sputtering source using a Au wire of 1 mm diameter placed on an Al support. Au ions were chosen due to their relatively large molecular weight which will lead to maximised displacive damage. The output beam of the ion source was mass analysed with an electrostatic magnet at a field of 703 mT resulting in an Au^{1-} beam of 15 μA. This beam was transported to the low energy end of the accelerator and injected into the accelerator column, with a base vacuum of 10^{-5} Pa. The terminal voltage was set at 2 MV; as a result, at the end of the first acceleration stage, the Au^{1-} beam acquired the energy of 2 MeV.

At the exit of the first acceleration stage, the 2 MeV Au^{1-} beam was injected into a charge-exchange device, consisting of a tube (1 m in length) filled with SF_6 gas at a pressure of 5×10^{-4} Pa. The interaction of the 2 MeV Au^{1-} beam with SF_6 gas resulted in the loss of electrons for both the Au^{1-} and SF_6, with the net effect of producing a range of charge states for Au, see Table 2.1.

Table 2.1. The range of charge states of Au and their corresponding fraction and final energies.

Charge	Fraction (%)	Final Energy (MeV)
+1	14	4
+2	17	6
+3	18	8
+4	15	10
+5	10	12
+6	6	14
+7	3	16
+8	1	18

The multiple-charge Au beam was injected into the second accelerating stage, and at the exit of it, each Au charge acquired the final energy corresponding to that particular charge state. This multiple-charge Au beam was mass analysed with an electrostatic magnet, which allow the selection of the 4 MeV Au^{1+} beam or the 12 MeV Au^{5+} beam with the appropriate magnetic field strength. For the 12 MeV Au^{5+} beam, the field strength was 1406 mT.

Six TEM samples (NbTiV, $Mo_{0.5}$NbTiV, MoNbTiV, NbTiVZr, $NbTiVZr_{0.5}$, $NbTiVZr_2$) were mounted on a metallic (Al) support with conductive carbon tape. The sample current, which is an indication of how many Au ions hit the sample surface, was measured to be around 500-600 nA. This current was the measure of the fluence, and not the run time, due to some variations in beam intensity. The conversion between the beam current in nA and the number of Au particles striking the sample is based on the charge of Au^{5+}, and knowing that one particle nA = 6.242×10^9 Au/s. It was calculated that these TEM disks received a dose equivalent of 10 dpa with 4 MeV Au^{1+} ions for a total fluence of 10^{14} ions/cm^2 in transmission.

A single bulk sample of $NbTiVZr_2$ was subsequently irradiated with a 12MeV Au^{5+} beam corresponding to 10^{16} ions/cm^2 total fluence in deposition.

During the irradiation, the sample temperature increased marginally, not exceeding 50 °C, which was monitored with a K-type thermocouple, placed at the back of the irradiated sample.

The $NbTiVZr_2$ bulk sample was analysed and then further irradiated with He^{2+} ions, using a similar methodology. He^{2+} ions were chosen as they are present in both fission and fusion reactors. It was calculated that a peak damage of 2 dpa was received by the material with a total fluence of 10^{15} ions/cm^2

2.12.1 SRIM

Stopping range in materials (SRIM) is estimated with software developed by Ziegler and Biersack [161] that can calculate the interaction of ions with matter. Here it is run using the TRIM functionality to simulate the ion bombardment experiments as described in Section 2.12. The theory employed by this method is known as the binary collision approximation [162] which takes a Monte Carlo approach. This

method has been developed over half a century and is now at a stage in which results can be obtained with a 2 – 6 % accuracy when compared to experiment [161].

The number of vacancies produced as a result of the primary knock-on atoms (PKAs) and subsequent recoiling atoms are recorded is a measure of vacancies/ion.Å which is used to estimate the dpa received by the sample according to Equation 2.34. Furthermore, the range of the PKAs and recoils are also obtained in a depth profile.

The following experimental parameters for each experiment were fed into the TRIM program for detailed calculations with full damage cascades for 1000 ions:

(1) 4 MeV Au ions into all six TEM disks of 10 nm thickness and density determined by DFT.
(2) 12 MeV Au ions into a $NbTiVZr_2$ bulk sample with infinite thickness and density of 6.53 g/cm^3.
(3) 700 KeV He ions into $NbTiVZr_2$ as previous.

The largest unknown variable for these calculations are the threshold displacement energies, E_d, for each element. By default these are set to 25 eV however this value is highly dependent on the crystallographic orientation and temperature of the sample. The effect of varying E_d is explored within this dissertation.

2.13 Neutron cross-section

The neutron cross-section is a measure of the likelihood of interaction between the material and a neutron. There are two main categories of cross sections: microscopic (measured in barns where 1 barn = $1x10^{-28}$ m^2) and macroscopic (m^2), which refer to the atomic and bulk scales, respectively. The microscopic cross-sections are determined by transmission measurements of neutrons through a plate of a pure metal of known density. By measuring the attenuation of neutrons the microscopic neutron cross-section can be obtained. Values for this project have been taken from reference [163]. The macroscopic cross section is then proportional to the density of the material and can be calculated by the equation:

$$\Sigma = N\sigma \tag{2.35}$$

where Σ is the macroscopic cross section, N is the atomic density and σ is the microscopic cross section. Σ is comprised of both scattering and absorption cross-sections, however, for a cladding material we are predominantly concerned with the absorption cross-sections (also referred to as the capture cross-section) and omit the scattering component from all calculations. For many nuclides of relatively high mass numbers, a certain relationship exists between the energy of the incident neutron and the absorption cross-section. Due to this relationship it is only sensible to quote cross-sections for thermal energies (~0.025 eV) where the neutron cross section is proportional to $1/v$ where v is the velocity of the neutron. For higher energy (fast) neutrons the material can be considered non-interacting. The separation between the thermal and fast energy regions is occupied by a "resonance" region which arises due to quantum interactions between the neutron binding energies and kinetic energies, see Figure 2.9.

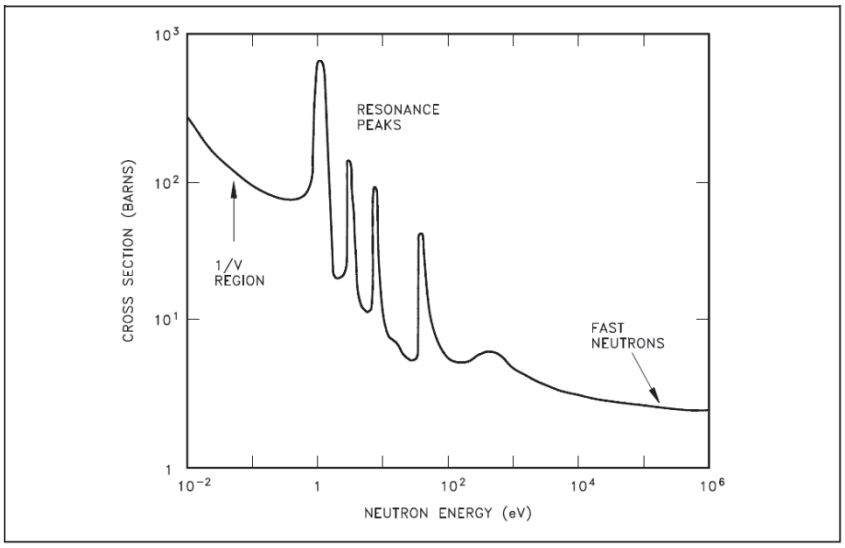

Figure 2.9. Taken from Ref. [164] typical neutron cross-section vs neutron energy relationship.

Ideally, the macroscopic thermal absorption cross-section is to be as low as possible for a fuel cladding, as to not interrupt the neutronics of the fission reaction. This requires both a low capture cross-section and low material density.

2.14 Nanoindentation

Nanoindentation was performed on all bulk as-cast samples to obtain a hardness and a Young's modulus. This technique was selected as it provides a reasonable estimate of mechanical properties and takes relatively little time to perform. The tests were conducted on the polished faces of the samples which were mounted on copper stubs. An Agilent G300 MTS nanoindenter was used to perform the experiment and Nanosuite software used to record and analyse the results. A Berkovich tip [165] was used and the area function was calibrated using a sample of known hardness before testing. The frame compliance was also calculated during calibration and temperature drift effects were monitored throughout the experiment (≤0.2 nm/s). An array of 5×5 indents were made using a continuous stiffness type measurement. Sufficient distance (50 μm) between points were allowed to account for the damaged zone around the indent. The Young's modulus was calculated according to the Oliver-Pharr methodology and the hardness (H) was calculated according to Equation 2.36 where the algorithms are built into the Nanosuite software. The average value between the 25 measured points on each sample were used as an estimate for the mechanical performance of each sample.

$$H = {P_{\max}}/{A_s}, \tag{2.36}$$

where $P_{\max}$ is the maximum load applied and A_s is the residual projected indentation area.

3

FORMATION AND STRUCTURE OF V-Zr AMORPHOUS ALLOY THIN FILMS

Results within this chapter have been published in Acta Materialia:

King, DJM. *et al.* Acta Mat **83** (2015) 269-275 [112]

3.1 Introduction

At the commencement of any new research effort it is imperative that the investigator's methods and results are validated against past literature. This notion is particularly important for theoretical techniques as some form of agreement between experiment and theory must be drawn for the method to be considered useful. For this reason an experimental and theoretical study of the binary V-Zr system was undertaken. This specific system was chosen as both of these elements are quite relevant to the nuclear industry due to their relatively small thermal neutron cross-sections [163]. Zr-based alloys are already extensively used for structural, in-core applications for the current generation of fission reactors [23], while V-based alloys are under consideration for structural components in fusion reactor environments, particularly the first-wall blanket [166]. However, there has been little consideration so far, in the nuclear industry and elsewhere, for binary alloys which simultaneously contain both V and Zr in significant proportions. When framing this system in the scope of HEAs one can think of V-Zr as a precursor to a larger system in which V and Zr are both present. However, the question remains – can these two elements co-exist within a solid solution? The literature on binary alloys would suggest not. In its elemental form, V is BCC while Zr is HCP below ~1136 K and BCC above that temperature [167]. Although they share the same structure at elevated temperatures, the Hume–Rothery rules for solid solution formation [168] predict that V and Zr should not be mutually soluble because their atomic radii differ by >15% and their electronegativities are dissimilar. Indeed, on normal solidification from the melt they form an intermetallic compound, V_2Zr, by peritectic transformation at ~1573 K, which has the C15 Laves phase structure [169]. Therefore, a mechanistic understanding of the thermodynamic behaviour; specifically, the aversion to form a solid solution, between these two species, is of great relevance to this dissertation.

The first step that was taken in this investigation was to synthesize a series of three V-Zr thin films: 2V:1Zr, 1V:1Zr and 1V:2Zr. Normally, such films are amorphous or glassy when produced at low temperatures [170], see Figure. 3.1.

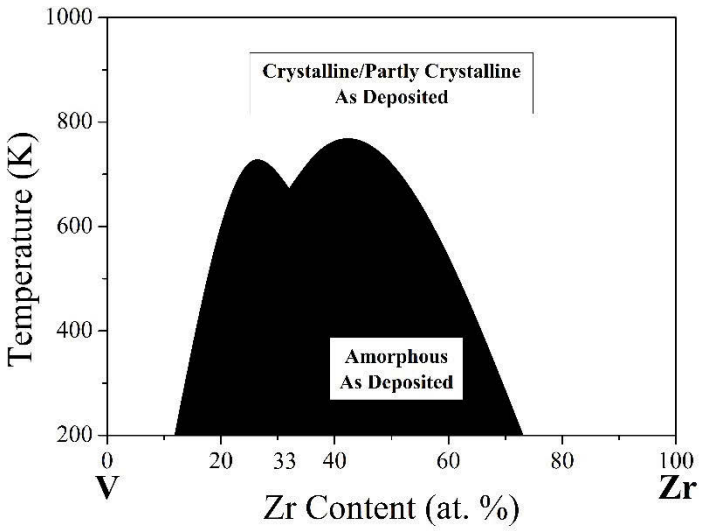

Figure 3.1. Glass-forming zone in the V–Zr system (adapted and redrawn from Eickert *et al*. [170]).

It might be expected that amorphous binary films (designated here as $(V,Zr)_{am}$) would crystallize to a product containing V_2Zr plus an element when heated, but instead such samples are reported to crystallize into a dual-phase mixture of elemental V and Zr phases, ostensibly because of the difficulty nucleating the complex Laves phase structure at relatively low temperatures [170]. There is, however, another possible explanation for the absence of V_2Zr in these samples. It may simply be that V_2Zr is not thermodynamically stable below some limiting temperature and instead, below that temperature, a dual-phase mixture of the elements is preferred. Formation of σ-phase in the Cr–Fe system would be an analogous example, where a mixture of two bcc elemental solid-solutions is more stable below ~773 K than σ -phase [171]. There is some theoretical support for this phenomenon occurring in V–Zr, with recent DFT calculations of the enthalpy of formation for V_2Zr showing this to be slightly positive [172] relative to its constituent elements.

Following the synthesis of the thin films. DFT calculations were performed to assess system stability. The simulation of the amorphous phase was attempted using *static* DFT which, at the time, had never been done before. This process led to a new method for the simulation of amorphous materials to be developed as demonstrated within this chapter.

3.2 V-Zr thin films

In this section, the results of co-depositing V and Zr onto Si wafers is described (see Section 2.5 for methodology). SEM-EDS analysis (with kind assistance from Mr. Joel Davis at ANSTO) of the three films was used to accurately determine the composition of the specimens and compare them to their target compositions of 2V:1Zr, 1V:1Zr and 1V:2Zr, see Table 3.1.

Table 3.1. Composition of thin films.

System	V (at. %)	Zr (at. %)
2V:1Zr	72.2	27.8
1V:1Zr	53.1	46.9
1V:2Zr	35.1	64.9

The target compositions were roughly achieved; the largest deviation was found to be for the 2V:1Zr composition, which had a V:Zr ratio of 2.6:1 instead of 2:1. This variation, although significant, was accounted for in the subsequent results and analysis. GIXRD was used to understand the crystal structure of the thin films. As expected from the literature [170], the equilibrium crystalline phases: BCC structured V, Laves phase V_2Zr and BCC/HCP structured Zr were not observed. Instead, all three patterns revealed a broad amorphous peak ranging from 30 to 45^o 2θ, see Figure 3.2a. The amorphous peak was observed to shift to a smaller angle as the Zr content was increased. The interatomic distances that correspond to these 2θ values are within the range expected of the V_2Zr Laves phase [173]. This shift of the central peak location (henceforth referred to as CPL) with increasing Zr content is attributed to the significantly larger atomic radius of Zr (1.60 Å) relative to V (1.34 Å) [174], which will increase the average distance

between atoms and hence produce a higher average interatomic distance. TEM analysis of the three thin films (performed by Dr. Liu at Monash University, Clayton, Australia) was used to confirm the amorphous nature of the three V–Zr compositions at the atomic scale. Figure 3.2b displays a representative SAEDP of a V–Zr film, showing diffuse rings characteristic of an amorphous material. The high-resolution BF-STEM image in Figure 3.2c exhibits the small randomly oriented "fringes" also expected for an amorphous material.

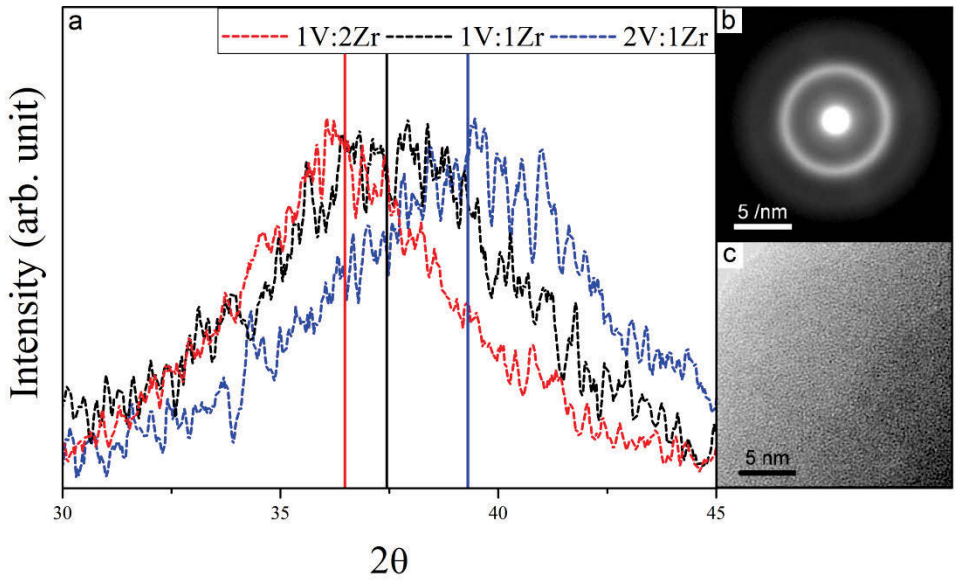

Figure 3.2. Experimental XRD patterns (dashed) for 1V:2Zr (red), 1V:1Zr (black) and 2V:1Zr (blue) amorphous thin films with the CPL indicated by vertical solid lines of matching colour. Representative (b) selected-area diffraction pattern of the 1V:1Zr film and (c) BF-STEM image of the same amorphous film demonstrating its amorphous nature (taken by Dr. Amelia Liu, Monash University, Australia).

This kind of phase contrast arises from a randomisation of the electron phase by the disordered object, subsequently convolved by the point spread function of the microscope [175]. There are no extended lattice fringes indicative of nanocrystallites. This amorphous diffraction pattern was observed from room temperature to 773 K during in-situ heating measurements.

3.3 Modelling the amorphous structures

The experimental results suggest that, in the absence of sufficient thermal activation (or time) to nucleate and grow a dual-phase microstructure (expected when considering the V–Zr phase diagram) an amorphous structure forms. However, as stated within the methodology (Section 2.2) modelling non-symmetric structures is somewhat difficult due to the periodicity imposed by the supercell method (especially in the limited system sizes feasible using DFT methods). Care must be taken to use sufficiently large supercells by selecting a suitable starting density to reduce imaging effects imposed by the periodicity.

As a result of the random nature of the disordered structures, twenty supercells (generated pseudo-randomly) are sampled for each composition and the combined results are used for analysis. This process should negate the effects of any accumulation and clustering of specific elements, which have been noted

to affect an amorphous system's stability [176]; furthermore, individual systems with lattice energies that were higher than the statistical range of normally distributed data were removed as outliers.

The effect of the initial supercell's density on the geometry-optimised structure was first considered. For each stoichiometry 54 atoms were placed in cubic supercells with edge lengths of 9×9×9 Å, 10×10×10 Å and 11×11×11 Å, henceforth referred to as 9 Å , 10 Å and 11 Å, respectively, to highlight the intial side lengths. The 20 individual simulated XRD patterns from each optimised supercell were averaged for each starting volume. A distinct change from a crystalline structure with defined peaks at high densities, to broad amorphous peaks with the lower starting density was observed. The peaks seen in the 9 Å and 10 Å supercell are indicative of crystalline ordering, see Figure 3.3.

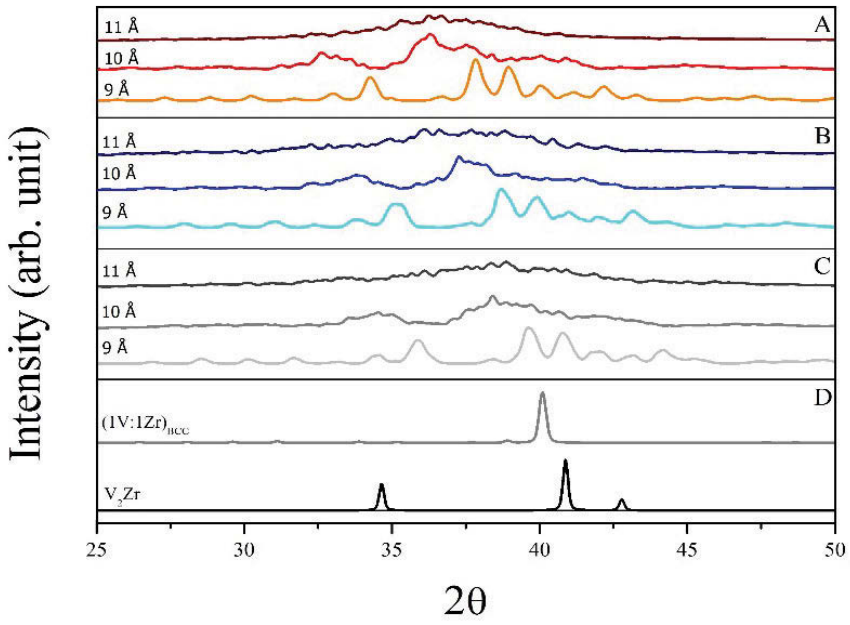

Figure 3.3. Average simulated XRD patterns of optimised (A) 1V:2Zr, (B) 1V:1Zr and (C) 2V:1Zr supercells with starting edge lengths of 11 Å, 10 Å and 9 Å located at the top, middle and bottom, respectively. These patterns are compared to (D) $(1V:1Zr)_{BCC}$ (grey) and V_2Zr (black) simulated XRD patterns.

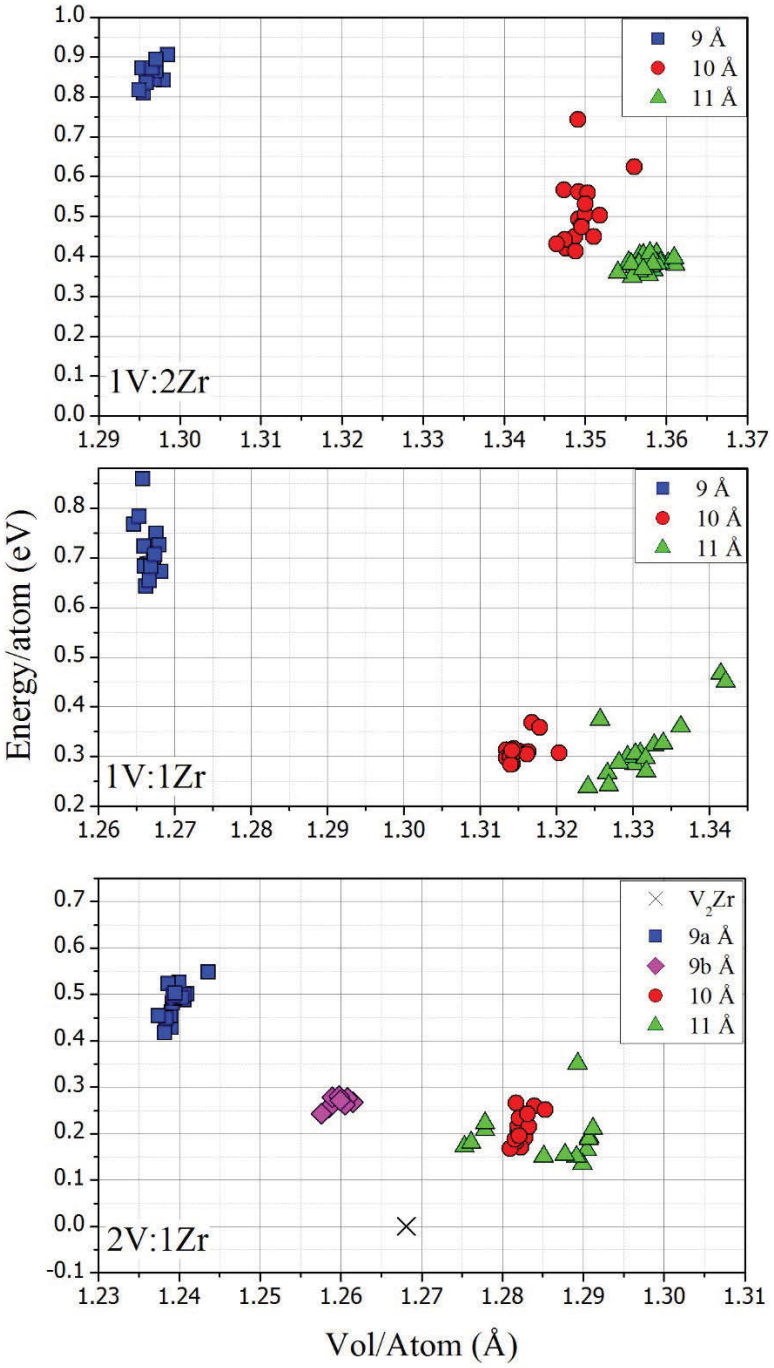

Figure 3.4. Lattice energy per atom (normalized to V_2Zr) vs. volume per atom of amorphous supercells of 1V:2Zr (top), 1V:1Zr (middle), 2V:1Zr (bottom) with starting densities of 9 Å (a) converged to 10^{-3} eV (blue square), (b) converged to 10^{-4} eV (magenta diamond), 10 Å (red circle) and 11 Å (green triangle) with V_2Zr as reference (cross).

When considering the volume and total energy of each supercell, across the three stoichiometries, the 9 Å supercells were both smaller in volume and higher in energy (less favourable) compared to the larger 10 Å and 11 Å systems, see Figure 3.4. By increasing the starting density to 10 Å the supercells minimise in volume during the structure optimisation and yield a lower energy per atom and higher volume per atom than the 9 Å, yet still display sharp peaks within their XRD pattern. Finally, the 11 Å supercells, which

are relatively similar in volume and energy per atom to that of the 10 Å, yield quite dissimilar XRD patterns. This suggests that the initial density of the supercell plays a pivotal role in accurately modelling an amorphous structure. Independent of the optimisation process, a more open structure is initially required to prevent intermediate-scale crystalline periodicity in the small supercells used in this approach. For 2V:1Zr, a second set of 9 Å (9b Å) supercells were run with a finer energy convergence criteria of 1×10^{-4} eV, which both expanded in volume and reduced in energy but did not have an effect on the perceived degree of crystallinity. The effect of scaling, by doubling and halving both starting volume and number of atoms in the supercell, was also explored. The smaller supercells exhibited sharper peaks analogous to the 9 Å supercells, whereas the larger supercells show a similar broad amorphous hump to that of the 11 Å system. The average lattice energy per atom of the larger and smaller supercells varied from the 11 Å by 1.7×10^{-2} eV and 3.2×10^{-2} eV, respectively. These results show that there is little further benefit in scaling to a larger supercell and that it is difficult to effectively simulate an amorphous material with a smaller system than those chosen in this study. For these reasons, the 11 Å supercells were used for comparison to the experimental data and for further analysis.

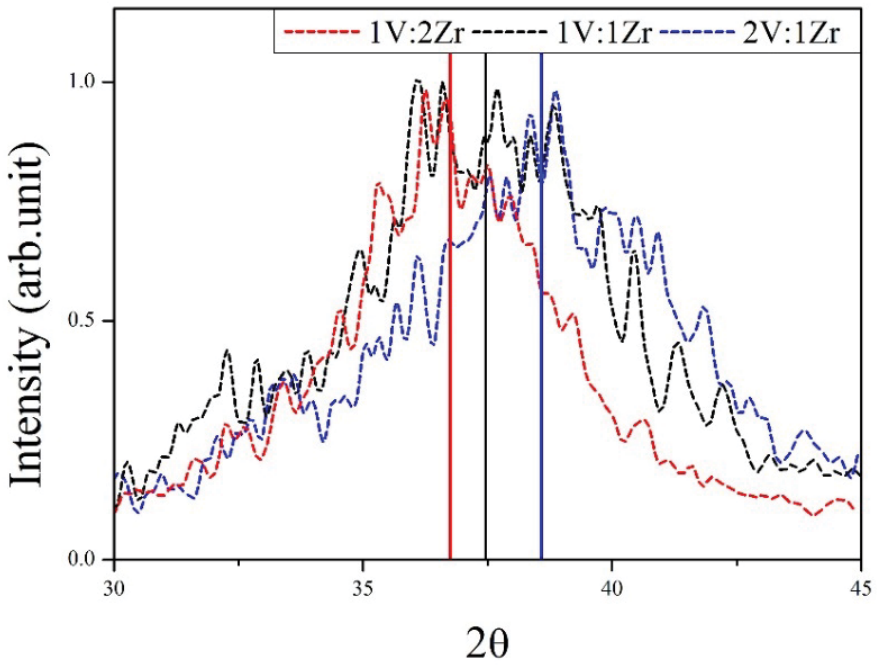

Figure 3.5. Average simulated XRD patterns (dashed) for 11 Å 1V:2Zr (red), 1V:1Zr (black) and 2V:1Zr (blue) amorphous supercells with the central peak location (CPL) indicated by vertical solid lines of matching colour.

When comparing the simulated XRD patterns of the modelled 2V:1Zr, 1V:1Zr and 1V:2Zr structures there is also a distinct similarity in the shift in CPL to that seen in the experimental equivalent, see Figure 3.5 and 3.4, respectively. To account for the slight difference in stoichiometry between model and experiment, a linear function was applied to the CPL (Å) as a function of Zr content (at.%). The difference in gradient and y-intercept was determined to be 1.3×10^{-3} Å/at. % and 0.05 Å, respectively. Since the statistical error associated with the simulated CPL was calculated to be of the order of 10^{-3} Å, it can be said that both experimental and simulated results are in strong agreement.

To investigate this shift in bond length further, a radial distribution function (RDF) was calculated for the modelled data to determine the approximate distance of first and second nearest neighbours in the three amorphous stoichiometries, see Figure 3.6. Unsurprisingly, the trend in the shift is in agreement with the XRD data. Further, the RDF produced by all three stoichiometries is in agreement with other experimental and theoretical predictions of amorphous solids showing short-range order which diminishes with distance [177, 178]. The data from the RDF should only be considered relevant up until the $L/2$ value of 5.5 Å (where L is the shortest edge length of the supercell). This is because of the periodic nature of the DFT method whereby any information past $L/2$ will correspond to self interactions.

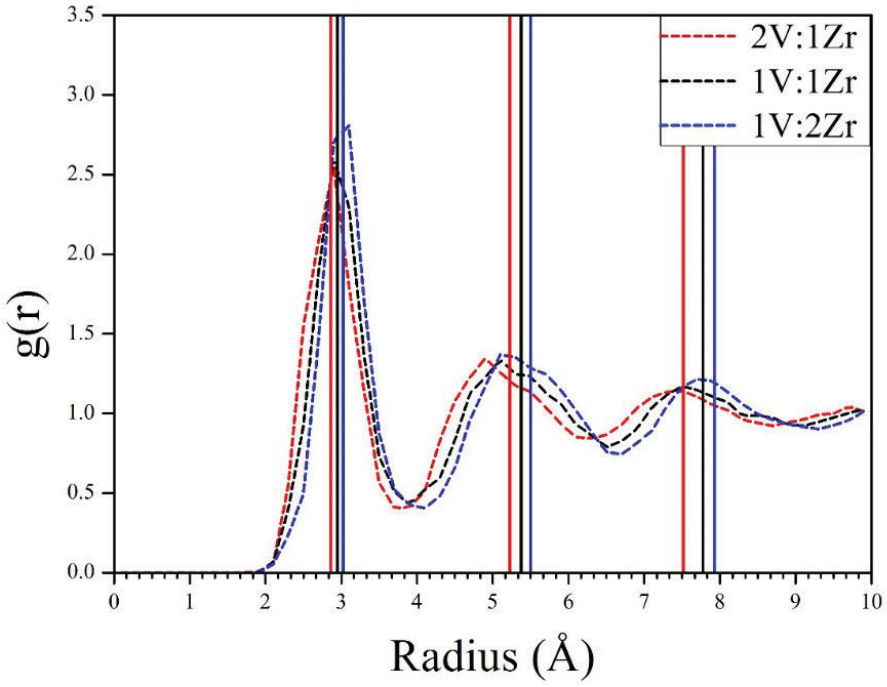

Figure 3.6. Average simulated radial distribution functions (dashed) for 2V:1Zr (red), 1V:1Zr (black) and 1V:2Zr (blue) amorphous supercells with the CPL of the first, second and third nearest neighbours indicated by vertical solid lines of matching colour.

When considering the average interatomic distance of the first nearest neighbours with the change in Zr content for $(V,Zr)_{am}$, V_2Zr, BCC V, BCC Zr and HCP Zr, we find that there is a variance in the behaviour of the systems with regards to Vegard's law [179], see Figure 3.7. The amorphous systems have longer average interatomic distances to their nearest neighbours than the predicted crystalline V–Zr systems. This is in line with the amorphous systems being more openly packed. The predicted densities of the three stoichiometries are 6.28, 6.23 and 6.46 gcm^{-3} for 2V:1Zr, 1V:1Zr and 1V:2Zr, respectively. These densities exist between that of BCC V (6.00 g cm^{-3}) and HCP Zr (6.52 g cm^{-3}) [180] but display a non-linear trend. The difference in trend between average bond length and density with varying Zr content could be related to short-range ordering of polyhedra [181] and/or alternations of their packing density. Cheng and Ma [182] describe the short-range polyhedral ordering as less frustrated when atoms of different sizes are present and chemically compatible. Their review highlights the variation in structure throughout amorphous metals, some areas being more ordered than others, and relates this to

connectivity/polytetrahedral packing. This is an interesting field and further study of the shortrange ordering within the V–Zr amorphous system using experiment and modelling would be worthwhile.

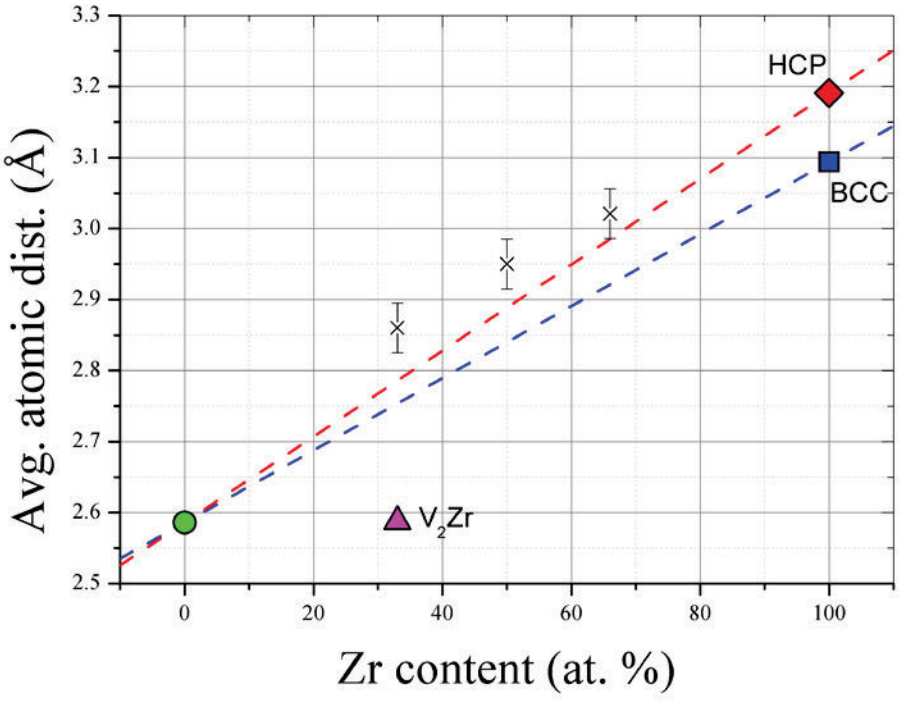

Figure 3.7. Calculated average interatomic distances to the first nearest neighbour for 1V:2Zr, 1V:1Zr and 2V:1Zr (crosses), compared to the modelled ideal crystalline structures of BCC V (circle), HCP Zr (diamond) and BCC Zr (square) and V_2Zr (triangle). Two linear functions (red and blue), representing Vegard's law, are fitted between bcc V and HCP Zr, and BCC V and BCC Zr, respectively.

3.4 Thermodynamic stablility of the phases

After gaining some confidence that the simulated amorphous structures are representative of the experiment, the thermodynamic stability, in comparison to the crystalline phases, is now investigated using DFT. Each stoichiometry is considered separately, initially focusing on the 2V:1Zr stoichiometry that is expected to form the intermetallic V_2Zr under certain circumstances. It should be noted that this section only considers the enthalpy of formation (which are averaged for the disordered structures). Work in the later chapters will address vibrational and configurational entropy as these are expected to have an impact on system stability [183]. Calculations of vibrational effects are currently extremely computationally expensive (as they cannot use symmetric effects to their advantage in the manner crystalline systems are able to do [183]).

3.4.1 V_2Zr

In agreement with prior literaure [172] the calculated formation enthalpy of V_2Zr is positive (unfavourable), according to equations:

$$2V_{BCC} + Zr_{BCC} \rightarrow V_2Zr_{Laves,}\ \Delta H = +0.12\ eV/atom \quad (3.1)$$

and

$$2V_{BCC} + Zr_{HCP} \rightarrow V_2Zr_{Laves,}\ \Delta H = +0.15\ eV/atom \quad (3.2)$$

At low temperatures V_2Zr is predicted to be unstable relative to its constituent elements, also seen in the work of Lumley *et al*. [172] but in disagreement with the accepted equilibrium phase diagram (meaning it may be thermally stabilised at room temperature). Of course, the metastable solid solution (whether BCC or amorphous) is even more energetically unfavourable relative to a mixture of the elements, for example:

$$2V_{BCC} + Zr_{HCP} \rightarrow (2V{:}1Zr)_{BCC,}\ \Delta H = +0.40\ eV/atom \quad (3.3)$$

Nevertheless, nucleation of a dual-phase structure of the elements requires thermal activation and would obviously be very slow at lower temperatures, and hence the possibility of a massive (i.e. no long-range mass transfer) transformation between the phases of the same composition but different structures is also worth considering:

$$(2V{:}1Zr)_{BCC} \rightarrow (2V{:}1Zr)_{am,}\ \Delta H = -0.15\ eV/atom \quad (3.4)$$

and

$$(2V{:}1Zr)_{am} \rightarrow V_2Zr_{Laves,}\ \Delta H = -0.11\ eV/atom \quad (3.5)$$

Therefore, on the basis of these calculations, it can be predicted that a physical vapour deposit would very likely form as $(2V,Zr)_{am}$ (agreeing with the experimental observations), with transformation to V_2Zr likely if the sample is subsequently heat treated to a sufficiently high temperature [170].

3.4.2 1V:1Zr and 1V:2Zr

Now the stability of materials with either the 1V:1Zr or 1V:2Zr stoichiometry are explored, starting with either a BCC or an amorphous structure. The key question is whether or not it will be energetically favourable for these structures to transform to a dual-phase mixture of V_2Zr Laves phase + Zr. The relevant transformations are given in Equations (3.6)–(3.8) for 1V:1Zr:

$$2(1V{:}1Zr)_{BCC} \rightarrow V_2Zr_{Laves} + Zr_{HCP,}\ \Delta H = -0.42\ eV/atom \quad (3.6)$$

$$2(1V{:}1Zr)_{am} \rightarrow V2Zr_{Laves} + Zr_{HCP,}\ \Delta H = -0.16\ eV/atom \quad (3.7)$$

$$(1V{:}1Zr)_{am} \rightarrow V_{BCC} + Zr_{HCP,}\ \Delta H = -0.28\ eV/atom \quad (3.8)$$

The reactions that can take place with the 1V:2Zr stoichiometry are provided in the following equations:

$$2(1V{:}2Zr)_{BCC} \rightarrow V_2Zr_{Laves} + 3Zr_{HCP,}\ \Delta H = -0.53\ eV/atom \quad (3.9)$$

$$2(1V{:}2Zr)_{am} \rightarrow V_2Zr_{Laves} + 3Zr_{HCP,}\ \Delta H = -0.15\ eV/atom \quad (3.10)$$

$$(1V{:}2Zr)_{am} \rightarrow V_{BCC} + 2Zr_{HCP,}\ \Delta H = -0.22\ eV/atom \quad (3.11)$$

It is clear from the above that the BCC solid solution is unstable relative to all the other considered possibilities, whilst the most stable structures are always the dual-phase mixtures of the elements which remain energetically favourable relative to a dual-phase microstructure of V_2Zr and Zr. Nevertheless, in the absence of sufficient thermal activation (and time) to nucleate and grow either of the dual-phase microstructures, it might be expected that the amorphous solid solution would be found and the amorphous structures will have a tendency to decompose to a dual-phase microstructure with associated negative formation enthalpies. These enthalpies of formation may be correlated with the drive of the amorphous structure to crystallize and segregate into nanoscale domains of V_2Zr and Zr; however, the kinetic effects required to form such a heterogeneous microstructure are neglected. Indeed, kinetic effects such as thermal activations at low temperatures have been noticed and well-studied in amorphous structures [184]. These thermal activations were found to play a key role in the temperature-dependent behaviour and structure. Nevertheless, we have shown in this section that considering enthalpy alone can provide some useful predictions of materials behaviour in amorphous metal systems.

3.5 In the context of HEAs

The method for simulating amorphous structures has many similarities with that of crystalline HEA solid solutions. In fact, when using the loose definition of HEAs, there is no requirement for the solid solution to be crystalline and it is entirely possible for a HEA to exhibit an amorphous structure. Some examples in which this is the case include: $Al_{0.24}Co_{0.20}Sc_{0.20}Y_{0.36}$ [185], CuNiPPdPt [186], CuNiPdTiZr [187], CuBeNiTiZr, [188]. However, these systems are quite dissimilar to those that the current project aims to study. This is because a single phase crystalline structure is not observed at equilibrium. In such systems the amorphous phase is not thermally stable and in most cases a multiphase crystal structure will result upon annealing. While it is no surprise that the enthalpy of mixing, of the amorphous configuration, should be largely positive (unfavourable) in energy, it is another question entirely as to the contribution made by the entropy. It is my belief that since amorphous structures are a non-equilibrium phenomena, to apply the concept of configurational entropy would not be sensible. This is supported by the fact that entropically stabilised phases are more favoured at high temperatures where the reverse is true for amorphous systems which are only stable at low temperatures.

Interestingly, when applying the concept of configurational entropy to the amorphous V-Zr system through the assessment of the Gibbs free energy ((Eq. 1.1) for the reverse reaction in Equation 3.8; the value obtained (+0.15 eV/atom) is still positive at the melting temperature of the alloy.

The “glass forming ability” [189] of metallic mixtures is still a hot topic in material science, and can be related to the cooling method/rate of the mixture. An interesting observation, however, is that amorphous and multiphase alloys seem to both contain elements with atomic radii that differ sufficiently ($\delta \geq 6.6$, see Equation 1.14) [43] which will not allow for a single phase crystalline solid solution. For example, CuZr, which is thought to be the best metallic glass former has $\delta = 11.1$ while VZr has $\delta = 8.84$. Therefore, one could speculate that by mixing elements with atomic radii between that of V and Zr it is possible for both of these elements to exist within a BCC solid solution in equal concentrations. This can be seen in the work by Senkov *et al*. who manufactured a NbTiVZr HEA [76].

3.6 Summary

A simple validation of techniques led to an interesting development of a new method for simulating amorphous materials. Crystallisation of the V_2Zr Laves phase in V–Zr alloys is predicted from the phase diagram but requires relatively high temperatures to occur. Instead, mixtures of V and Zr that were co-deposited at room temperature using magnetron sputtering were observed to form amorphous solid solutions. Calculations of formation enthalpies confirmed that an amorphous solid solution would be significantly more stable than a random body-centred solid solution of the elements, in agreement with the experimental results. The effect of varying the starting densities within the amorphous supercells was investigated. It was found that a larger, more open structure is required, prior to the optimisation process, to effectively simulate an amorphous system. Smaller supercells tended to crystallize and displayed sharp peaks similar to that of V_2Zr and $(V,Zr)_{BCC}$. Similar trends in both simulated and experimental XRD patterns, related to the average interatomic distance, were identified by the shift in CPL with varying Zr content. This was due to the relatively large atomic radius of Zr, compared to V, causing an increase in average interatomic distance. The modelled amorphous systems were further characterised through a radial distribution function. A positive deviation from Vegard’s law was identified in the distance to the first nearest neighbour. Changes to the nearest-neighbour distances in the three formulations studied may indicate changes in the short-range order of the amorphous structure. Due to the large agreement between experiment, theory and past literature, it is safe to conclude that the techniques used are now validated. Within the next chapter, I extend these computational techniques to well-known HEA systems.

4

AB INITIO INVESTIGATION OF THE $Al_xCoCrFeNi$ HIGH-ENTROPY ALLOY

Results within this chapter have been published in the following publications:

Middleburgh, SC. *et al.* J Alloy Compd **599** (2014) 179-182 [190]

King, DJM. *et al*. JOM **67** (2015) 2375-2380 [37]

4.1 Introduction

In the previous chapter both computational and experimental techniques were validated against past literature for a standard binary system – V-Zr. The purpose of this chapter is to use the computational techniques that were developed and validated to investigate the energetics of two well-known HEA systems: Co-Cr-Fe-Ni and Al-Co-Cr-Fe-Ni. Both of these systems are of particular interest within the HEA community as CoCrFeNi is the first composition found to form a single phase HEA (SPHEA) and the Al_xCoCrFeNi series displays a shift from FCC → FCC + BCC → BCC as the Al content is increased [4, 56], see Section 1.4.1. A number of papers differentiate the BCC phases observed into two types: disordered A2 and ordered B2 (analogous to the NiAl phase) [65]. Studies on these systems represent ~25% of the total literature on HEAs to-date and continue to attract new research efforts. A vast majority of these studies have been purely experimental and reports of high hardness [65], corrosion resistance [101, 190], wear resistance [191] and fatigue behaviour [192] have been made. Theoretical studies that focus on these systems include: Zhang *et al.*'s [193] use of CALPHAD to aid alloy design and Poletti and Battezzati [63] who used a number of criteria, both theoretical and experimental, to predict new HEAs and their likely structure. Zaddach *et al.* [194] utilised the SQS method to calculate the elastic properties of CoCrFeNi and Niu *et al.* [35] examined its magnetic ordering. Tian *et al.* [108] investigated this shift in packing with Al content using DFT. However, a quantitative understanding of the energetics involved in these systems and the effect of ordering within these alloys was still lacking.

In this chapter I will begin with the CoCrFeNi system, where the vacancy and interstitial formation energy of each element is considered. I will then look at the effect of ordering in this four element system before investigating the effects of Al addition. All calculations were performed by myself and Dr. Simon Middleburgh. The methodology development that facilitated this work and development of the discussion were my major inputs.

4.2 CoCrFeNi

Instead of the standard 48-54 atom supercells, a smaller 32 atom supercell was constructed for this system and the data was averaged over 20 supercells using the brute force method. The spread in energy was found to be ±0.06 eV/atom which is to be expected, see Section 2.2. Two of the twenty arrangements varied by > 0.5 eV and were omitted from analysis. The average formation enthalpy of these 18 supercells was found to be positive ~1 eV highlighting the need for configurational entropy (and temperature) for the solid solution to form. SQS was performed to compare to the brute force method for this system and a lattice parameter of 3.54 Å was determined compared to 3.51 Å of the current method. This difference of 0.03 Å is well within 1% of the experimental results [194].

The vacancy formation energies were calculated using the previously described methodology, see Section 2.3. The vacancies are considered to segregate from the matrix to form FCC-Co, BCC-Cr, FCC-Fe and FCC-Ni. A very interesting result arises from these calculations; Cr has a significant negative vacancy formation energy i.e. Cr will spontaneously segregate to a secondary phase, see Figure 4.1. This may be explained qualitatively by the fact that the high temperature structure of Cr (BCC) differs from that of the other constituent elements (FCC).

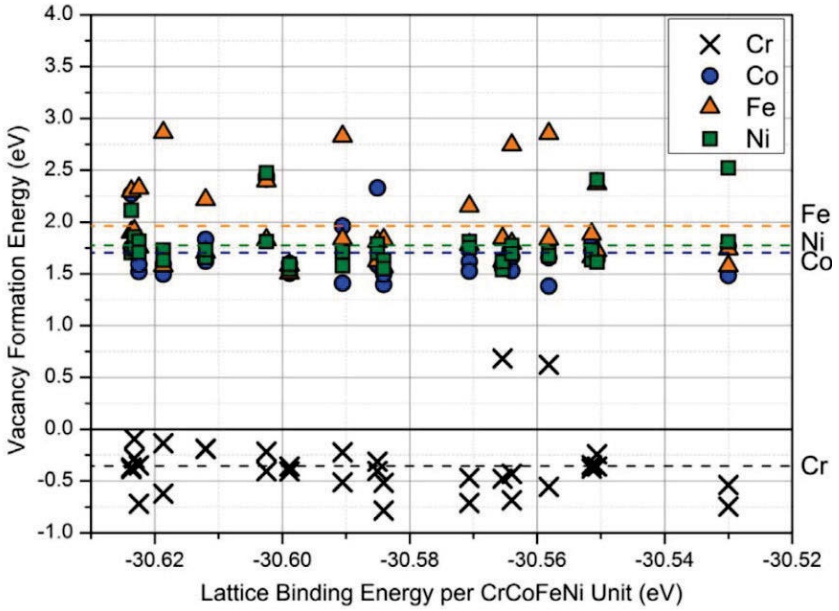

Figure 4.1. Vacancy formation energy for Co, Cr, Fe and Ni in CoCrFeNi HEA as a function of supercell stability. The average value is highlighted with a dashed line for each species.

However, to what degree Cr will precipitate from solution and at what temperature this phenomenon may occur is still relatively unknown. In an attempt to address these questions, vacancy formation energies were calculated for a Cr-depleted stoichiometry, $CoCr_{0.55}FeNi$, see Figure 4.2. Results similar to the equimolar alloy were found with the average Cr vacancy formation energy being -0.55 eV, which would suggest the Cr segregation would not be stabilised by a depletion of Cr

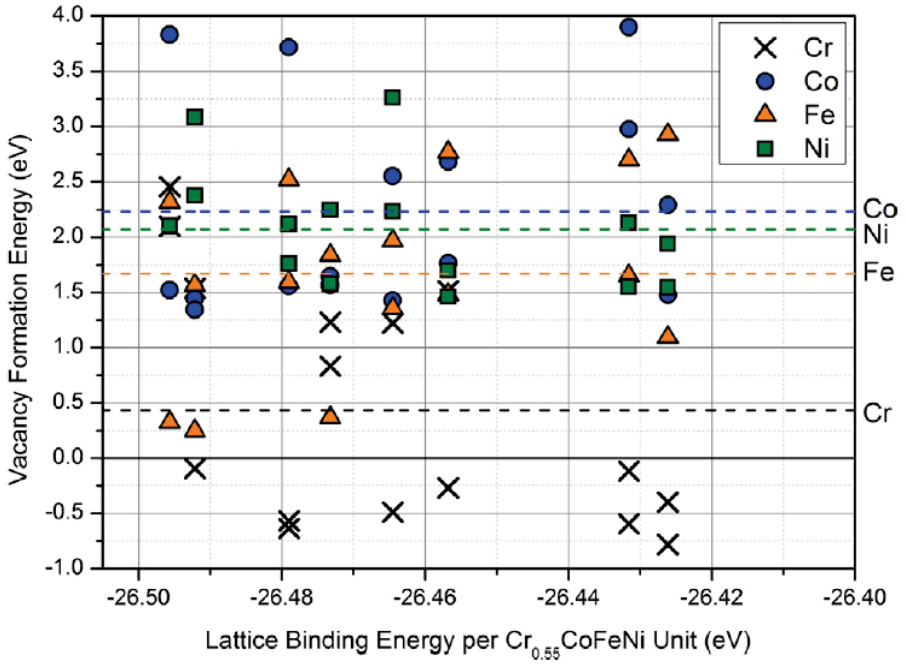

Figure 4.2. Vacancy formation energy for Cr, Co, Fe and Ni in $Cr_{0.55}CoFeNi$ HEA as a function of supercell stability. The average value is highlighted with a dashed line for each species.

However, 6 of the 16 supercells yielded a positive formation enthalpy. This, coupled with the larger spread in data suggests there may be a more complex behaviour involved. Certainly, the configurational entropy of the solid solution will decrease as Cr is removed but it seems the energetic effects cannot be modelled with such a small supercell due to the local environment around the vacancies having such a large influence on stability. Nevertheless, it is not unreasonable to conclude that the segregated Cr could form a Cr_2O_3 precipitate within the bulk or even a protective oxide layer for the alloy. Observations of that give support to this proposed mechanism have been reported in recent experimental studies [195, 196].

Interstitial defects are now considered; the formation of interstitial defects is only likely under non-equilibrium conditions, e.g. during a radiation cascade (similar to other close packed metallic systems [197]), but can provide further insight into the elemental interactions with the solid solution matrix. Ten supercells containing *a*(0.5, 0.5, 0.5) octahedral self-interstitials of each element were created and the structure was minimised (the tetrahedral interstitial site was universally less favourable). The stability of each interstitial defect is tested by comparison of their defect energies, see Figure 4.3.

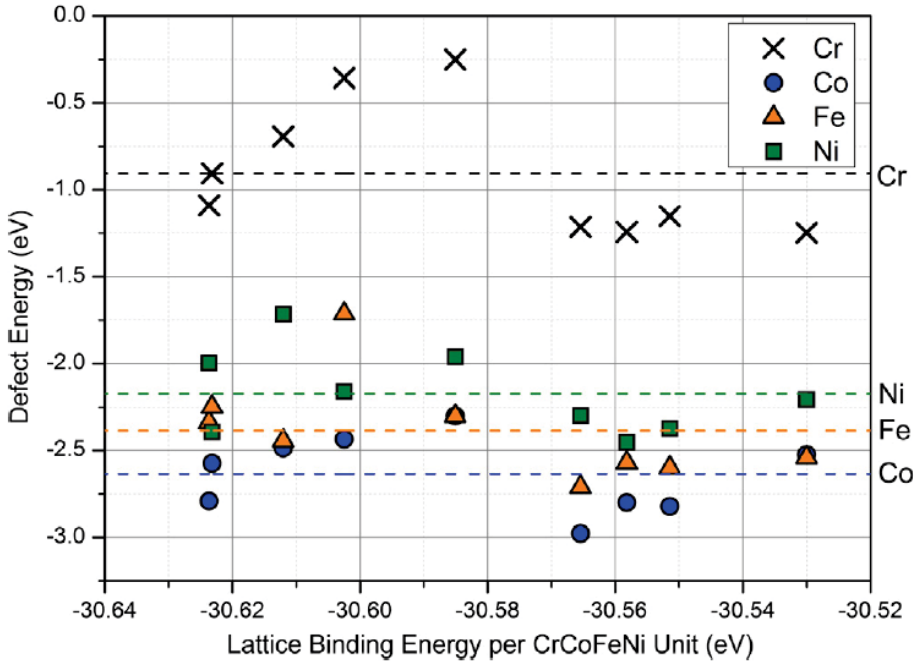

Figure 4.3. Defect energy of interstitial species in CrCoFeNi as a function of lattice stability. Mean defect energies are highlighted as a dashed line for each species.

A slight variation in the defect energies within CoCrFeNi is seen with low energy arrangements providing higher defect energies. There is certainly an energetic preference for Co to form interstitial defects particularly over Cr interstitials which suggests Cr segregation will be limited to vacancy mediated mechanisms. Interestingly, of the 40 interstitial defects investigated, 36 formed split interstitials of the <001> orientation (similar to FCC-Ni, Co and Fe). Of these split interstitials ~70% involved a Co atom highlighting the aforementioned preference for this specie to be involved with this type of defect.

Finally, vacancy migration energies are considered to assess the relative difficulty in migration of a particular element. Here the climbing nudged elastic band method was employed. Six images along the reaction coordinate were used for each migration calculation and ten migrations were considered for each element. Cr was predicted to migrate with the lowest activation energy, 0.8(4) eV, which is within the range of BCC-Cr (0.68 – 0.95 eV) [198, 199]. Co was predicted to migrate with an energy of 1.1(4) eV which is also comparable to pure FCC-Co migration energies (0.94 – 1.19 eV) [200, 201]. Fe was predicted to migrate with an energy of 1.3(3) eV, far higher than experimentally and theoretically predicted (~0.65 eV [202]). Ni was predicted to migrate with an energy of 1.3(6) eV which compares extremely well with previously published values of 1.3 –1.5 eV [203, 204].

Work by Tsai *et al*. [51] reports experimental data that is in strong agreement with these theoretical results. The order of activation energies for the elements is found to be Cr < Co < Fe = Ni with a large discrepancy between the HEA and FCC-Fe. These combined findings somewhat support the notion of "sluggish" diffusion within HEAs but only for Fe. The change in behaviour of Fe relative to its elemental solid may be due to a combination of effects such as frustrated lattice, change in behaviour from low temperature ferrite to high temperature austenite or magnetic properties (as seen in FeCr [205]).

Interestingly, a ferrimagnetic behaviour is observed in this CoCrFeNi system with Co, Fe and Ni species producing a dominant magnetic moment in the same direction and Cr opposing this moment. This same effect is observed in a recent DFT study by Niu *et al*. [35] where it is hypothesised Cr will display the same behaviour in the CoCrFeNi system as it does in the FeCr binary; a Cr-Cr nearest neighbour is energetically unfavourable and will adopt a $L1_2$ structure (analogous to the $AuCu_3$ intermetallic) to minimise its energy. Indeed, when Niu *et al*. ordered the CoCrFeNi system in this way (Cr on the Au site and Co, Fe and Ni randomly distributed across the Cu sites) a largely more favourable formation enthalpy is calculated. They also factored in the diminished configurational entropy for the partially ordered system using the equation:

$$S_{\text{config}} = S_{\text{config}}^{\text{CC-site}} + S_{\text{config}}^{\text{FC-site}}, \tag{4.1}$$

where the CC-site refers to the "cubic corner" site (Au site) and FC-site is the face centred site (Cu site). Before this particular paper by Niu *et al*. [35] was published, I had developed an almost identical methodology for calculating the configurational entropy of a partially ordered system.

Both methods assume each lattice site is isolated and each sublattice and their relative contributions to 1 mole of atoms is used as a weighting. In my method, this is done by expanding $n_{tot} = \sum_{k=1}^{l} n_k$, where the total number of moles n_{tot} is the sum of the number of moles n of sublattice k for l number of sublattices. Therefore,

$$S_{conf} = -R\left[\sum_{k=1}^{1} n_k \sum_{i=1, i\neq m}^{j} x_{i,k} \ln(x_{i,k})\right], \tag{4.2}$$

where m is any element that is not included on the sublattice k and $x_{i,k}$ is the atomic fraction of the i^{th} element normalised to sublattice k. Using this method, the same value is obtained for the Gibbs entropy for a fully disordered system as-well-as an amended value for a partially ordered system.

This concept of partial ordering was also explored within the current study. Initially, the type of ordering was assumed to be that with Fe on the FC-site, however in light of results by Niu *et al*. [35] Cr ordering was also explored and also determined to be more favourable.

4.3 $Al_xCoCrFeNi$

In this section, the crystallographic and thermodynamic effects of systematic additions of Al to the CoCrFeNi system are examined in detail. As mentioned, the notion of partial ordering is explored with a main focus on the BCC packing in the $Al_xCoCrFeNi$ system, see Figure 4.4.

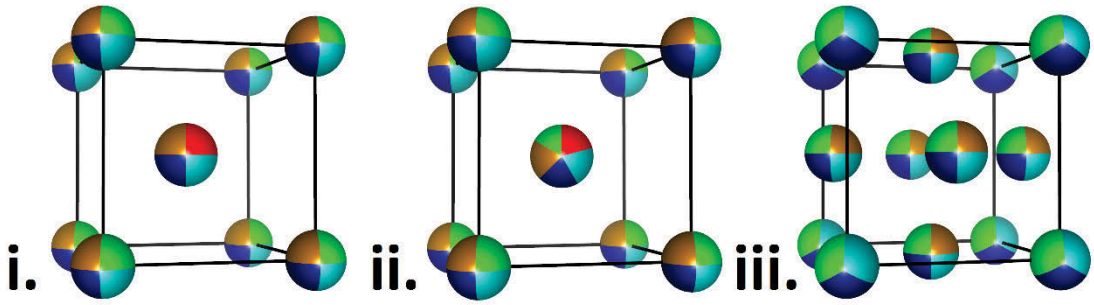

Figure 4.4. Partially ordered structures with BCC packing include: (i) Al and Ni constrained to the centre and corner sites, respectively, and (ii) Al constrained to the centre site. (iii) Is the partially ordered $L1_2$ structure with Fe constrained to the FC-site. In these models Al is represented as red, Ni – green, Fe – gold, Co – light blue, Cr – dark blue.

Both FCC and BCC packed, fully disordered and partially ordered structures were modelled as x was varied from 0 – 2.40 at. ratio, in four steps. The disordered supercells that were built with FCC symmetry retained their structure after the energy minimisation process, regardless of Al content. The lattice parameter increased with increasing Al content, as expected given the larger metallic radius of Al (1.43 Å [174]) compared to Co (1.25 Å), Cr (1.36 Å), Fe (1.26 Å), Ni (1.24 Å). The lattice parameter was predicted to increase from 3.519 – 3.556 Å between $0 \geq x \geq 0.57$, equating to a difference of 0.037 Å, which is in excellent agreement with the experimental differences observed by Wang *et al* (0.025 Å between $0 \geq x \geq 0.5$).

The simulated XRD pattern for the four FCC $Al_xCoCrFeNi$ systems can be seen in Figure 4.5. The main (111) peak at ~45° 2θ shifts from higher to lower angle as the Al content is increased, as expected, while the (200) peak at ~50° diminishes in intensity. It should be noted that the two compositions with the highest Al contents are not observed to have FCC packing, experimentally.

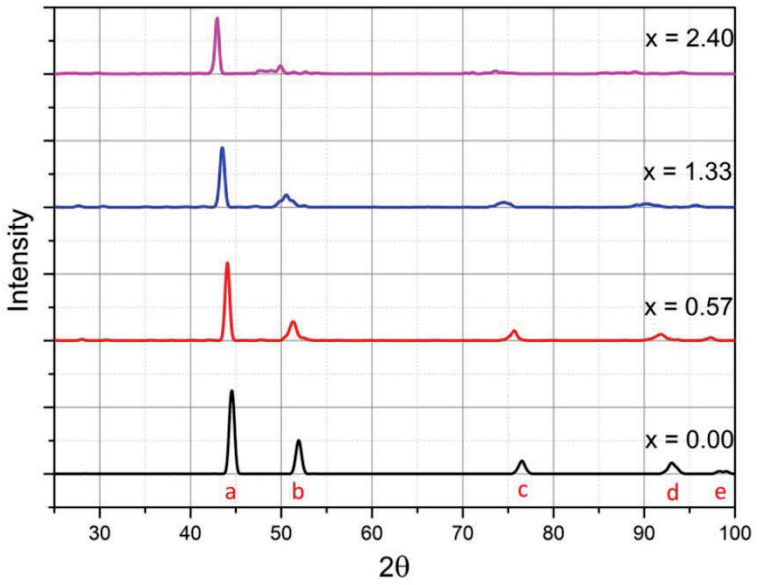

Figure 4.5. Simulated XRD patterns of FCC $Al_xCoCrFeNi$ with x = 0.00, 0.57, 1.33 and 2.40. The peaks are indexed as follows: (a) (111), (b) (200), (c) (220), (d) (311), and (e) (222).

Surprisingly, the disordered supercells that were initially given a BCC packing transformed into a wide variety of simple structures (through simple movements of the atomic positions away from the ideal BCC sites). At atomic ratios of 0 and 0.15 Al, more than 50 % of the disordered structures relaxed to an $R\bar{3}m$ symmetry (hexagonal). At x = 0.50 and x = 0.91, the disordered structures also relaxed to a range of structures: 40 % remained BCC with $Im\bar{3}m$ symmetry, 25 % relaxed to the $R\bar{3}m$ symmetry, and 10 % transformed to a FCC $Fm\bar{3}m$ symmetry, while the remainder transformed to lower symmetries of $Fmmm$ and $IA\bar{3}d$. At high Al concentrations, 70% of the structures relaxed to an $Fm\bar{3}m$ symmetry with the remainder adopting $R\bar{3}m$ and $Im\bar{3}m$. Furthermore, none of the alternative symmetries that arose from the initial BCC packing were found to have lower formation enthalpy than the FCC systems. It is clear that BCC packing is not energetically favoured when the atomic species are randomly placed on the lattice sites.

The effect of partially ordering the BCC packed structures by limiting Al to the centre site of the unit cells (as suggested by Wang *et al*. [57] in past work) was then considered. For the compositions with low Al concentrations of x = 0.15 and x = 0.50 at. frac., fewer alternative structures are formed, with only 30 % of the supercells found to transform to the $R\bar{3}m$ symmetry. For the three higher concentrations of Al all supercells maintained their BCC packing. This is a significant finding that suggests that atomic-scale ordering (or at least partial ordering Al) is a pivotal property required in the formation of the single-phase BCC $Al_xCoCrFeNi$ HEA. The simulated XRD patterns for the Al-ordered BCC systems with the three highest Al concentrations are shown in Figure 4.6.

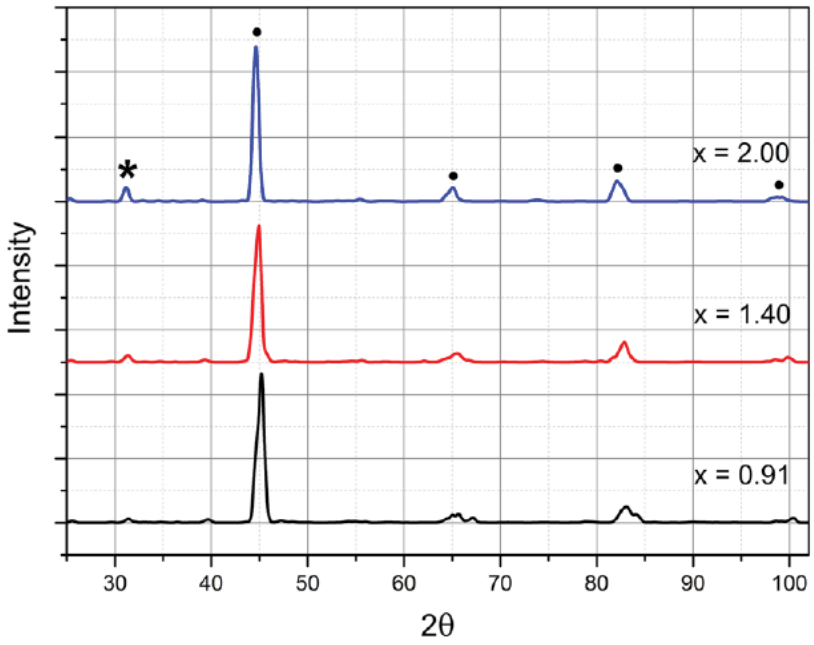

Figure 4.6. Simulated XRD patterns of BCC $Al_xCoCrFeNi$ with x = 0.91, 1.40, and 2.00. Peaks labelled with the ● symbol are the ideal BCC peaks [from low to high angle these are indexed as (110), (200), (211), and (200)], while the * indicates the (100) ordering peak.

The peaks that are characteristic to the BCC phase are labelled with the ● symbol and remain for all patterns. A peak at ~31°, labelled with the * symbol, increases in intensity with higher Al contents. Wang *et al*. [57] attribute this peak to the (100) plane and another peak ~55 ° to (111) which only arise with ordering. The (100) plane within the atomic model is, of course, ordered with Al atoms giving rise to a regular plane spacing of ~3 Å. When simultaneously restricting Al to the centre site and Ni to the corner site [Fig. 4.4(i)] the peak at ~55 ° is observed, see Figure 4.7.

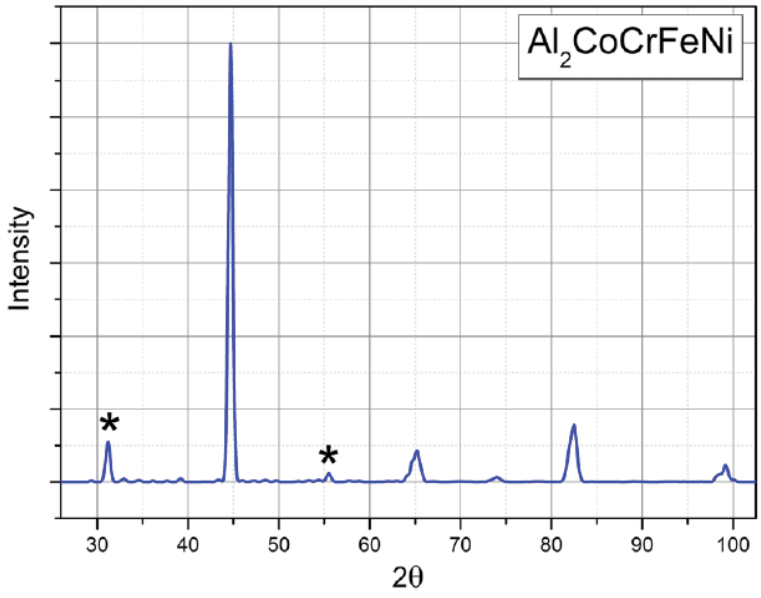

Figure 4.7. Simulated XRD pattern of BCC $Al_2CoCrFeNi$ with simultaneous ordering of Al and Ni on separate sublattices. The * symbols highlight the experimentally observed ordering peaks [57].

This XRD pattern is very similar between all compositions with only a shift in peak position when Al is varied. This shift corresponds to a change in lattice parameter of 0.02 Å between x = 0.9 and x = 2.0. Similar behaviour to the Al-ordered supercells was observed during optimisation: the systems with the higher Al retained their BCC packing while the two systems with the lower Al content changed to the hexagonal system in 30 % of the cases.

It seems that an ordering of Al is required for a BCC packing to be stable in the $Al_xCoCrFeNi$ system. Importantly, it is the enthalpy contributions that arise from the interaction between Al and the constituent elements in a partially ordered arrangement, rather than entropic contributions of disorder or atomic size effect previously postulated in prior literature [5], that lead to a BCC packing.

4.4 Phase Stability

In this section the energetics associated with the $Al_xCoCrFeNi$ series will be discussed. When x = 0, the formation enthalpy of the partially ordered $AuCu_3$ structure [Fig 4.4(iii)] is found to be the lowest by 0.03 eV/atom compared to the fully disordered FCC structure. This small difference can be overcome by the difference in contribution of the configurational entropy. Using Equation 4.2 the configurational entropy for the partially ordered structure is 2.37×10^{-5} $eV.atom^{-1}.K^{-1}$ which is 9.58×10^{-5} $eV.atom^{-1}.K^{-1}$ less than the fully disordered entropy. Therefore the disordered structure will be entropically stabilised at some temperature (~600 K), see Figure 4.8. Niu *et al*'s ordering of Cr at the FC-site shifts this transition temperature to 626 K due to the slightly more favourable enthalpy of formation. A previous study attempting to observe this long range ordering in the CoCrFeNi system was conducted by Lucas *et al*. [53] using XRD and neutron diffraction on samples that had been thermally aged at 753 K (where the fully disordered structure would be stable) for two weeks and returned a null result. This new finding may shed some light as to why they did not observe this phenomenon.

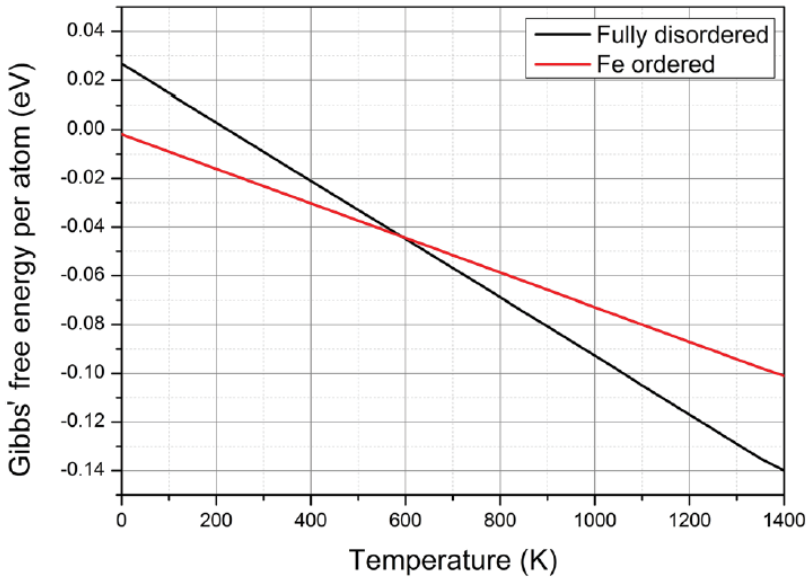

Figure 4.8. Calculated variation in Gibbs free energy of the disordered and partially ordered (Fe-ordered) CoCrFeNi systems with temperature.

With the addition of Al, a change of behaviour that corresponds extremely well with experimental findings is observed, see Figure 4.9. When $0.57 \leq x \leq 0.91$ the calculations predict that the preferred symmetry changes from FCC to an ordered BCC phase. This transition was experimentally observed to occur between $0.5 \leq x \leq 0.9$ by Wang *et al.* [57]. As the transition is not found to be very sharp (energetically), the formation of a dual phase (FCC and BCC) can be expected (and is experimentally observed). When considering configurational entropy, due to the discrepancy between the partially ordered and fully disordered structures the transition point is expected to shift to higher Al contents with increasing temperature. Since the configurational entropy is proportional to the Al concentration the shift in transition point is not strictly linear but can be approximated to the function $T = 3805x - 2183$ where T is the temperature and x is the Al content in at. frac., at which the transition is expected to occur.

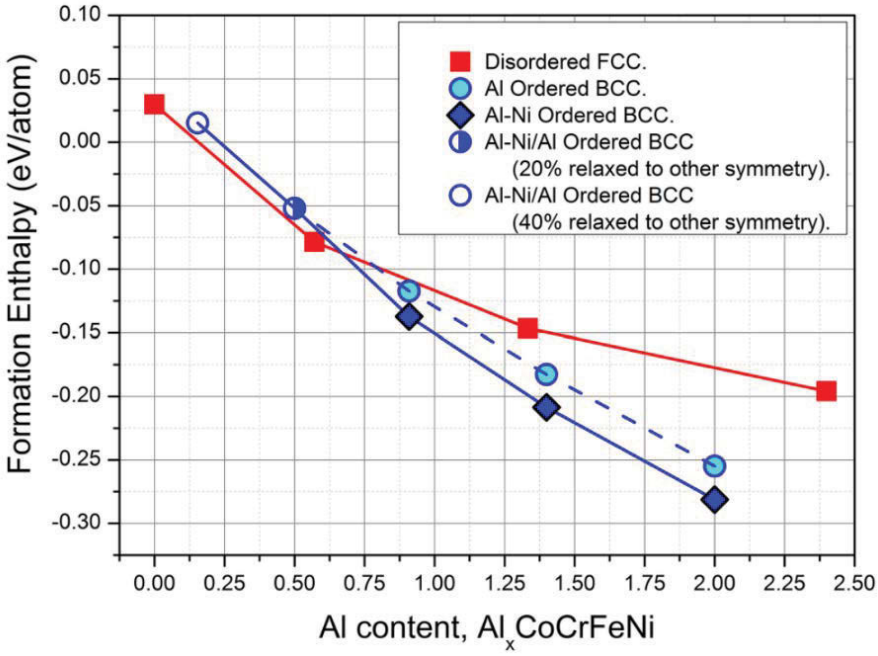

Figure 4.9. Variation in formation enthalpy of Al$_x$CoCrFeNi. Completely disordered face-centred cubic (red), Al-ordered body-centred cubic (light blue), and Ni-Al-ordered body centred cubic (blue) structures are plotted. The values for completely disordered body-centred cubic are not included as the simulation predicted this phase to be unstable at all Al contents.

The enthalpies of formation of the Al-ordered and the Al-Ni-ordered BCC phases were very similar at low Al concentrations (and combined in Figure 4.9). However, at higher Al contents there is a notable divergence in the relative stabilities (although both are more favourable than the FCC system). Although the Al-ordered system will have a larger configurational entropy than that of the Al *and* Ni ordered system, this contribution is insufficient to offset the effects of enthalpy across all temperatures to the melting point.

4.4.1 Phase segregation

Some experimental studies, mainly conducting thermal aging experiments, have found notable co-segregation of Ni and Al leaving a Cr-Fe-rich phase [206]. This was briefly investigated by considering

the following reaction from the single phase $Al_{1.4}CoCrFeNi$ composition to form a dual phase Al-Ni-rich and poor phase in similar stoichiometries to those reported by Wang *et al*. [57].

$$Al_{28}Co_{20}Cr_{20}Fe_{20}Ni_{20} \rightarrow Al_7Co_{14}Cr_{14}Fe_{14}Ni_5 + Al_{21}Co_6Cr_6Fe_6Ni_5 \quad (4.3)$$

These compositions are idealised compositions similar to the $Al_{1.5}$ alloy measured by Wang *et al*. [57]. The compositions do not vary more than 10 at. % compared to experiment; however, as a result of this discrepancy, care should be taken when directly comparing these theoretical results to experiment.

The Al atoms are once again limited to the body-centred site, while the Ni atoms are limited to the remaining site of the BCC unit cell. The energy released as a result of the partition is 0.01 eV per atom; when considering enthalpy alone, a dual phase is stable. From the data it is predicted that the configurational entropy of the single phase will overcome the enthalpy advantage of the dual phase, when x = 1.4, at 1250 K. Experimental observations by Wang *et al*. [57] show a dual phase when quenching from 1373 K; therefore our predictions, which do not consider other forms of entropy, should be treated with caution. Nevertheless, it is predicted that a transition from dual phase to single phase can be expected before the melting point at ~1650 K).

4.5 Summary

For the first time, the energetic drive for Cr segregation in the Co-Cr-Fe-Ni system was quantified using DFT. It was found that equi-molar Cr is not thermodynamically stable within the FCC HEA matrix and will preferentially segregate into Cr metal; however, the extent of the segregation is unclear. This mechanism could lead to the formation of a Cr_2O_3 oxide scale on the exterior of the alloy and that will help resist further oxidation (similar to stainless steels [207]). It could also lead to the formation of precipitates within the matrix itself. Further simulation and experiment is being conducted in future work. The migration of Cr is predicted to be a vacancy-mediated process which may be hindered due to magnetic effects originating from the opposing spin of Cr [205]. Another retarding effect could be the depletion of Cr from the HEA matrix, again further work is required. Migration energies of the other species were also explored and it was found that Cr had the lowest activation energy for migration followed by Co, Fe, and then Ni.

To address the notion of partial ordering within HEAs a new method for calculating the configurational entropy was developed. When comparing this method to a method developed concurrently by Niu *et al*. [35] it was found that there is a slight deviation between the two which is due to the improper normalisation in Niu's method.

The $Al_xCoCrFeNi$ system was then investigated for $0 \leq x \leq 2.40$. Disordered FCC and BCC packed structures as-well-as partially ordered $L1_2$ and B2 configurations were simulated and compared. Surprisingly, it was found that the disordered FCC phase was more stable than the disordered BCC phase for all values of x. The degree of unfavourability of the BCC phase such that the initial structures no longer maintained their $Im\bar{3}m$ symmetry, relaxing to a range of different structures. It seems that for a

BCC packed phase in the $Al_xCoCrFeNi$ system to be stable, it must adopt a partial ordering whereby Al-Al nearest neighbours are forbidden i.e. Al is restricted to the corner site of the BCC unit cell and the other atoms are disordered across the remaining site. When simulating the XRD patterns of these configurations, additional reflections can be observed at ~31° and 55° which have been experimentally observed in past studies on this system [57].

Two arrangements were examined when simulating the $L1_2$ ordering: (i) Fe was restricted to the face-centred site while the remaining elements were disordered and (ii) Cr was restricted to fully occupy the corner site while the remaining elements randomly occupied the face-centred sites. When Fe is ordered and configurational entropy is considered, it is predicted that this partially ordered phase is only stable from 0 K – 600 K at which point the fully disordered FCC phase will become stable. However, when Cr is ordered, this transition temperature is increased to 626 K.

For the addition of Al, this phenomenon was also investigated using the B2 type ordering restricting Al to the corner site of the BCC unit cell and Ni to the centre site. It was found that, at Al atomic fractions of 0 – 0.62, the fully disordered FCC phase will transition to the partially ordered B2 structure. When accounting for temperature (and therefore configurational entropy), the transition Al concentration will transition in a relatively linear trend.

Finally, the drive for phase segregation in the $Al_{1.4}CoCrFeNi$ HEA was investigated. It was found that the system does favour a dual phase microstructure with partial ordering from 0 K – 1250 K. However, due to the increased configurational entropy of the single phase disordered system, above this temperature the single phase will be stabilised. The experimental transition temperature is reported to be ~1373 K which warrants further investigation.

Thus far it is clear that Al-Co-Cr-Fe-Ni is a complex and perhaps unique system that utilises the strong energetic drive for NiAl ordering to change its morphology and crystal structure. Initially, with low Al contents, Al can be seen as a solute atom which can be added as a minor alloying addition to the Co-Cr-Fe-Ni FCC matrix. However, once Al has passed a certain threshold concentration, there is a phase segregation as the two competing structures (FCC and BCC) attempt to reach equilibrium. When Al is in sufficient concentration Co, Cr, Fe will act as solute atoms which are included in the B2 NiAl matrix to form a partially ordered HEA. This behaviour, combined with the low cost and abundance of each element, gives credence to its use as a structural alloy in the future.

5

PREDICTING THE FORMATION AND STABILITY OF SINGLE PHASE HIGH-ENTROPY ALLOYS

Results within this chapter have been published in the following publication:

King, DJM. *et al*. Acta Materialia **104** (2015) 172-179 [9]

5.1 Introduction

Within the previous chapters I have shown how DFT can be used to model HEA systems and benchmarked results from this computational technique to that of experimentation. However, there still remains a task – to design a HEA that could be potentially used in a nuclear application. This task requires careful consideration of the individual components of the alloy and the chemical interactions upon alloying. In a practical sense, to qualify as a nuclear relevant material the resultant alloy should display a low thermal neutron cross section ($\leq$ 2.6 barns), have the ductility of a BCC, FCC or HCP material, maintain its structural integrity during irradiation and at temperature ranges from 250 – 1300 ^{o}C, and resist corrosion, oxidation and the effects of displacive radiation damage. Two of these properties can be somewhat predicted using the rule of mixtures (thermal neutron cross section and melting temperature) but a big unknown (at least during the early stages of this project) is how to formulate a HEA that exhibits a single phase crystal structure. This is a large problem faced by the HEA community and many attempts have been made by developing predictive parameters, see Section 1.4. As previously mentioned, it was initially thought that single phase high entropy alloys (SPHEAs) would form as a result of a large configurational entropy alone. Later, the Ω parameter was introduced by Yang *et al*. [43], which includes an enthalpy term, yet cannot delineate multi-phase HEAs from SPHEAs. Nevertheless it is this method that continues to be used to this day. In this chapter, I introduce a new method inspired by Yang *et al*., but as a more inclusive representation. This method was originally developed to search through the Periodic Table to find combinations of elements for a new HEA that would be relevant to the nuclear industry. Indeed it can be used for this purpose, but now it seems that it can be applied to HEAs as a whole and serves as the next step in HEA phase prediction. I will begin by critically assessing the previous methods formulated by Yang *et al*. and testing their method against 185 previously experimentally studied alloys (see appendix). These alloys are separated into three categories:

1. Solid solutions: Systems that display reflections, in diffraction data, analogous to BCC, FCC or HCP and are devoid of intermetallics. These are single-phase materials although they might display some chemical segregation due to coring during dendritic solidification.
2. Intermetallic/multiphase: Systems that display reflections, in diffraction data, of an intermetallic compound or of a second solid solution or element.
3. Exceptions: Systems that display reflections, in diffraction data, analogous to BCC, FCC or HCP and are devoid of intermetallic phases but are predicted by the current method to form an intermetallic/multiphase structure.

I will then introduce the new method, again, testing against these 185 systems as well as comparing the level of theory to DFT and experimental results. I will then explore the CoCrFeNi system as a specific case study before finally making novel predictions.

5.2 Previous methods

To understand the current methods used to predict HEA formation, it is useful to follow the development of theoretical understanding of HEAs. Much of this information can be found in Section 1.4 so only a brief synopsis is presented here.

It was first assumed that it was only necessary to have five or more elements in near equimolar concentrations for the configurational entropy to be sufficient enough to stabilise the solid solution phase in an HEA [5]. It was quickly found that this is not the case and the enthalpy of mixing must also be considered. However, calculating the enthalpy of mixing of a highly concentrated solid solution with many components is not a trivial task. Miedema's semi-empirical macroscopic atom model (see Section 2.4) was already being used for highly concentrated *amorphous* solid solutions through a weighted sum of the enthalpies of mixing between the binary liquid alloys that make up the amorphous solid [151]. This concept was then applied to HEAs, however, instead of adapting Miedema's model to calculate the enthalpy of mixing for the intermetallics and crystalline solid solutions; the methodology remained directed to the amorphous situation. When comparing the results obtained for intermetallics and crystalline solid solutions and to that of the amorphous phases (Eqn. 2.16, 2.19 and 2.24, respectively), across the 185 previously studied alloys, an error as large as 67 kJ/mol was found. It seems that Miedema's approach to calculate anything other than the amorphous phase was forgotten. It was therefore assumed that this calculation was indicative of the chemical similarity between the constituent elements i.e. When ΔH is ~0 the species are chemically similar. This concept was formulated into the Ω parameter (Eq. 1.14) which is a ratio between $T\Delta S$ and ΔH. The original results obtained using this parameter can be seen in Figure 1.2. This method was again used for the 185 alloy systems, see Figure 5.1. Again no delineation between the alloys that formed a single phase solid solution to those that formed a multiphase/intermetallic structure could be made. However, all alloys that form a single phase solid solution are contained within the rectangle made by $\Omega \geq 1.1$ and $\delta \leq 6.6$ (Eqn. 1.15). This suggested that the full picture was still not yet realised.

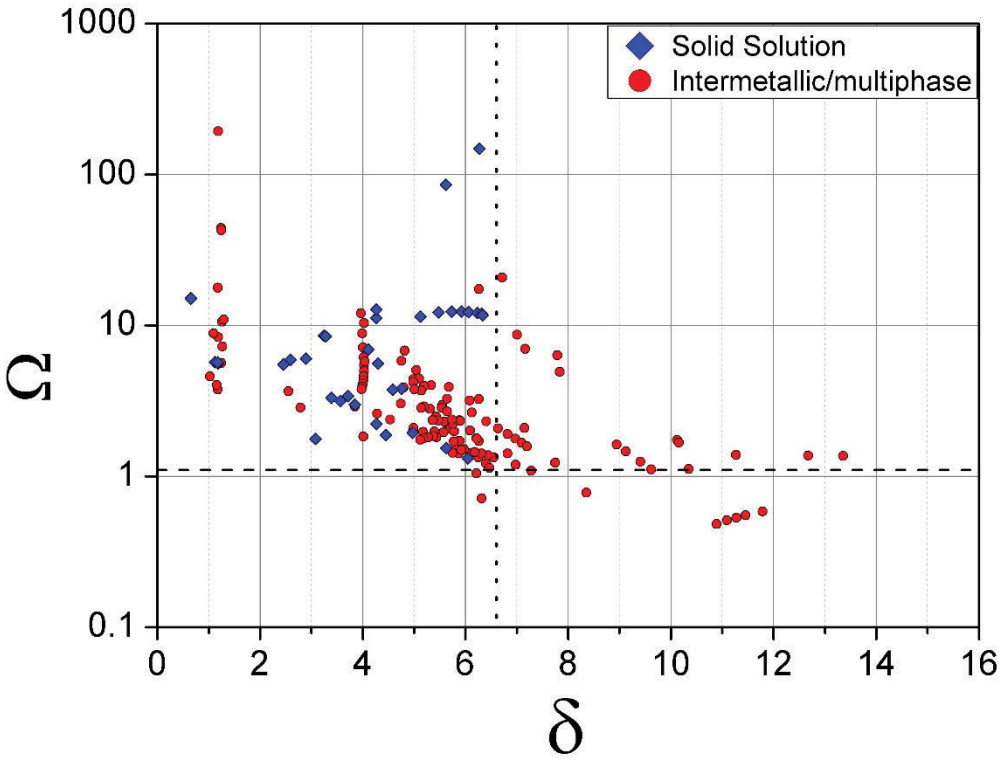

Figure 5.1. A comparison of 185 systems, experimentally determined to create a solid solution (blue diamond) or intermetallic/multiphase (red circle) structure, plotted for Yang *et al*'s predictive parameters whereby $\Omega \geq 1.1$ and $\delta \leq 6.6$ predict the formation of a SPHEA.

There have been various other methodologies that have been developed in an attempt to predict the formation of HEAs [47, 48] but none have gained as much traction as the Ω parameter. One example is a purely geometrical parameter developed by Singh *et al*. which combines ΔS_{conf} and δ [47]:

$$\Lambda = \frac{\Delta S_{conf}}{\delta^2} \tag{5.1}$$

In this case HEA formation has been predicted when $\Lambda \geq 0.96$. A second parameter (also of geometric nature),

$$\gamma = \frac{\omega_S}{\omega_L}, \tag{5.2}$$

was introduced recently by Wang *et al.* [48] where,

$$\omega_S = 1 - \sqrt{\frac{(r_S + \bar{r}) - \bar{r}^2}{(r_S + \bar{r})^2}} \ , \tag{5.3}$$

$$\omega_L = 1 - \sqrt{\frac{(r_L + \bar{r}) - \bar{r}^2}{(r_L + \bar{r})^2}}, \tag{5.4}$$

and the labels *S* and *L* denote the smallest and largest atomic radius contributions, respectively. It is postulated that a value of $\gamma < 1.175$ predicts HEA formation. These methods are highly reliant on the values used for atomic radius. There are several measures of this, but here it is the so-called 'metallic radius' that is required. Even this can take on different values depending on the coordination number of the structure, which is often corrected to a nominal radius for a twelve-coordinated atom, the so-called Goldschmidt radius.

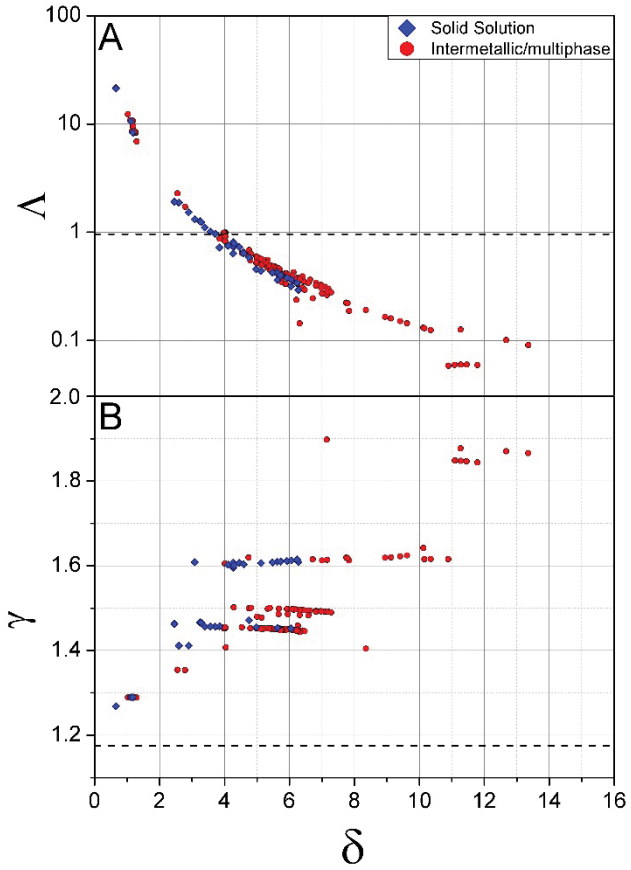

Figure 5.2. A comparison of 185 systems experimentally determined to create a disordered (blue diamond) or ordered (red circle) plotted for: A. Singh *et al.*'s predictive parameter whereby $\Lambda \geq 0.96$ predict the formation of a HEA and B. Wang *et al.*'s predictive parameter whereby a value of $\gamma < 1.175$ predicts HEA formation.

I believe it is counterproductive to discount thermodynamic effects related to the alloying of different species because the enthalpy pertaining to the formation of different phases will have a large influence on the outcome. A more accurate prediction of phase formation can be gained by including more information about the competing phases within the system. This is largely reflected by the success of the CALPHAD method which performs calculations of the Gibbs free energy of every known phase of the species in question and determines the lowest energy phase. Unfortunately, not every materials researcher has access or knows how to operate CALPHAD. Furthermore, CALPHAD requires experimental and

theoretical data to perform its calculations and is computationally intensive. So the new method that I propose is a compromise between the Ω value and CALPHAD.

5.3 The Φ value

In simple terms, two values are compared to assess the suppression of an ordered phase through the formation of a random solid solution:

1. ΔG_{ss}, the change in Gibbs free energy for the formation of a fully disordered solid solution from a mixture of its individual elements.
2. ΔG_{max}, the lowest (intermetallic) or highest (segregated) possible change in Gibbs free energy obtainable from the formation of binary systems from the constituents of the mixture.

The values for the Gibbs free energy (Eq. 1.1) are calculated using the enthalpy of mixing of the solid solution. ΔH_{ss}, and intermetallic, ΔH_{int}, are calculated using Equations (2.18) and (2.15), respectively. The temperature is taken as the melting temperature from the rule of mixtures and ΔS_{conf} from Eqn. (1.10). The contributions of other sources of entropy to ΔS are assumed to be very similar and therefore cancel between ΔG_{ss} and ΔG_{max}. Since ΔS_{conf} is zero for ordered intermetallics, it is assumed that $\Delta G_{int} = \Delta H_{int}$.

The binary system that yields the largest magnitude of ΔG_{max} is determined by ranking the magnitude of ΔG_{int} of all the possible binaries obtainable by the system. This value is then scaled to maintain stoichiometry of the system.

These values are combined to form a new parameter:

$$\Phi = \frac{\Delta G_{ss}}{-\left|\Delta G_{\max}\right|} \tag{5.5}$$

Where a value of $\Phi \geq 1$ would suggest a stable solid solution at the system's melting temperature and negative values of Φ would suggest the solid solution has positive formation enthalpy and will not form.

5.3.1 Assessing the accuracy

Since the Φ value relies heavily on Miedema's empirical approach, an assessment of the method compared to that of experimental and quantum mechanical enthalpies should be made. Although the quantum mechanical basis for Miedema's model is tenuous at best [208], past studies have shown that the values obtained show a very similar trend when compared to experiment [209] and *ab initio* techniques [210]. As mentioned, Pt-Al and Mo-Nb-Ti-$V_{0.25}$ systems were selected to make further comparisons. Pt-Al was chosen as it presents a large range of intermetallic compounds all of which having a wealth of experimental and theoretical data. Mo-Nb-Ti-$V_{0.25}$ was chosen as it represents a system that is devoid of intermetallic compounds, save for a metastable $NbTi_4$ phase [211].

The formation enthalpies of ten binary intermetallic compounds within the Pt-Al system were calculated using Miedema's model and DFT, see Figure 5.3. There is a clear underestimation of the magnitude when

compared to the convex hull, with a difference as large as ~20 kJ/mol for Al contents of 50 at. %. This effect is also seen in the comparison of the formation enthalpy of the solid solution for Mo-Nb-Ti-$V_{0.25}$, see Figure 5.4. Importantly, however, the trends between the datasets remain the same. Although the magnitudes of values are not accurate, the relative values are very similar and therefore can be compared within the same model.

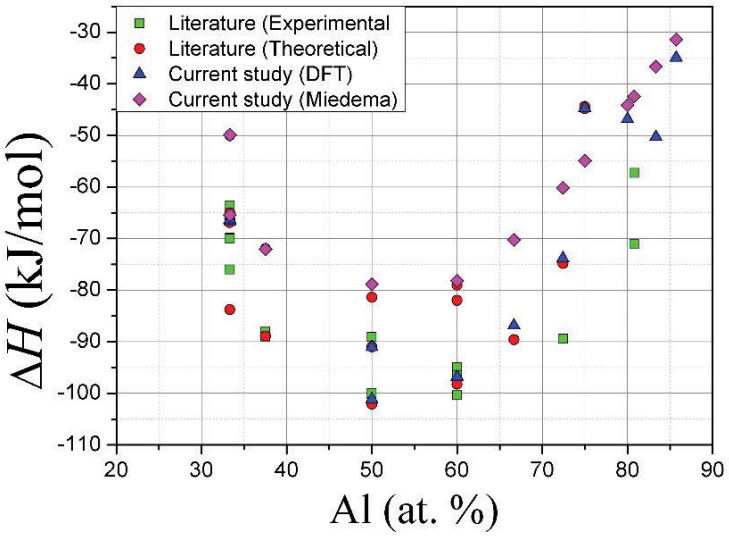

Figure 5.3. Formation enthalpies obtained for various compounds of the Pt-Al system, using: Literature values [212] obtained experimentally (green square) and theoretically (red circle) compared to values obtained from calculations in the current study using DFT (blue triangle) and Miedema's model (magenta diamond).

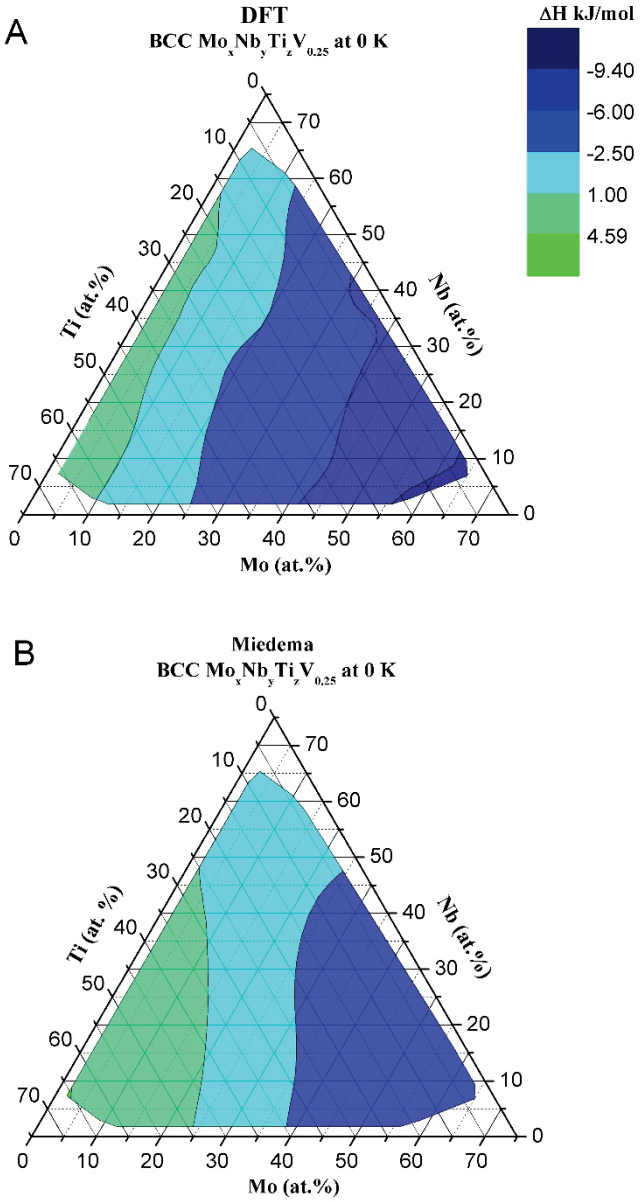

Figure 5.4. Formation enthalpies for the formation of a BCC solid solution in the Mo-Nb-Ti-V0.25 system comparing values obtained from A. DFT calculations to B. Miedema's model. The colours ranging from green → blue denote the formation enthalpies from 4.59 → -9.40 kJ/mol.

Next, I apply this methodology to known SPHEAs by exploring three different systems: An alloy that, (i) forms a single phase solid solution – CoCrFeNi [56], (ii) has a segregation of 1 element – CoCrCuFeNi [213, 214], and (iii) forms an intermetallic compound – AlCoCrFeNi [65, 215].

5.3.2 Benchmarking to experimental literature

i) Single phase solid solution - CoCrFeNi:

$Co + Cr + Fe + Ni \rightarrow (CoCrFeNi)_{ss}$

$\Delta G_{ss} = -23.43$ kJ/mol (from Eq. (1.1))

$Cr + Ni \rightarrow CrNi$

$\Delta G_{int} = -10.08$ kJ/mol (from Eq. (2.15))

Since ΔG_{int} of CrNi is of the largest magnitude of the possible intermetallics, this value is extended to include all four elements. This implies the formation of CoFe is also of the same magnitude and that the ordered result is of the largest possible magnitude (overestimating the drive for precipitation).

i.e. $Co + Cr + Fe + Ni \rightarrow CrNi + CoFe$

$\Delta G_{max} = -20.16$ kJ/mol

Following, $\Phi = 1.16$ (Eq. (5.5)), predicting a single phase solid solution is thermodynamically stable at the system's melting temperature.

ii) Segregated - CoCrCuFeNi:

$Co + Cr + Cu + Fe + Ni \rightarrow (CoCrCuFeNi)_{ss}$

$\Delta G_{ss} = -21.08$ kJ/mol

$Cu + Fe \rightarrow CuFe$

$\Delta G_{int} = +19.14$ kJ/mol

$Co + Cr + Cu + Fe + Ni \rightarrow CuFe + MM + M$

$\Delta G_{max} = +38.28$ kJ/mol

where, *M* is used to denote an arbitrary allocation of the remaining elements.

In this case, even though the multiphase assessment is less favourable than the single phase, $\Phi = 0.55$ indicates that a single phase solid solution is not thermodynamically stable. This is because the ΔG_{max} of the binary compounds are sufficiently endothermic and are past the threshold in which they will properly mix within a single phase solid solution

iii) Intermetallic - AlCoCrFeNi:

$Al + Co + Cr + Fe + Ni \rightarrow (AlCoCrFeNi)_{ss}$

$\Delta G_{ss} = -33.89$ kJ/mol

$Al + Ni \rightarrow AlNi$

$\Delta G_{int} = -47.33$ kJ/mol

$Al + Co + Cr + Fe + Ni \rightarrow AlNi + MM + M$

$$\Delta G_{max} = -94.66 \text{ kJ/mol}$$

Equating to, $\Phi = 0.36$, also predicting a single phase solid solution is not stable.

Figure 5.5 shows a clear distinction between the HEAs reported to display a disordered solution (blue) to those that were reported to display intermetallic/multiphase phases (red), at $\Phi = 1$ (dashed line), with the exception of 16 systems (green) that were reported to be single phase solid solutions.

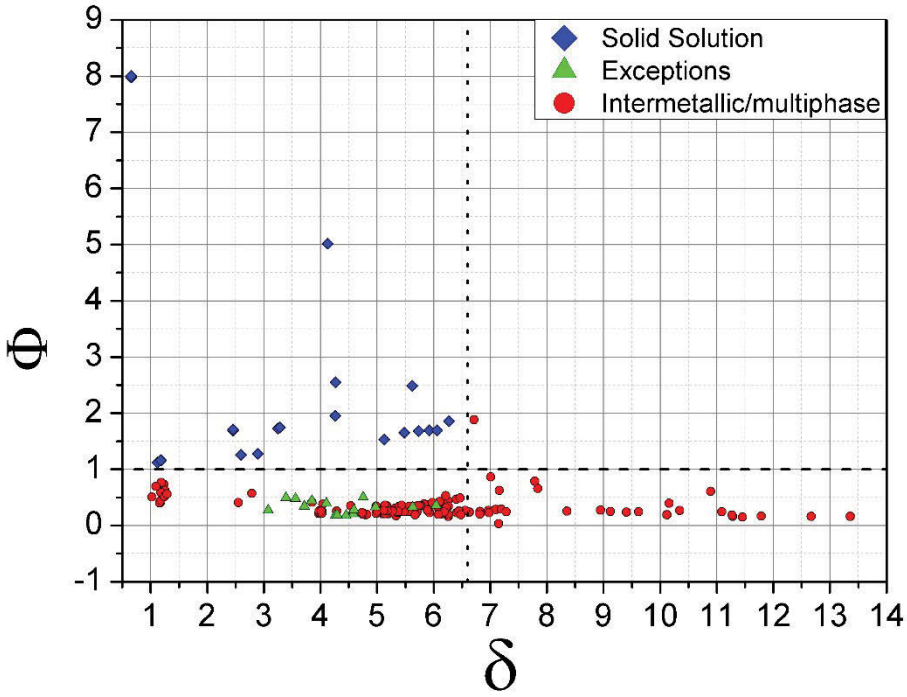

Figure 5.5. A comparison of 185 systems experimentally determined to create a solid solution (blue diamond), intermetallic/multiphase (red circle) structure and those that are an exception (green triangle) to the $\Phi \geq 1$ criteria (dashed line) plotted against a geometrical parameter δ.

The δ value (Eq. (1.15)) from the Hume-Rothery rules is again employed as previous results by Yang *et al*. [43] suggest that no SPHEA exists for $\delta \geq 6.6$. Interestingly, the $NbTiV_2Zr$ alloy is the only system that has both $\Phi > 1$ and $\delta > 6.6$. Senkov *et al*. [76] reported a tri-phase BCC microstructure with segregation between V and Zr into phases with the compositions $Nb_{0.2}Ti_{0.2}V_{0.1}Zr_{0.5}$, $Nb_{0.2}Ti_{0.2}V_{0.5}Zr_{0.1}$ and $Nb_{0.2}Ti_{0.2}V_{0.4}Zr_{0.1}$. A thermodynamic analysis reveals the V_2Zr C15 Laves phase is the most likely candidate for compound formation which, itself, has a positive formation enthalpy [172]. Therefore, it is plausible that a multiphase microstructure is preferred. This aligns with the findings of Senkov *et al*., where homogenisation of this alloy does not occur after annealing [76].

Figure 5.6 highlights the relationship between the enthalpy of mixing of the intermetallic with the largest magnitude, ΔH_{max}, and alloy prediction. For $\Delta H_{max} < 0$ kJ/mol, if a binary intermetallic compound is stable enough ($\leq$ 17.5 kJ/mol), the complete solid solution is destabilised. When $\Delta H_{max} > 0$ kJ/mol a similar effect is observed. However, a positive Gibbs free energy denotes an unstable reaction for the formation of the binary intermetallic. Therefore, the physical premise of this observed relationship is that

the chemical interaction between the two elements in the hypothetical binary system is sufficiently unfavourable, so that within the solid solution, this interaction will also act to cause instability and subsequently segregation.

Due to the conservative nature of this method, it is possible that some SPHEAs exist for $\Phi < 1$. The inclusion of enthalpies of formation of the less favourable intermetallics, ternary intermetallics, minor alloying/segregation and multiple solid solutions will act to lower the magnitude of the ΔG_{max} value. However, to include these factors does not allow for a quick and simple calculation to be implemented into a single parameter. I therefore proceed with the current method as a first approximation for SPHEA formation.

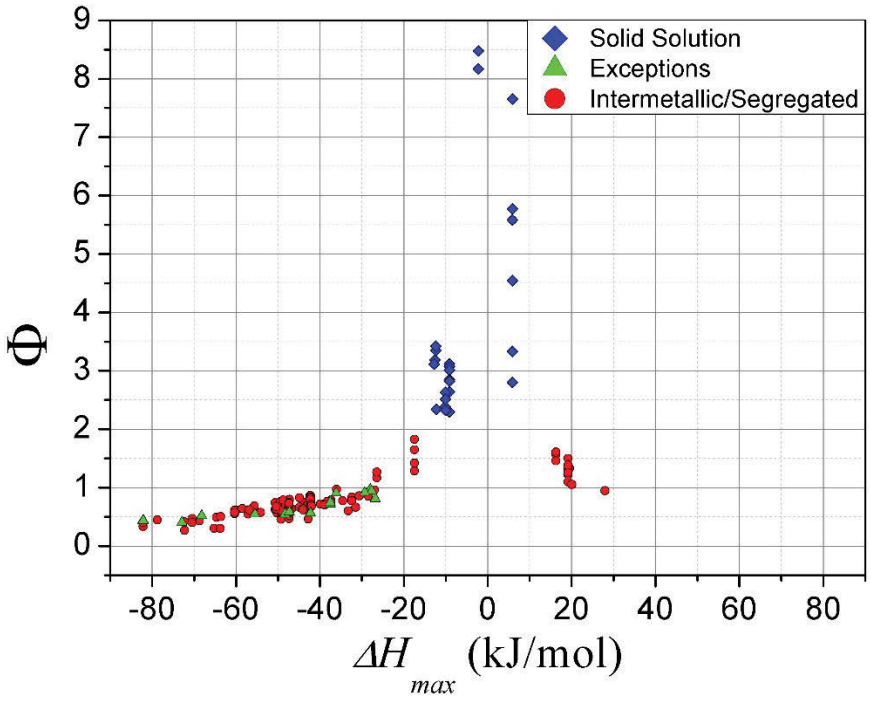

Figure 5.6. A comparison of 185 systems experimentally determined to create a solid solution (blue diamond), intermetallic/multiphase (red circle) and those that are an exception to the $\Phi \geq 1$ criteria (green triangle) plotted against the largest binary enthalpy contribution, ΔH_{max}.

5.4 Predicting precipitation temperatures

It is possible to estimate the temperature at which the solid solution will destabilise by calculating the temperature at which the alloy is predicted to have a value of $\Phi = 1$ (instead of calculating Φ at the alloy's predicted melting temperature). These results were found to be in agreement with past experimental results, especially for systems with higher transition temperatures. For example, this method predicts that NbTaTiHfZr, NbHfTiZr and MoNbTaVW are stable above 1162 K, 1359 K and 1580 K, respectively; this aligns well with the results by Senkov *et al.* [83], Wu *et al.* [216] and Zou *et al* [217] who studied the homogenisation and structural stability during annealing of these alloys at 1473 K, 1573 K and 2073 K, respectively. However, difficulties in accurately identifying the temperature in which precipitates occur at low temperatures arise due to kinetic effects. This is highlighted in a study by Tsai *et al.* [51] on the

CoCrFeMnNi system whereby high activation energies for diffusion within the alloy were measured and which evidently retard the development of the equilibrium structures.

5.5 Exploring the Co-Cr-Fe-Ni system

The Co-Cr-Fe-Ni system is now explored in detail. All stoichiometries with a step-size of 1 at. % are computed and shown in Figure 5.7. By considering all of the potential stoichiometries, it is predicted that the $Co_{0.43}Cr_{0.01}Fe_{0.07}Ni_{0.49}$ composition, which has a value of $\Phi = 8.93$, will be the most stable stoichiometry. This prediction arises as Cr-Fe forms a strong σ phase intermetallic in their binary phase diagram [218] but complete segregation of these species will lead to a less favourable Gibbs free energy of the solid solution phase. The balance of this interplay results in a Co- and Ni-rich alloy. The equimolar alloy is comparatively less compositionally stable with a value of $\Phi = 1.16$. To benchmark these results, the segregation of Co, Cr, Fe, and Ni, from the equimolar system is tracked by the magenta, black, blue and red lines, respectively. This method predicts that this system favours the segregation of Cr from the equimolar system as the temperature is reduced and the segregation of all other species has a relatively negligible effect. This is evident as Φ increases as Cr content is decreased, a behaviour supported by both experimental [195] and computational work [190]. This model also predicts that the removal of Ni will also contribute to a slightly higher stability compared to the equimolar alloy, but less Cr is required to segregate to achieve a higher stability. The precipitation temperature of Cr is estimated to be 1156 K when Cr is at 11.8 at. %. Due to kinetic hindrance at lower temperatures, prolonged annealing times [219] may be required to observe further Cr segregation.

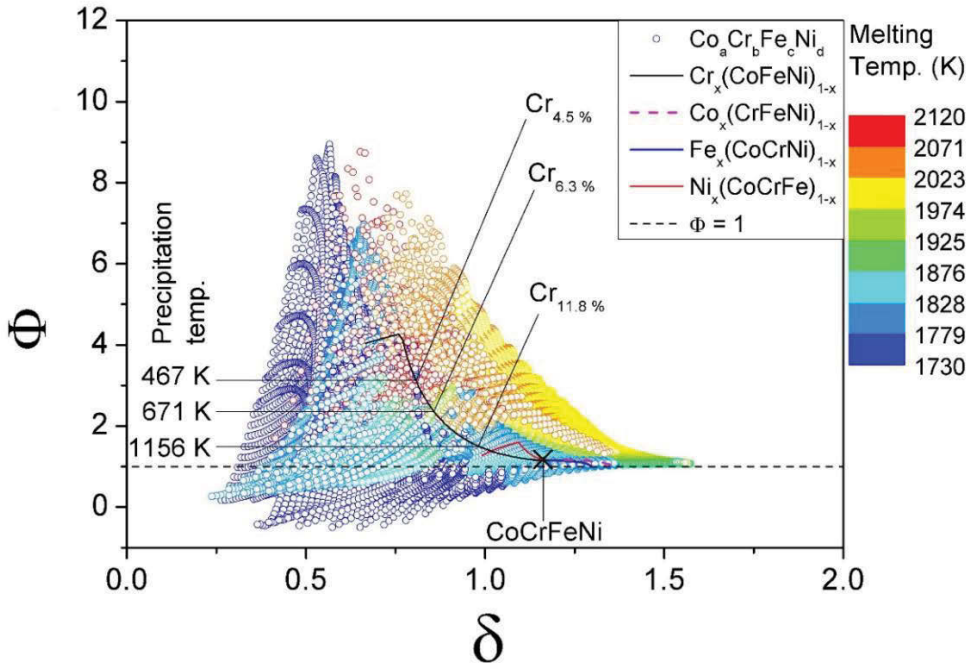

Figure 5.7. All possible compositions in the $Co_aCr_bFe_cNi_d$ system (open coloured circles). Melting temperatures of 1730 → 2120 K are represented as colours from blue → red. The equimolar CoCrFeNi system (cross) and the segregation of each element Cr (black solid), Co (red solid), Fe (black dashed) and Ni (orange solid) lines are overlayed. The precipitations temperatures at three Cr contents are displayed and $\Phi = 1$ cut-off is denoted by the grey dashed line.

5.6 Exceptions to the model

Of the 185 alloys used to benchmark this new method, 16 exceptions were found. All of these exceptions include Al and also display H_{max} values of the same magnitude as the intermetallic/multiphase systems screened (Figure 5.6). It has been reported that HEAs with Al can exist in the form of partially ordered BCC alloys, the nature of which might not be evident through standard experimental analysis [109, 220]. I now use DFT to investigate this drive for ordering, on the atomic scale, for one of the exceptions (AlCoFeNi), using the average of twenty pseudo-randomly generated configurations.

For a fully disordered AlCoFeNi BCC HEA:

ΔH_{dis} = -22.79 kJ/mol

In contrast, partial ordering in which Al and Ni are restricted to the centre and corner site of the BCC lattice, respectively, and Co and Fe are allowed to occupy either, has a significantly more negative enthalpy of mixing:

ΔH_{ord} = -28.85 kJ/mol

The configurational entropy of the partially ordered system was calculated using a method previously reported [109]. The partially ordered configurational entropy was calculated to be 2.88 J/K/mol less than that of the fully disordered system. Figure 5.8 shows the Gibbs free energy as a function of temperature for these two configurations, accounting for the difference in ΔS_{conf}, with a comparison to a dual phase AlNi + CoFe intermetallic formation.

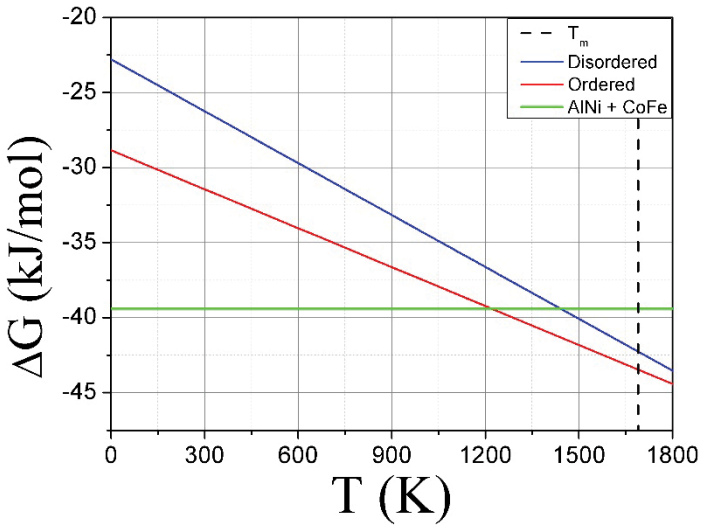

Figure 5.8. Gibbs free energy as a function of temperature for competing phases: Disordered solid solution of AlCoFeNi (blue), partially ordered solid solution of AlCoFeNi (red), and AlNi and CoFe B2 intermetallic compounds (green). The predicted melting temperature is denoted by the black dashed line.

Here it is clear that the AlCoFeNi system favours a partially ordered crystal structure compared to the fully disordered alternative. Under the assumption that this system does not favour a different ordering, it

is predicted that the partially ordered system with BCC packing will be adopted under equilibrium conditions at temperatures ≥1220 K. These findings may provide some insight into the high hardness and yield strength reported by Zuo *et al*. [221] for this material. It is possible that this relationship exists in the other 15 Al-containing exceptions as well. However, it should be noted that in this specific example I consider the enthalpy of mixing of CoFe (-13.93 kJ/mol) which is substantially more positive than AlNi. Certainly when scaling the magnitude of CoFe to that of AlNi (as is done in the current Φ evaluation) the notion of partial ordering is irrelevant and a prediction of intermetallic/multi-phase is made. Furthermore, when considering alloys such as $Al_{0.4}Hf_{0.6}NbTaTiZr$, which are found to maintain a single phase microstructure after annealing [77], and do not have any intuitive B2 type ordering, it is likely that for these systems, the current method is too conservative and may omit them from the solid solution category. It is also possible that nanoscale precipitates were overlooked within the experiments themselves. In the $Al_{0.3}CoCrFeNi$ HEA, for example, Shun *et al*. [80] observed homogeneous nanoscale precipitates [49] in the as-cast condition using TEM. After aging at 1173 K for 72 hours, a B2 ordering was reported which is in excellent agreement with the DFT predictions of this similar system.

5.7 Predicting new high-entropy alloy systems

Having established that the Φ value gives a good first approximation to SPHEA stability and formation, the next step is to search through all permutations of a mixture of 73 elements from the periodic table, looking for alloys that satisfy $\Phi \geq 1$ and $\delta \leq 6.6$. Table 5.1 lists the top 50 four element systems sorted by estimated price. The resultant structures can then be ranked for properties that scale with the rule-of-mixtures such as bulk modulus, thermal neutron cross-section, melting temperature etc. A total of 186,299,362 equimolar systems were screened (1,088,431 4 element, 15,020,335 5 element, and 170,230,452 6 element systems), 1970 potential SPHEAs were identified (636 4 element, 983 5 element, and 306 6 element) using Miedema's model.

The capability was integrated into a web-interface (by Andrew G. McGregor) and may be freely accessed at www.alloyASAP.com.

Table 5.1. 50 predicted equimolar 4 element alloys sorted by price with values (March 2015) of Φ, δ, melting temperature (T_m) and maximum melting temperature of their elemental constituents (T_{max}).

System	**Price (USD/kg) [222]**	Φ	δ	T_m (K)	T_{max} (K)
CoFeMnMo	780	1.30	4.39	2000	2896
CoCrFeMn	1040	1.38	0.88	1810	2130
CrFeMnMo	1450	1.26	4.03	2090	2896
CoCrMnMo	1580	1.38	4.20	2080	2896
CoCrFeMo	1580	1.39	4.32	2150	2896

FeMnMoV	2230	1.07	4.04	2100	2896
CoFeMnNi	2260	1.01	0.89	1710	1808
CrFeMnV	2480	1.08	2.42	1900	2163
CrMnMoNb	2710	1.18	5.86	2320	2896
CrMnMoV	3020	1.64	3.67	2180	2896
CrFeMoV	3030	1.13	3.88	2250	2896
CoCrMnNi	3060	1.07	1.25	1790	2130
CoCrFeNi	3070	1.16	1.18	1860	2130
HfMoNbZr	3420	1.53	5.87	2570	2896
CuMnNbV	3430	1.48	5.65	1940	2742
CrMnMoNi	3470	1.03	4.39	2070	2896
CrFeMoNi	3470	1.06	4.49	2140	2896
MnMoNbV	3490	1.66	5.09	2330	2896
CdCuNbV	3520	1.12	6.57	1710	2742
CrMnMoTa	3550	1.32	5.86	2460	3293
CdMnNbTa	3570	1.55	6.44	2040	3293
CoCrMoNi	3600	1.10	4.62	2130	2896
CuHgNbV	3730	1.07	6.57	1620	2742
CrNbVZn	3740	1.00	4.83	1930	2742
CrMnNbV	3740	1.20	5.65	2140	2742
HgMnNbTa	3770	1.99	6.44	1950	3293
MnMoNbTa	4020	1.86	5.56	2610	3293
CdCuNbTa	4050	2.70	6.13	2000	3293

CrMnMoTi	4160	1.03	6.11	2120	2896
CuHgNbTa	4260	2.59	6.13	1910	3293
HfMoTaZr	4270	1.62	5.87	2710	3293
CuMnTaV	4270	1.55	5.65	2080	3293
CrMoNbV	4290	1.39	4.83	2480	2896
MnMoTaV	4330	1.95	5.09	2470	3293
CdCuTaV	4360	1.22	6.57	1850	3293
HfMoNbV	4400	1.65	6.50	2580	2896
CuHgTaV	4570	1.17	6.57	1760	3293
CrMnTaV	4590	1.34	5.65	2280	3293
MoNbTaZr	4620	1.75	5.16	2760	3293
MnMoNbTi	4630	1.19	5.71	2280	2896
CrMoNbTa	4820	1.54	5.27	2770	3293
HfMoTiZr	4870	1.44	5.77	2370	2896
HfMoNbTa	4930	1.95	4.90	2860	3293
MnMoTiV	4940	1.13	5.33	2130	2896
HfNbTaZr	4990	2.23	4.43	2670	3293
NbTaVZn	5050	1.00	4.29	2220	3293
MnNbTaV	5050	2.42	5.88	2430	3293
CrMoTaV	5130	1.54	4.83	2620	3293
CdNbTaV	5140	3.48	4.34	2200	3293
CrMnTiV	5200	1.07	5.95	1940	2163

5.8 Summary

A new method for predicting formation of SPHEAs has been developed, using Miedema's model as a basis. Although the absolute values provided by the Miedema methodology are not rigorously accurate, the trend in alloy systems is essentially the same as that predicted by DFT calculations and experiment. The benefit of using the Miedema methodology, described in the chapter, is the ability to work through very large numbers of alloy compositions, far more permutations – by orders of magnitude – than would be feasible using DFT.

A new parameter, Φ, the ratio between the Gibbs free energy of a completely disordered solid solution to that of the most likely intermetallic or segregated binary system, is defined. This method takes into account both the intermetallic and solid solution enthalpy of mixing in a regular solution model and is validated by applying it to 185 experimentally verified systems from the literature. It is determined that the formation of HEA random solid solutions is favoured when $\Phi > 1$. Of these benchmarked systems, 16 exceptions were found. These were systems reported in the literature as SPHEAs but not identified as such by the current methodology. DFT calculations suggest that partial atomic ordering may occur in these discrepancies. While the onset of partial atomic ordering would stabilise the structures more than a model based on a random solid solution would predict, it is unreasonable to conclude that this is the case for all of the exceptions. In certain systems, the current approach may be too stringent in the calculation of the ordered/multiphase enthalpies of mixing. If more possible phases are calculated there would be a balancing effect to the enthalpy term in which a favourable SPHEA would be predicted. This would explain the omission of Al from any equimolar SPHEA prediction.

Nevertheless, the new stability parameter can also be used to predict the temperature at which the single phase solid solution will begin to form precipitates. This type of calculation can be used to predict whether compositions will precipitation harden or decompose at a certain temperature. Conversely, one can use this method to design an alloy that is not expected to have ageing effects below a given operation temperature. These effects, combined with the scalable material properties are combined in the ASAP code to provide a method to aid alloy design and discovery, optimising for specific material properties.

6

RADIATION DAMAGE IN Nb-Ti-V-Zr AND Mo-Nb-Ti-V HIGH-ENTROPY ALLOYS

6.1. Introduction

Since the concept of HEAs became a popular topic within the materials community; their ability to perform as part of a nuclear power system has been speculated. The earliest relevant publication on this topic was in 2014 by Egami *et al*. [223] where the $Nb_{33}Hf_{46}Zr_{21}$ single phase BCC ternary alloy was subjected to >50 dpa by electron beam damage at 103 K. It was observed that the material would only segregate into a multiphase microstructure once irradiated past this dose. It was suggested that unlike conventional materials, HEAs may be extremely radiation resistant due to high levels of disorder, allowing radiation damage to heal more rapidly. The first investigation of the effects of radiation damage on a HEA was done by the same group [224] on the CoCrCuFeNi HEA using electron irradiation. Although it is reported that the FCC phase shows high phase stability against irradiation (as it remains as the main constituent phase over 40 dpa at room temperature and 773 K) many intermetallic phases were also observed to precipitate after irradiation and annealing. Precipitation after annealing is unsurprising given the instability and tendency to order in this specific system (see Chapter 4). Very recently, a publication aimed at assessing the radiation behaviour of HEAs for advanced reactors was published by Liaw *et al*. [225]. The experimental sections are primarily focused on the Al-Co-Cr-Cu-Fe-Ni system and its variants leaving some speculation as to the behaviour of more exotic compositions. Characteristics such as swelling, phase segregation and amorphisation were observed using ion irradiation up to 64 dpa.

In the present project it is hypothesised that, due to the near equimolar concentrations and random occupation of the locations of the elements on each lattice site, a substitutional defect will be equivalent (and therefore not a defect at all) and vacancy re-combination will also be facilitated, therefore fewer residual defects will remain in the lattice compared to an intermetallic compound where lattice sites are more rigidly defined.

When searching for a suitable HEA to test this hypothesis, V and Zr were first chosen since they have nuclear applications due to their relatively low thermal neutron cross sections (5 barns and 0.185 barns). However problems arose, as they cannot form a crystalline solid solution together when in a binary system (see Chapter 3). The Al-Co-Cr-Fe-Ni system and its variations are not particularly good candidates due to their susceptibility to segregate and form intermetallic compounds (see Chapter 4). In Chapter 5, it was shown that it is possible to use the ASAP method (developed as part of this Ph.D. thesis) to predict new single phase high-entropy alloys (SPHEAs) with specific properties. In this chapter the ASAP methodology is used to attempt to answer the question posed by this thesis: *are HEAs applicable to the nuclear industry*? If so, such an alloy should possess characteristics such as low thermal neutron cross section, strength, ductility, thermal stability and corrosion resistance or a combination thereof depending on the application. Of course, not all of these can be designed for or tested within this dissertation. The best possible outcome would be to identify a HEA with characteristics superior to conventional nuclear materials. This would make HEAs a prime candidate for use in advanced reactors and signify a large step forward addressing the material challenges faced within the nuclear industry.

The parameters that were optimised during the ASAP calculation were as follows: (1) Minimisation in thermal neutron cross section (predicted from the rule of mixtures), (2) ductility (inherent to a single phase BCC or FCC crystal structure, searching preferentially for BCC structures due to their increased

resistance to swelling [226]), and (3) thermodynamic stability to prevent radiation induced segregation. In numerical terms, the latter two parameters are defined as VEC < 6.87, $\Phi \geq 1$ and $\delta \leq 6.6$ (see Chapter 5). The top 5 candidates (ranked in order of decreasing stability) were as follows:

1. NbTiVZr 2. MoNbTiV 3. MoNbTiZr 4.CrMoNbV 5. CrMoNbTi

The SPHEAs containing radioactive elements were not considered due to the difficulties in experimentation, the top two candidate systems: Nb-Ti-V-Zr and Mo-Nb-Ti-V, will be the focus of this chapter. This is the first time a refractory HEA has been studied with displacive radiation damage.

A total of six alloys were produced via arc melting (see Section 2.6) for the purposes of this study:

1. NbTiV 2. $Mo_{0.5}$NbTiV 3. MoNbTiV 4. $NbTiVZr_{0.5}$ 5. NbTiVZr 6. $NbTiVZr_2$

These will henceforth be labelled as:

1. NbTiV 2. $Mo_{0.5}$HEA 3. MoHEA 4. $Zr_{0.5}$HEA 5. ZrHEA 6. Zr_2HEA

Within this chapter, experimental and theoretical characterisation of the as-cast samples were performed using standard laboratory instruments and DFT calculations, respectively. These samples were then irradiated using ion bombardment and further characterised.

6.2 As-cast alloys

All as-cast alloys were found to form a single phase BCC microstructure. The $Mo_{0.5}$HEA and MoHEA were found to form a dendritic structure due to the quenching effect by rapid cooling after the arc melting process was terminated. SEM-EDS analysis revealed that the chemical composition was observed to deviate from their nominal compositions, see Table 6.1.

Table 6.1. Chemical compositions of as-cast alloys provided through EDS analysis using (see Section 2.10).

Sample ID	**EDS analysis (at. %)**				
	Mo	**Nb**	**Ti**	**V**	**Zr**
NbTiV		26.2	36.9	37.0	
$Mo_{0.5}$HEA	10.8	28.2	30.5	30.5	
Dendrite	14.4	32.1	26.5	27.0	
Interdendrite	7.2	24.3	34.4	34.1	
MoHEA	14.6	23.7	30.5	31.2	
Dendrite	20.3	28.6	25.2	25.9	
Interdendrite	8.8	18.8	35.9	36.5	
$Zr_{0.5}$HEA		30.1	28.1	28.4	13.4
ZrHEA		25.6	25.7	24.7	24.0
Zr_2HEA		19.0	20.6	20.6	39.8

The measured deviation (and a number of subsequent observations) can be attributed to the high melting temperatures of Mo and Nb, which prevented their full dissolution from solid to liquid during the arc

melting process. This resulted in inclusions containing pure regions of unmelted Mo and Nb in the as-cast specimens.

Atomic models for DFT analysis were constructed with compositions as close to the as-cast alloys as possible, using 54 atom supercells, see Table 6.2.

Table 6.2. Chemical compositions of 54 atom supercells.

Sample ID	**Supercell stoichiometries (at. %)**				
	Mo	**Nb**	**Ti**	**V**	**Zr**
NbTiV		25.9	37.0	37.0	
$Mo_{0.5}$HEA	11.1	28.7	29.6	30.6	
Dendrite	14.8	31.5	25.9	27.8	
Interdendrite	7.4	25.9	33.3	33.3	
MoHEA	14.8	24.1	30.6	30.6	
Dendrite	20.4	27.8	25.9	25.9	
Interdendrite	9.3	20.3	35.2	35.2	
$Zr_{0.5}$HEA		35.2	25.9	25.9	13.0
ZrHEA		27.8	24.1	24.1	24.1
Zr_2HEA		20.4	20.4	20.4	38.9

Separate simulations of the dendrite and interdendrite composition were performed to better replicate the experimental findings.

6.2.1 NbTiV

This ternary alloy was produced as a comparison and validation of experimental techniques. It was confirmed to produce a single phase solid solution as found by Enomoto *et al*. [227]. The SEM backscatter micrograph (Figure 6.1a) shows little contrast and is otherwise featureless due to the similar melting temperatures of the constituents which allows for a more homogenous matrix upon cooling. However, macroscopic regions of undissolved pure Nb were also present and seen in the XRD pattern (Figure 6.1b).

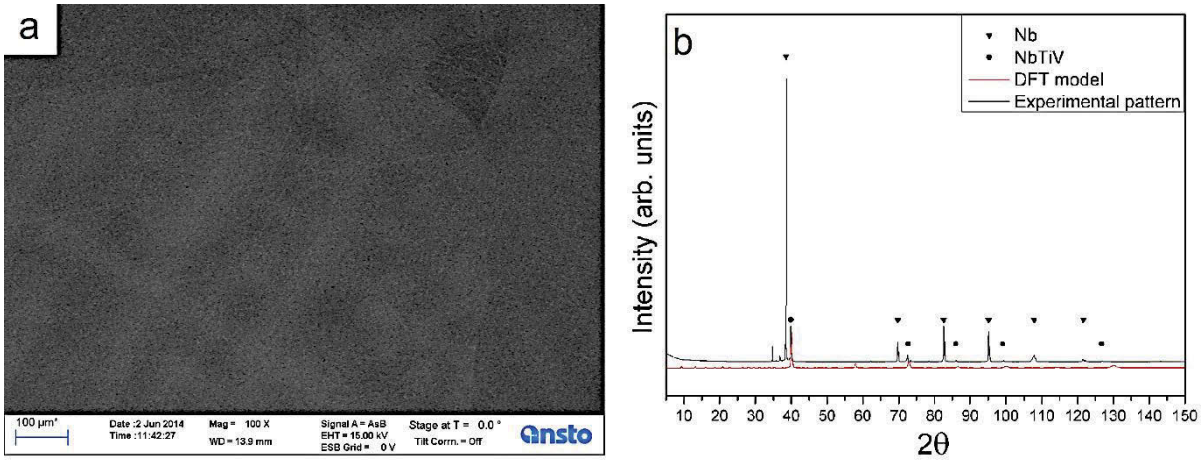

Figure 6.1. The bulk as-cast NbTiV sample as analysed using (a) SEM backscatter (b) XRD, where the experimental XRD pattern (black line) is compared to the simulated XRD pattern of the DFT model (red line). Reflections of pure Nb and HEA matrix are labelled by the triangles and circles, respectively.

Spectral lines from tungsten contamination were also observed within the XRD pattern, preceding each main reflection. Rietveld refinement indicates the lattice parameter corresponding to the main reflections to be 3.196(2) Å and the simulated lattice parameter is determined to be 3.179(1) Å. This difference in lattice parameter is possibly due to the strain effects in the as-cast sample and approximations used within the DFT method, see Section 2.1.2. Due to the periodicity of the theoretical method, reflections are seen at low 2θ values of the simulated XRD pattern.

6.2.2 $Mo_{0.5}$HEA and MoHEA

As previously mentioned in Section 6.2, the $Mo_{0.5}$HEA and MoHEA samples consisted of a BCC crystal structure with dendritic microstructure, see Figure 6.2 and 6.3. Dendrite cores were slightly enriched in the high melting point elements Nb and Mo, relative to the interdendritic regions, which were enriched with the lower melting point elements Ti and V, see Table 6.1. Rietveld refinement of the XRD patterns reveal a lattice parameter of 3.196(3) Å and 3.186(2) Å for $Mo_{0.5}$HEA and MoHEA, respectively. The average lattice parameters obtained by DFT were within ~0.3 % of these values: 3.1855(7) Å and 3.176(1) Å for $Mo_{0.5}$HEA and MoHEA, respectively. Again, Mo and Nb were observed as undissolved regions within the bulk and the pure Mo reflection is seen in the XRD pattern, see Figure 6.2 and 6.3 (i). From the composition and structure, the solid solutions of these two alloys can be seen to be examples of the same phase.

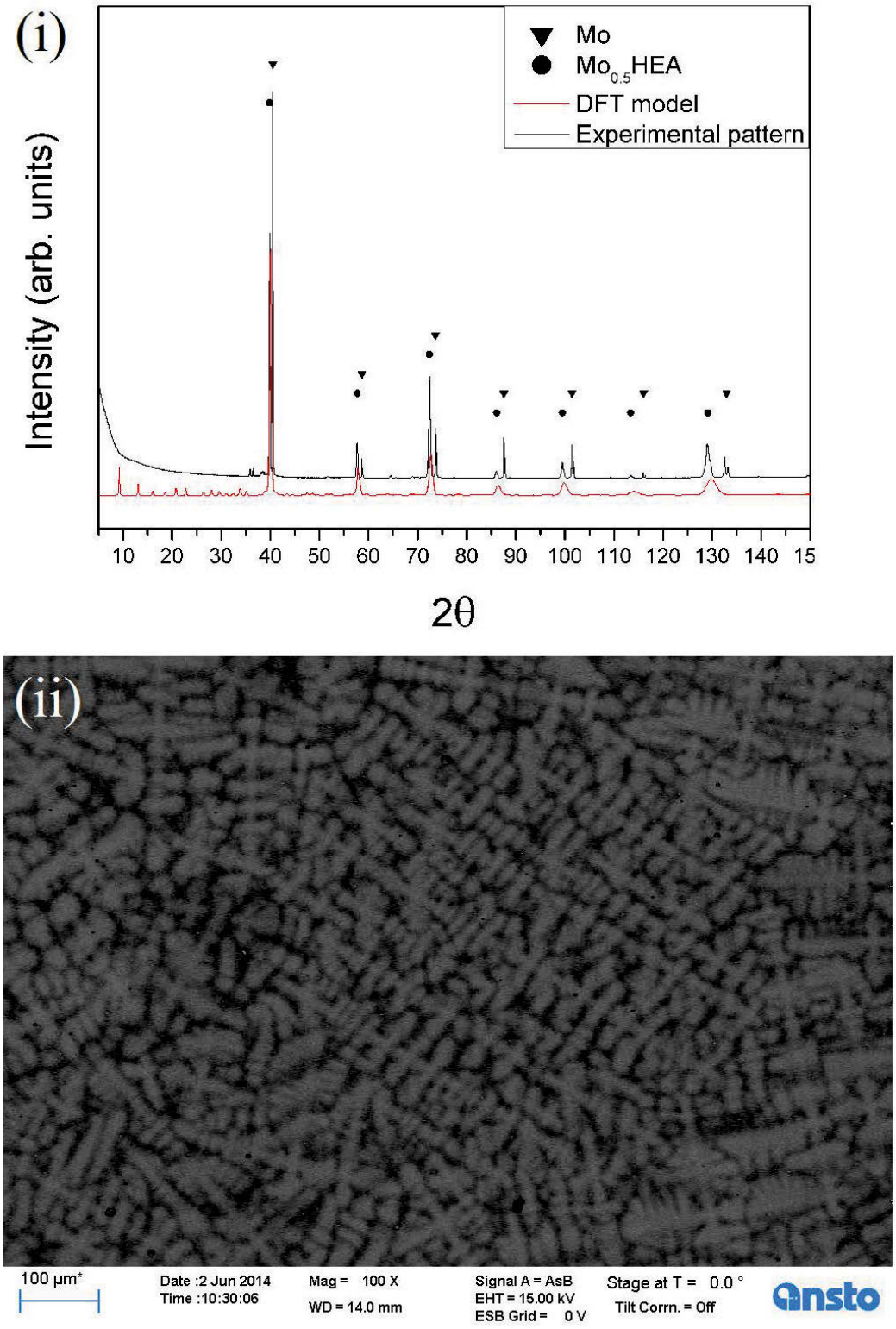

Figure 6.2. $Mo_{0.5}$HEA (i) experimental XRD pattern (black line) with reflections of pure Mo and HEA matrix labelled by the triangles and circles, respectively. Simulated XRD pattern (red line) of DFT modelled HEA is overlaid for comparison. (ii) SEM-BSE micrographs displaying the contrast in BSE intensity due to the dendrite (lighter) and interdendrite (darker) morphology.

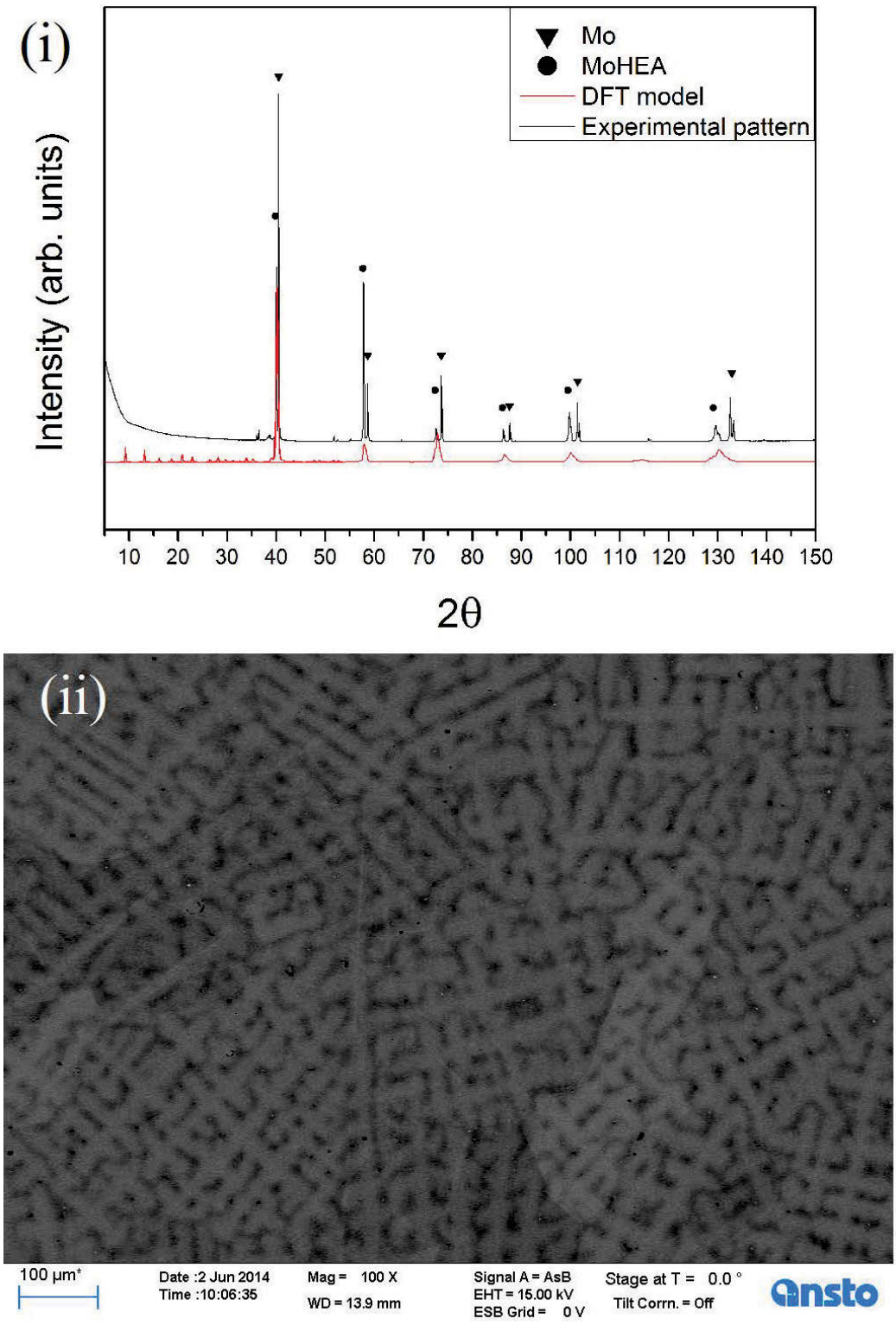

Figure 6.3. MoHEA (i) experimental XRD pattern (black line) with reflections of pure Mo and HEA matrix labelled by the triangles and circles, respectively. Simulated XRD pattern (red line) of DFT modelled HEA is overlaid for comparison. (ii) SEM-BSE micrographs displaying the contrast in BSE intensity due to the dendrite (lighter) and interdendrite (darker) morphology.

It is expected that annealing or mechanical cold working of these alloys will lead to a homogenisation [76], although further studies should be done to test this.

6.2.3 $Zr_{0.5}$HEA and ZrHEA

The $Zr_{0.5}$HEA and ZrHEA exhibit similar non-equilibrium morphology as the $Mo_{0.5}$HEA and MoHEA HEAs, with Nb (the highest melting temperature element) solidifying first, Ti and V evenly dispersing and Zr (the lowest melting temperature element) segregating to the extremities of the grains. Five point scans were done perpendicular to the boundary between the matrix and the undissolved Nb, but no concentration gradient was detected, see Figure 6.4. Dendrites form in the $Zr_{0.5}$HEA and the coring of grains occurs in the ZrHEA, see Figure 6.5 (i) and 6.6 (i), respectively. The XRD patterns reveal a single phase BCC crystal structure with a lattice parameter of 3.267(7) Å and 3.302(5) Å for $Zr_{0.5}$HEA and ZrHEA, respectively. At these lattice parameters the Nb peaks are combined with the HEA peaks to produce a relatively broad, shouldered peak. The lattice parameters of the modelled systems were calculated to be 3.25(1) Å and 3.30(1) Å for $Zr_{0.5}$HEA and ZrHEA, respectively. In previous work by Senkov *et al*. on ZrHEA, a lattice parameter of 3.325 Å was measured [76], which is in excellent agreement with both theoretical and experimental lattice parameters within the current study.

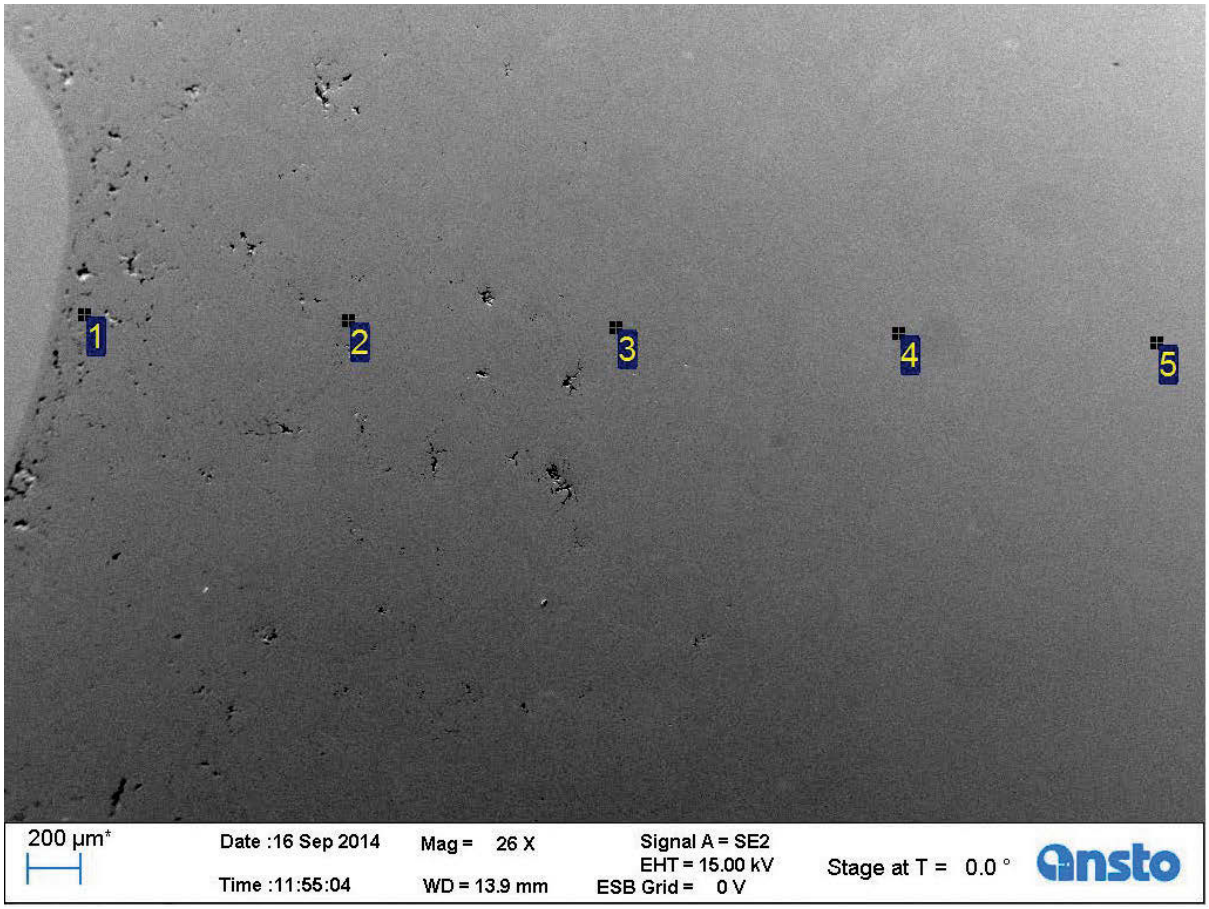

Figure 6.4. SEM-SE image of the polished $Zr_{0.5}$HEA surface where EDS analysis was performed at points 1 – 5 away from the undissolved Nb (light grey on left). Small pores (black regions) are also present.

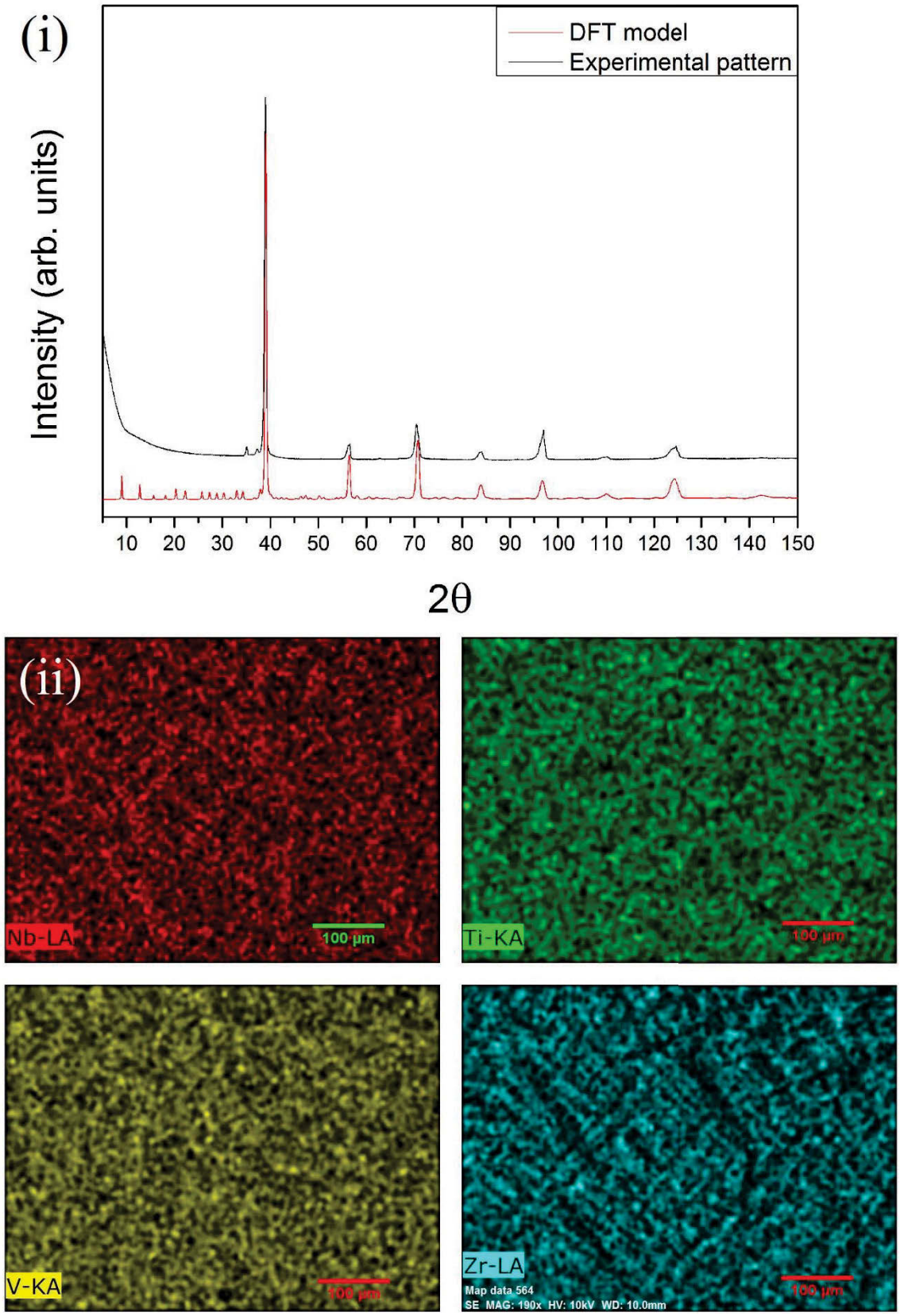

Figure 6.5. $Zr_{0.5}$HEA (i) experimental XRD pattern (black line) and simulated XRD pattern (red line) of DFT modelled HEA is overlaid for comparison. (ii) SEM-EDX maps display contrast in colour between regions of Nb (red) and Zr (blue) with Ti (green) and V (yellow) evenly dispersed.

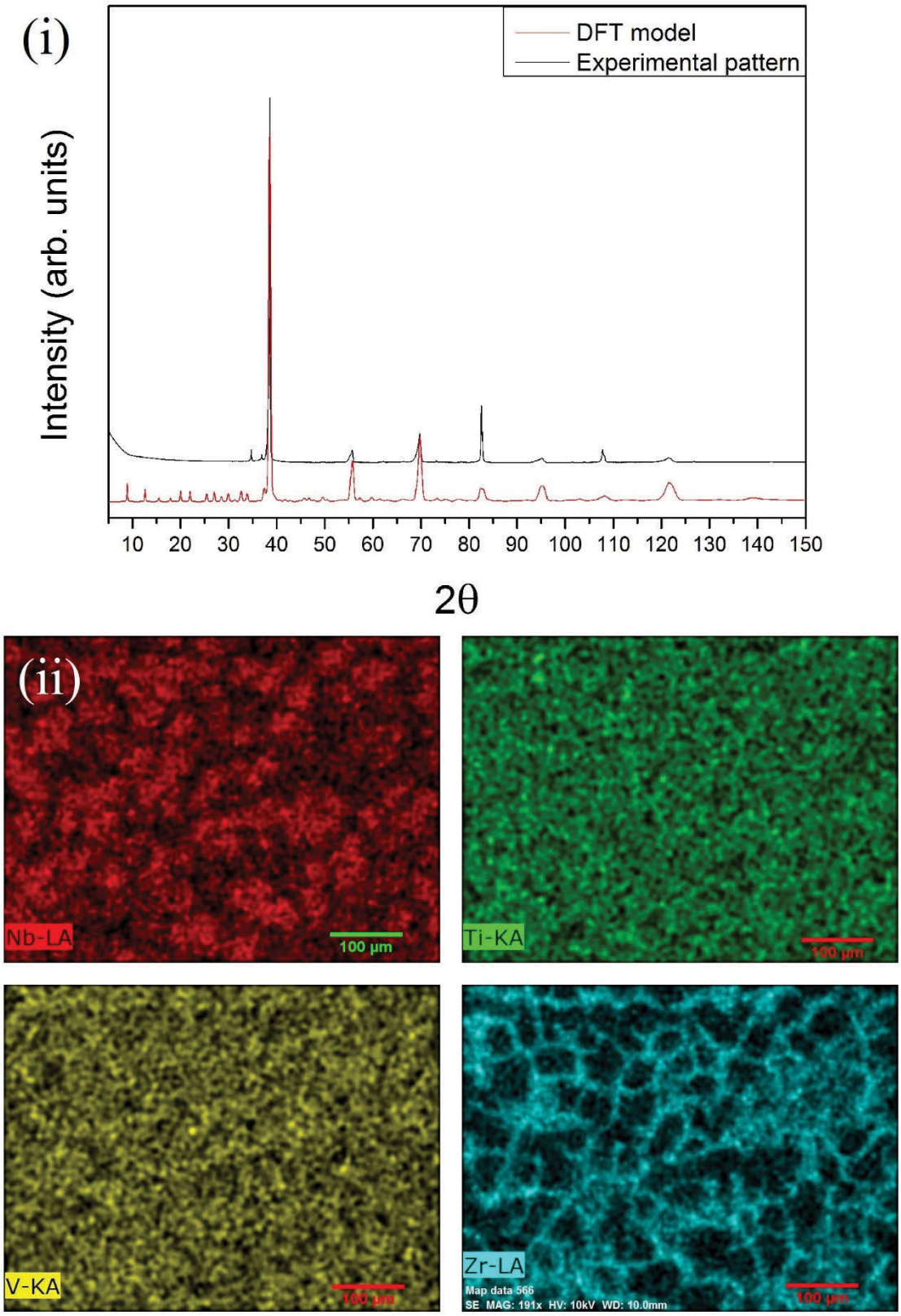

Figure 6.6. ZrHEA (i) experimental XRD pattern (black line) and simulated XRD pattern (red line) of DFT modelled HEA is overlaid for comparison. (ii) SEM-EDX maps display contrast in colour between regions of Nb (red) and Zr (blue) with Ti (green) and V (yellow) evenly dispersed.

6.2.4 Zr_2HEA

Of the six alloys produced within this study, Zr_2HEA seems to be the most homogeneous in microstructure. No contrast can be seen within the SEM-EDX maps and only BCC reflections are observed within the XRD pattern, see Figure 6.7. Rietveld refinement determines the experimental lattice parameter to be 3.367(3) Å and the DFT modelled structure to be 3.360(1) Å.

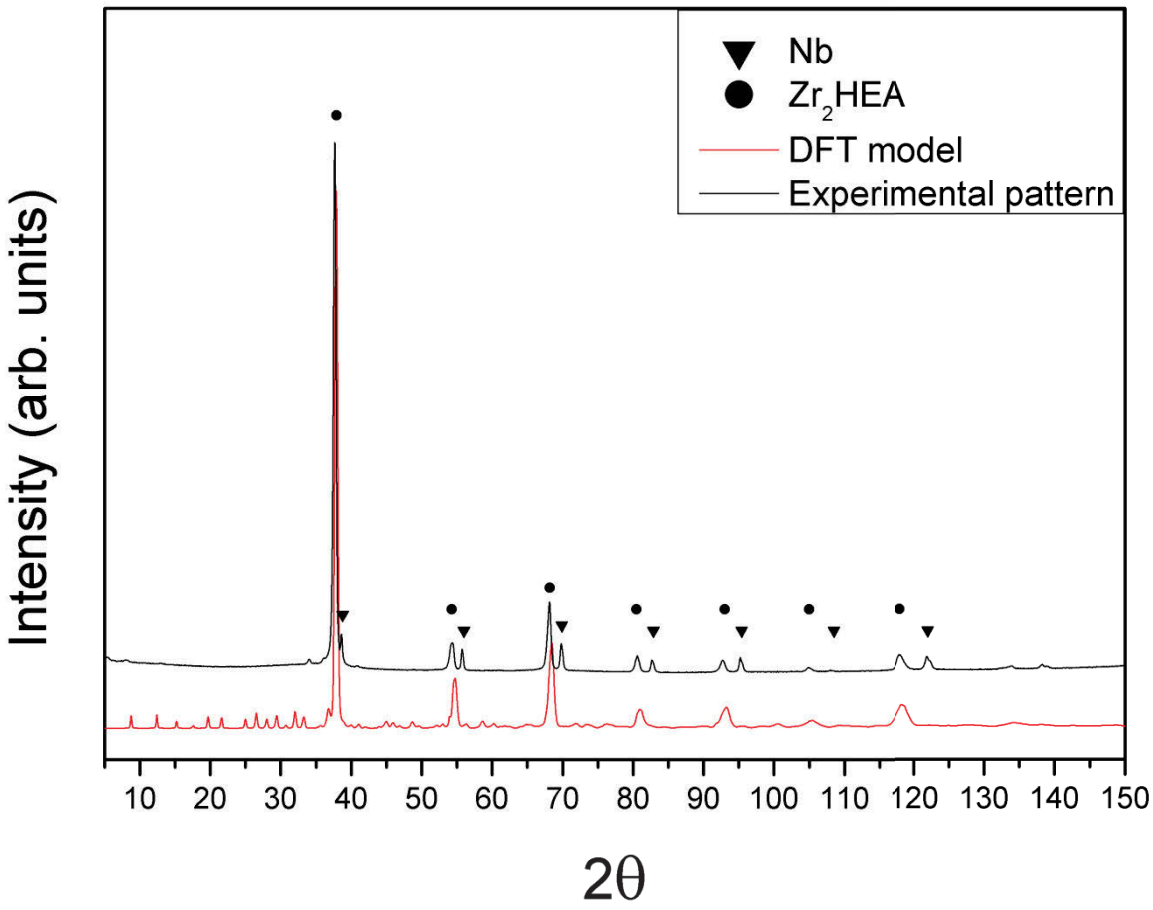

Figure 6.7. Zr HEA experimental XRD pattern (black line) and simulated XRD pattern (red line) of DFT modelled HEA is overlaid for comparison. Reflections of pure Nb and HEA matrix are labelled by the triangles and circles, respectively.

6.3 Predicted performance

As mentioned previously, a structural material for use in a light-water reactor must possess the following traits: strong and ductile mechanical performance, low thermal neutron cross section, maintenance of structural integrity at temperature ranges from 250 – 1300 °C and resistance to corrosion, oxidation (in air and water) and displacive radiation damage. A preliminary assessment of the alloys within this chapter is now made within this section.

6.3.1 Mechanical performance

An estimation of the Young's modulus and hardness of the materials is made from nanoindentation measurements, see Section 2.14 for methodology. Care must be taken when quoting the *magnitude*s of the

Young's modulus from this method, however relative ranking of values is generally reliable [228]. Furthermore, as-cast mechanical performance measurements are not indicative of the annealed/operational state of the alloy, as a higher concentration of defects and changes in morphology are expected to be present.

Table 6.3. Young's modulus and hardness as determined by nanoindentation experiments for the respective systems.

System	Young's modulus (GPa)	Hardness (Hv)
NbTiV	116(1)	305(1)
$Mo_{0.5}$HEA	136(2)	408(2)
MoHEA	142(3)	439(2)
$Z_{0.5}$HEA	109(1)	439(1)
ZrHEA	101(2)	458(2)
Zr_2HEA	98(2)	438(1)
Zr alloys [229, 230]	90-100	~170
Stainless steels [231, 232]	~200	~129

It was found that the Young's moduli were in between that of the conventional Zr alloys and stainless steels, see Table 6.3. Hardnesses were measured as double that of the conventional alloys but this is to be expected due to the non-equilibrium microstructure. In work by Senkov *et al*. [233] the compression modulus and hardness of the homogenised ZrHEA was measured to be 80(8) GPa and 336(3) Hv, respectively [233]. Also, in a DFT study by Tian *et al*. [118] the Young's modulus of ZrHEA was predicted to be between the ranges of 97.7 – 140.2 GPa (between the different crystal orientations), which these experimental values agree with. This, coupled with the current results, allows an estimation of the Young's modulus and hardness of these materials on the order of 75 – 123 GPa and 163 – 357 Hv, respectively, if the samples were to be annealed. Compared to current structural materials (Chapter 1.4.2.) there is no mechanical superiority at room temperature. However, Mo alloys are currently being investigated as Gen III+ cladding materials due to their superior high temperature performance and Zr alloys are known to be relatively radiation tolerant. It is their mechanical behaviour at elevated temperatures and after displacive radiation damage that may provide HEAs an opportunity in the nuclear industry. For this reason, it is well worth investigating them further.

6.3.2 Neutron cross sections

While the macroscopic thermal neutron absorption cross sections (Σ_a) of these alloys have not been measured directly, an estimation of their magnitude can be made using a weighted average of the microscopic thermal neutron absorption cross sections (σ_a) of the constituent elements in their pure state, and the theoretical densities can be obtained using the DFT models, see Section 2.13 for methodology.

Table 6.4. Comparison of microscopic thermal neutron absorption cross section (σ_a), density (ρ) (theoretical values in bold) and macroscopic thermal neutron absorption cross section (Σ_a).

Alloy	σ_a (barns) [163]	ρ (g/cm^3)	Σ_a (cm^{-2})
NbTiV	4.44	**6.27**	**0.28**
$Mo_{0.5}$HEA	3.96	**6.89**	**0.25**
MoHEA	4.06	**6.92**	**0.25**
$Zr_{0.5}$HEA	3.05	**6.70**	**0.18**
ZrHEA	3.32	**6.60**	**0.18**
Zr_2HEA	2.58	**6.53**	**0.14**
Zircaloys	0.20	6.56 [25]	8.8×10^{-3}
Steel	2.56	~7.90 [234]	0.22

From Table 6.4, it is clear to see that Zircaloys have a far superior Σ_a value than is obtained by steel or any of the HEAs produced within this study. Nevertheless, stainless steels are used as cladding material in some current reactors (e.g. the Advanced Gas-cooled Reactor [235]). It should be noted that the density of ZrHEA, experimentally measured by Senkov *et al.* (6.52 g/cm^3) [76], is lower than the theoretical density obtained within this study. This discrepancy can be accounted for adjusting for slight difference in stoichiometry between the current study and that of Senkov.

6.3.3 Stability

The task of experimentally assessing the effects of prolonged elevated temperatures on HEAs was not feasible within the current work, however, a number of aging studies have been conducted by others on various related systems [236, 237]. On the basis of this evidence, it is expected that SPHEAs will transform to multiphase microstructures at lower temperatures. However, there is still debate as to whether the kinetics of the decomposition phase transformation at the lower temperatures are fast enough to cause nucleation of equilibrium phases over industrially relevant time scales [55]. When considering the set of six alloys produced within this study; no intermetallics exist within the Mo-Nb-Ti-V binary systems. The V_2Zr Laves phase may precipitate within the Nb-Ti-V-Zr HEA systems, however, previous work has shown that this phase has a positive formation enthalpy at 0 K [112]. In addition, α-Ti is known to segregate in the Nb-Ti-V ternary and binary phase diagrams [227]. Furthermore, it is possible to only consider the decomposition of the solid solution phase to a segregation of the species in their pure state. Using both DFT and ASAP methods it is possible to estimate at what temperatures the solid solution will no longer be thermodynamically stable within these systems, see Figure 6.8.

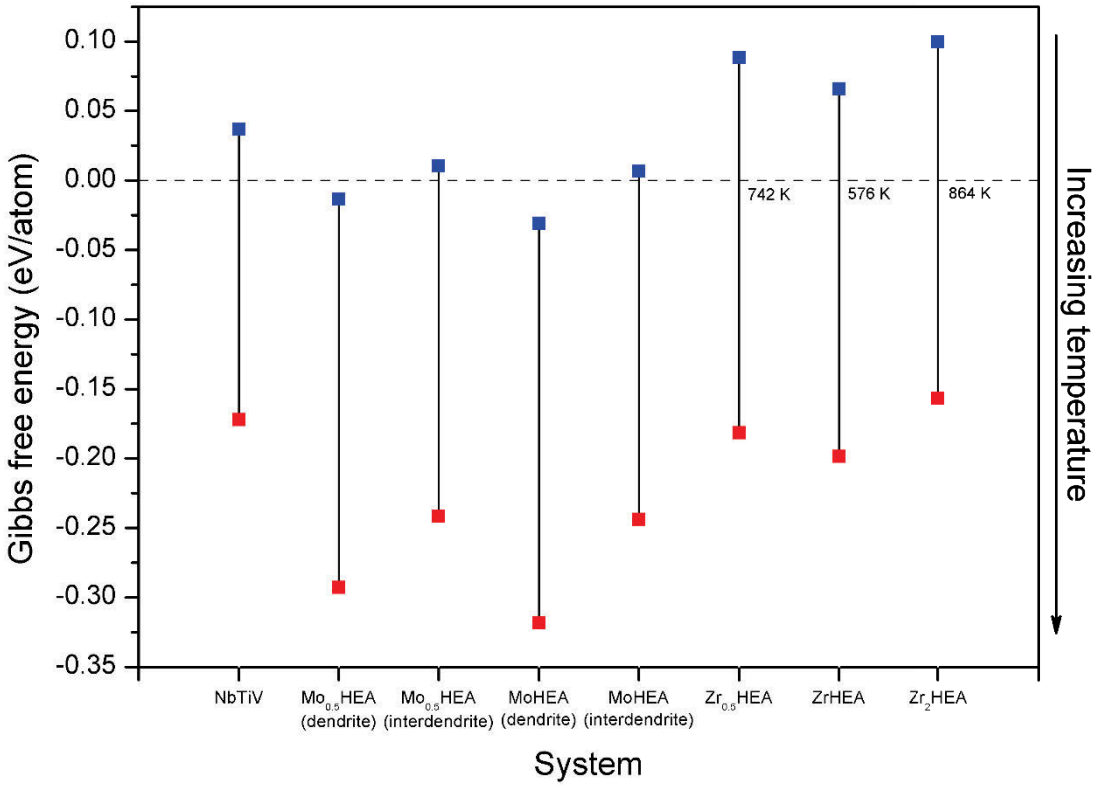

Figure 6.8. Gibbs free energy at 0 K (blue square) and at the predicted melting temperature (red square) with all temperatures between (solid line) for each system studied within this chapter. Temperatures that intersect $\Delta G = 0$ for the Zr containing HEAs are labelled in Kelvin.

Using the equation for Gibbs free energy (Eq. 1.1) and substituting ΔH for the formation enthalpy obtained by DFT and taking ΔS as purely the configurational enthalpy, ΔG can be estimated at elevated temperatures. Interestingly, of the eight simulated systems, only two (the $Mo_{0.5}$HEA and MoHEA dendrites), are predicted to be stable at 0 K. This suggests all the other solid solution phases are entropically stabilised. Assuming no intermetallics or more favourable phases form in preference to elemental segregation, it can be predicted that the $Zr_{0.5}$HEA, ZrHEA and Zr_2HEA will decompose below temperatures of 742 K, 576 K and 864 K, respectively. This could be problematic, as the outlet temperature of a typical water reactor is of the order of ~600 K. When using the ASAP method, all but NbTiV are predicted to decompose to a multiphase microstructure within this temperature range, due to cohesive forces between Nb and Mo and Nb and Zr. Senkov *et al* [233] has studied ZrHEA at elevated temperatures (room temperature to 1473 K) where it was found that submicron-sized particles can precipitate to the grain boundaries with a cooling rate of 10 K/min and, after cooling from compression deformation at 1273 K, a tri-phase morphology is observed but presumed metastable. Further investigation through prolonged annealing at select temperatures is required to gain further insight into the high temperature stability of these alloys.

6.3.4 Radiation tolerance

In this section, residual defect concentrations as a result of displacive radiation damage are assessed using a combination of experiment and DFT simulations. It is assumed that Frenkel pairs (a vacancy and

interstitial) are formed during a displacement event. By simulating isolated defects i.e. non-interacting vacancies and interstitials, differences in volume between the two can be quantified and also measured experimentally, allowing for an estimation of the defect concentrations as a result of the radiation damage. Irradiation of all samples in the form of TEM disks and a single bulk sample of Zr_2HEA was conducted, see Section 2.12 for methodology.

6.3.4.1 Vacancy defects

To simulate an isolated vacancy defect within the modelled structures, one atom of each element was pseudo-randomly chosen and removed to create a 53 atom supercell. Using a modified Kroger-Vink notation [238] and Nb as an example:

$$Nb_A \rightarrow V_A + Nb(s)$$

where Nb_A is a Nb on a lattice site in the HEA and V_A is the vacant site. The designation A is used here as the lattice sites are assumed to be shared by all elements. This process was repeated twice for each element in 10 of the 20 supercells, totalling 80 simulations for a four element system. The vacancy formation enthalpy was then averaged for each element in each system and the standard deviation was calculated.

Table 6.5. Average vacancy formation energies of Mo, Nb, Ti, V, Zr for each respective system compared to the pure BCC metals.

	Vacancy formation energy (eV)					
System	**Mo**	**Nb**	**Ti**	**V**	**Zr**	**Average**
NbTiV	-	1.8(4)	1.8(6)	2.0(3)	-	1.9(3)
$Mo_{0.5}$HEA (dendrite)	1.8(4)	1.5(4)	1.5(3)	1.4(3)	-	1.5(2)
$Mo_{0.5}$HEA (interdendrite)	2.3(3)	2.1(4)	1.8(3)	2.0(3)	-	2.1(2)
MoHEA (dendrite)	2.6(4)	2.7(3)	2.5(3)	2.4(4)	-	2.6(2)
MoHEA (interdendrite)	2.1(3)	2.7(4)	1.7(4)	2.2(5)	-	2.2(3)
$Zr_{0.5}$HEA	-	2.2(5)	1.8(5)	1.8(5)	1.7(6)	1.9(3)
ZrHEA	-	1.4(6)	1.4(5)	1.3(6)	1.2(4)	1.3(4)
Zr_2HEA	-	1.2(5)	1.5(4)	1.0(6)	1.3(5)	1.3(4)
Mo [239]	2.4	-	-	-	-	-
Nb [240]	-	2.9	-	-	-	-
Ti (HCP [241]/BCC[242])	-	-	1.6/2.20	-	-	-
V [240]	-	-	-	2.8	-	-
Zr [241]	-	-	-	-	1.7	-

From Table 6.5 the standard deviation in vacancy formation energies is quite large, ranging (0.3-0.6 eV). This large spread in energies suggests that local configurations around the vacancies have a large influence on their stability. It is important, however, that all vacancy formation energies are positive as negative energies would suggest instability (similar to the findings in Chapter 4). When comparing to the elements in their pure form some vacancies have significantly lower energies e.g. Zr_2HEA has a vacancy formation energy of 1.0(6) eV for V which is less than half of that as pure BCC-V. It is possible that this will have detrimental effects on the radiation tolerance of the materials; further vacancy migration calculations are required.

6.3.4.2 Interstitial defects

A similar method was used to study the interstitial defects within these materials. Single self-interstitial atoms for each element were placed at the *a*(0.5, 0.5, 0) octahedral site within the same BCC unit cell of the 55 atom supercells and then minimised using DFT. This process was repeated 20 times with a total of 80 interstitial calculations for the four element systems. It was observed that for a majority of the cases the interstitial atom would migrate to a lattice site and form a split interstitial around that site. Using the example of a Nb interstitial forming a split interstitial with Ti, the Ti and Nb formation energy is determined by (see also Section 2.3):

$$Nb_i + Ti_A \rightarrow Nb_i + Ti_i$$

From past work on BCC metals [199, 243], it is assumed that the <111> dumbbell/crowdion interstitial configuration will be the most energetically preferable within these HEAs and therefore the main form present.

Table 6.6. Interstitial formation energies in eV (first sub-column) and percentage orientation occurrences (second sub-column) for $Mo_{0.5}$HEA dendrite/interdendrite and MoHEA dendrite/interdendrite and <100>, <110>, <111> and alternate configurations.

Dumbbell Orientations	**$Mo_{0.5}$HEA dendrite**		**$Mo_{0.5}$HEA interdendrite**		**MoHEA dendrite**		**MoHEA interdendrite**	
<100>	-		3.1	3 %	-		-	
<110>	3.0	3 %	-		2.3	3 %		8 %
<111>	2.5(6)	39 %	2.2(4)	61 %	2.7(8)	62 %	2.1(4)	66 %
Alternate config.	3(1)	59 %	2.2(5)	36 %	2.6(7)	38 %	2.1(5)	26 %

Of the 80 supercells, a large portion (≥ 18 %) for each alloy were found to relax to seemingly randomly orientated dumbbell configurations (reported here as "alternate config.") around a single lattice site, see Table 6.6 and 6.7. When analysing the energy minimisation process it is evident that the interstitial atom migrates from the octahedral site to "knock" a neighbouring atom from its lattice site to form this dumbbell configuration. In some instances the whole column of atoms is shifted to form a crowdion interstitial. Although in almost all of the cases, it is the atoms in the <111> direction that are displaced, the orientation of the displaced atoms do not always align in the <111> direction when the energy has reached its minimum. Interestingly, the NbTiV alloy conforms to the behaviour predicted in the literature [243]. Once the fourth element is added, a large variability in orientations is observed.

Table 6.7. Interstitial formation energies in eV (first sub-column) and percentage orientation occurrences (second sub-column) for NbTiV, $Zr_{0.5}$HEA, ZrHEA and Zr_2HEA and <100>, <110>, <111>, AC dumbbell configurations.

Dumbbell Orientations	**NbTiV**		**$Zr_{0.5}$HEA**		**ZrHEA**		**Zr_2HEA**	
<100>	-		2.6(6)	8 %	2.9(6)	31 %	1.6(3)	5 %
<110>	1.7	3 %	1.6(5)	15 %	2(1)	14 %	1.7(5)	10 %
<111>	1.5(4)	97 %	1.7(7)	55 %	1.7(4)	31 %	1.5(5)	67 %
Alternate config.	-		1.9(5)	22 %	2.2(7)	24 %	2(1)	18 %

There are also more occurrences of <100> and <110> orientations with the addition of Zr. An equal number of <100> dumbbell orientations were found as the <111> in ZrHEA. When considering the formation enthalpies of <100> and <111> orientations in ZrHEA, the former is much less favourable. These two findings suggest that certain local configurations around the interstitial atom may cause the <111> configuration to become less energetically favourable when compared the alternative orientations.

In the Mo-containing HEAs, an elemental preference for V to become an interstitial atom was found: 78 – 97% of the interstitially defected supercells relaxed to form a dumbbell in which one of the atoms was V.

Table 6.8. Average interstitial formation energy of Mo, Nb, Ti, V, Zr for the respective systems compared to the pure BCC metals in a <111> split interstitial orientation (with the exception of Ti and Zr which are HCP basal octahedral).

	Interstitial formation energy (eV)					
System	**Mo**	**Nb**	**Ti**	**V**	**Zr**	**Average**
NbTiV	-	3.207(2)	3.204(1)	3.201(1)	-	3.204(1)
$Mo_{0.5}$HEA (dendrite)	2.8(9)	3(1)	2.1(9)	2.6(6)	-	2.6(4)
$Mo_{0.5}$HEA (interdendrite)	2.2(4)	2.3(5)	2.2(5)	2.0(4)	-	2.2(2)
MoHEA (dendrite)	2.8(8)	2.9(9)	2.4(6)	2.4(5)	-	2.6(4)
MoHEA (interdendrite)	2.3(9)	2.0(4)	2.2(2)	2.0(3)	-	2.1(3)
$Zr_{0.5}$HEA	-	2.1(9)	2.2(8)	2.0(7)	3(1)	2.3(4)
ZrHEA	-	1.8(8)	1.9(8)	1.6(5)	1.8(6)	1.8(3)
Zr_2HEA	-	2.0(6)	1.5(5)	1.5(6)	2.0(9)	1.8(3)
Mo [199]	7.417	-	-	-	-	-
Nb [243]	-	5.832	-	-	-	-
Ti (HCP) [244]	-	-	2.29	-	-	-
V [199]	-	-	-	3.367	-	-
Zr (HCP [244]/BCC [245])	-	-	-	-	2.93/3.0	-

The magnitudes of the average interstitial formation energy of Mo is significantly lower, and V is slightly lower, in the HEAs than that of the elements in their pure form, see Table 6.8. NbTiV continues to behave in a conventional manner for unknown reasons. It is possible the addition of a fourth element imposes a larger strain within the lattice, which could stabilise the point defect. However, the δ value (which attempts to predict steric distortion) of NbTiV is within the range of the four element systems. Further strain field analysis should be performed.

These findings have large implications for the understanding of deformation mechanics. It is known that BCC HEAs exhibit low room temperature plasticity compared to conventional materials [233]. Further investigation into the defect mobility within these HEAs may provide further insights. However, this is not the focus of the current study and will be continued in future work.

6.3.4.3 Frenkel defects

It is possible to estimate the unbound Frenkel energies associated with each element by combining the isolated vacancy and interstitial calculations, Table 6.9.

Table 6. 9. Unbound Frenkel defect energies for each element within each system in eV.

System	Mo	Nb	Ti	V	Zr
NbTiV	-	3.7(6)	**2.7(7)**	3.6(4)	-
$Mo_{0.5}$HEA (dendrite)	6.8(7)	6.3(7)	**3.7(7)**	4.1(7)	-
$Mo_{0.5}$HEA (interdendrite)	4.9(4)	4.9(3)	**2.6(5)**	3.9(3)	-
MoHEA (dendrite)	6.1(4)	6.2(4)	**4.2(3)**	4.5(3)	-
MoHEA (interdendrite)	4.7(3)	4.6(4)	**2.1(5)**	3.9(8)	-
$Zr_{0.5}$HEA	-	5(1)	**2.6(8)**	3.0(8)	5(1)
ZrHEA	-	4.8(5)	**2.8(5)**	3.3(6)	3.6(5)
Zr_2HEA	-	4.0(7)	**2.0(6)**	2.9(5)	2.5(6)
Mo	9.5	-	-	-	-
Nb	-	4.7	-	-	-
Ti (BCC)	-	-	6.7	-	-
V	-	-	-	5.5	-
Zr (BCC)	-	-	-	-	1.8

Table 6.9 reports the formation energies of non-interacting Frenkel defects. For Mo, Ti and V, the Frenkel energies in the HEAs are significantly lower than the elements in their pure form. There is little to no measurable difference for Nb, and Zr has a larger Frenkel energy than in pure BCC Zr. Although the standard deviations are large, the average formation energies of Ti suggest an energetic preference for Ti to form a Frenkel defect over the other species across all systems. This finding may suggest that Ti will preferentially segregate from the BCC matrix (a phenomenon known to occur in the NbTiV system [227]).

The net volume change of a Frenkel defect can be estimated by assessing the average defect volume of a vacancy, $v(V_A)$, and an interstitial $v(A_i)$ weighted by the probability of the defect forming for each element. The volumes have been converted to average lattice parameters for direct comparison to experiment, see Table 6.10.

Table 6.10. Average change in lattice parameters of the HEA supercells with a single vacancy, $v(V_A)$, and interstitial, $v(A_i)$ defect, with the estimated Frenkel defect $\sqrt[3]{\text{volume}}$, $v(F_A)$, in each column, respectively.

System	$v(V_A)$ (Å)	$v(A_i)$ (Å)	$v(F_A)$ (Å)
NbTiV	-0.72(9)	0.93(4)	0.21(9)
$Mo_{0.5}$HEA (dendrite)	-0.65(6)	0.95(4)	0.30(7)
$Mo_{0.5}$HEA (interdendrite)	-0.68(6)	0.93(2)	0.24(6)
MoHEA (dendrite)	-0.60(6)	0.95(2)	0.35(6)
MoHEA (interdendrite)	-0.72(9)	0.93(4)	0.21(9)
$Zr_{0.5}$HEA	-0.75(9)	0.96(1)	0.20(9)
ZrHEA	-0.80(5)	0.96(5)	0.16(7)
Zr_2HEA	-0.79(7)	0.96(1)	0.17(6)
Mo	-0.72	0.97	0.25
Nb	-0.78	0.99	0.20
Ti (BCC)	-0.79	0.96	0.16
V	-0.61	0.90	0.29
Zr (BCC)	-0.79	1.14	0.35

Due to the large standard deviations there is little variability in the predicted swelling behaviour due to Frenkel defects, between the various phases. An estimated defect concentration of 1.85% or 9.76×10^{20} Frenkel pairs/cm^3 is predicted to be present for a lattice parameter increase of 0.17(6) – 0.35(6) Å between irradiated and non-irradiated samples.

6.3.4.4 Ion irradiation

Of the six alloys, Zr_2HEA was chosen as the most promising candidate material as it has a low thermal neutron cross section, the most homogeneous microstructure (although a composition somewhere in between the ZrHEA and Zr_2HEA may be superior) and should exhibit a minimal level of swelling from intrinsic defects compared to the other HEAs produced. In addition to TEM samples of each alloy, further radiation experiments were performed on the bulk sample of Zr_2HEA, see Section 2.12 for methodology.

Using SRIM simulations, a peak damage of 20-30 dpa in the TEM and Zr_2HEA bulk sample was predicted. The magnitude of the peak damage will vary depending on the threshold displacement energy, E_d, of each element. It has been speculated that highly alloyed mixtures lead to decreased E_d values compared to their constituent metals [225] and from the defect calculations in Section 6.3.4.3 it is reasonable to assume that the systems in the current study will also experience this reduction. Although no formal relationship between Frenkel defect energy and E_d has been established; E_d is generally 4 – 10 times larger than the Frenkel defect energy [246]. By taking the ratio between the Frenkel defect formation energy and E_d for the elements in their pure form and applying it to the current Frenkel defect energies, new E_d values are estimated within the current study, see Table 6.11.

Table 6.11. Average threshold displacement energy of Mo, Nb, Ti and V from their pure BCC metals and theoretically predicted from Frenkel defect energies.

	Mo	Nb	Ti	V	Zr
Literature BCC metals (eV) [247]	65	78	30	57	40
Theoretical ($NbTiVZr_2$)	-	66	9	30	56

The effect of varying E_d has a significant effect on dpa caused by Au ions, however, almost negligible for He ions due to their relatively small atomic mass. E_d values obtained from literature and the SRIM default (E_d = 25 eV) (thought to be a good approximation for metals [248]) were compared to the E_d values calculated within the current study, see Figure 6.9. The peak dpa remains at the same depth within the sample due to the energy of the Au ions (12 MeV). Within the TEM samples, 4 MeV was sufficient for complete transmission of the Au ions, however in the bulk sample the Au and He atoms were embedded within the sample, see Figure 6.10.

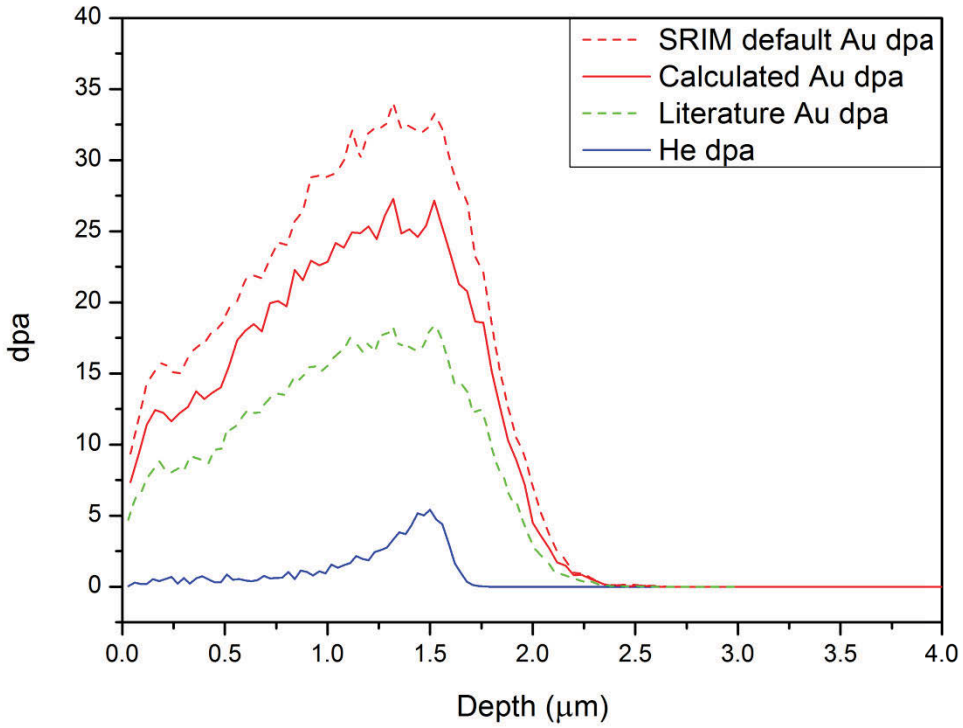

Figure 6.9. SRIM simulated damage profile within the $NbTiVZr_2$ bulk sample using the default E_d (red dashed), calculated E_d (red solid) and literature E_d (green dashed) using Au^{5+} and He^{+} (blue) ions.

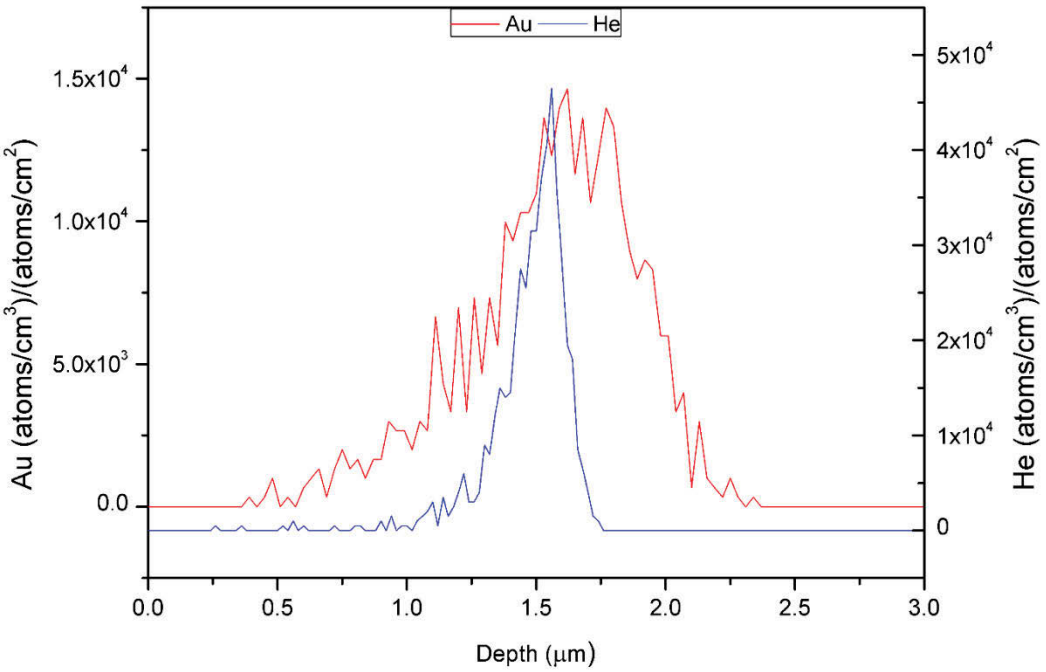

Figure 6.10. Distribution of Au atoms (red, y_1-axis) and He atoms (blue, y_2-axis) as a function of depth in the Zr_2HEA bulk sample.

6.3.4.4.1 TEM samples

A pair of TEM disks was produced for each alloy and one disk of each pair was irradiated using 4 MeV Au^{1+} ions in transmission. The SAED patterns for all disks revealed diffraction patterns indicative of single phase BCC structure and were indexed as such, see Figure 6.11 and 6.12.

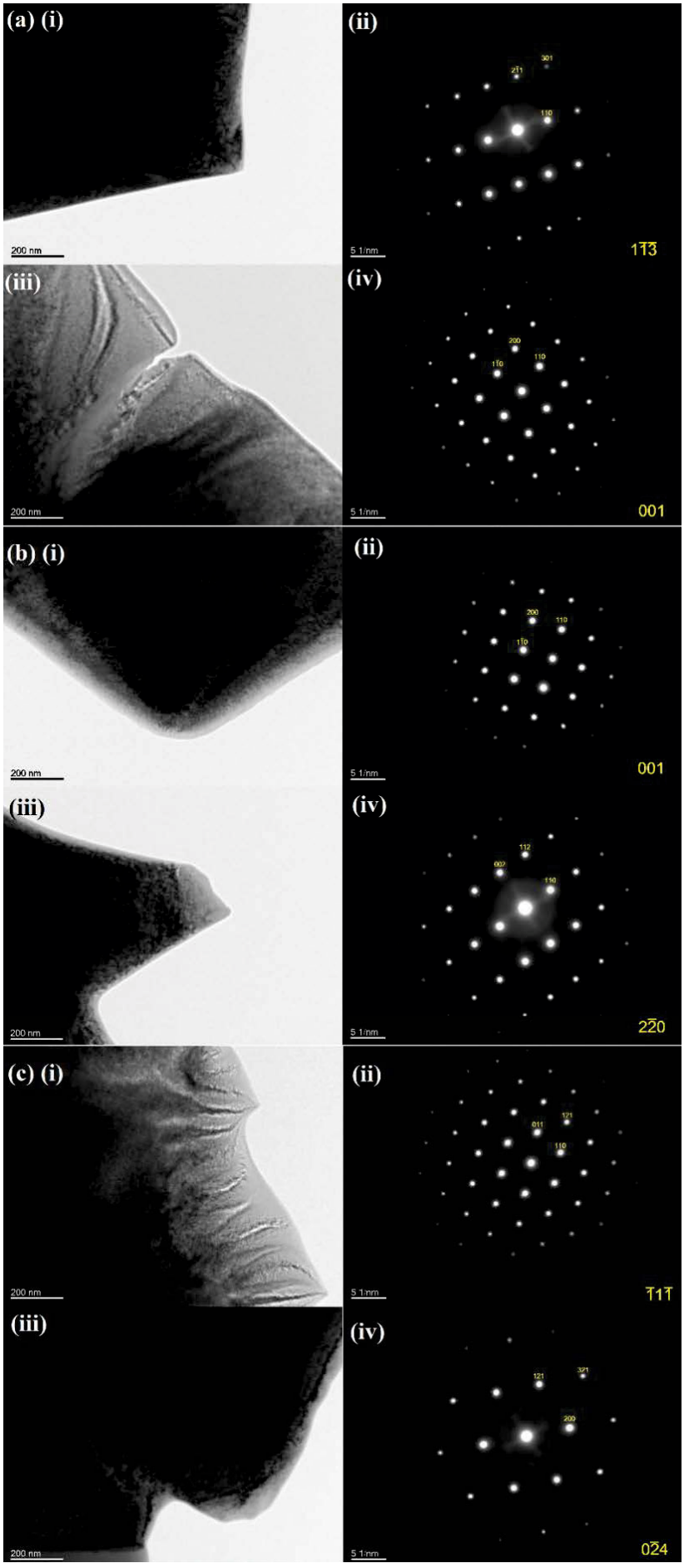

Figure 6.11. (i), (iii) BF-TEM image and corresponding (ii), (iv) SAED pattern of (i), (ii) unirradiated and (iii), (iv) irradiated TEM disks for (a) $Mo_{0.5}$HEA, (b) MoHEA and (c) NbTiV.

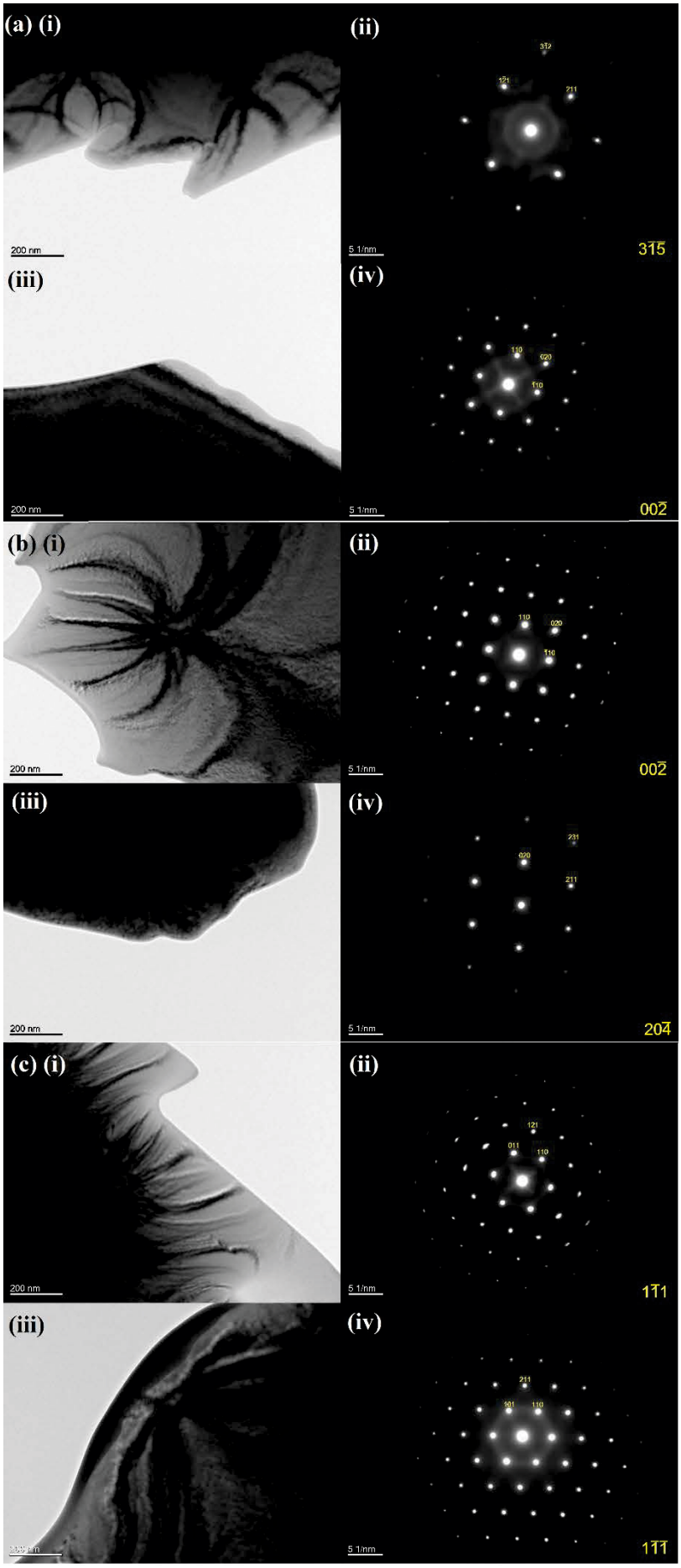

Figure 6.12. (i), (iii) BF-TEM image and corresponding (ii), (iv) SAED pattern of (i), (ii) unirradiated and (iii), (iv) irradiated TEM disks for (a) ZrHEA, (b) $Zr_{0.5}$HEA and (c) Zr_2HEA.

The SAED patterns were used to estimate the *d*-spacing between the respective planes of atoms to calculate the lattice parameter, see Section 2.11. ImageJ was used to measure the distance between 3 – 6 diffraction spots in 3 different directions, which were then averaged for each sample. When accounting for the standard deviation in measured data, it was found that there was little to no observable change in lattice parameter between unirradiated and irradiated samples, see Table 6.12.

Table 6.12. Lattice parameter of each sample in the unirradiated and irradiated condition with the difference between the two.

System	Unirradiated (Å)	Irradiated (Å)	Difference (Å)
NbTiV	3.24(4)	3.24(2)	-0.00(4)
$Mo_{0.5}$HEA	3.20(1)	3.23(3)	0.04(3)
MoHEA	3.24(3)	3.29(1)	0.06(4)
$Zr_{0.5}$HEA	3.28(1)	3.28(2)	0.00(2)
ZrHEA	3.33(3)	3.34(1)	0.01(3)
Zr_2HEA	3.393(7)	3.374(9)	-0.02(1)

Qualitatively, some amorphous regions were identified in the NbTiV, ZrHEA and Zr_2HEA with an average distance to first nearest neighbour of ~2.6 Å and no deviation in composition, see Figure 6.13. Interestingly, an amorphous region was also observed in an *unirradiated* sample of Zr_2HEA, which casts doubt as to whether it is caused by Au^{5+} ions. It is possible that amorphisation occurred during sample preparation (either mechanical or during ion polishing).

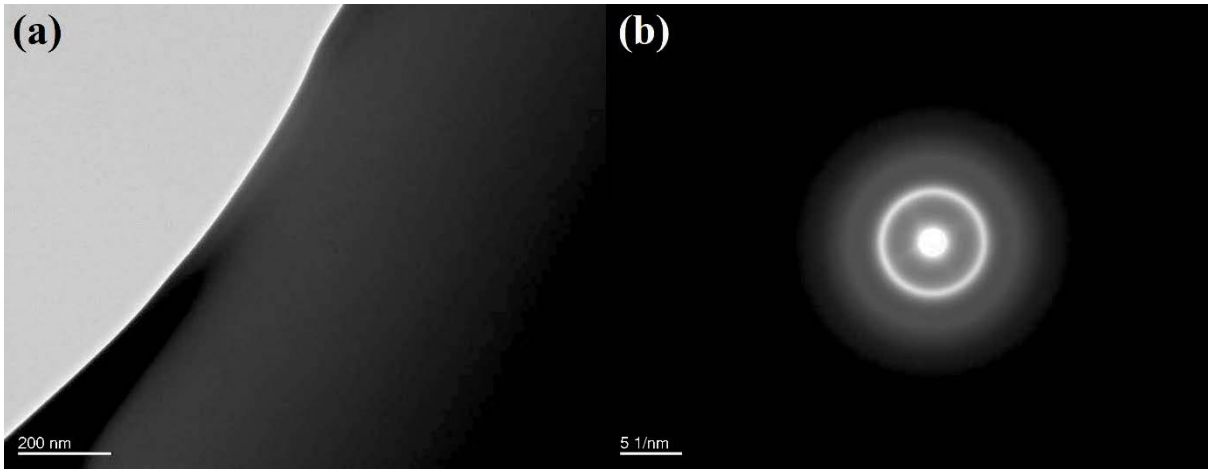

Figure 6.13. (a) BF-TEM image and (b) corresponding amorphous SAED pattern in the irradiated Zr_2HEA.

Nevertheless, the retention of a BCC phase with little to no change in lattice parameter after 10 dpa Au^{5+} damage is a very promising result. However, due to the thickness of the TEM disks, the portion of residual defects may differ from that of a bulk sample. For further analysis, in-situ TEM measurements during the bombardment process, like those performed at the Argonne National Lab [249], should be carried out to allow for a better understanding of the origin of the amorphous regions and degree of relaxation after bombardment.

6.3.4.4.2 Zr_2HEA bulk sample

In this section, GIXRD is used to measure the change in lattice parameter as a function of depth before and after Au^{5+} and He^{+} bombardment. By assessing the concentration of Au, from the surface to each depth probed by the XRD analysis, an estimation of the contribution to the XRD signal by the embedded Au ions is made.

The maximum value was calculated to be ~0.1 % of the total volume of atoms probed by the X-rays, using the material density reported in Table 6.4. It is therefore not expected that reflections that satisfy the Bragg condition between Au atoms will be present in the XRD patterns, as the signal will be indistinguishable from the background contributions.

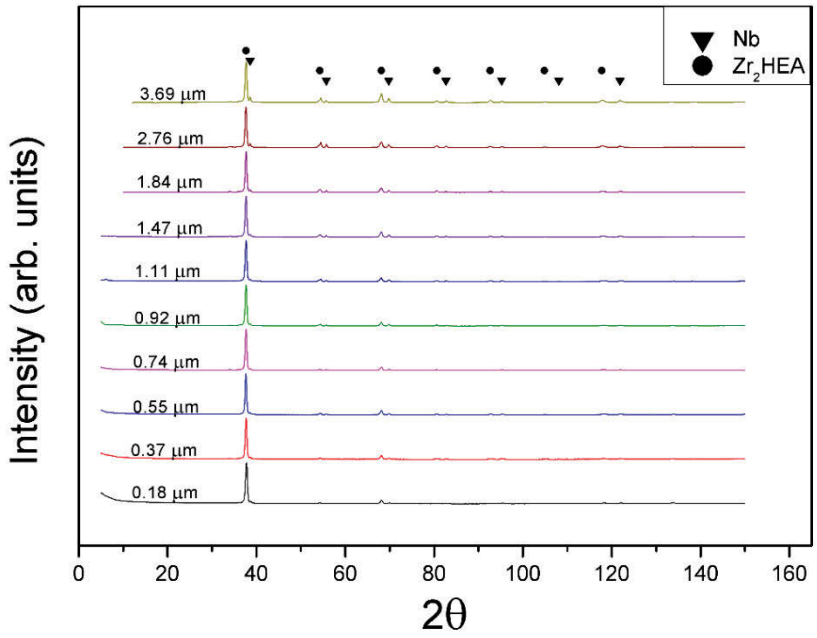

Figure 6.14. GIXRD patterns of the unirradiated Zr_2HEA bulk sample with maximum depths in which 99% of the intensity was obtained numerically labelled in µm. Reflections identified as the Nb phase are denoted by the triangle symbol and the ZrHEA matrix as a circle.

Figure 6.14 shows the XRD pattern of the unirradiated Zr_2HEA bulk sample at depths of 0.18 – 3.69 µm. As previously mentioned, two BCC phases are identified to be that of the HEA matrix and undissolved Nb which reaches a peak volume fraction of 4.74 % at 3.69 µm. A small shift in lattice parameter of 0.0050(6) Å, is observed between 0.18 – 0.55 µm, possibly due to different stresses induced by the quenching of the arc melting process and mechanical polishing.

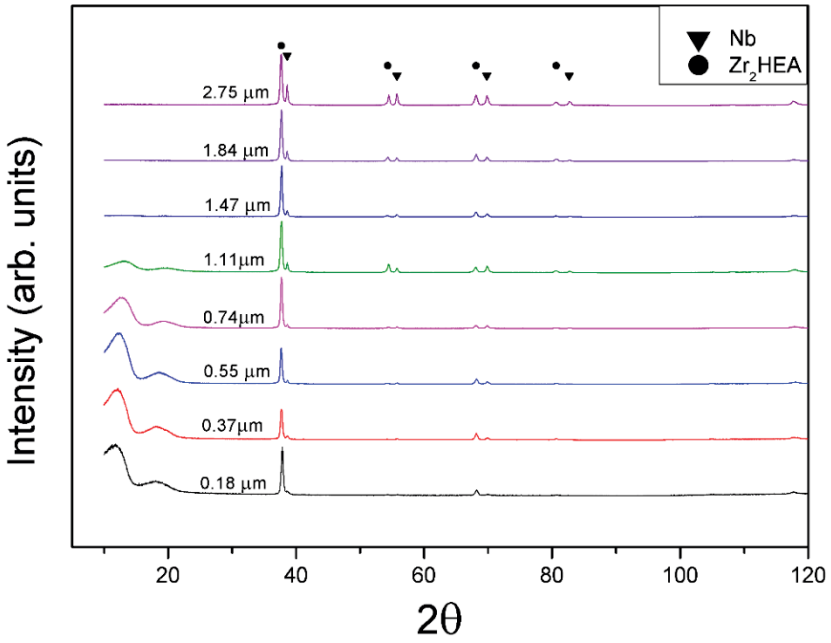

Figure 6.15. GIXRD patterns of the post-irradiated Zr_2HEA bulk sample with maximum depths in which 99% of the intensity was obtained numerically labelled in µm. Reflections identified as the Nb phase are denoted by the triangle symbol.

After initial irradiation of the material by Au^{5+} ions, a non-crystalline feature at low 2θ is observed between depths of 0.18 – 1.11 µm, see Figure 6.15. This feature remains after He^{+} irradiation but intensities are slightly reduced from 0.18 – 1.11 µm and increased from 1.47 – 1.84 µm. Unlike the diffuse rings observed in the amorphous SAED patterns, the broad peaks in the XRD data correspond to larger distances of ~7.6 Å and ~4.9 Å. The nature of this disordering remains unidentified, however it is evident that these features occur at relatively shallow depths and are spaced relatively far apart. However, it should be noted that care must be taken when quoting discrete depths of features recorded by X-ray analysis as information pertaining to the shallower depths will also be included in each pattern [250]. Nevertheless, the maximum volume fraction of the non-crystalline region was observed ~0.5 Å from the surface, see Figure 6.16, which does not correspond to the region at which the peak dpa is expected to occur (Figure 6.9). Figure 6.16 also shows the lattice parameters of Zr_2HEA in the unirradiated, Au^{5+} irradiated and He^{+} condition. There is a small minimisation of the lattice after Au^{5+} irradiation, of the order of ~0.001 Å (with the exception of one data point), which may be due to an annealing effect from the damage, reducing the total defect concentration within the lattice from the as-cast condition. The standard deviation associated with these measurements was of the order of 1×10^{-4} Å.

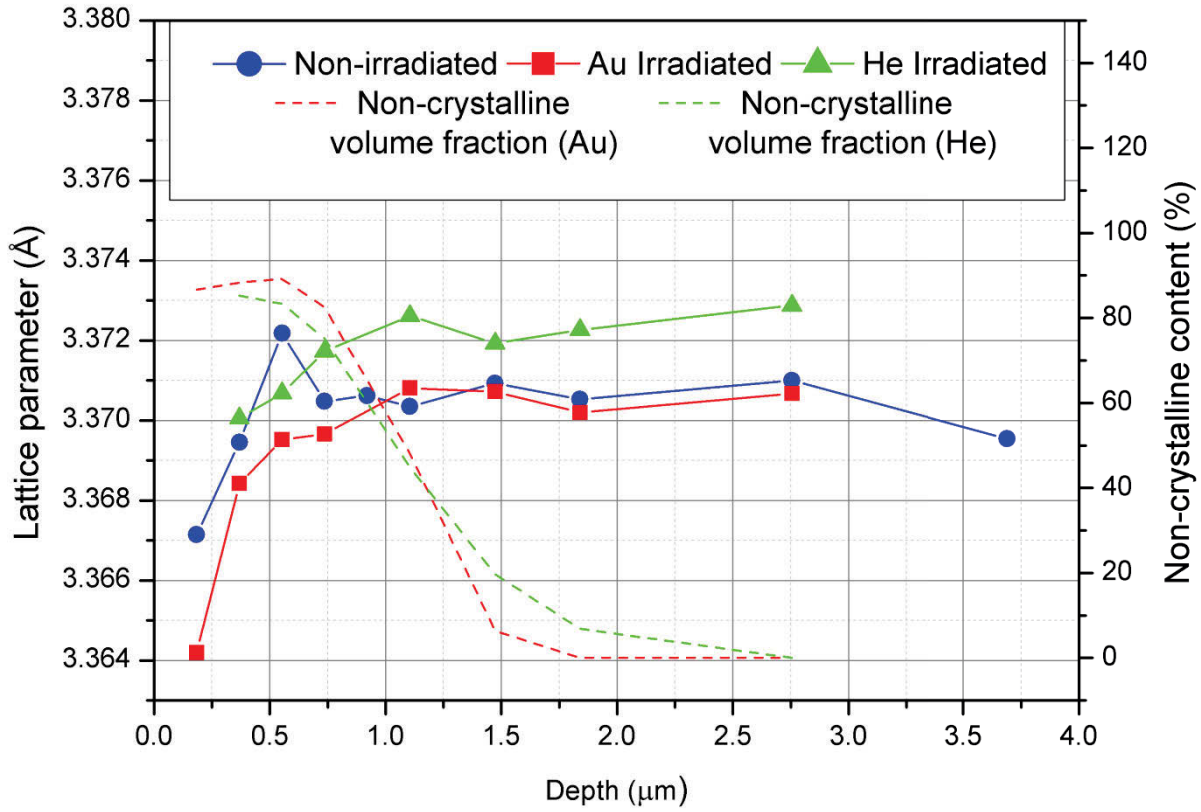

Figure 6.16. Comparison between lattice parameters with changing depth within Zr_2HEA in the as-cast (blue circle), Au^{5+} irradiated (red square) and He^{+} irradiated (green triangle) state on the y_1 axis. Non-crystalline volume fraction in the Au^{5+} irradiated (dashed red line) and He^{+} irradiated (dashed green line) state on the y_2 axis.

After He^{+} irradiation the lattice parameter increased again, past that of the as-cast state. It is possible that the deposited He^{+} ions have stabilised the vacancy defects [251] and defect clusters [252]. From the previous defect calculations in Section 6.3.4.3, it is estimated that the defect concentration has increased by 0.02 % or 1.84×10^{18} Frenkel pairs/cm^3 between the post Au^{5+} irradiated and post He^{+} irradiated state. This value is a typical defect concentration of an as-cast material at room temperature [253, 254]. The estimated concentration of He^{+} ions embedded within the material is ~0.7 % of the atoms within the XRD interaction volume which is more than sufficient to saturate the residual vacancy defects. Secondary effects such as void nucleation and swelling may also occur at higher temperatures [255]. A DFT study investigating the interaction between fission and fusion products, such as He, is required for further insight.

The maintenance of the BCC matrix of these HEAs after exposure to a relatively high dpa at room temperature is a very positive result. Unlike Zircaloys or Zr-alloys, the current HEAs have no precipitate phases (which are susceptible to amorphisation by irradiation [256]). The precipitation of intermetallic phases during irradiation, which is known to occur in the Al-containing HEAs [225], Zircaloys [257], austenitic Fe-Cr-Ni [258] and W-alloys [259, 260] is not evident within the present XRD patterns, nor observed under TEM in the current study. Due to the chemical similarity of the elements within each HEA, it is more likely that segregation of the elements into their pure phases or a secondary solid solution phases may occur.

Moreover, the elements that typically form precipitate phases during irradiation, such as Cr or Al, are present within the conventional alloys to assist with oxidation/corrosion resistance [88]. Therefore, it is expected that the oxidation resistance of the current HEAs may be impaired due to their absence. However, Ti and Zr alloys are relatively corrosion resistant in their own right [261]. Cr was added as a fifth element to the Nb-Ti-V-Zr system by Senkov *et al*. where it was found to precipitate to the Cr_2Zr Laves phase [76]. However, recent identification of new Al-containing SPHEAs [77] could be an attractive alternative for increased oxidation/corrosion resistance within reactor settings.

Regarding the broad reflections at low 2θ in the XRD patterns, if these are caused by defect clusters, it may be possible that increased temperatures will accelerate nucleation and further contribute to the disorder in the form of void swelling [262]. Nevertheless, annealing experiments must be performed, both during bombardment and after, for further insight into phase stability and defect behaviour to be obtained. Furthermore, to elucidate a mechanism behind this non-crystalline feature, further analysis using SEM, 3D TEM or small angle X-ray scattering methods could be used.

6.4 Summary

A set of six alloys (four novel SPHEAs), predicted by the ASAP code, were produced via arc melting and the as-cast samples were experimentally characterised using SEM, XRD and *ab-initio* techniques. All samples were determined to be of single phase BCC structure although some regions of un-melted pure Mo and Nb were also identified. Partial segregation of the lower melting temperature elements was observed in dendritic and grain coring morphologies due to the rapid solidification process. The modelled structures were found to have very similar lattice parameters to experimental findings. These models were then used to predict the thermodynamic stability of the alloys. It was predicted that the Mo-containing HEAs would be stable from very low temperatures up to their melting temperature whereas the Zr containing HEAs will destabilise from 576 – 864 K and below, assuming no intermetallics or phase segregation is favoured in preference to elemental segregation. This finding is problematic due to the operational temperature ranges of current reactors being within these bounds [17]. However, experimental verification is still required. Preliminary mechanical testing revealed an increased hardness compared to conventional materials (most likely due to the non-equilibrium microstructures) and the measured Young's modulus is in general agreement with previous experimental work by Senkov *et al* [233] and theoretical work by Tian *et al* [118]. These values were within the range of Zr alloys and steels.

Interstitial calculations showed interesting behaviour upon the relaxation of a self-interstitial placed at the octahedral site. It seems that the V atoms are preferentially displaced from their lattice site (up to 97 % of the time in the MoHEA interdendrite) along the <111> direction, however, the resulting dumbbell interstitial defect does not necessarily align exactly to the <111> direction. Conversely, Zr interstitials are the least preferable of the species considered, occurring in as little as 3 % of the cases in the $Zr_{0.5}$HEA. However, in calculations of the formation energies of Frenkel defects (vacancy and interstitial combined), no trend or preference between the different species were found due to the large standard deviations and all were determined to be positive. It is expected that the local configuration around the octahedral interstitial atom has a large influence on the orientation and species in the subsequent dumbbell

arrangement. The magnitude of interstitial formation energy of Mo is significantly lower in the Mo containing HEAs than the pure metal, which may have adverse effects on their radiation tolerance. Strangely, NbTiV defect behaviour conforms to the conventional BCC metal with a small spread in energies and <111> orientations. It is possible the addition of a fourth element, such as Mo or Zr (which have relatively small and large metallic radii respectively), imposes a strain within the lattice stabilising the point defects.

After obtaining defect volumes for both vacancies and interstitials, the unbound Frenkel defect volume was calculated. It was determined that a change in lattice parameter between 0.17(6) – 0.35(6) Å will correspond to a change in defect concentration of 1.85 % or 9.76×10^{20} Frenkel pairs/cm^3. The Frenkel defect energies of Mo, Ti and V in the HEAs show a marked decrease compared to the elements in their pure form; it is possible that the highly alloyed nature of the solid solution contributes to this effect and may lead to more damage received by the materials by lowering the threshold displacement energy.

Au^{5+} ion bombardment experiments were carried out on all samples as TEM disks, in transmission, to ~ 20 dpa. Analysis revealed no change or insufficient accuracy to measure change in lattice parameter between the non-irradiated and irradiates samples, which all maintained their BCC structure. Amorphous regions were observed in NbTiV, ZrHEA and Zr_2HEA irradiated samples as well as in the non-irradiated sample of Zr_2HEA, with an average distance to first nearest neighbour of ~2.6 Å. It is possible that the sample preparation method (mechanical or ion polishing) led to this structure.

Zr_2HEA was selected for further irradiation experiments using Au^{5+} and He^+ ions on a bulk sample to an estimated peak of ~25 dpa. GIXRD was used to study the bulk samples from 0.18 – 3.69 μm in depth. It was found that after Au^{5+} irradiation a non-crystalline feature remained at depths of 0.18 – 1.11 μm with volume fractions of up to 90 %. The corresponding distances of these disordered features do not align with the observed amorphous pattern in the TEM SAED patterns. Nor do they correspond to depth at which the peak damage occurred. It is possible that defect clusters remain within the material. The Zr_2HEA BCC matrix and Nb phases remained after both Au^{5+} and He^+ irradiation with a slight decrease in lattice parameter after Au^{5+} irradiation, which may be due to a defect "annealing" effect from the as-cast condition. He^+ irradiation lowered the volume fraction of the non-crystalline regions slightly and increased the overall lattice parameter of the Zr_2HEA matrix at all depths. Even though the peak damage caused by He^+ bombardment was only ~5 dpa an increase in defect concentration occurred. This increase is estimated to be on the order of 1.84×10^{18} Frenkel pairs/cm^3 between the post Au^{5+} irradiated and post He^+ irradiated state possibly due to He stabilisation of vacancies.

7

CONCLUSIONS AND FUTURE WORK

The work presented in Chapter 3 was performed on two nuclear relevant elements: V and Zr; the thermodynamic component of the investigation showed that mutual solubility between the two elements is highly unfavourable at equal or near equal concentrations: instead an amorphous structure will form under non-equilibrium conditions. Given enough temperature (or time) the two species will segregate into their pure metals. Even the intermetallic V_2Zr Laves phase has a positive enthalpy of mixing at 0 K and seems to have difficulty nucleating at higher temperatures. Recent insights provided through HEA research would attribute the observed relationship to the difference in atomic radius (represented by δ) between V and Zr. In fact, for any system with a $\delta \geq 6.6$ intermetallic, multiphase or amorphous structures are observed. The latter was modelled here for the first time using static DFT and is the main focus of Chapter 3. Using the techniques developed, further insight into the short range ordering can be studied. This topic is of great interest within the materials community and a comparative study between the newly-developed model and experimental TEM analysis using state of the art aberration-corrected scanning/transmission electron microscopy techniques will be conducted in the future. The relationship between local structures and glass forming ability is still not fully understood. Voronoi analysis will be used to compare the nature of the short range ordering between theory and experiment.

For both V and Zr to exist within a crystalline solid solution in equal concentrations, current theory suggests, additional elements are required to both lower the average distance in atomic radii and provide a larger configurational entropy. However, not *any* elements can be included in the mixture. Chemically similar elements, that do not form strong intermetallic compounds and which do not have a positive enthalpy of mixing with the other species, are required. So then, when is an alloy considered a HEA? The original definition included any alloy with five or more elements within 5 – 35 at. % regardless of microstructure. However this definition loses sight of the key aspect of HEAs that make their concept technologically relevant, i.e. their ability to form a single-phase solid solution that leads to their superior mechanical properties. The revised definition provided within this dissertation differentiates the more general type of HEAs from single phased HEAs (SPHEAs) where both are mixtures of four or more elements where three of the elements are within 0.33 – 1 atomic ratio to the element with the highest concentration and the latter must be able to form a single phase solid solution below the solidus. Four element systems were included in this definition because it has since been found that they have a higher likelihood of forming a single phase solid solution. However, the debate as to what exactly constitutes a HEA, i.e. the arbitrary designation of four/five or more element solid solutions, is still unresolved. Chapter 6 demonstrates the ability for V and Zr to exist together in a single phase solid solution in equal concentrations within NbTiVZr. Future work will attempt to identify the threshold at which the solid solution is stabilised with incremental additions of Nb and Ti. The contributions from enthalpy, entropy and δ will be assessed and a quantitative measure of the HEA classification will attempt to be identified. Furthermore, the influence of lattice strain due to atomic radii mismatch will be investigated and the correlation between δ and lattice strain will attempt to be quantified from the DFT models.

The flagship, four element, FCC HEA CoCrFeNi is explored in Chapter 4. The solid solution is found to have a positive (unfavourable) formation enthalpy suggesting that it is indeed entropically stabilised. Interestingly, Cr has a negative vacancy formation enthalpy from the modelled complete solid solution

which would suggest preferential segregation to Cr metal, carbides or oxides. This system is also thought to undergo a transition from fully disordered FCC to partially ordered $L1_2$ structure below 626 K. A method for calculating the reduction in configurational entropy within the partially ordered structure is also provided within this account which is used to predict this ordered-disordered transition temperature. From here it is possible to anneal samples below this threshold for prolonged periods eg. 500 K for 2000 hrs in attempt to identify this partially ordered phase.

The addition of Al to form the $Al_xCoCrFeNi$ HEA is also considered because an interesting shift from FCC → FCC + BCC → BCC with increasing Al contents is observed in experimental literature. This behaviour is modelled using DFT, for $0 \leq x \leq 2.4$ atomic ratio, where it is found that the disordered BCC solid solution of these five elements is unstable for all compositions. For BCC packing to become stable it is necessary for Al and Ni to be situated on separate lattice sites, analogous to the ordered NiAl B2 intermetallic compound. The XRD patterns of the ordered and disordered BCC packed systems are relatively similar, except that the former presents two additional peaks at ~31° and ~55° 2θ using a Cu Kα X-ray source. There is interest in the addition of Al to refractory systems as it is both light weight and neutron transparent.

Results within Chapter 5 emphasise the importance of the enthalpy of formation of the solid solution which has been neglected within predictive models up until this point. Through a comparison between the Gibbs free energy of a solid solution to that of a mixture of binary intermetallic compounds for any given mixture of elements, a good first approximation to the SPHEA formability is possible. To make this assessment quickly, Miedema's model (a semi-empirical approach) was employed to calculate the enthalpies of mixing. This method was implemented into a computer code christened as Alloy Search and Predict (ASAP) and tested by applying it to 185 previously experimentally studied HEA alloy compositions. It correctly predicted all but sixteen. Of these sixteen systems, fifteen contained Al; one of these (AlCoFeNi) was further investigated using DFT where it was found that it was very likely that partial ordering would be present, similar to that observed in Chapter 4. Although it is not necessarily the case for all the sixteen, it seems that partial ordering is a factor that requires further investigation. In future work a combined study using DFT and XRD analysis will be applied to CoCrFeNi samples annealed below 626 K for three weeks in order to identify the extent of any of partial ordering. The ASAP method can also be used to search the periodic table for SPHEAs using any combination of elements. When searching ~186,000,000 equimolar 4-, 5- and 6-element systems ~1900 novel SPHEA compositions were predicted. Some of these will be manufactured using arc melting and additive manufacturing to verify these new discoveries. Additional software implementation to better model lower order systems will be included in the future. Furthermore, a computational interface between the ASAP software and VASP will be constructed to build a more comprehensive data base of enthalpies of mixing.

Six alloy systems predicted using the ASAP software were produced via arc melting. These were NbTiV, $Mo_{0.5}$NbTiV, MoNbTiV, $NbTiVZr_{0.5}$, NbTiVZr and $NbTiVZr_2$ and the results are described in Chapter 6. All were found to display a single phase BCC structure in the as-cast state. DFT models were also produced for these systems with excellent agreement in lattice parameter. It is expected that these refractory systems will perform the best within an in-core, light-water reactor environment due to their

low thermal neutron cross-sections, BCC crystal structures, high melting temperatures and relatively low number of precipitates in the binary phase diagrams for each individual element. Indeed, from the rule of mixtures, the thermal neutron cross-sections of the Zr containing alloys were smaller than that of steels. However, when assessing the thermodynamic stability of these systems, problems may be encountered below temperatures of 576 – 864 K where the elements are predicted to segregate from the BCC solid solution.

TEM disks of the six systems showed no change in morphology or lattice parameter after ~20 dpa of Au^{5+} irradiation in transmission. However, the bulk $NbTiVZr_2$ sample displayed significant disordering in the XRD pattern 0.18 – 1.11 μm from the surface where 13 – 23 dpa, by Au^{5+} and ~5 dpa by He^{+} ions, is calculated to occur. The exact nature of this feature remains unknown although it is most likely due to defect clusters. Interestingly, these do not occur at the depth at which the peak dpa (~25) is expected (1.5 μm). Calculations of the defect formation energies reveal that unbound Frenkel pairs of Mo, Ti and V are significantly more favourable in the melts compared to their pure metals. Furthermore, many of the interstitial configurations found after energetic minimisation did not correspond to the typical <111> dumbbells or crowdion arrangements, expected in a BCC crystal. Instead, a significant portion were aligned in seemingly random directions. This behaviour is not observed in the ternary NbTiV system which is one of the few instances a difference in behaviour between a highly alloyed ternary and HEA system has been seen. Further work in this area, through strain field analysis, should be conducted to determine whether the addition of a fourth element could contribute to this behaviour.

Despite the relatively large degree of displacive radiation damage, a BCC matrix still remained. By combining the Frenkel defect volume to the change in lattice parameter from experiment, the change in defect concentration between the Au^{5+} irradiated and He^{+} irradiated sample of 0.02 % was estimated.

Altogether, the absence of extensive amorphisation or swelling after a dose, which would typically be received by a cladding material after several years in a light water reactor, is a very promising result. The available evidence indicates that HEAs should be considered relevant to the nuclear industry. Nevertheless, further studies at elevated temperatures and more in-depth characterisation are required to determine the mechanism behind the nucleation of the non-crystalline region.

References

1. Klemm, D., R. Klemm and A. Murr, *Gold of the Pharaohs - 6000 years of gold mining in Egypt and Nubia.* Journal of African Earth Sciences, 2001. **33**(3-4): p. 643-659.
2. Gibbs, J.W., *On the Equilibrium of Hterogeneous Substances.* Transactions of the Connecticut Academy of Arts and Sciences, 1874-1878. **3**(108-248): p. 343-524.
3. Huang, K., *A study on the multicomponent alloy systems containing equal-mole elements*, in *M.S. Thesis*. 1996: Taiwan.
4. Chen, T., *Electrical properties of simple-phase high-entropy AlxCoCrFeNi (0≤ x≤ 2) alloys*. 1996, MS thesis, National Tsing Hua University, Hsinchu, Taiwan ROC.
5. Yeh, J., S. Chen, S. Lin, J. Gan, T. Chin, T. Shun, C. Tsau and S. Chang, *Nanostructured High-Entropy Alloys with Multiple Principal Elements: Novel Alloy Design Concepts and Outcomes.* Advanced Engineering Materials, 2004: p. 299-303.
6. Cantor, B., I. Chang, P. Knight and A. Vincent, *Microstructural development in equiatomic multicomponent alloys.* Materials Science and Engineering A, 2004: p. 213–218.
7. Davidson, J.A. and L.H. Tuneberg, *Niobium-titanium-zirconium-molybdenum (nbtizrmo) alloys for dental and other medical device applications*. 2001, Google Patents.
8. Kleykamp, H., *The chemical state of the fission products in oxide fuels.* Journal of Nuclear Materials, 1985. **131**(2–3): p. 221-246.
9. King, D.J.M., S.C. Middleburgh, A.G. McGregor and M.B. Cortie, *Predicting the formation and stability of single phase high-entropy alloys.* Acta Materialia, 2016. **104**: p. 172-179.
10. *Nuclear Power Reactors in the World.* Online, 2011.
11. Fisher, S., J. Hardbottle and N. Aldridge, *Radiation hardening in Magnox pressure-vessel steels.* Philosophical Transactions of the Royal Society A-Mathematical Physical and Engineering Sciences, 1985: p. 301-332.
12. Allen, T.R., P.J. King and L. Nelson. *General corrosion properties of titanium based alloys for the fuel claddings in the supercritical water-cooled reactor*. in *Environmental Degradation of Materials in Nuclear Power System - Water Reactors*. 2005. Japan: The Minerals, Metals and Materials Society.
13. Matsuo, Y., Y. Suda and N. Suda, *Patent No: 4963323.* Japan, 1990.
14. Naslain, R., *Design, preparation and properties of non-oxide CMCs for application in engines and nuclear reactors: an overview.* Composites Science and Technology, 2004: p. 155-170.
15. Nanstad, R.K., *Encyclopedia of Materials Science and Engineering*. 1986, Bever, M. B.: New York. p. 3928.
16. Olander, D., *Nuclear fuels - Present and future.* Journal of Nuclear Materials, 2009: p. 1-22.
17. *A Technology Roadmap for Generation IV Nuclear Energy Systems*. 2002, U.S. DOE Nuclear Energy Research Advisory Committee.
18. Allen, T., J. Busby, M. Meyer and D. Petti, P, *Material challenges for nuclear systems.* Materials Today, 2010: p. 15-23.
19. Yvon, P. and F. Carré, *Structural materials challenges for advanced reactor systems.* Journal of Nuclear Materials, 2009: p. 217-222.
20. Smith, C., *Nuclear Reactor Materials*. 1967, Detroit: Addison-Wesley.
21. Urbanic, V. and T. Heidrick, *High-temperature oxidation of Zircaloy-2 and Zircaloy-4 in steam.* Journal of Nuclear Materials, 1978: p. 251-261.
22. Bradbrook, J., G. Lorimaer and N. Ridley, *The precipitation of zirconium hydride in zirconium and Zircaloy-2.* Jounral of Nuclear Materials, 1972: p. 142-160.
23. Ursu, I., *Physics and Technology of Nuclear Materials*. 1985, Bucharest: Pergamon Press.
24. Tanaka, S., *Accident at the Fukushima Dai-ichi Nuclear Power Stations of TEPCO -Outline & lessons learned-.* Proceedings of the Japan Academy, 2012: p. 471-484.
25. Whitmarsh, C., *Review of Zircaloy-2 and Zircaloy-4 properties relevant to N.S. Savannah reactor design*. 1962, Oak Ridge National Laboratory: Tennessee.
26. Speidel, M. and R. Magdowski, *Stress corrosion cracking of nuclear reactor pressure vessel and piping steels.* International Journal of Pressure Vessels and Piping, 1988: p. 119-142.
27. Lucas, G., *The evolution of mechanical property change in irradiated austenitic stainless steels.* Journal of Nuclear Materials, 1993: p. 287-305.
28. Fultz, B., *Vibrational thermodynamics of materials.* Progress in Materials Science, 2010. **55**(4): p. 247-352.
29. van de Walle, A. and G. Ceder, *The effect of lattice vibrations on substitutional alloy thermodynamics.* Reviews of Modern Physics, 2002. **74**(1): p. 11-45.

30. Benisek, A. and E. Dachs, *The vibrational and configurational entropy of disordering in Cu3Au.* Journal of Alloys and Compounds, 2015. **632**(0): p. 585-590.
31. Swalin, R., *Thermodynamics of Solids*. 1991, Wiley: New York. p. 21.
32. Feller, W., *Stirling's formula.* An introduction to probability theory and its applications, 1968. **1**: p. 50-53.
33. Hildebrand, J.H., *A quantitative treatment of deviations from Raoult's law.* Proceedings of the National Academy of Sciences of the United States of America, 1927. **13**: p. 267-272.
34. Hardy, H.K., *A "sub-regular" solution model and its application to some binary alloy systems.* Acta Metallurgica, 1953. **1**(2): p. 202-209.
35. Niu, C., A.J. Zaddach, A.A. Oni, X. Sang, J.W. Hurt, J.M. LeBeau, C.C. Koch and D.L. Irving, *Spin-driven ordering of Cr in the equiatomic high entropy alloy NiFeCrCo.* Applied Physics Letters, 2015. **106**(16): p. 161906.
36. Santodonato, L.J., Y. Zhang, M. Feygenson, C.M. Parish, M.C. Gao, R.J. Weber, J.C. Neuefeind, Z. Tang and P.K. Liaw, *Deviation from high-entropy configurations in the atomic distributions of a multi-principal-element alloy.* Nature communications, 2015. **6**.
37. King, D.M., S.C. Middleburgh, L. Edwards, G.R. Lumpkin and M. Cortie, *Predicting the Crystal Structure and Phase Transitions in High-Entropy Alloys.* JOM, 2015: p. 1-6.
38. Ye, Y.F., Q. Wang, J. Lu, C.T. Liu and Y. Yang, *Design of high entropy alloys: A single-parameter thermodynamic rule.* Scripta Mater, 2015. **104**(0): p. 53-55.
39. Wissner-Gross, A.D. and C.E. Freer, *Causal entropic forces.* Physical review letters, 2013. **110**(16): p. 168702.
40. Zhou, Y., Y. Zhang, Y. Wang and G. Chen, *Microstructure and compressive properties of multicomponent Alx(TiVCrMnFeCoNiCu)100-x high-entropy alloys.* Materials Science and Engineering A, 2007: p. 260-265.
41. Li, B., Y. Wang, M. Ren, C. Yang and H. Fu, *Effects of Mn, Ti and V on the microstructure and properties of AlCrFeCoNiCu high entropy alloy.* Materials Science and Engineering: A, 2008. **498**(1): p. 482-486.
42. Chen, Y.-L., Y.-H. Hu, C.-A. Hsieh, J.-W. Yeh and S.-K. Chen, *Competition between elements during mechanical alloying in an octonary multi-principal-element alloy system.* Journal of Alloys and Compounds, 2009. **481**(1): p. 768-775.
43. Yang, X. and Y. Zhang, *Prediction of high-entropy stabilized solid-solution in multi-component alloys.* Materials Chemistry and Physics, 2012: p. 233-238.
44. Boer, F.R.d., *Cohesion in metals: transition metal alloys*. Cohesion and structure ;v. 1. 1988, Amsterdam ; New York : New York, N.Y., U.S.A.: North-Holland ; Sole distributors for the U.S.A. and Canada, Elsevier Scientific Pub. Co. xvi, 758 p.
45. Takeuchi, A. and A. Inoue, *Quantitative evaluation of critical cooling rate for metallic glasses.* Materials Science and Engineering: A, 2001. **304–306**(0): p. 446-451.
46. Takeuchi, A. and A. Inoue, *Mixing enthalpy of liquid phase calculated by miedema's scheme and approximated with sub-regular solution model for assessing forming ability of amorphous and glassy alloys.* Intermetallics, 2010. **18**(9): p. 1779-1789.
47. Singh, A.K., N. Kumar, A. Dwivedi and A. Subramaniam, *A geometrical parameter for the formation of disordered solid solutions in multi-component alloys.* Intermetallics, 2014. **53**: p. 112-119.
48. Wang, Z.J., Y.H. Huang, Y. Yang, J.C. Wang and C.T. Liu, *Atomic-size effect and solid solubility of multicomponent alloys.* Scripta Materialia, 2015. **94**: p. 28-31.
49. Zhang, Y., T.T. Zuo, Z. Tang, M.C. Gao, K.A. Dahmen, P.K. Liaw and Z.P. Lu, *Microstructures and properties of high-entropy alloys.* Progress in Materials Science, 2014. **61**(0): p. 1-93.
50. Jones, N.G., J.W. Aveson, A. Bhowmik, B.D. Conduit and H.J. Stone, *On the entropic stabilisation of an Al0.5CrFeCoNiCu high entropy alloy.* Intermetallics, 2014. **54**: p. 148-153.
51. Tsai, K., M. Tsai and J. Yeh, *Sluggish diffusion in Co-Cr-Fe-Mn-Ni high-entropy alloys.* Acta Materialia, 2013: p. 4887-4897.
52. Tsai, C., Y. Chen, M. Tsai, J. Yeh, T. Shun and S. Chen, *Deformation and annealing behaviors of high-entropy alloy Al0.5CoCrCuFeNi.* Journal of Alloys and Compounds, 2009: p. 427-435.
53. Lucas, M., G. Wilks, L. Mauger, J.A. Munoz, O. Senkov, E. Michel, J. Horwath, S. Semiatin, M.B. Stone and D.L. Abernathy, *Absence of long-range chemical ordering in equimolar FeCoCrNi.* Applied Physics Letters, 2012. **100**(25): p. 251907.
54. Tsai, M., J. Yeh and J. Gan, *Diffusion barrier properties of AlMoNbSiTaTiVZr high-entropy alloy layer between copper and silicon.* Thin Solid Films, 2008: p. 5527-5530.
55. Jones, N., K. Christofidou and H. Stone, *Rapid precipitation in an Al0⊙5CrFeCoNiCu high entropy alloy.* Materials Science and Technology, 2015: p. 1743284715Y. 0000000004.

56. Chou, H., Y. Chang, S. Chen and J. Yeh, *Microstructure, thermophysical and electrical properties in AlxCoCrFeNi (0<x<2) high-entropy alloys.* Materials Science and Engineering B, 2009: p. 184-189.
57. Wang, W., W. Wang, S. Wang, Y. Tsai, C. Lai and J. Yeh, *Effects of Al addition on the microstructure and mechanical property of AlxCoCrFeNi high-entropy alloys.* Intermetallics, 2012: p. 44-51.
58. Yeh, J.W., Y.L. Chen, S.J. Lin and S.K. Chen, *High-entropy alloys - A new era of exploitation.* Advanced Structural Materials III, 2007. **560**: p. 1-9.
59. Wang, F., Y. Zhang and G. Chen, *Atomic packing efficiency and phase transition in a high entropy alloy.* Journal of Alloys and Compounds, 2009: p. 321-324.
60. Greenwood, N. and A. Earnshaw, *Chemistry of the Elements (2nd Edition)*. 1997: Butterworth-Heinemann.
61. Guo, S., C. Ng, J. Lu and C. Liu, *Effect of valence electron concentration on stability of fcc or bcc phase in high entropy alloys.* Journal of Applied Physics, 2011: p. 103505-1 - 103505-5.
62. Rothery, W.H., *Researches on the nature, properties, and conditions of formation of intermetallic compounds, with special reference to certain compounds of tin-I -V.* Journal of the Institute of Metals, 1926. **35**: p. 295-354.
63. Poletti, M.G. and L. Battezzati, *Electronic and thermodynamic criteria for the occurrence of high entropy alloys in metallic systems.* Acta Materialia, 2014. **75**(0): p. 297-306.
64. Mizutani, U., *Hume-Rothery rules for structurally complex alloy phases*. 2010: CRC Press.
65. Kao, Y., T. Chen, S. Chen and J. Yeh, *Microstructure and mechanical property of as-cast, homogenized, and deformed AlxCoCrFeNi (0<x<2) high-entropy alloys.* Journal of Alloys and Compounds, 2009: p. 57-64.
66. Wu, Z., H. Bei, F. Otto, G.M. Pharr and E.P. George, *Recovery, recrystallization, grain growth and phase stability of a family of FCC-structured multi-component equiatomic solid solution alloys.* Intermetallics, 2014. **46**(0): p. 131-140.
67. Otto, F., A. Dlouhý, C. Somsen, H. Bei, G. Eggeler and E.P. George, *The influences of temperature and microstructure on the tensile properties of a CoCrFeMnNi high-entropy alloy.* Acta Materialia, 2013. **61**(15): p. 5743-5755.
68. Gali, A. and E.P. George, *Tensile properties of high- and medium-entropy alloys.* Intermetallics, 2013. **39**(0): p. 74-78.
69. Otto, F., Y. Yang, H. Bei and E.P. George, *Relative effects of enthalpy and entropy on the phase stability of equiatomic high-entropy alloys.* Acta Materialia, 2013. **61**(7): p. 2628-2638.
70. Gludovatz, B., A. Hohenwarter, D. Catoor, E.H. Chang, E.P. George and R.O. Ritchie, *A fracture-resistant high-entropy alloy for cryogenic applications.* Science, 2014. **345**(6201): p. 1153-8.
71. Hoyt, J.J., M. Asta and A. Karma, *Atomistic and continuum modeling of dendritic solidification.* Materials Science and Engineering: R: Reports, 2003. **41**(6): p. 121-163.
72. Liu, W., Y. Wu, J. He, T. Nieh and Z. Lu, *Grain growth and the Hall-Petch relationship in a high-entropy FeCrNiCoMn alloy.* Scripta Materialia, 2013: p. 526-529.
73. Salishchev, G.A., M.A. Tikhonovsky, D.G. Shaysultanov, N.D. Stepanov, A.V. Kuznetsov, I.V. Kolodiy, A.S. Tortika and O.N. Senkov, *Effect of Mn and V on structure and mechanical properties of high-entropy alloys based on CoCrFeNi system.* Journal of Alloys and Compounds, 2014. **591**: p. 11-21.
74. Senkov, O.N., G.B. Wilks, D.B. Miracle, C.P. Chuang and P.K. Liaw, *Refractory high-entropy alloys.* Intermetallics, 2010. **18**(9): p. 1758-1765.
75. Senkov, O.N. and C.F. Woodward, *Microstructure and properties of a refractory NbCrMo0.5Ta0.5TiZr alloy.* Materials Science and Engineering a-Structural Materials Properties Microstructure and Processing, 2011. **529**: p. 311-320.
76. Senkov, O.N., S.V. Senkova, C. Woodward and D.B. Miracle, *Low-density, refractory multi-principal element alloys of the Cr-Nb-Ti-V-Zr system: Microstructure and phase analysis.* Acta Materialia, 2013. **61**(5): p. 1545-1557.
77. Senkov, O.N., S.V. Senkova and C. Woodward, *Effect of aluminum on the microstructure and properties of two refractory high-entropy alloys.* Acta Materialia, 2014. **68**(15): p. 214-228.
78. Senkov, O.N., C. Woodward and D.B. Miracle, *Microstructure and Properties of Aluminum-Containing Refractory High-Entropy Alloys.* Journal of Minerals, Metals & Materials Society, 2014. **66**(10): p. 2030-2042.
79. Singh, S., N. Wanderka, B. Murty, U. Glatzel and J. Banhart, *Decomposition in multi-component AlCoCrCuFe high entropy alloy.* Acta Materialia, 2011: p. 182-190.

80. Shun, T. and Y. Du, *Microstructure and tensile behaviours of FCC Al0.3CoCrFeNi high entropy alloy.* Journal of Alloys and Compounds, 2009: p. 157-160.
81. Miracle, D.B., J.D. Miller, O.N. Senkov, C. Woodward, M.D. Uchic and J. Tiley, *Exploration and Development of High Entropy Alloys for Structural Applications.* Entropy, 2014. **16**(1): p. 494-525.
82. Neuhäuser, H. and C. Schwink, *Solid solution strengthening.* Materials science and technology, 1993.
83. Senkov, O.N., J.M. Scott, S.V. Senkova, D.B. Miracle and C.F. Woodward, *Microstructure and room temperature properties of a high-entropy TaNbHfZrTi alloy.* Journal of Alloys and Compounds, 2011. **509**(20): p. 6043-6048.
84. Sauthoff, G., *Multiphase intermetallic alloys for structural applications.* Intermetallics, 2000. **8**(9–11): p. 1101-1109.
85. Westbrook, J.H. and R.L. Fleischer, *Intermetallic Compounds, Basic Mechanical Properties and Lattice Defects of*. 2000: Wiley.
86. Wang, Y., S. Ma, X. Chen, J. Shi, Y. Zhang and J. Qiao, *Optimizing mechanical properties of AlCoCrFeNiTi x high-entropy alloys by tailoring microstructures.* Acta Metallurgica Sinica (English Letters), 2013. **26**(3): p. 277-284.
87. Qiao, J.W., S.G. Ma, E.W. Huang, C.P. Chuang, P.K. Liaw and Y. Zhang, *Microstructural characteristics and mechanical behaviors of AlCoCrFeNi high-entropy alloys at ambient and cryogenic temperatures*, in *Nano-Scale and Amourphous Materials*, R.M. Wang, Y. Wu, and X.F. Wu, Editors. 2011, Trans Tech Publications Ltd: Stafa-Zurich. p. 419-425.
88. Ryan, M.P., D.E. Williams, R.J. Chater, B.M. Hutton and D.S. McPhail, *Why stainless steel corrodes.* Nature, 2002. **415**(6873): p. 770-774.
89. Stott, F., G. Wood and J. Stringer, *The influence of alloying elements on the development and maintenance of protective scales.* Oxidation of metals, 1995. **44**(1-2): p. 113-145.
90. Senkov, O., S. Senkova, D. Dimiduk, C. Woodward and D. Miracle, *Oxidation behavior of a refractory $NbCrMo_{0.5}Ta_{0.5}TiZr$ alloy.* Journal of Materials Science, 2012. **47**(18): p. 6522-6534.
91. Merz, M.D., *The oxidation resistance of fine-grained sputter-deposited 304 stainless steel.* Metallurgical Transactions A, 1979. **10**(1): p. 71-77.
92. Chuang, M., M. Tsai, W. Wang, S. Lin and J. Yeh, *Microstructure and wear behavior of AlxCo1.5CrFeNi1.5Tiy.* Acta Materialia, 2011: p. 6308-6317.
93. Huang, C., Y. Zhang, J. Shen and R. Vilar, *Thermal stability and oxidation resistance of laser clad TiVCrAlSi high entropy alloy coatings on Ti–6Al–4V alloy.* Surface & Coatings Technology, 2011: p. 1389-1395.
94. DeVan, J. and P. Tortorelli, *The oxidation-sulfidation behavior of iron alloys containing 16–40 AT% aluminum.* Corrosion Science, 1993. **35**(5): p. 1065-1071.
95. Chen, S.-T., W.-Y. Tang, Y.-F. Kuo, S.-Y. Chen, C.-H. Tsau, T.-T. Shun and J.-W. Yeh, *Microstructure and properties of age-hardenable Al x CrFe 1.5 MnNi 0.5 alloys.* Materials Science and Engineering: A, 2010. **527**(21): p. 5818-5825.
96. Frankel, G., *Pitting corrosion of metals a review of the critical factors.* Journal of the Electrochemical Society, 1998. **145**(6): p. 2186-2198.
97. Chen, Y., U. Hong, H. Shih, J. Yeh and T. Duval, *Electrochemical kinetics of the high entropy alloys in aqueous environments - a comparison with type 304 stainless steel.* Corrosion Science, 2005: p. 2679-2699.
98. Hsu, Y., W. Chiang and J. Wu, *Corrosion behavior of $FeCoNiCrCu_x$ high-entropy alloys in 3.5% sodium chloride solution.* Materials Chemistry and Physics, 2005: p. 112-117.
99. Ren, B., Z. Liu, D. Li, L. Shi, B. Cai and M. Wang, *Corrosion behavior of CuCrFeNiMn high entropy alloy system in 1M sulfuric acid solution.* Materials and Corrosion, 2012: p. 828-834.
100. Lee, C., C. Chang, Y. Chen, J. Yeh and H. Shih, *Effect of the aluminium content of AlxCrFe1.5MnNi0.5 high-entropy alloys on the corrosion behaviour in aqueous environments.* Corrosion Science, 2008: p. 2053-2060.
101. Lin, C. and H. Tsai, *Evolution of microstructure, hardness, and corrosion properties of high-entropy Al0.5CoCrFeNi alloy.* Intermetallics, 2011: p. 288-294.
102. Hongbao, C., W. Ying, W. Jinyong, G. Xuefeng and F. Hengzhi, *Microstructural evolution and corrosin behavior of directionally solidified FeCoNiCrAl high entropy alloy.* China Foundry, 2011: p. 259-263.
103. Lee, C., Y. Chen, C. Hsu, J. Yeh and H. Shih, *Enhancing pitting corrosion resistance of AlxCrFe1.5MnNi0.5 high-entropy alloys by anodic treatment in sulfuric acid.* Thin Solid Films, 2008: p. 1301-1305.

104. Kao, Y.-F., T.-D. Lee, S.-K. Chen and Y.-S. Chang, *Electrochemical passive properties of AlxCoCrFeNi (x= 0, 0.25, 0.50, 1.00) alloys in sulfuric acids.* Corrosion Science, 2010. **52**(3): p. 1026-1034.
105. Zhang, C., F. Zhang, S.L. Chen and W.S. Cao, *Computational Thermodynamics Aided High-Entropy Alloy Design.* Journal of Minerals, Metals & Materials Society, 2012. **64**(7): p. 839-845.
106. Chang, Y.A., S. Chen, F. Zhang, X. Yan, F. Xie, R. Schmid-Fetzer and W.A. Oates, *Phase diagram calculation: past, present and future.* Progress in Materials Science, 2004. **49**(3–4): p. 313-345.
107. Kao, Y., S. Chen, T. Chen, P. Chu, J. Yeh and S. Lin, *Electrical, magnetic, and Hall properties of AlxCoCrFeNi high-entropy alloys.* Journal of Alloys and Compounds, 2011: p. 1607-1614.
108. Tian, F.Y., L. Delczeg, N.X. Chen, L.K. Varga, J. Shen and L. Vitos, *Structural stability of NiCoFeCrAlx high-entropy alloy from ab initio theory.* Physical Review B, 2013. **88**(8): p. 5.
109. King, D.J.M., S.C. Middleburgh, L. Edwards, G.R. Lumpkin and M. Cortie, *Predicting the crystal structure and phase transitions in high entropy alloys.* Journal of Minerals, Metals & Materials Society, 2015.
110. Senkov, O.N., J.D. Miller, D.B. Miracle and C. Woodward, *Accelerated exploration of multi-principal element alloys with solid solution phases.* Nat Commun, 2015. **6**.
111. Chen, S.-L., S. Daniel, F. Zhang, Y. Chang, X.-Y. Yan, F.-Y. Xie, R. Schmid-Fetzer and W. Oates, *The PANDAT software package and its applications.* Calphad, 2002. **26**(2): p. 175-188.
112. King, D.J.M., S.C. Middleburgh, A.C.Y. Liu, H.A. Tahini, G.R. Lumpkin and M.B. Cortie, *Formation and structure of V–Zr amorphous alloy thin films.* Acta Materialia, 2015. **83**: p. 269-275.
113. Wei, S.H., L.G. Ferreira, J.E. Bernard and A. Zunger, *Electronic properties of random alloys: Special quasirandom structures.* Physical Review B, 1990. **42**(15): p. 9622-9649.
114. Zunger, A., S.H. Wei, L.G. Ferreira and J.E. Bernard, *Special quasirandom structures.* Physical Review Letters, 1990. **65**(3): p. 353-356.
115. Van de Walle, A., P. Tiwary, M. De Jong, D. Olmsted, M. Asta, A. Dick, D. Shin, Y. Wang, L.-Q. Chen and Z.-K. Liu, *Efficient stochastic generation of special quasirandom structures.* Calphad, 2013. **42**: p. 13-18.
116. Pokluda, J., M. Černý, M. Šob and Y. Umeno, *Ab initio calculations of mechanical properties: Methods and applications.* Progress in Materials Science, 2015. **73**: p. 127-158.
117. Cao, P., X. Ni, F. Tian, L.K. Varga and L. Vitos, *Ab initio study of AlxMoNbTiV high-entropy alloys.* Journal of Physics: Condensed Matter, 2015. **27**(7): p. 075401.
118. Tian, F.Y., L.K. Varga, N.X. Chen, J. Shen and L. Vitos, *Ab initio design of elastically isotropic TiZrNbMoVx high-entropy alloys.* Journal of Alloys and Compounds, 2014. **599**: p. 19-25.
119. Li, X., F. Tian, S. Schönecker, J. Zhao and L. Vitos, *Ab initio-predicted micro-mechanical performance of refractory high-entropy alloys.* Scientific reports, 2015. **5**.
120. Troparevsky, M.C., J.R. Morris, P.R. Kent, A.R. Lupini and G.M. Stocks, *Criteria for Predicting the Formation of Single-Phase High-Entropy Alloys.* Physical Review X, 2015. **5**(1): p. 011041.
121. Kresse, G. and J. Furthmüller, *Software VASP, vienna (1999).* Phys. Rev. B, 1996. **54**(11): p. 169.
122. Born, M. and R. Oppenheimer, *Zur Quantentheorie der Molekeln.* Annalen der Physik, 1927. **389**(20): p. 457-484.
123. Hooke, R., *A description of helioscopes, and some other instruments John Martin, London (1676).* See anagram on title page concerning "The true Mathematical and Mechanical form of all manner of Arches.
124. Hohenberg, P. and W. Kohn, *Inhomogeneous Electron Gas.* Physical Review, 1964. **136**(3B): p. B864-B871.
125. Hartree, D.R. *The wave mechanics of an atom with a non-Coulomb central field. Part I. Theory and methods*. in *Mathematical Proceedings of the Cambridge Philosophical Society*. 1928. Cambridge Univ Press.
126. Hartree, D.R. *The wave mechanics of an atom with a non-Coulomb central field. Part II. Some results and discussion*. in *Mathematical Proceedings of the Cambridge Philosophical Society*. 1928. Cambridge Univ Press.
127. Kohn, W. and L.J. Sham, *Self-Consistent Equations Including Exchange and Correlation Effects.* Physical Review, 1965. **140**(4A): p. A1133-A1138.
128. Perdew, J.P., K. Burke and M. Ernzerhof, *Generalized gradient approximation made simple.* Physical review letters, 1996. **77**(18): p. 3865.

129. Burke, K., *Perspective on density functional theory.* The Journal of chemical physics, 2012. **136**(15): p. 150901.
130. Lejaeghere, K., V. Van Speybroeck, G. Van Oost and S. Cottenier, *Error estimates for solid-state density-functional theory predictions: an overview by means of the ground-state elemental crystals.* Critical Reviews in Solid State and Materials Sciences, 2014. **39**(1): p. 1-24.
131. Anisimov, V.I., J. Zaanen and O.K. Andersen, *BAND THEORY AND MOTT INSULATORS - HUBBARD-U INSTEAD OF STONER-I.* Physical Review B, 1991. **44**(3): p. 943-954.
132. Delley, B., *An all-electron numerical method for solving the local density functional for polyatomic molecules.* The Journal of chemical physics, 1990. **92**(1): p. 508-517.
133. Delley, B., *From molecules to solids with the DMol3 approach.* The Journal of chemical physics, 2000. **113**(18): p. 7756-7764.
134. Blaha, P., K. Schwarz, G. Madsen, D. Kvasnicka and J. Luitz, *wien2k.* An augmented plane wave+ local orbitals program for calculating crystal properties, 2001.
135. Soler, J.M., E. Artacho, J.D. Gale, A. García, J. Junquera, P. Ordejón and D. Sánchez-Portal, *The SIESTA method for ab initio order-N materials simulation.* Journal of Physics: Condensed Matter, 2002. **14**(11): p. 2745.
136. Gonze, X., J.-M. Beuken, R. Caracas, F. Detraux, M. Fuchs, G.-M. Rignanese, L. Sindic, M. Verstraete, G. Zerah and F. Jollet, *First-principles computation of material properties: the ABINIT software project.* Computational Materials Science, 2002. **25**(3): p. 478-492.
137. Clark, S.J., M.D. Segall, C.J. Pickard, P.J. Hasnip, M.I. Probert, K. Refson and M.C. Payne, *First principles methods using CASTEP.* Zeitschrift für Kristallographie, 2005. **220**(5/6/2005): p. 567-570.
138. Wigner, E.P. and F. Seitz, *On the constitution of metallic sodium*, in *Part I: Physical Chemistry. Part II: Solid State Physics*. 1997, Springer. p. 365-371.
139. Monkhorst, H.J. and J.D. Pack, *Special points for Brillouin-zone integrations.* Physical Review B, 1976. **13**(12): p. 5188.
140. Francis, G. and M. Payne, *Finite basis set corrections to total energy pseudopotential calculations.* Journal of Physics: Condensed Matter, 1990. **2**(19): p. 4395.
141. Blöchl, P.E., *Projector augmented-wave method.* Physical Review B, 1994. **50**(24): p. 17953.
142. Kresse, G. and D. Joubert, *From ultrasoft pseudopotentials to the projector augmented-wave method.* Physical Review B, 1999. **59**(3): p. 1758.
143. Torrent, M., F. Jollet, F. Bottin, G. Zérah and X. Gonze, *Implementation of the projector augmented-wave method in the ABINIT code: Application to the study of iron under pressure.* Computational Materials Science, 2008. **42**(2): p. 337-351.
144. Kittel, C., *Introduction to solid state physics*. 2005: Wiley.
145. Bakker, H., *Enthalpies in Alloys: Miedema's Semi-empirical Model*. 1998: Trans Tech Publications.
146. Miedema, A., R. Boom, F. De Boer, G. Rooymans and A. Rabenau, *Crystal Structure and Chemical Bonding in Inorganic Chemistry.* North-Holland/American Elsevier, 1975: p. 163.
147. Chelikowsky, J.R. and J.C. Phillips, *QUANTUM-DEFECT THEORY OF HEATS OF FORMATION AND STRUCTURAL TRANSITION ENERGIES OF LIQUID AND SOLID SIMPLE METAL-ALLOYS AND COMPOUNDS.* Physical Review B, 1978. **17**(6): p. 2453-2477.
148. Zhang, R.F., *Miedema Calculator.* http://www.zrftum.wordpress.com, 2009.
149. Eshelby, J., *The continuum theory of lattice defects.* Solid state physics, 1956. **3**: p. 79-144.
150. Niessen, A.K. and A.R. Miedema, *The enthalpy effect on forming diluted solid solutions of two 4d and 5d transition metals.* Berichte der Bunsengesellschaft für physikalische Chemie, 1983. **87**(9): p. 717-725.
151. Takeuchi, A. and A. Inoue, *Classification of bulk metallic glasses by atomic size difference, heat of mixing and period of constituent elements and its application to characterization of the main alloying element.* Materials Transactions, 2005. **46**(12): p. 2817-2829.
152. Choy, K.L., *Chemical vapour deposition of coatings.* Progress in Materials Science, 2003. **48**(2): p. 57-170.
153. Rietveld, H., *Line profiles of neutron powder-diffraction peaks for structure refinement.* Acta Crystallographica, 1967. **22**(1): p. 151-152.
154. Rietveld, H., *A profile refinement method for nuclear and magnetic structures.* Journal of applied Crystallography, 1969. **2**(2): p. 65-71.
155. Bruker, A., *TOPAS V3: General profile and structure analysis software for powder diffraction data.* User's Manual, Bruker AXS, Karlsruhe, Germany, 2005.
156. Pestov, S., *jEdit open source programmer's text editor*. 2002, http://www.jedit.org/.

157. Lumpkin, G.R., K.L. Smith, M.G. Blackford, R. Gieré and C. Terry Williams, *Determination of 25 elements in the complex oxide mineral zirconolite by analytical electron microscopy.* Micron, 1994. **25**(6): p. 581-587.
158. Brown, R.b.P.D., *Transmission Electron Microscopy-A Textbook for Materials Science, by David B. Williams and C. Barry Carter.* Microscopy and Microanalysis, 1999. **5**(06): p. 452-453.
159. Minehara, E., S. Abe, T. Yoshida, Y. Sato, M. Kanda, C. Kobayashi and S. Hanashima, *On the production of the KrF− and XeF− Ion beams for the tandem electrostatic accelerators.* Nuclear Instruments and Methods in Physics Research Section B: Beam Interactions with Materials and Atoms, 1984. **5**(2): p. 217-220.
160. Zinkle, S.J. and J.T. Busby, *Structural materials for fission & fusion energy.* Materials Today, 2009. **12**(11): p. 12-19.
161. Ziegler, J. and J. Biersack, *The Stopping and Range of Ions in Matter*, in *Treatise on Heavy-Ion Science*, D.A. Bromley, Editor. 1985, Springer US. p. 93-129.
162. Robinson, M.T. and I.M. Torrens, *Computer simulation of atomic-displacement cascades in solids in the binary-collision approximation.* Physical Review B, 1974. **9**(12): p. 5008.
163. Sears, V., *Neutron scattering lengths and cross sections.* Neutron News, 1992: p. 29-37.
164. Handbook, D.F., *Nuclear Physics and Reactor Theory.* Washington DC: Department of Energy, 1993.
165. Khrushchov, M. and E. Berkovich, *Methods of determining the hardness of very hard materials: the hardness of diamond.* Industrial diamond review, 1951. **11**: p. 42-49.
166. Smith, D., H. Chung, B. Loomis, H. Matsui, S. Votinov and W. Witzenburg, *Development of vanadium-base alloys for fusion first-wall—blanket applications.* Fusion Engineering and Design, 1995: p. 399-410.
167. Young, D.A., *Phase Diagrams of the Elements*. 1975, Virginia, USA: University of California.
168. Hume-Rothery, W., *Atomic Theory for Students of Metallugy*. 1969, London.
169. Enomoto, M., *The Ti-V-Zr System.* Journal of Phase Equilibria, 1992: p. 206-210.
170. Eickert, S., H. Hecht and G. Minnigerode, *Formation area of amorphous thin V-Zr films prepared by cocondensation on hot substrates.* Zeitschrift für Physik B Condensed Matter, 1992: p. 35-38.
171. Kabliman, E.A., A.A. Mirzoev and A.L. Udovskii, *First-Principles Simulation of an Ordered Sigma Phase of the Fe-Cr System in the Ferromagnetic State.* Physics of Metals and Metallography, 2009. **108**(5): p. 435-440.
172. Lumley, S., S. Murphy, P. Burr, R. Grimes, P. Chard-Tuckey and M. Wenman, *The stability of alloying additions in Zirconium.* Journal of Nuclear Materials, 2013. **437**(1): p. 122-129.
173. Fruchart, D., A. Rouault, C.B. Shoemaker and D.P. Shoemaker, *NEUTRON-DIFFRACTION STUDIES OF THE CUBIC ZRCR2DX AND ZRV2DX(HX)PHASES.* Journal of the Less-Common Metals, 1980. **73**(2): p. 363-368.
174. Mantina, M., R. Valero, C. Cramer and D. Truhlar, *Atomic radii of the elements*, in *CRC Handbook of Chemistry and Physics*, T. Bruno, et al., Editors. 2013, Taylor and Francis Group LLC: Internet Version. p. 9-49 - 9-50.
175. Howie, A., *Application of electron optical techniques to the study of amorphous materials.* Philosophical Magazine, 2010. **90**(35-36): p. 4647-4660.
176. Fan, Y., T. Iwashita and T. Egami, *Evolution of elastic heterogeneity during aging in metallic glasses.* Physical Review E, 2014. **89**(6): p. 7.
177. Sheng, H.W., W.K. Luo, F.M. Alamgir, J.M. Bai and E. Ma, *Atomic packing and short-to-medium-range order in metallic glasses.* Nature, 2006. **439**(7075): p. 419-425.
178. Štich, I., R. Car and M. Parrinello, *Amorphous silicon studied by ab initio molecular dynamics: Preparation, structure, and properties.* Physical Review B, 1991. **44**(20): p. 11092-11104.
179. Vegard, L., *Die Konstitution der Mischkristalle und die Raumfüllung der Atome.* Zeitschrift für Physik, 1921. **5**(1): p. 17-26.
180. Hammond, C., *Melting, Boiling, Triple, and Critical Points of the Elements*, in *CRC Handbook of Chemistry and Physics*. 2013, Taylor and Francis Group, LLC: Online. p. 4-121 - 4-213.
181. Wakeda, M., Y. Shibutani, S. Ogata and J. Park, *Relationship between local geometrical factors and mechanical properties for Cu–Zr amorphous alloys.* Intermetallics, 2007. **15**(2): p. 139-144.
182. Cheng, Y.Q. and E. Ma, *Atomic-level structure and structure-property relationship in metallic glasses.* Progress in Materials Science, 2011. **56**(4): p. 379-473.
183. Lumley, S.C., R.W. Grimes, S.T. Murphy, P.A. Burr, A. Chroneos, P.R. Chard-Tuckey and M.R. Wenman, *The thermodynamics of hydride precipitation: The importance of entropy, enthalpy and disorder.* Acta Materialia, 2014. **79**(0): p. 351-362.

184. Rodney, D., A. Tanguy and D. Vandembroucq, *Modeling the mechanics of amorphous solids at different length scale and time scale.* Modelling and Simulation in Materials Science and Engineering, 2011. **19**(8): p. 49.
185. Li, Y., S. Poon, G. Shiflet, J. Xu, D. Kim and J. Löffler, *Formation of bulk metallic glasses and their composites.* MRS bulletin, 2007. **32**(08): p. 624-628.
186. Takeuchi, A., N. Chen, T. Wada, Y. Yokoyama, H. Kato, A. Inoue and J. Yeh, *Pd20Pt20Cu20Ni20P20 high-entropy alloy as a bulk metallic glass in the centimeter.* Intermetallics, 2011: p. 1546-1554.
187. Takeuchi, A., J.Q. Wang, N. Chen, W. Zhang, Y. Yokoyama, K. Yubuta and S.L. Zhu, *Al0.5TiZrPdCuNi High-Entropy (H-E) Alloy Developed through Ti20Zr20Pd20Cu20Ni20 H-E Glassy Alloy Comprising Inter-Transition Metals.* Materials Transactions, 2013. **54**(5): p. 776-782.
188. Ding, H.Y. and K.F. Yao, *High entropy Ti20Zr20Cu20Ni20Be20 bulk metallic glass.* Journal of Non-Crystalline Solids, 2013. **364**: p. 9-12.
189. Lu, Z.P. and C.T. Liu, *A new glass-forming ability criterion for bulk metallic glasses.* Acta Materialia, 2002. **50**(13): p. 3501-3512.
190. Middleburgh, S.C., D.M. King, G.R. Lumpkin, M. Cortie and L. Edwards, *Segregation and migration of species in the CrCoFeNi high entropy alloy.* Journal of Alloys and Compounds, 2014. **599**: p. 179-182.
191. Wu, J., S. Lin, J. Yeh, S. Chen, Y. Huang and H. Chen, *Adhesive wear behavior of AlxCoCrCuFeNi high-entropy alloys as a function of aluminium content.* Wear, 2006: p. 513-519.
192. Hemphill, M., T. Yuan, G. Wang, J. Yeh, C. Tsai, A. Chuang and P. Liaw, *Fatigue behavior of Al0.5CoCrCuFeNi high entropy alloys.* Acta Materialia, 2012: p. 2723-5734.
193. Zhang, Y., X. Yang and P. Liaw, *Alloy design and properties optimization of high-entropy alloys.* Journal of Minerals, Metals and Materials, 2012: p. 831-838.
194. Zaddach, A.J., C. Niu, C.C. Koch and D.L. Irving, *Mechanical Properties and Stacking Fault Energies of NiFeCrCoMn High-Entropy Alloy.* JOM, 2013. **65**(12): p. 1780-1789.
195. Abhaya, S., R. Rajaraman, S. Kalavathi and G. Amarendra, *Positron annihilation studies on FeCrCoNi high entropy alloy.* Journal of Alloys and Compounds, 2015. **620**: p. 277-282.
196. Butler, T.M., J.P. Alfano, R.L. Martens and M. Weaver, *High-Temperature Oxidation Behavior of Al-Co-Cr-Ni-(Fe or Si) Multicomponent High-Entropy Alloys.* Jom, 2015. **67**(1): p. 246-259.
197. Middleburgh, S. and R. Grimes, *Defects and transport processes in beryllium.* Acta Materialia, 2011: p. 7095-7103.
198. Wynblatt, P., *Calculation of vacancy migration energy in cubic crystals.* Journal of Physics and Chemistry of Solids, 1968: p. 215-&.
199. Nguyen-Manh, D., A. Horsfield and S. Dudarev, *Self-interstitial atom defects in bcc transition metals: Group-specific trends.* Physical Reveiw B, 2006: p. 020101.
200. LaBrosse, M., L. Chen and J. Johnson, *First principles study of vacancy and tungsten diffusion in fcc cobalt.* Modelling and Simulation in Materials Science and Engineering, 2010: p. 015008.
201. Li, B., Q. Zhang, L. Chen, P. Cui and X. Pan, *Vacany-mediated diffusion of carob in cobalt and its influence on CO activation.* Physical Chemistry Chemical Physics, 2010: p. 7848-7855.
202. Domain, C. and C. Becquart, *Ab initio calculations of defects in Fe and dilute Fe-Cu alloys.* Physical Review B, 2002: p. 024103.
203. Johnson, R., *Point-defect calculations for an fcc lattice.* Physical Review, 1966: p. 423-&.
204. Baskes, M., *Determination of modified embedded atom method parameters for nickel.* Materials Chemistry and Physics, 1997: p. 152-158.
205. Ropo, M., K. Kokko, M.P.J. Punkkinen, S. Hogmark, J. Kollár, B. Johansson and L. Vitos, *Theoretical evidence of the compositional threshold behavior of FeCr surfaces.* Physical Review B, 2007. **76**(22): p. 220401.
206. Wang, W.-R., W.-L. Wang and J.-W. Yeh, *Phases, microstructure and mechanical properties of AlxCoCrFeNi high-entropy alloys at elevated temperatures.* Journal of Alloys and Compounds, 2014. **589**(0): p. 143-152.
207. Ryan, M., R. Newman and G. Thompson, *A scanning tunnelling microscopy study of structure and structural relaxation in passive oxide films on Fe-Cr alloys.* Philosophical Magazine B, 1994. **70**(2): p. 241-251.
208. Pettifor, D., *A quantum-mechanical critique of the Miedema rules for alloy formation.* Solid State Physics, 1987. **40**: p. 43-92.
209. Zhu, J.H., C.T. Liu, L.M. Pike and P.K. Liaw, *Enthalpies of formation of binary Laves phases.* Intermetallics, 2002. **10**(6): p. 579-595.

210. Chelikowsky, J.R., *Microscopic basis of Miedema's theory of alloy formation.* Physical Review B, 1982. **25**(10): p. 6506-6508.
211. Zhang, Y.L., H.S. Liu and Z.P. Jin, *Thermodynamic assessment of the Nb-Ti system.* Calphad-Computer Coupling of Phase Diagrams and Thermochemistry, 2001. **25**(2): p. 305-317.
212. Kim, D., V. Manga, S. Prins and Z.-K. Liu, *First-principles calculations and thermodynamic modeling of the Al–Pt binary system.* Calphad, 2011. **35**(1): p. 20-29.
213. Tong, C., M. Chen, S. Chen, J. Yeh, T. Shun, S. Lin and S. Chang, *Mechanical performance of the AlxCoCrCuFeNi high-entropy alloy system with multiprincipal elements.* Metallurgical and Materials Transactions A, 2005: p. 1264-1271.
214. Praveen, S., B. Murty and R. Kottada, *Alloying behavior in muli-component AlCoCrCuFe and NiCoCrCuFe high entropy alloys.* Materials Science and Engineering A, 2012: p. 83-89.
215. Li, C., M. Zhao, J. Li and Q. Jiang, *B2 structure of high-entropy alloys with addition of Al.* Journal of Applied Physics, 2008: p. 113504-1 - 113504-6.
216. Wu, Y.D., Y.H. Cai, T. Wang, J.J. Si, J. Zhu, Y.D. Wang and X.D. Hui, *A refractory Hf25Nb25Ti25Zr25 high-entropy alloy with excellent structural stability and tensile properties.* Materials Letters, 2014. **130**: p. 277-280.
217. Zou, Y., S. Maiti, W. Steurer and R. Spolenak, *Size-dependent plasticity in an $Nb_{25}Mo_{25}Ta_{25}W_{25}$ refractory high-entropy alloy.* Acta Materialia, 2014. **65**: p. 85-97.
218. Zhang, F., C. Zhang, S.L. Chen, J. Zhu, W.S. Cao and U.R. Kattner, *An understanding of high entropy alloys from phase diagram calculations.* Calphad-Computer Coupling of Phase Diagrams and Thermochemistry, 2014. **45**: p. 1-10.
219. Ng, C., S. Guo, J. Luan, S. Shi and C. Liu, *Entropy-driven phase stability and slow diffusion kinetics in an Al0.5CoCrCuFeNi high entropy alloy.* Intermetallics, 2012: p. 165-172.
220. Yeh, J.W., S.Y. Chang, Y.D. Hong, S.K. Chen and S.J. Lin, *Anomalous decrease in X-ray diffraction intensities of Cu-Ni-Al-Co-Cr-Fe-Si alloy systems with multi-principal elements.* Materials Chemistry and Physics, 2007. **103**(1): p. 41-46.
221. Zuo, T.T., R.B. Li, X.J. Ren and Y. Zhang, *Effects of Al and Si addition on the structure and properties of CoFeNi equal atomic ratio alloy.* Journal of Magnetism and Magnetic Materials, 2014. **371**: p. 60-68.
222. Sigma-Aldrich, *https://www.sigmaaldrich.com.* Accessed online May, 2015.
223. Egami, T., W. Guo, P. Rack and T. Nagase, *Irradiation Resistance of Multicomponent Alloys.* Metallurgical and Materials Transactions A, 2014. **45**(1): p. 180-183.
224. Nagase, T., P.D. Rack, J.H. Noh and T. Egami, *In-situ TEM observation of structural changes in nano-crystalline CoCrCuFeNi multicomponent high-entropy alloy (HEA) under fast electron irradiation by high voltage electron microscopy (HVEM).* Intermetallics, 2015. **59**: p. 32-42.
225. Liaw, P.K., T. Egami, C. Zhang, F. Zhang and Y. Zhang, *Radiation behavior of high-entropy alloys for advanced reactors*. 2015: SciTech Connect. p. 1-121.
226. Zinkle, S.J. and L.L. Snead, *Designing Radiation Resistance in Materials for Fusion Energy*.* Annual Review of Materials Research, 2014. **44**: p. 241-267.
227. Enomoto, M., *The Nb-Ti-V system (niobium-titanium-vanadium).* Journal of Phase Equilibria, 1991. **12**(3): p. 359-362.
228. Fischer-Cripps, A.C., *Factors Affecting Nanoindentation Test Data*. 2000: Springer.
229. Northwood, D., I. London and L. Bähen, *Elastic constants of zirconium alloys.* Journal of nuclear materials, 1975. **55**(3): p. 299-310.
230. Torimaru, T., T. Yasuda and M. Nakatsuka, *Changes in mechanical properties of irradiated Zircaloy-2 fuel cladding due to short term annealing.* Journal of Nuclear Materials, 1996. **238**(2–3): p. 169-174.
231. Ledbetter, H., *Stainless-steel elastic constants at low temperatures.* Journal of Applied Physics, 1981. **52**(3): p. 1587-1589.
232. Peckner, D. and I.M. Bernstein, *Handbook of stainless steels*. 1977: McGraw-Hill New York, NY.
233. Senkov, O.N., S.V. Senkova, D.B. Miracle and C. Woodward, *Mechanical properties of low-density, refractory multi-principal element alloys of the Cr-Nb-Ti-V-Zr system.* Materials Science and Engineering a-Structural Materials Properties Microstructure and Processing, 2013. **565**: p. 51-62.
234. Haynes, W.M., *CRC handbook of chemistry and physics*. 2014: CRC press.
235. Klueh, R.L., *Ferritic/martensitic steels for advanced nuclear reactors.* Transactions of the Indian Institute of Metals, 2009. **62**(2): p. 81-87.
236. Ren, B., Z. Liu, B. Cai, M. Wang and L. Shi, *Aging behavior of a CuCr2Fe2NiMn high-entropy alloy.* Materials and Design, 2012: p. 121–126.

237. Wen, L., H. Kou, J. Li, H. Chang, X. Xue and L. Zhou, *Effect of aging temperature on microstructure and properties of AlCoCrCuFeNi high-entropy alloy.* Intermetallics, 2009: p. 266-269.
238. Kröger, F. and H. Vink, *Relations between the concentrations of imperfections in crystalline solids.* Solid State Physics-Advances in research and applications, 1956: p. 307-435.
239. Masuda, K., *Vacancies and small vacancy clusters in BCC transition metals: calculation of binding energy, atomic relaxation and electronic and vibrational densities of states.* Journal de Physique, 1982. **43**(6): p. 921-930.
240. Korhonen, T., M. Puska and R. Nieminen, *Vacancy-formation energies for fcc and bcc transition metals.* Physical Review B, 1995. **51**(15): p. 9526.
241. Korzhavyi, P.A., I.A. Abrikosov, B. Johansson, A. Ruban and H.L. Skriver, *First-principles calculations of the vacancy formation energy in transition and noble metals.* Physical Review B, 1999. **59**(18): p. 11693.
242. Le Bacq, O., F. Willaime and A. Pasturel, *Unrelaxed vacancy formation energies in group-IV elements calculated by the full-potential linear muffin-tin orbital method: Invariance with crystal structure.* Physical Review B, 1999. **59**(13): p. 8508.
243. Derlet, P.M., D. Nguyen-Manh and S.L. Dudarev, *Multiscale modeling of crowdion and vacancy defects in body-centered-cubic transition metals.* Physical Review B, 2007. **76**(5): p. 054107.
244. Vérité, G., C. Domain, C.-C. Fu, P. Gasca, A. Legris and F. Willaime, *Self-interstitial defects in hexagonal close packed metals revisited: Evidence for low-symmetry configurations in Ti, Zr, and Hf.* Physical Review B, 2013. **87**(13): p. 134108.
245. Willaime, F. and C. Massobrio, *Development of an N-body interatomic potential for hcp and bcc zirconium.* Physical Review B, 1991. **43**(14): p. 11653.
246. Kittiratanawasin, L., R. Smith, B.P. Uberuaga and K. Sickafus, *Displacement threshold and Frenkel pair formation energy in ionic systems.* Nuclear Instruments and Methods in Physics Research Section B: Beam Interactions with Materials and Atoms, 2010. **268**(19): p. 2901-2906.
247. Broeders, C.H.M. and A.Y. Konobeyev, *Defect production efficiency in metals under neutron irradiation.* Journal of Nuclear Materials, 2004. **328**(2–3): p. 197-214.
248. Nastasi, M., J. Mayer and J.K. Hirvonen, *Ion-solid interactions: fundamentals and applications*. 1996: Cambridge University Press.
249. Kirk, M.A., P.M. Baldo, A.C. Liu, E.A. Ryan, R.C. Birtcher, Z. Yao, S. Xu, M.L. Jenkins, M. Hernandez-Mayoral and D. Kaoumi, *In situ transmission electron microscopy and ion irradiation of ferritic materials.* Microscopy research and technique, 2009. **72**(3): p. 182-186.
250. Randle, V. and O. Engler, *Introduction to texture analysis: macrotexture, microtexture and orientation mapping*. 2000: CRC press.
251. Alatalo, M., M.J. Puska and R.M. Nieminen, *First-principles study of He in Si.* Physical Review B, 1992. **46**(19): p. 12806-12809.
252. Morishita, K., R. Sugano and B.D. Wirth, *MD and KMC modeling of the growth and shrinkage mechanisms of helium–vacancy clusters in Fe.* Journal of Nuclear Materials, 2003. **323**(2–3): p. 243-250.
253. Logan, R.M. and D.T.J. Hurle, *Calculations of point defect concentrations and nonstoichiometry in GaAs.* Journal of Physics and Chemistry of Solids, 1971. **32**(8): p. 1739-1753.
254. Straumanis, M. and C. Kim, *Phase extent of gallium arsenide determined by the lattice constant and density method.* Acta Crystallographica, 1965. **19**(2): p. 256-259.
255. Odette, G.R., M.J. Alinger and B.D. Wirth, *Recent developments in irradiation-resistant steels*, in *Annual Review of Materials Research*. 2008, Annual Reviews: Palo Alto. p. 471-503.
256. Lefebvre, F. and C. Lemaignan, *Analysis with heavy ions of the amorphisation under irradiation of Zr(Fe,Cr)2 precipitates in zircaloy-4.* Journal of Nuclear Materials, 1990. **171**(2–3): p. 223-229.
257. Griffiths, M., *A review of microstructure evolution in zirconium alloys during irradiation.* Journal of Nuclear Materials, 1988. **159**: p. 190-218.
258. Allen, T.R. and G. Was, *Modeling radiation-induced segregation in austenitic Fe–Cr–Ni alloys.* Acta materialia, 1998. **46**(10): p. 3679-3691.
259. Nemoto, Y., A. Hasegawa, M. Satou and K. Abe, *Microstructural development of neutron irradiated W–Re alloys.* Journal of nuclear materials, 2000. **283**: p. 1144-1147.
260. Lee, J., C.R. Lear, X. Zhang, P. Bellon and R.S. Averback, *Irradiation-Induced Nanoprecipitation in Ni-W Alloys.* Metallurgical and Materials Transactions A, 2015. **46**(3): p. 1046-1061.
261. Leyens, C. and M. Peters, *Titanium and titanium alloys*. 2003: Wiley Online Library.

262. Kulcinski, G. and J. Brimhall, *SWELLING IN REFRACTORY METALS DURING HIGH TEMPERATURE ION BOMBARDMENT*. 1971, Battelle-Northwest, Richland, Wash. Pacific Northwest Lab.
263. Shun, T. and Y. Du, *Age hardening of the $Al_{0.3}CoCrFeNiC_{0.1}$ high entropy alloy.* Journal of Alloys and Compounds, 2009: p. 269-272.
264. Chen, M.R., S.J. Lin, J.W. Yeh, S.K. Chen, Y.S. Huang and C.P. Tu, *Microstructure and properties of Al0.5CoCrCuFeNiTix (x=0-2.0) high-entropy alloys.* Materials Transactions, 2006. **47**(5): p. 1395-1401.
265. Chen, M., S. Lin, J. Yeh, S. Chen, Y. Huang and M. Chuang, *Effect of vanadium addition on the microstructure, hardness, and wear resistance of Al0.5CoCrCuFeNi high-entropy alloy.* Metallurgical and Materials Transactions, 2006: p. 1363-1369.
266. Hsu, U., U. Hung, J. Yeh, S. Chen, Y. Huang and C. Yang, *Alloying behavior of iron, gold and silver in AlCoCrCuNi-based equimolar high-entropy alloys.* Materials Science and Engineering A, 2007: p. 460-461.
267. Zhang, Y., Y.J. Zhou, X.D. Hui, M.L. Wang and G.L. Chen, *Minor alloying behavior in bulk metallic glasses and high-entropy alloys.* Science in China Series G-Physics Mechanics & Astronomy, 2008. **51**(4): p. 427-437.
268. Chen, J.H., P.H. Hua, P.N. Chen, C.M. Chang, M.C. Chen and W.T. Wu, *Characteristics of multi-element alloy cladding produced by TIG process.* Materials Letters, 2008. **62**(15): p. 2490-2492.
269. Zhou, Y.J., Y. Zhang, T.N. Kim and G.L. Chen, *Microstructure characterizations and strengthening mechanism of multi-principal component AlCoCrFeNiTi0.5 solid solution alloy with excellent mechanical properties.* Materials Letters, 2008. **62**(17-18): p. 2673-2676.
270. Lin, Y.C. and Y.H. Cho, *Elucidating the microstructure and wear behavior for multicomponent alloy clad layers by in situ synthesis.* Surface & Coatings Technology, 2008. **202**(19): p. 4666-4672.
271. Hu, Z., Y. Zhan, G. Zhang, J. She and C. Li, *Effect of rare earth Y addition on the microstructure and mechanical properties of high entropy AlCoCrCuNiTi alloys.* Materials and Design, 2010: p. 1599-1602.
272. Zhu, J.M., H.M. Fu, H.F. Zhang, A.M. Wang, H. Li and Z.Q. Hu, *Microstructure and compressive properties of multiprincipal component AlCoCrFeNiCx alloys.* Journal of Alloys and Compounds, 2011. **509**(8): p. 3476-3480.
273. Chang, Z.C., S.C. Liang, S. Han, Y.K. Chen and F.S. Shieu, *Characteristics of TiVCrAlZr multi-element nitride films prepared by reactive sputtering.* Nuclear Instruments & Methods in Physics Research Section B-Beam Interactions with Materials and Atoms, 2010. **268**(16): p. 2504-2509.
274. Cunliffe, A., J. Plummer, I. Figueroa and I. Todd, *Glass formation in a high entropy alloy system by design.* Intermetallics, 2012: p. 204-207.
275. Liu, L., J. Zhu, C. Zhang, J. Li and Q. Jiang, *Microstructure and the properties of FeCoCuNiSnx high entropy alloys.* Materials Science and Engineering A, 2012: p. 64-68.
276. Singh, A.K. and A. Subramaniam, *On the formation of disordered solid solutions in multi-component alloys.* Journal of Alloys and Compounds, 2014. **587**: p. 113-119.
277. Tong, C.J., Y.L. Chen, S.K. Chen, J.W. Yeh, T.T. Shun, C.H. Tsau, S.J. Lin and S.Y. Chang, *Microstructure characterization of $Al_xCoCrCuFeNi$ high-entropy alloy system with multiprincipal elements.* Metallurgical and Materials Transactions A-Physical Metallurgy and Materials Science, 2005. **36A**(4): p. 881-893.
278. Li, C., J. Li, M. Zhao and Q. Jiang, *Effect of alloying elements on microstructure and properties of multiprincipal elements high-entropy alloys.* Journal of Alloys and Compounds, 2009: p. 752–757.
279. Ma, L.Q., L.M. Wang, T. Zhang and A. Inoue, *Bulk glass formation of Ti-Zr-Hf-Cu-M (M=Fe, Co, Ni) alloys.* Materials Transactions, 2002. **43**(2): p. 277-280.
280. Zhou, Y.J., Y. Zhang, Y.L. Wang and G.L. Chen, *Solid solution alloys of AlCoCrFeNiTix with excellent room-temperature mechanical properties.* Applied Physics Letters, 2007. **90**(18): p. 3.
281. Wang, F. and Y. Zhang, *Effect of Co addition on crystal structure and mechanical properties of Ti0.5CrFeNiAlCo high entropy alloy.* Materials Science and Engineering A, 2008: p. 214-216.
282. Yeh, J.-W., S.-J. Lin, T.-S. Chin, J.-Y. Gan, S.-K. Chen, T.-T. Shun, C.-H. Tsau and S.-Y. Chou, *Formation of simple crystal structures in Cu-Co-Ni-Cr-Al-Fe-Ti-V alloys with multiprincipal metallic elements.* Metallurgical and Materials Transactions A, 2004. **35**(8): p. 2533-2536.
283. Wang, X., Y. Zhang, Y. Qiao and G. Chen, *Novel microstructure and properties of multicomponent $CoCrCuFeNiTi_x$ alloys.* Intermetallics, 2007. **15**(3): p. 357-362.

284. Hsu, C.Y., W.R. Wang, W.Y. Tang, S.K. Chen and J.W. Yeh, *Microstructure and Mechanical Properties of New AlCoxCrFeMo0. 5Ni High-Entropy Alloys.* Advanced Engineering Materials, 2010. **12**(1-2): p. 44-49.
285. Hsu, C., T. Sheu, J. Yeh and S. Chen, *Effect of iron content on wear behavior of $AlCoCrFe_xMo_{0.5}Ni$ high-entropy alloys.* Wear, 2010: p. 653-659.
286. Shun, T.T., C.H. Hung and C.F. Lee, *Formation of ordered/disordered nanoparticles in FCC high entropy alloys.* Journal of Alloys and Compounds, 2010. **493**(1-2): p. 105-109.
287. Tung, C., W. Yeh, T. Shun, S. Chen, Y. Huang and H. Chen, *On the elemental effect of AlCoCrCuFeNi high-entropy Alloy system.* Materials Letters, 2007: p. 1-5.
288. Hsieh, K., C. Yu, W. Hsieh, W. Chiang, J. Ku, J. Lai, C. Tu and C. Yang, *The microstructure and phase equilibrium of new high performance high-entropy alloys.* Journal of Alloys and Compounds, 2009: p. 209-212.
289. Shun, T., C. Hung and C. Lee, *The effects of secondary elemental Mo or Ti addition in $Al_{0.3}$CoCrFeNi high-entropy alloy on age hardening at 700.* Journal of Alloys and Compounds, 2010: p. 55-58.
290. Ren, B., Z. Liu, D. Li, L. Shi, B. Cai and M. Wang, *Effect of elemental interaction on microstructure of CuCrFeNiMn high entropy alloy system.* Journal of Alloys and Compounds, 2010: p. 148–153.
291. Durga, A., K.C. Kumar and B.S. Murty, *Phase Formation in Equiatomic High Entropy Alloys: CALPHAD Approach and Experimental Studies.* Transactions of the Indian Institute of Metals, 2012. **65**(4): p. 375-380.
292. Senkov, O.N., F. Zhang and J.D. Miller, *Phase Composition of a CrMo0.5NbTa0.5TiZr High Entropy Alloy: Comparison of Experimental and Simulated Data.* Entropy, 2013. **15**(9): p. 3796-3809.
293. Dong, Y., Y.P. Lu, J.R. Kong, J.J. Zhang and T.J. Li, *Microstructure and mechanical properties of multi-component $AlCrFeNiMo_x$ high-entropy alloys.* Journal of Alloys and Compounds, 2013. **573**: p. 96-101.
294. Liu, C.M., H.M. Wang, S.Q. Zhang, H.B. Tang and A.L. Zhang, *Microstructure and oxidation behavior of new refractory high entropy alloys.* Journal of Alloys and Compounds, 2014. **583**: p. 162-169.
295. Dong, Y., K.Y. Zhou, Y. Lu, X.X. Gao, T.M. Wang and T.J. Li, *Effect of vanadium addition on the microstructure and properties of AlCoCrFeNi high entropy alloy.* Materials & Design, 2014. **57**: p. 67-72.
296. Poletti, M.G., G. Fiore, B.A. Szost and L. Battezzati, *Search for high entropy alloys in the X-NbTaTiZr systems (X = Al, Cr, V, Sn).* Journal of Alloys and Compounds, 2015. **620**: p. 283-288.
297. Wang, Z.Q., X.R. Wang, H. Yue, G.T. Shi and S.H. Wang, *Microstructure, thermodynamics and compressive properties of AlCoCrCuMn-x (x = Fe, Ti) high-entropy alloys.* Materials Science and Engineering a-Structural Materials Properties Microstructure and Processing, 2015. **627**: p. 391-398.
298. Lilensten, L., J.P. Couzinie, L. Perriere, J. Bourgon, N. Emery and I. Guillot, *New structure in refractory high-entropy alloys.* Materials Letters, 2014. **132**: p. 123-125.
299. Couzinie, J.P., G. Dirras, L. Perriere, T. Chauveau, E. Leroy, Y. Champion and I. Guillot, *Microstructure of a near-equimolar refractory high-entropy alloy.* Materials Letters, 2014. **126**: p. 285-287.
300. Shun, T.-T., C.-H. Hung and C.-F. Lee, *Formation of ordered/disordered nanoparticles in FCC high entropy alloys.* Journal of Alloys and Compounds, 2010. **493**(1–2): p. 105-109.
301. Zhang, Y., X.F. Wang, G. Chen and Y. Qiao, *Effect of Ti on the microstructure and properties of $CoCrCuFeNiTi_x$ high-entropy alloys.* Annales de Chimie Science des Matériaux, 2007. **32**(1): p. 103-104.

Appendix

Previously characterised HEAs

Table S1. 193 experimentally studied systems from literature used to benchmark the current method separated into sections: Intermetallic/segregated, solid solution, exceptions. Phases are denoted as B = BCC, F = FCC, H = HCP (that is followed by segregated element in brackets, if applicable), σ = sigma phase, B2 = ordered BCC, Am = amorphous, tet = tetragonal, orth = orthorhombic, ? = unknown.

System	Phases	References
Intermetallic/segregated		
$Al_{0.3}CoCrFeNiC_{0.1}$	F + k1	[263]
AlCoCrFeNi	B + $L1_2$	[79]
$Al_{0.5}CoCrCuFeNi$	F + F(Cu)	[264]
$Al_{0.5}CoCrCuFeNiTi_{0.2}$	F + F(Cu)	[264]
$Al_{0.5}CoCrCuFeNiTi_{0.4}$	F + B + B + F(Cu)	[264]
$Al_{0.5}CoCrCuFeNiTi_{0.8}$	F + B + B + CoCr + F(Cu)	[264]
$Al_{0.5}CoCrCuFeNiTi$	F + B + B + CoCr + F(Cu)	[264]
$Al_{0.5}CoCrCuFeNiTi_{1.2}$	F + B + B + Ti_2Ni + CoCr + F(Cu)	[264]
$Al_{0.5}CoCrCuFeNiTi_{1.4}$	F + B + B2 + Ti_2Ni + F(Cu)	[264]
$Al_{0.5}CoCrCuFeNiTi_{1.6}$	F + B + B2 + Ti_2Ni + F(Cu)	[264]
$Al_{0.5}CoCrCuFeNiTi_{1.8}$	F + B + B2 + Ti_2Ni + F(Cu)	[264]
$Al_{0.5}CoCrCuFeNiTi_2$	F + B + B2 + Ti_2Ni + F(Cu)	[264]
CoCrCuFeNi	F + F(Cu)	[213]
$Al_{0.5}CoCrCuFeNi$	F + F(Cu)	[213]
$Al_{1.0}CoCrCuFeNi$	B + B2 + F(Cu)	[213]
$Al_{1.5}CoCrCuFeNi$	B + B2 + F(Cu)	[213]
$Al_{2.0}CoCrCuFeNi$	B + B2 + F(Cu)	[213]
$Al_{2.5}CoCrCuFeNi$	B + B2 + F(Cu)	[213]
$Al_{3.0}CoCrCuFeNi$	B + B2 + F(Cu)	[213]

$Al_{0.5}CoCrCuFeNi$	F + F(Cu)	[265]
$Al_{0.5}CoCrCuFeNiV_{0.2}$	F + F(Cu)	[265]
$Al_{0.5}CoCrCuFeNiV_{0.4}$	F + B + F(Cu)	[265]
$Al_{0.5}CoCrCuFeNiV_{0.6}$	F + B + F(Cu)	[265]
$Al_{0.5}CoCrCuFeNiV_{0.8}$	F + B + F(Cu)+ σ	[265]
$Al_{0.5}CoCrCuFeNiV$	F + B + F(Cu) + σ	[265]
$Al_{0.5}CoCrCuFeNiV_{1.2}$	B + F(Cu)	[265]
$Al_{0.5}CoCrCuFeNiV_{1.4}$	B + F(Cu)	[265]
$Al_{0.5}CoCrCuFeNiV_{1.6}$	B + F(Cu)	[265]
$Al_{0.5}CoCrCuFeNiV_{1.8}$	B + F(Cu)	[265]
$Al_{0.5}CoCrCuFeNiV_{2}$	B + F(Cu)	[265]
AlCuNi	B + F(Cu)	[220]
AlCoCrCuNi	B + B2 + F(Cu)	[266]
AgAlCoCrCuNi	B + F(Cu) + Ag	[266]
AlAuCoCrCuNi	F + AuCu	[266]
$Al_4Cu_{48}Zr_{48}$	Am + $Cu_{10}Zr_7$ + CuZr	[267]
$Al_{3.96}Cu_{47.52}Zr_{47.52}Y_1$	Am + CuZr	[267]
$Al_{3.92}Cu_{47.04}Zr_{47.04}Y_2$	Am	[267]
$Al_{3.88}Cu_{46.56}Zr_{46.56}Y_3$	Am + $Cu_{10}Zr_7$ + CuZr	[267]
$Al_{3.80}Cu_{45.6}Zr_{45.6}Y_5$	Am + $Cu_{10}Zr_7$ + CuZr	[267]
$Al_{8.45}Co_{10.37}Cr_{9.79}Fe_{48.54}Mo_{13.22}Ni_{9.63}$	B + Tet	[268]
$Al_{14.10}Co_{16.48}Cr_{16.63}Fe_{16.28}Mo_{18.8}Ni_{18.8}$	B + Tet	[268]
$Al_{19.93}Co_{18.24}Cr_{17.39}Fe_{17.22}Ni_{17.81}Ti_{9.41}$	B + B2	[269]
AlCoCrFeNiW	F + B2 + W	[270]
$AlCoCr_2FeNi$	B + B2 + L12	[215]
AlCoCrFeNi	B + B2 + L12	[215]

$Al_{1.5}CoCrFeNi$	B + B2	[215]
$Al_2CoCrFeNi$	B + B2	[215]
$Al_{2.5}CoCrFeNi$	B + B2	[215]
$Al_3CoCrFeNi$	B + B2	[215]
AlCoCrCuNiTi	B + F(Cu) + Cr	[271]
$AlCoCrCuNiTiY_{0.5}$	$Cu + Cu_2Y + Cr + AlNi_2Ti$	[271]
$AlCoCrCuNiTiY_{0.8}$	$AlNi_2Ti + Cu_2Y$	[271]
AlCoCrCuNiTiY	$AlNi_2Ti + Cu_2Y + Cr + ?$	[271]
AlCoCrFeNi	B + B2	[272]
AlCrNTiVZr	Am	[273]
CuNiPPdPt	$F + (Pd,Ni) + Ni_3P + PtP_2$	[186]
$CrMo_{0.5}NbTa_{0.5}TiZr$	B + B + Laves	[75]
$CuNbNi_{0.57}TiZr$	B + Nb + ?	[274]
$CuNbNi_{0.71}TiZr$	B + Nb + ?	[274]
CuNbNiTiZr	$B + Nb + Cu_{10}Zr_7 + ?$	[274]
$CuNbNi_{1.3}TiZr$	$B + Nb + Cu_{10}Zr_7 + Ni_{42}(Zr,Ti)_{58} + ?$	[274]
CoCuFeNi	F + F(Cu)	[275]
$Cu_{23.2}Co_{26.5}Fe_{24.9}Ni_{25.4}$	F + F(Cu)	[276]
CuCoCrFeNi	F + F(Cu)	[214]
$Co_{20.9}Cr_{21.4}Cu_{16.5}Fe_{20.8}Ni_{20.5}$	F + F(Cu)	[277]
$Cu_{0.5}CoCrFeNi$	F + F(Cu)	[98]
ZrCrFeNiCu	B2 + ?	[278]
ZrHfTiCuFe	Am + ?	[279]
ZrHfTiCuCo	Am + ?	[279]
AlCuNi	F + B2	[220]
AlTi1.5CoCrFeNi	B + B2	[280]

$Al_{28.5}Cr_{27.3}Fe_{24.9}Ni_{19.3}$	B + B2	[276]
AlTiCoCrNiCu	B2 + F + σ	[271]
AlTiCoCrFeNi	B + B2	[280]
$Al_{30.13}Co_{17.65}Cr_{17.96}Fe_{17.29}Ni_{16.97}$	B + B2	[65]
$Al_{38.9}Co_{12.6}Cr_{11.2}Cu_{11.7}Fe_{13.5}Ni_{12.1}$	F + F(Cu) + B2	[277]
$Al_{36.3}Co_{13.0}Cr_{11.8}Cu_{11.3}Fe_{14.1}Ni_{13.4}$	F + F(Cu) + B2	[277]
$Al_{25.53}Co_{19.24}Cr_{19.06}Fe_{19.11}Ni_{19.06}$	B + B2	[65]
$Al_{27.44}Co_{18.69}Cr_{18.26}Fe_{17.95}Ni_{17.66}$	B + B2	[65]
$AlTi_{0.5}CoCrFeNi$	B + B2	[281]
AlCoCuNi	F + B2	[220]
$AlTi_{0.5}Co_{2.0}CrFeNi$	F + B2	[281]
$AlTi_{0.5}Co_{3.0}CrFeNi$	F + B2	[281]
$Al_{28.5}Co_{13.8}Cr_{13.9}Cu_{13.5}Fe_{15.5}Ni_{14.8}$	F + F(Cu) + B2	[277]
$Al_{21.4}Cu_{7.8}Co_{23.5}Fe_{25.1}Ni_{22.2}$	F + F(Cu) + B2	[276]
$AlCu_{0.5}CoCrNi$	B2 + F	[282]
CuTiCoCrFeNi	F + L	[283]
$Al_{20.12}Co_{19.58}Cr_{20.7}Fe_{20.33}Ni_{19.27}$	F + B2	[65]
$Al_{24.3}Co_{15.5}Cr_{15.6}Cu_{13.7}Fe_{15.6}Ni_{15.3}$	F + F(Cu) + B2	[277]
$AlMo_{0.5}Co_{0.5}CrFeNi$	B2 + F + σ	[284]
$AlMo_{0.5}CoCrFe_{0.6}Ni$	B2 + F + σ	[285]
AlCuCoCrNi	F + B2 + F	[220]
$AlMo_{0.5}CoCrFeNi$	B2 + F + σ	[285]
$Al1_{7.33}Co_{21.15}Cr_{20.93}Fe_{20.18}Ni_{20.43}$	F + B2	[65]
$Ti_{11.3}Co_{22.9}Cr_{20.2}Fe_{20.3}Ni_{25.3}$	F + H + L12	[286]
$CuTi_{0.8}CoCrFeNi$	F + L	[283]
$AlMo_{0.5}CoCrFe_{1.5}Ni$	B2 + σ	[285]

$AlMo_{0.5}Co_{1.5}CrFeNi$	B2 + F + σ	[284]
$Al_{15.66}Co_{21.19}Cr_{21.54}Fe_{20.92}Ni_{20.69}$	F + B2	[285]
$AlMo_{0.5}Co_{2.0}CrFeNi$	B2 + F + σ	[284]
$AlCu_{0.5}CoCrFeNi$	B2 + F	[287]
$AlCuCo_{0.5}CrFeNi$	B2 + F + F(Cu)	[287]
$AlCuCoCr_{0.5}FeNi$	B2 + F + F(Cu)	[287]
$AlCuCoCrFeNi_{0.5}$	B2 + F + F(Cu)	[287]
$AlCuCoCrFe_{0.5}Ni$	B2 + F + F(Cu)	[287]
$Al_{16.6}Co_{17.0}Cr_{17.2}Cu_{15.6}Fe_{16.8}Ni_{16.8}$	F + F(Cu) + B2	[277]
$Al_{12.1}Co_{22.63}Cr_{21.55}Fe_{21.66}Ni_{22.06}$	F + B2	[288]
$CuTi_{0.5}CoCrFeNi$	F + L12	[283]
$Al_{0.3}Ti_{0.1}CoCrFeNi$	F + L12	[289]
$Al_{8.03}Co_{22.63}Cr_{23.44}Fe_{23.22}Ni_{22.69}$	F + B2	[65]
$Al_{9.4}Co_{17.7}Cr_{18.2}Cu_{17.7}Fe_{18.0}Ni_{19.0}$	F + Cu + L12	[277]
$Mn_2CrFeNi_2Cu$	F + F(Cu)	[290]
MoCrFeNiCu	F + F(Cu)	[278]
$Mn_2CrFe_2NiCu_2$	F + B + F(Cu)	[290]
$Mn_2Cr_2Fe_2Ni_2Cu$	F + F(Cu)	[290]
MnCrFeNiCu	F + B + F(Cu)	[290]
$MnCr_2Fe_2NiCu$	F + B + F(Cu)	[290]
CuMnCoCrFeNi	F + F(Cu)	[6]
$MnCrFe_2Ni_2Cu_2$	F + F(Cu)	[290]
CrCuMnNi	B + F(Cu)	[291]
CrNbTiZr	B + Laves	[76]
CrNbTiVZr	B + Laves	[76]
$CrMo_{0.5}NbTa_{0.5}TiZr$	B + B + Laves	[292]

AlCrFeNi	B + B2	[293]
$AlCrFeMo_{0.2}Ni$	B + B2	[293]
$AlCrFeMo_{0.5}Ni$	B + B2	[293]
$AlCrFeMo_{0.8}Ni$	B + B2 + σ	[293]
AlCrFeMoNi	B + B2 + σ	[293]
$Al_{0.5}CrMoNbTi$	B + B + Ti	[294]
$Al_{0.5}CrMoNbTiV$	B + Ti	[294]
CoCrFeNiV	F + σ	[73]
CoCrFeMnNiV	F + σ + tet	[73]
AlCoCrFeNi	B + AlNi	[295]
$AlCoCrFeNiV_{0.2}$	B + AlNi	[295]
$AlCoCrFeNiV_{0.5}$	B + ?	[295]
$AlCoCrFeNiV_{0.8}$	B + ?	[295]
AlCoCrFeNiV	B + ?	[295]
NbSnTaTiZr	B + SnZr	[296]
CrNbTaTiZr	B + HCP + Laves	[296]
AlNbTaTiZr	B + B + AlZr	[296]
AlCoCrCuMnFe	B + B + F(Cu) + ?	[297]
AlCoCrCuMnTi	B + B + F + $AlCu_2$ + ?	[297]
$NbTiV_2Zr$	B	[76]
Solid Solution		
NbHfTiZr	B	[216]
NbTiVZr	B	[76]
CoCrFeMnNi	F + F	[73]
NbTaTiVZr	B + B	[296]
$Ti_{35}Zr_{27.5}Hf_{27.5}Nb_5Ta_5$	Orth + HCP	[298]

NbHfTaTiZr	B + B	[299]
CoFeNi	F	[221]
MoNbTaW	B	[217]
CoCrFeNi	F	[73]
MoNbTiZr	B + B	[193]
$MoNbTiV_{0.25}Zr$	B + B	[193]
$MoNbTiV_{0.5}Zr$	B + B	[193]
$MoNbTiV_{0.75}Zr$	B + B	[193]
MoNbTiVZr	B + B	[193]
CoCrFeMnNi	F	[6]
$W_{27.3}Nb_{22.7}Mo_{25.6}Ta_{24.4}$	B	[74]
$W_{21.1}Nb_{20.6}Mo_{21.7}Ta_{15.6}V_{21.0}$	B	[74]
$Mo_{0.3}CoCrFeNi$	F	[300]
$Co_{24.90}Cr_{25.12}Fe_{24.58}Ni_{25.90}$	F	[98]
$Co_{32.9}Fe_{34.0}Ni_{33.1}$	F	[276]
CoCrFeNi	F	[301]
$CoCrFeMo_{0.22}Ni$	F	[301]
MoNbTaW	B	[74]
MoNbTaVW	B	[74]
NbTaTiHfZr	B	[83]
Exceptions		
$Al_{0.5}CrMoNbV$	B + B	[294]
$Al_{0.5}NbTa_{0.8}Ti_{1.4}V_{0.2}Zr_{1.3}$	B + B	[78]
$Al_{0.3}NbTaTi_{1.4}Zr_{1.3}$	B + B	[78]
$Al_{0.25}CoFeNi$	F	[221]
$Al_{0.5}CoFeNi$	F + B	[221]

$Al_{0.75}CoFeNi$	F + B	[221]
AlCoFeNi	B	[221]
$AlMo_{0.5}NbTaTiZr$	B + B	[78]
$Al_{6.0}Mo_{2.5}Co_{22.2}Cr_{25.6}Fe_{21.0}Ni_{22.7}$	F + F	[286]
$Al_{5.89}Co_{23.21}Cr_{24.49}Fe_{23.82}Ni_{22.59}$	F	[65]
$Al_{6.6}Co_{23.2}Cr_{23.4}Fe_{23.3}Ni_{23.5}$	F	[263]
$AlMo_{0.5}NbTa_{0.5}TiZr$	B + B	[78]
$Al_{0.4}Hf_{0.6}NbTaTiZr$	B	[78]
$AlNb_{1.5}Ta_{0.5}Ti_{1.5}Zr_{0.5}$	B + B	[78]
$Al_{0.4}Hf_{0.6}NbTaTiZr$	B + B	[78]
$Al_{0.3}NbTa_{0.8}Ti_{1.4}V_{0.2}Zr_{1.3}$	B + B	[78]